

PROCEEDINGS

OF 5TH INTERNATIONAL CONFERENCE ON
COMMUNICATIONS, ELECTROMAGNETICS AND MEDICAL
APPLICATIONS (CEMA'10)

Organized by:



FACULTY OF TELECOMMUNICATIONS
TECHNICAL UNIVERSITY OF SOFIA, BULGARIA



NATIONAL TECHNICAL UNIVERSITY OF ATHENS, GREECE,
SCHOOL OF ELECTRICAL AND COMPUTER ENGINEERING

NATIONAL TECHNICAL
UNIVERSITY OF ATHENS,
GREECE



SCHOOL OF ELECTRICAL
AND COMPUTER
ENGINEERING

Athens, Greece
07th - 9th October, 2010

KING 2001, Sofia

Edited by Prof. Dr. Eng. **Dimiter Tz. Dimitrov**

All rights reserved. This book, or parts there of, may not be reproduced in any form or by any means, electronic or mechanical, including photocopying or any information storage and the retrieval system now known or to be invented without written permission from the Publisher.

ISSN: 1314-2100

Printed in Bulgaria
KING 2001, Sofia



P. Frangos



D. Dimitrov

Dear Colleagues,

It is our privilege to thank all of you for your contributions submitted at 5th regular International Conference on 'Communication, Electromagnetic and Medical Applications' CEMA'10. This is a conference which should help future collaboration in the area of engineering, especially in the area of communication technologies and medical applications. This is an important scientific event not only in Balkan region, but in Europe, also. The International Conference on Communication, Electromagnetism and Medical Applications CEMA'10 is dedicated to all essential aspects of the development of global information and communication technologies, and their impact in medicine, as well. The objective of Conference is to bring together lecturers, researchers and practitioners from different countries, working on the field of communication, electromagnetism, medical applications and computer simulation of electromagnetic field, in order to exchange information and bring new contribution to this important field of engineering design and application in medicine. The Conference will bring you the latest ideas and development of the tools for the above mentioned scientific areas directly from their inventors. The objective of the Conference is also to bring together the academic community, researchers and practitioners working in the field of Communication, Electromagnetic and Medical Applications, not only from all over Europe, but also from America and Asia, in order to exchange information and present new scientific and technical contributions. Many well known scientists took part in conference preparation as members of International Scientific Committee or/and as reviewers of submitted papers. I would like to thank all of them for their efforts, for their suggestions and advices.

On behalf of the International Scientific Committee, we would like to wish you successful presentations of your papers, successful discussions and new collaborations for your future scientific investigations. Engineering and medicine should provide high level of living for all people.

P. Frangos
Conference Chairman

D. Dimitrov
Conference Vice Chairman

INTERNATIONAL SCIENTIFIC COMMITTEE

Honorary Chairman:

Prof. N. UZUNOGLU, National Technical University of Athens, Greece

Chairman:

P. FRANGOS, National Technical University of Athens, Greece

Vice Chairmen:

D. TZ. DIMITROV, Technical University of Sofia, Bulgaria
L. SVILAINIS, Kaunas University of Technology, Lithuania

Members:

AMPILOVA, N.	University of Perersburg, Russia
BEHARI, J.	Jawaharlal Nehru University, New Delhi, India
BEKJARSKY, A.	Technical University of Sofia, Bulgaria
BERG, H.	Bioelectrochemical laboratory, Jena, Germany
CARVAHLO, V.	Inst. Sup. de Engenharia do Porto, Portugal
DEKERIS, B.	Kaunas University of Technology, Lithuania
DEMIREV, V.	Technical University of Sofia, Bulgaria
DIB, N.	Jordan University of Science and Technology, Jordan
DONTSCHewa, M.	University of Applied Sciences, Dornbirn, Austria
DUMBRAVA, V.	Kaunas University of Technology, Lithuania
EIDUKAS, D.	Kaunas University of Technology, Lithuania
ESCUDEIRO, N.	Inst. Sup. de Engenharia do Porto, Portugal
GAGO-RIBAS, E.	University of Oviedo, Spain
GOUSSETIS, G.	Heriot - Watt University, United Kingdom
GRIGORIEV, A.	St. Petersburg University, Russia.
GUERGOV, S.	Technical University of Sofia, Bulgaria
HOEYE, S.	University of Oviedo, Spain
HOFMANN, M.	University of Ulm, Germany
HRISTOV, H.	UTFSM, Valparaíso, Chile
HRISTOV, V.	University of Blagoevgrad, Bulgaria
ILIEV, I.	Technical University of Sofia, Bulgaria
JORDANOVA, L.	Technical University of Sofia, Bulgaria
KIROV, G.	Technical University, Varna, Bulgaria
KLIROS, G.	Hellenic Air-Force Academy, Greece
KRIVICKAS, R.	Kaunas University of Technology, Lithuania
MALHEIRO, B.	Inst. Sup. de Engenharia do Porto, Portugal
MALLET, G.	University "Sophia Antipolis", Nice, France
MATSOPOULOS, G.	National Technical University of Athens, Greece
MARTINS, M.	Instituto Superior Técnico, Lisboa, Portugal
MILOVANOVIC, B.	University of Nis, Serbia
MORALES-GONZALES, M.	University of Valladolid, Spain
NIKITA, K.	National Technical University of Athens, Greece
M. NIKOLOVA, M.	High Naval School, Varna, Bulgaria
PETROVSKA, J.	Medical University of Sofia, Bulgaria
PRATO, F.	University of Western Ontario, Canada
ROTH, H.	University of Siegen, Germany
SAUTBEKOV, S.	Euroasian University, Astana, Kazakhstan
SAVOV, A.	Medical University of Sofia, Bulgaria
SAVOV, S.	Technical University of Varna, Bulgaria
SCHADE, H-P.	Technical University of Ilmenau, Germany
SEBASTIAN, J.	Universidad Complutense de Madrid, Spain
SONG, L.	Technical University of Harbin, China
USHEVA, A.	University of Boston, USA

REVIEWERS

BALZANO, Q.	University of Maryland, USA
BEHARI, J.	Jawaharlal Nehru University ,New Delhi, India
BERG, H.	Technical University of Jena, Germany
BOEMO,E.	Technical University of Madrid, Spain
DIMITROV, D.	Technical University of Sofia, Bulgaria
DONTSHEWA, M.	University of Applied Sciences, Dornbirn, Austria
GOUSSETIS, G.	Heriot - Watt University, United Kingdom
HOEYE, S.	University of Oviedo, Spain
MALLET, G.	University "Sophia Antipolis", Nice, France
MARINKEV, V.	Medical University of Plovdiv, Bulgaria
PETROVSKA, J.	Medical University of Sofia, Bulgaria
PRATO, F.	University of Western Ontario, Canada
ROTH, H.	University of Siegen, Germany
SAVOV, A.	Medical University of Sofia, Bulgaria
SCHADE, H-P.	Technical University of Ilmenau, Germany
SONG, L.	Technical University of Harbin, China
USHEVA, A.	University of Boston, USA
VLADIMIROV, K.	Medical University of Sofia, Bulgaria

REGISTRATION

October, 07th 09h - 16h

The conference registration desk will be at:

University Administration Building
Ceremonies Room (zero level of building)
National Technical University of Athens, Greece

CONFERENCE PROGRAM

7th October

Opening ceremony

9h 30min -10 h

University Administration Building
Ceremonies Room (zero level of building)
National Technical University of Athens, Greece

SCIENTIFIC PROGRAM

7th October

FIRST SESSION

10h - 12h

University Administration Building
Ceremonies Room (zero level of building)
National Technical University of Athens, Greece

Chairman: Prof. L. Svilainis, Kaunas University of Technology, Lithuania

FDTD MODELING OF REFRACTOMETRIC OPTICAL SENSORS BASED ON QUASI-ONE-DIMENSIONAL PHOTONIC CRYSTALS, G. S. Kliros and K. A. Papageorgiou, Hellenic Air-Force Academy, Department of Aeronautical Sciences, Division of Electronics and Communication Engineering, Greece.

MODIFIED SOLUTION OF SOMMERFELD'S PROBLEM, S. S. Sautbekov, R. N. Kasimkhanova, Euroasian National University, Astana, Kazakhstan, P. V. Frangos, Division of Information Transmission Systems and Materials Technology, School of Electrical and Computer Engineering, National Technical University of Athens, Greece.

UNIFORM RECTANGULAR SMART ANTENNA - MICROSTRIP ELEMENT MODELING AND SIGNAL DIRECTION ESTIMATION, Vyara Yordanova Vasileva, Technical University of Varna, Bulgaria.

AN AUTOFOCUSING ALGORITHM FOR POST-PROCESSING ISAR IMAGING BASED ON IMAGE ENTROPY MINIMIZATION, E. Kallitsis¹, G. Boulதாகி¹, A. Karakasiliotis¹, I. Tseremoglou¹, E. Stergiannis¹, H. Hristakis¹, E. Grigoratou², A. Vagianou² and P. Frangos¹ ¹National Technical University of Athens, Greece, ²Hellenic Air Force Academy, Athens, Greece.

STUDY OF THE INTERACTION OF RADIATED EM FIELDS WITH HUMAN OPERATORS, M. J. Martins, J. F. Rodrigues, DEEC, IST-UTL, Lisbon, Portugal

RANDOM PHASE SPREAD CODING MULTIPLE ACCESS - THE NEW COMPETITOR OF CDMA IN THE BROADBAND WIRELESS NETWORKS,
D-r Veselin Demirev, Radio Communications and Video Technologies Department, TU-Sofia.

THE REGULATORY ASPECTS OF SCP-RPSC TECHNOLOGY - COULD THEY SOLVE THE VMES PROBLEMS, D-r Veselin Demirev, Radio Communications and Video Technologies Department, TU-Sofia, Bulgaria.

A NEW WIRELESS PRS-OFDM SIMULATION MODEL, Stanyo Kolev, Faculty of Communication, TU - Sofia, Bulgaria.

Lunch

12h - 13h30

SECOND SESSION

13h 30 - 15 h

University Administration Building
Ceremonies Room (zero level of building)
National Technical University of Athens, Greece

Chairman: Ass. Prof. G. Kliros, National Technical University of Athens, Greece

AN APPROACH TO INTERACTIVE E-LEARNING: THE COMMUNICATION SYSTEMS IN MEDICINE COURSE, Vicktoria Antonova¹, Dimiter Dimitrov¹, Carlos Vaz de Carvalho²

KEEPING UP-TO-DATE IN THE MEDICAL FIELD AT NO COST, Nuno Escudeiro¹, Paula Escudeiro², ^{1,2}Instituto Superior de Engenharia do Porto, Portugal

THE INVESTIGATION OF ULTRASONIC PREAMPLIFIER COMPLEX PERFORMANCE, L. Svilainis, A. Chaziachmetovas, V. Dumbrava, Signal processing department, Kaunas University of Technology Lithuania.

THE INVESTIGATION OF FILTERS FOR REAL-TIME DATA ACQUISITION, L. Svilainis, S. Kitov, V. Dumbrava, Signal processing department, Kaunas University of Technology, Kaunas, Lithuania.

THE ELECTROMAGNETIC INTERFERENCE OF ULTRASONIC PULSER -PREAMPLIFIER, A. Chaziachmetovas¹, A. Citavicius², L. Svilainis¹, ¹Signal processing department, Kaunas University of Technology, ²Electronics and measurement systems department, Kaunas University of Technology, Lithuania.

SIMULATION OF SELECTIVE REPEAT AUTOMATIC RETRANSMISSION REQUEST SCHEME, Valentin Hristov, Department of Computer Systems and Technology at South West University, Blagoevgrad, Bulgaria.

A SIMPLE AND ACCURATE METHOD FOR ACHIEVEMENT OF A UNIFORM ON-AXIS MAGNETIC FIELD OF LONG SOLENOID, Sava Vasilev Savov, Department of Electrical Engineering, Technical University of Varna, Bulgaria

THIRD SESSION

15h 30 – 17h

University Administration Building
Ceremonies Room (zero level of building)
National Technical University of Athens, Greece

Chairman: Prof. R. Kuntchev, Technical University of Sofia, Bulgaria

ARCHIVING AND CONTENT PROTECTION OF VISUAL MEDICAL INFORMATION WITH INVERSE PYRAMID DECOMPOSITION, Roumen Kountchev, Technical University of Sofia, Bulgaria, Roumiana Kountcheva, T&K Engineering Co. Sofia, Bulgaria.

METHOD FOR WATERMARKING OF MEDICAL IMAGES BASED ON FAST COMPLEX HADAMARD TRANSFORM, Rumen Parvanov Mironov, Roumen Kirilov Kountchev, Faculty of Telecommunications, Technical University of Sofia, Bulgaria.

VOLUMETRIC IMAGE PROCESSING BY THREE-DIMENSIONAL FILTERS, Dimitar G. Valchev, Technical University of Varna, Bulgaria.

ASYMPTOTIC STATE OF ONE-DIMENSIONAL SOM AT RAYLEIGH POINT DENSITY INPUT, Ivo R. Draganov and Antoaneta A. Popova, Radiocommunications and Videotechnologies Dept., Technical University - Sofia, Bulgaria.

DISSIMILARITY-BASED METRIC FOR MEDICAL DATA CLASSIFICATION, Agata Manolova, Technical University Sofia, Bulgaria.

PRACTICAL ADAPTIVE FILTERING ON FPGA, Rosen Spirov¹, Faculty of Electronics, Technical University - Varna, Bulgaria.

08th October

FOURTH SESSION

9h – 11h

University Administration Building
Ceremonies Room (zero level of building)
National Technical University of Athens, Greece

Chairman : Prof. K. Nikita, NTUA, Greece

TEXTURE RECOGNITION AS A QUANTITATIVE ANALYSIS OF UNDERDOSES IN PHARMACOLOGY AND MEDICINE, Natalia Ampilova, St. Petersburg State University, Dept. Computer Science, Evgeny Gurevich, Sofia & Jacobs Foundation, Igor Soloviev, St. Petersburg State University, Dept. Computer Science.

EXPERIMENTAL AND NUMERICAL ASSESSMENT OF TISSUE TEMPERATURE ELEVATION DUE TO MOBILE PHONE USE, Maria Christopoulou¹, Irene Karanasiou², Konstantina S. Nikita¹ and Nikolaos K. Uzunoglu², ¹Biomedical Simulations and Imaging Unit,

²Microwave and Fiber Optics Lab, School of Electrical and Computer Engineering, National Technical University of Athens.

TRAINING OF PERCEPTRON NEURAL NETWORK USING PIECEWISE LINEAR ACTIVATION FUNCTION, Maria P. Barbarosou¹, Technological Educational Institute of Piraeus, Greece, Nicholas G. Maratos², National Technical University of Athens, Greece.

THE MEASURE OF ECG COMPLEXITY BY MATRIX ANALYSIS, Liepa Bikulciene^{1,3}, Zenonas Navickas¹, Alfonsas Vainoras², Rasa Šmidtaitė¹, ¹Kaunas University of Technology, ²Kaunas University of Medicine, Institute of Cardiology, ³Lithuanian Academy of Physical Education.

THE DYNAMIC INTERRELATIONS OF THREE ECG SIGNAL PARAMETERS, Kristina Berškienė¹, Alfonsas Vainoras², Gediminas Jaruševičius², Zenonas Navickas³ ¹Lithuanian University of Health Sciences, Medical Academy, Kaunas, Lithuania, ²Institute of Cardiology, Lithuanian University of Health Sciences, Medical Academy, Kaunas, Lithuania, ³Kaunas University of Technology, Kaunas, Lithuania.

E-HEALTH INFORMATION AND SIMULATION MODELING, Roumiana Yossifova Ilieva, Dept. Economics, Industrial Engineering and Management, Faculty of Management, Technical University of Sofia, Bulgaria.

MODIFIED MIND MAPPING FOR E-HEALTH MODELING, Roumiana Yossifova Ilieva, Dept. Economics, Industrial Engineering and Management, Faculty of Management, Technical University of Sofia, Bulgaria.

AN EOG BASED HUMAN COMPUTER INTERFACE SYSTEM FOR ONLINE CONTROL Carlos A. Vinhais, Fábio A. Santos, Joaquim F. Oliveira, Departamento de Física, ISEP - Instituto Superior de Engenharia do Porto, Portugal.

FIFTH SESSION

11h 30 – 13h

University Administration Building
Ceremonies Room (zero level of building)
National Technical University of Athens, Greece

Chairman: Prof. D. Dimitrov, Technical University of Sofia, Bulgaria

EDGE DETECTION IN ULTRASOUND MEDICAL IMAGES USING WAVELET DECOMPOSITION, Veska M. Georgieva, Faculty of Telecommunications, Technical University of Sofia, Bulgaria.

GUI FOR EDGE DETECTION IN MEDICAL IMAGES, Veska M. Georgieva, Faculty of Telecommunications, Technical University of Sofia, Bulgaria, Sofiya P. Shtarbova, Faculty of Computer Systems and Control, Technical University of Sofia, Bulgaria.

DEVELOPMENT OF A MOBILE TELEMEDICINE SYSTEM WITH MULTI COMMUNICATION LINKS FOR URBAN AND RURAL AREAS IN BULGARIA, Deyan M. Milev, Radiocommunications and Videotechnologies Department, Technical University – Sofia, Bulgaria.

VULNERABILITY OF MEDICAL IT SYSTEMS MANAGEMENT LIFE-CYCLE, Lidya Jordanova, Tzveta Dimitrova, Faculty of Telecommunication, Technical University - Sofia, Bulgaria.

COMPUTER SIMULATION OF INTERPOLATION OF THE SPECTRUM OF ECG SIGNAL, Mariya Nikolova¹, ¹Department of Mathematics and Informatics, N. Y. Vaptsarov, Naval Academy, Varna, Bulgaria, Tzveta Dimitrova², ²Technical University of Sofia, Bulgaria.

NETWORK PERIMETER SECURITY FOR MEDICAL INFORMATION SYSTEMS, Tzveta Dimitrova, Faculty of Telecommunication, Technical University - Sofia, Bulgaria.

CLOSING SESSION

13 h- 13h 30

University Administration Building
Ceremonies Room (zero level of building)
National Technical University of Athens, Greece

SOCIAL PROGRAM

Social Program SCHEDULE

- **Conference Dinner** (optional) will be given in the heart of the old city of Athens, near Acropolis of Athens, on Friday, October 7, in the evening. Participants can pay for this on site. More information regarding Conference Dinner will be provided during the first day of the Conference (October 7).
- Furthermore, a **tour** to the famous ‘**Acropolis of Athens**’, and its corresponding ‘**New Acropolis Museum**’, will take place on Saturday October 09, beginning 11:00 a.m. Participants can also pay on site.
- In addition, more touristic information about Athens and Greece can be provided by the Conference Organizers.

CONTACT US:

<http://www.tu-sofia.bg/fktt/cema10/>

GENERAL INFORMATION AND SUBMISSION OF CONTRIBUTIONS

Prof. Dr. D. Dimitrov

Faculty of Telecommunications

Technical University of Sofia

8, Kliment Ohridsky str.

1756 Sofia, Bulgaria

Phone/Fax: ++359 2 9652278

E-mail: dcd@tu-sofia.bg

Prof. Dr. P. Frangos

National Technical University of Athens

School of Electrical and Computer Engineering

9, Iroon Polytechniou Str.,

157 73 Zografou, Athens, Greece

Phone: 00 30 210 772 3694

Fax: 00 30 210 772 2281

E-mail: pfrangos@central.ntua.gr

TABLE OF CONTENTS

FDTD MODELING OF REFRACTOMETRIC OPTICAL SENSORS BASED ON QUASI-ONE-DIMENSIONAL PHOTONIC CRYSTALS	1
<i>G. S. Kliros, K. A. Papageorgiou</i>	
MODIFIED SOLUTION OF SOMMERFELD'S PROBLEM	5
<i>S. S. Sautbekov, R.N. Kasimkhanova, P. V. Frangos</i>	
UNIFORM RECTANGULAR SMART ANTENNA – MICROSTRIP ELEMENT MODELING AND SIGNAL DIRECTION ESTIMATION	9
<i>Vyara Yordanova Vasileva</i>	
AN AUTOFOCUSING ALGORITHM FOR POST-PROCESSING ISAR IMAGING BASED ON IMAGE ENTROPY MINIMIZATION	13
<i>E. Kallitsis, G. Boultradakis, A. Karakasiliotis, I. Tseremoglou, E. Stergiannis, H. Hristakis, E. Grigoratou, A. Vagianou, P. Frangos</i>	
STUDY OF THE INTERACTION OF RADIATED EM FIELDS WITH HUMAN OPERATORS	19
<i>M. J. Martins, J. F. Rodrigues</i>	
RANDOM PHASE SPREAD CODING MULTIPLE ACCESS – THE NEW COMPETITOR OF CDMA IN THE BROADBAND WIRELESS NETWORKS	22
<i>Veselin Demirev</i>	
THE REGULATORY ASPECTS OF SCP-RPSC TECHNOLOGY – COULD THEY SOLVE THE VMES PROBLEMS	25
<i>Veselin Demirev</i>	
A NEW WIRELESS PRS-OFDM SIMULATION MODEL	29
<i>Stanyo Kolev</i>	
AN APPROACH TO INTERACTIVE E-LEARNING: THE COMMUNICATION SYSTEMS IN MEDICINE COURSE	31
<i>Vicktoria Antonova, Dimiter Dimitrov, Carlos Vaz de Carvalho</i>	
KEEPING UP-TO-DATE IN THE MEDICAL FIELD AT NO COST	35
<i>Nuno Escudeiro, Paula Escudeiro</i>	
THE INVESTIGATION OF ULTRASONIC PREAMPLIFIER COMPLEX PERFORMANCE	39
<i>L. Svilainis, A. Chaziachmetovas, V. Dumbrava</i>	
THE INVESTIGATION OF FILTERS FOR REAL-TIME DATA ACQUISITION	43
<i>L. Svilainis, S. Kitov, V. Dumbrava</i>	
THE ELECTROMAGNETIC INTERFERENCE OF ULTRASONIC PULSER – PREAMPLIFIER	47
<i>A. Chaziachmetovas, A.Citavicius, L. Svilainis</i>	
SIMULATION OF SELECTIVE REPEAT AUTOMATIC RETRANSMISSION REQUEST SCHEME	50
<i>Valentin Hristov</i>	
ARCHIVING AND CONTENT PROTECTION OF VISUAL MEDICAL INFORMATION WITH INVERSE PYRAMID DECOMPOSITION	54
<i>Roumen Kountchev, Roumiana Kountcheva</i>	
METHOD FOR WATERMARKING OF MEDICAL IMAGES BASED ON FAST COMPLEX HADAMARD TRANSFORM	58
<i>Rumen Parvanov Mironov, Roumen Kirilov Kountchev</i>	
VOLUMETRIC IMAGE PROCESSING BY THREE-DIMENSIONAL FILTERS	62
<i>Dimitar G. Valchev</i>	

ASYMPTOTIC STATE OF ONE-DIMENSIONAL SOM AT RAYLEIGH POINT DENSITY INPUT	65
<i>Ivo R. Draganov, Antoaneta A. Popova</i>	
DISSIMILARITY-BASED METRIC FOR MEDICAL DATA CLASSIFICATION	69
<i>Agata Manolova</i>	
PRACTICAL ADAPTIVE FILTERING ON FPGA.....	73
<i>Roumen Spirov</i>	
TEXTURE RECOGNITION AS A QUANTITATIVE ANALYSIS OF UNDERDOSES IN PHARMACOLOGY AND MEDICINE.....	78
<i>Natalia Ampilova, Evgeny Gurevich, Igor Soloviev</i>	
EXPERIMENTAL AND NUMERICAL ASSESSMENT OF TISSUE TEMPERATURE ELEVATION DUE TO MOBILE PHONE USE	82
<i>Maria Christopoulou, Irene Karanasiou, Konstantina S. Nikita, Nikolaos K. Uzunoglu</i>	
TRAINING OF PERCEPTRON NEURAL NETWORK USING PIECEWISE LINEAR ACTIVATION FUNCTION.....	85
<i>Maria P. Barbarosou, Nicholas G. Maratos</i>	
THE MEASURE OF ECG COMPLEXITY BY MATRIX ANALYSIS	89
<i>Liepa Bikulciene, Zenonas Navickas, Alfonsas Vainoras, Rasa Šmidlaitė</i>	
THE DYNAMIC INTERRELATIONS OF THREE ECG SIGNAL PARAMETERS	93
<i>Kristina Berškienė, Alfonsas Vainoras, Gediminas Jaruševičius, Zenonas Navickas</i>	
E-HEALTH INFORMATION AND SIMULATION MODELING	97
<i>Roumiana Yossifova Ilieva</i>	
MODIFIED MIND MAPPING FOR EHEALTH MODELING.....	101
<i>Roumiana Yossifova Ilieva</i>	
A SIMPLE AND ACCURATE METHOD FOR ACHIEVEMENT OF A UNIFORM ON-AXIS MAGNETIC FIELD OF LONG SOLENOID	104
<i>Sava Vasilev Savov</i>	
EDGE DETECTION IN ULTRASOUND MEDICAL IMAGES USING WAVELET DECOMPOSITION.....	108
<i>Veska M. Georgieva</i>	
GUI FOR EDGE DETECTION IN MEDICAL IMAGES.....	112
<i>Veska M. Georgieva, Sofiya P. Shtarbova</i>	
DEVELOPMENT OF A MOBILE TELEMEDICINE SYSTEM WITH MULTI COMMUNICATION LINKS FOR URBAN AND RURAL AREAS IN BULGARIA	116
<i>Deyan M. Milev</i>	
VULNERABILITY OF MEDICAL IT SYSTEMS MANAGEMENT LIFE-CYCLE	120
<i>Lidya Jordanova, Tzveta Dimitrova</i>	
COMPUTER SIMULATION OF INTERPOLATION OF THE SPECTRUM OF ECG SIGNAL	124
<i>Mariya Nikolova, Tzveta Dimitrova</i>	
NETWORK PERIMETER SECURITY FOR MEDICAL INFORMATION SYSTEMS	128
<i>Tzveta Dimitrova</i>	
AN EOG BASED HUMAN COMPUTER INTERFACE SYSTEM FOR ONLINE CONTROL	132
<i>Carlos A. Vinhais, Fábio A. Santos, Joaquim F. Oliveira</i>	

FDTD MODELING OF REFRACTOMETRIC OPTICAL SENSORS BASED ON QUASI-ONE-DIMENSIONAL PHOTONIC CRYSTALS

G. S. Kliros and K. A. Papageorgiou

*Hellenic Air-Force Academy, Department of Aeronautical Sciences
Division of Electronics and Communication Engineering
Dekeleia Air-Force Base, Attica GR-1010, Greece
gksma@hol.gr*

Abstract

We report on the design of a refractometric optical sensor based on a quasi-one dimensional photonic crystal structure etched in a Si_3N_4 ridge waveguide grown on top of a SiO_2 substrate. A photonic crystal based on this kind of structure exhibits a photonic bandgap for TE polarized light. The finite difference time domain method (FDTD) is employed in order to design the device and investigate its transmission spectra and sensitivity characteristics. The shift in the central wavelength of the reflectivity spectrum, due to change in the refractive index, when the low-index areas of the photonic crystal are infiltrated with different fluids, is found to be linear and hence, suitable for refractometric sensing applications.

1. INTRODUCTION

Integrated optical sensors has a high potential to be employed as a device in many areas such as, microbiology, environmental safety, defence and aerospace technology. Their main advantages are immunity to electromagnetic interference, high compactness and robustness and prospects of mass production, and also they have fast responsivity and higher sensitivities when compared to Micro-Electro-Mechanical Systems (MEMS). In a variety of environmental, biomedical and aerospace applications, the measurement of the refractive index is very important since is strongly related to structure composition.

Photonic crystals (PC) and photonic band gap structures (PBG) [1] are very promising building blocks for photonic components of submicron scale which is comparable to that of their electronic counterparts. Two-dimensional (2D) PCs formed in a dielectric slab waveguide structure have attracted much interest recently for realizing novel micro-optoelectronic devices [2-4]. A structure having a periodic index modulation in one dimension is known as a one-dimensional photonic crystal (1D-PC). If the structure has nonperiodic features in the other two dimensions, it is denoted as a quasi-1D PC which is essentially a 'Bragg grating'. A Bragg grating with a strong index modulation shows a typical property of PCs: an extended transmission stop-band. The width of this stopband and the steepness of its edges increase with the strength of the refractive index modulation. For sensing appli-

cations, one has to exploit the steep edges of the stop-band in a strong grating [5].

In this paper, motivated by the recent interest in developing quasi-1D PC sensors [6,7], we designed and simulated a wide ridge-type channel waveguide of silicon nitride with a 1D PC etched into the core layer. The reflectivity spectra of the device has been obtained using the FDTD method. The sensitivity of our device is determined by observing the shift in the central wavelength of reflectivity spectrum as a function of the change in effective refractive index.

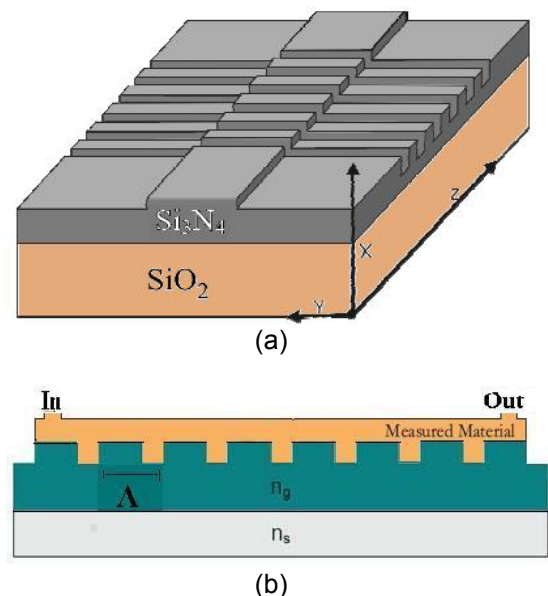


Fig.1. (a) Schematic 3D drawing of the waveguide with a 1D photonic crystal, and (b) Cross-section of the quasi one-dimensional photonic crystal sensor with a cuvette placed on top.

2. DEVICE DESIGN AND MODELING

A schematics of the 3D-structure as well as the cross-section of the device is shown in Fig.1. The sensing element is a strong grating in a Si₃N₄ ridge waveguide ($n_g=2.01$) with period $\Lambda=628.2$ nm grown on top of a SiO₂ substrate ($n_s=1.46$) resulting in TE single-mode operation at wavelengths around the modern telecommunications wavelength of $\lambda=1.55$ μm . The light is guided by the photonic crystal structure in the horizontal plane and is confined by the classical ridge waveguide in the vertical direction. The sensitivity of the sensor for changes in the refractive index can be simulated by infiltrating the grooves of the grating with different fluids through the cuvette, as it is shown schematically in Fig. 1(b).

The simulation is performed using the Finite Difference Time Domain Method (FDTD) with Perfectly Matched Layer (PML) boundary conditions. Since the waveguide thickness is very small and there is no structural variation in the y-direction uniformly over the x-z plane, the structure can be analysed as a quasi-1D device without losing much generality. FDTD method relies on the discretization of Maxwell's equations and provides the description of the time evolution of the electromagnetic field without any assumption about the number and the characteristics of the propagating modes.

According to FDTD method on a Yee cell [8], a simple set of discrete field equations is obtained for TE-polarized wave propagation:

$$E_x^{n+1}(i) = E_x^n(i) + \frac{Dt}{\epsilon(i)Dz} \times \left[H_y^{n+\frac{1}{2}}(i+1/2) - H_y^{n+\frac{1}{2}}(i-1/2) \right] \quad (1)$$

$$H_y^{n+\frac{1}{2}}(i+1/2) = H_y^{n-\frac{1}{2}}(i+1/2) + \frac{\Delta t}{\mu(i)\Delta z} [E_x^n(i+1) - E_x^n(i)] \quad (2)$$

where Δt and Δx are the finite difference cells in the temporal and spatial domain, respectively. A 1D-mesh grid with size of $\Delta x=12.035$ nm were used in the simulation. The time step is based on the Courant's condition $\Delta t = \Delta x / \sqrt{2}c$, where c is the velocity of light in vacuum. The simulation is run for 131.072 (2^{17}) time steps to get a fine spectral resolution. Vector-based computations are employed instead of element-based ones using MATLAB tech-

nical language in order to reduce the computation time considerably. The source employed was a Gaussian modulated continuous wave at central wavelength of 1.55 μm having a broad spectral bandwidth. By Fast-Fourier-Transforming the electric field component, sampled at the output ports, the frequency response of the device under investigation was obtained, with just a single simulation run.

In order to get an exact Bragg wavelength from the FDTD simulation, the effective index corresponding to TE-mode propagating in the ridge waveguide, is set to a value which is obtained from a Beam Propagation Method (BPM) mode solver [9]. For first-order gratings like in Fig. 1(b), the Bragg conditions are expressed as

$$\Lambda_{tooth} = \frac{\lambda_{Bragg}}{4n_{eff,tooth}}, \quad \Lambda_{groove} = \frac{\lambda_{Bragg}}{4n_{eff,groove}} \quad (3)$$

For the desired Bragg wavelength of 1.55 μm , $\Lambda_{tooth}=240.7\text{nm}$ and $\Lambda_{groove}=387.5$ nm so that a grating period $\Lambda= 628.2$ nm, is obtained. The number of periods chosen was 64, resulting in an overall grating length of 40.2 μm .

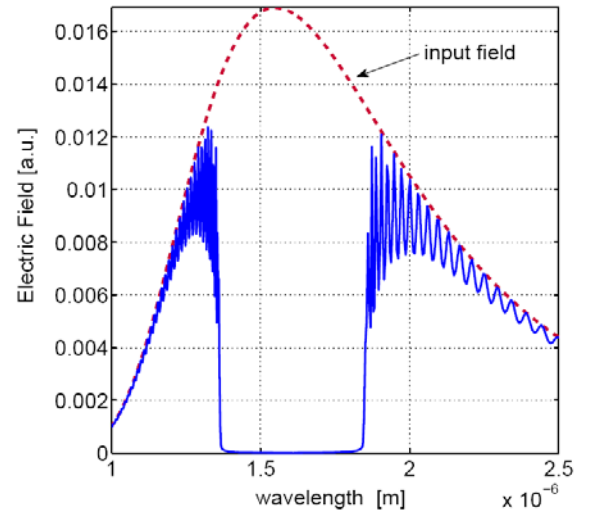


Fig. 2. Spectral dependence of the electric field intensity when the grooves are filled with air. The dashed line represents the spectral dependence of the input pulse.

3. RESULTS AND DISCUSSION

Fig. 2 shows the spectral intensity of both the input and the transmitted electric field for air-filled grooves. The wide stop band in the transmission spectrum would allow a high free spectral range, so that the Bragg wavelength can be tuned over a

wide range of wavelengths. Table I reports the shift of the central wavelength when the grating grooves are infiltrated by different fluids with increasing refractive indices. Experimentally, a continuous change in refractive index could be realized by mixing together two fluids with different indexes. As it is seen, the central wavelength i.e. the wavelength exactly in the middle of the stopband defined by the -3 dB point of the stopband edges, is shifted towards higher wavelength values as a consequence of the change of the guided mode effective index. Figs. 3(a)-(c) illustrate the effect of fluid refractive index change on the reflectivity of the quasi-1D photonic crystal structure. Both edges of the stopband are shifted toward longer wavelengths. A small wavelength shift of such an edge can cause a large change in the transmitted power from a source having an appropriate wavelength.

Grating sensitivity describes the device efficiency when it works as a sensor. In this work, we define the sensitivity as

$$S = \frac{\partial \lambda_{\text{centre}}}{\partial n_c} \quad (4)$$

and therefore, it can be easily calculated using the data of Table I.

Table I: Resonance central wavelength for different refractive indices

n_c	λ_{low} (nm)	λ_{high} (nm)	λ_{centre} (nm)
1.00	1356.7	1857.8	1607.2
1.05	1409.6	1874.8	1642.2
1.10	1466.4	1881.4	1673.9
1.15	1520.2	1896.0	1708.1
1.20	1576.0	1912.0	1744.0
1.25	1631.5	1929.7	1780.6
1.30	1687.3	1944.4	1815.9
1.35	1749.5	1956.4	1852.9
1.40	1806.5	1974.8	1890.7
1.45	1863.2	1993.9	1928.5
1.50	1921.0	2013.5	1967.3

Fig. 4 presents the central wavelength shift ($\Delta \lambda_{\text{centre}}$) as a function of the change in fluid refractive index by infiltration of the grating grooves, where the reference wavelength is the central wavelength for air-filled grooves. From the graph, it is observed a 7 nm shift of the centre wavelength for a change in refractive index $\delta n_c = 0.1$ and therefore an average sensitivity $S \sim 70$ nm per unit refractive index change is obtained. Furthermore, the central wavelength shift is linear and hence, the device is extremely suitable for sensing applications.

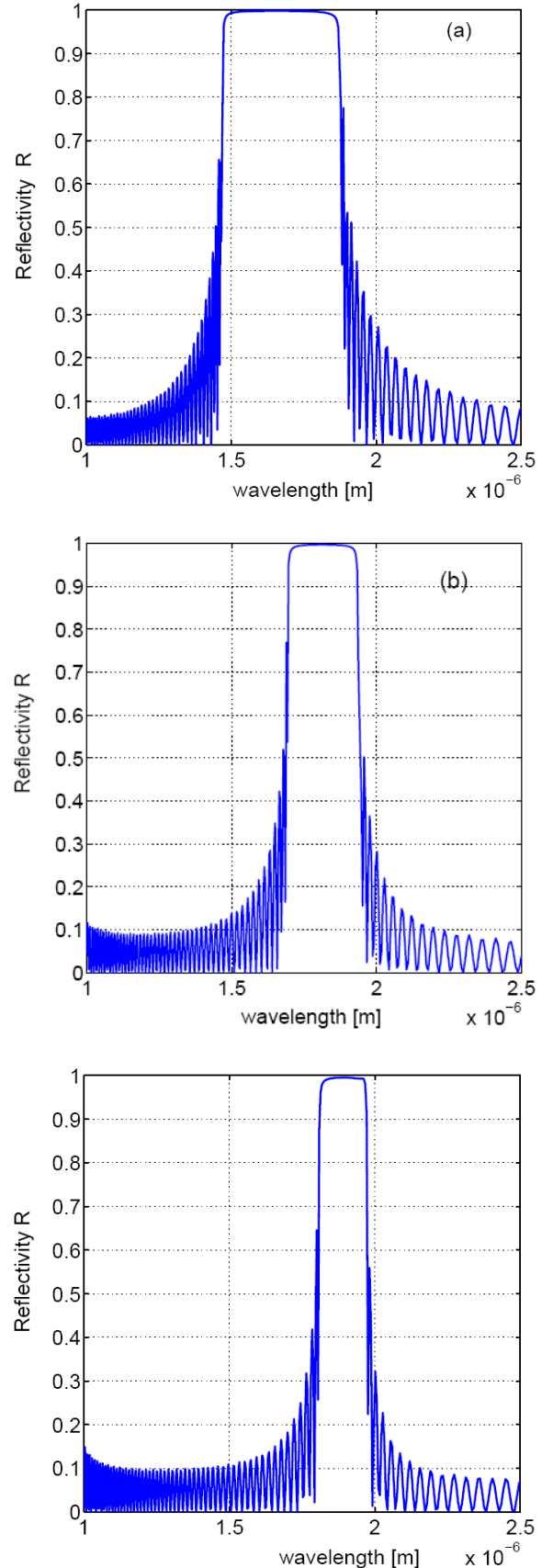


Fig. 3. Computed reflectivity spectra when the refractive index of infiltrated grating grooves is (a) $n_c=1.1$, (b) $n_c=1.3$ and (c) $n_c=1.4$

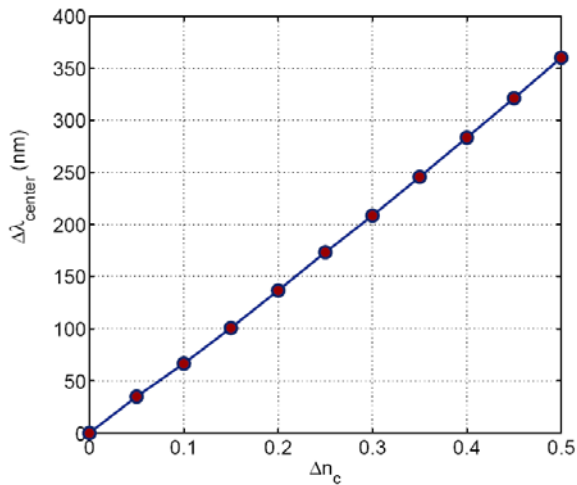


Fig. 4. Sensitivity characteristic curve showing the simulated changes in central wavelength versus changes in refractive index.

4. CONCLUSION

We have designed and simulated a very compact refractometric sensor based on quasi-1D photonic crystal. The FDTD simulation method is employed, in order to investigate its transmission spectra and sensitivity characteristics. For the working wavelength of $\sim 1.55 \mu\text{m}$, the transmission spectra has been calculated by changing the refractive index of different fluids in the grooves of the grating. It has been found that increasing the refractive index, the wavelength position of both the lower and upper band edge are shifted with the largest shift appeared in the lower wavelength band edge. The shift in the central wavelength is found to be approximately linear and hence, the device is extremely suitable for sensing applications. The simulated structure shows good performance in terms of compactness, sensitivity and free spectral range. The performance of the designed device as temperature, pressure or strain sensor based on the

thermo-elastic and thermo-optic effects [10] will be reported in a future paper.

References

- [1] P. Markos and C. M. Soukoulis, *Wave Propagation: From Electrons to Photonic Crystals and Left-handed Materials*, Princeton University Press, New Jersey, 2008.
- [2] R. V. Nair and R. Vijaya, Photonic crystal sensors: An overview, *Progress in Quantum Electronics*, vol. 34, 2010, pp. 89-134.
- [3] G. S. Kliros, A. N. Fotiadis, G. P. Tziopis, Optical Simulation of Silicon-Based Complete Photonic Bandgap Modulator, *Proc. of 21th IEEE Int. Conference on Microelectronics*, Marrakesh, Morocco, 2009, pp. 219-221.
- [4] G. Kliros, K. Papageorgiou, Refractometric Optical Sensor based on Tapered Photonic Crystal Waveguide, *J. Optoelectronics Adv. Mater.*, vol.12 (7), 2010, pp. 1530-1533.
- [5] W. C. L. Hopman *et. al.*, Quasi-1D Photonic Crystal as a Compact Building-Block for Refractometric Optical Sensors," *IEEE J. Sel. Top. Quant. Electron.* vol. 11, 2005, pp. 11-16.
- [6] V. M. N. Passaro *et. al.*, Design of Bragg Grating Sensors Based on Sub-micrometer Optical Rib Waveguides in SOI, *IEEE Sensors J.* vol. 8, 2008, pp.1603-1611.
- [7] A. Banerjee, Binary number sequence multilayer structure based on refractometric optical sensing element, *J. Electromagn. Waves Appl.*, vol. 22, 2008, pp. 2439 - 2449.
- [8] A. Taflove, *Computational Electrodynamics: The Finite-Difference Time-Domain Method*, 2nd edn., Artech House, 2000.
- [9] Em. E. Kriezis *et. al.*, Full vector beam propagation method for axially dependent 3-D structures *IEEE Trans. Magnetics*, vol. 33 (2), 1997, pp. 1540-1543.
- [10] H. M. Chong, R. De La Rue, Tuning of photonic crystal waveguide microcavity by thermo-optic effect, *IEEE Photon. Techn. Lett.*, vol. 16 (6), 2004, pp. 1528-1530.

MODIFIED SOLUTION OF SOMMERFELD'S PROBLEM

S. S. Sautbekov, R.N. Kasimkhanova,

*Euroasian National University,
5 Munaitpassov Str., Astana, Kazakhstan, e-mail: kasim_rai@mail.ru.*

P. V. Frangos

*Division of Information Transmission Systems and Materials Technology,
School of Electrical and Computer Engineering, National Technical University of Athens,
9 Iroon Polytechniou Str., Zografou, Athens, Greece,
e-mail: pfrangos@central.ntua.gr*

Abstract

The new rigorous boundary method based on solving Sommerfeld's problem for isotropic media is provided. Scattering of electromagnetic waves radiated by electrical point dipole near the plane surface boundary is considered in this paper. The problem is divided into two independent problems. Solution of each problem is investigated in the form of superposition of plane waves and reduced to the solution of system of algebraic equations. The solution of the boundary problem is represented in integral form for the general case. It coincides with the known solution by Sommerfeld, which is obtained from the solution of an ordinary differential equation. The new method may be used also in boundary problems for anisotropic media, which case will be investigated by our research group in the near future.

1. INTRODUCTION

Solving boundary problems is one of the actual problems of modern electrodynamics. The rigorous solving of the simplest key problem was considered by Sommerfeld in wave diffraction theory for the first time. This problem deals with the elementary dipole and with planar interface between two isotropic media. Helmholtz's equation was reduced to solving the ordinary differential equations and the rigorous solution was presented in the integral form by means of vector potentials by Sommerfeld [1]. This boundary problem (method of its solution and the obtained integral) is traditionally named the Sommerfeld problem in diffraction theory. It was considered in the work too [2] where the solution is derived with the help of Hertz vectors in the same way. Asymptotic analysis of Sommerfeld solution was researched by Malyuzhinets [3]. Many various methods such as the method of equivalent boundary conditions, the image method, Green's function method were developed to solve boundary problem on the basis of Sommerfeld problem. The method of equivalent boundary conditions is one of the effective methods for simplifying of boundary problems solving. For example, impedance boundary conditions of Schukin-Leontovich are applied for the problem of anisotropic media too [4]. The image method was first presented by Wait [5] and later by several other authors. For example, the rigorous solutions are obtained for cases of anisotropic half-

space with perfectly electrically or magnetically conducting surface [6], for anisotropic half-space bounded by an anisotropic surface [7] and for a similarly anisotropic half-space and boundary [8] on the basis of the method of images. But there can be difficulties in determination of a image's form and its location. In the work [9] perfect conductor case with mixed-partial derivative boundary condition is considered on the basis of Green's function method for an anisotropic half-space.

In this work the modified new method of rigorously solving boundary problem is proposed on the basis of Sommerfeld key problem. The according to the proposed method the boundary problem is reduced to solving of system of algebraical equations concerning of Fourier component of density of surface current due to using the boundary conditions. The total electromagnetic field is determined through density of surface current induced on the interface. Thus the convenience and simplicity of calculation and the deep physical transparency are the main property of presented method. The method can be used in rigorously solving more difficult problems of electrodynamics particularly for cases of anisotropic media.

2. STATEMENT OF THE BOUNDARY PROBLEM

The system of Maxwell equations for stationary electromagnetic field is considered:

$$\begin{cases} \text{rot } \mathbf{E} + i\omega\mu_0\mu\mathbf{H} = 0, \\ \text{rot } \mathbf{H} - i\omega\varepsilon_0\varepsilon\mathbf{E} = \mathbf{j}, \end{cases} \quad (1)$$

where \mathbf{H}, \mathbf{E} are intensities of magnetic and electric fields, ε and μ are dielectric and magnetic permeability of medium, \mathbf{j} is current density of external source. Time dependence is taken in the form of $e^{i\omega t}$.

Let the interface is the plane $x = 0$. Electric and magnetic permeability of the higher and lower half-spaces are characterized by the corresponding values: ε_1, μ_1 и ε_2, μ_2 . For external source we choose elementary Hertz radiator located in a point along axis $x = x_0$ of the higher half-space and with the dipole momentum \mathbf{p} directed along the axis x .

It is required to satisfy the electrodynamics boundary conditions on the planar interface ($x=0$), i.e. continuity of the tangential components of intensities.

It is necessary to determine electromagnetic field in any point of the space.

3. THE METHOD OF SOLVING BOUNDARY PROBLEM

3.1. General solution of system of Maxwell equations

Let's present the general solution of Maxwell's equations for isotropic media:

$$\begin{aligned} \mathbf{H} &= -iF^{-1}[\tilde{\psi}[\mathbf{k}, \tilde{\mathbf{J}}]] \\ \mathbf{E} &= -\frac{i}{\omega\varepsilon\varepsilon_0}F^{-1}[\tilde{\psi}(\varepsilon\mu k_0^2 \tilde{\mathbf{J}} - (\mathbf{k}, \tilde{\mathbf{J}})\mathbf{k})] \end{aligned} \quad (2)$$

where F^{-1} is operator of inverse Fourier transformations, $\tilde{\mathbf{J}}$ is Fourier component of density of surface current, $\tilde{\psi} = (\varepsilon\mu k_0^2 - k_\rho^2 - k_x^2)^{-1}$, \mathbf{k} is wave vector, r is radius vector.

Since the dipole moment is directed along the normal vector of the planar surface. It is obvious that problem is axisymmetric. Therefore it is convenient to consider the problem solution (2) in cylindrical frame:

$$\begin{aligned} \mathbf{H} &= -\frac{ie_\alpha}{(2\pi)^3} \int_0^\infty \int_0^{2\pi} \int_{-\infty}^\infty k_x \tilde{\mathbf{J}}(k_\rho) \tilde{\psi} k_\rho \exp(i\mathbf{k}\mathbf{r}) \\ & dk_\rho d\alpha dk_x, \end{aligned}$$

$$\begin{aligned} \mathbf{E} &= -\frac{i}{(2\pi)^3 \varepsilon\varepsilon_0\omega} \int_0^\infty \int_0^{2\pi} \int_{-\infty}^\infty (\varepsilon\mu k_0^2 \mathbf{e}_\rho - \mathbf{k}k_\rho) \\ & \tilde{\mathbf{J}}(k_\rho) \tilde{\psi} k_\rho \exp(i\mathbf{k}\mathbf{r}) dk_\rho d\alpha dk_x. \end{aligned} \quad (3)$$

Using the following known identities for Bessel functions:

$$\begin{aligned} \frac{1}{2\pi} \int_0^{2\pi} \exp(ik_\rho \rho \cos \alpha) d\alpha &= J_0(k_\rho \rho), \\ \int_0^\infty J_0(k_\rho \rho) dk_\rho &= \frac{1}{2} \int_{-\infty}^\infty H_0^{(1)}(k_\rho \rho) dk_\rho, \end{aligned}$$

and taking into account the scalar product $\mathbf{k}\mathbf{r} = k_\rho \rho \cos(\alpha - \beta) + k_x x$ (β is angle between unit vectors \mathbf{e}_ρ and \mathbf{e}_z), the general solution of Maxwell's equations (3) can be put into the form:

$$\begin{aligned} \mathbf{H} &= -\frac{ie_\alpha}{8\pi^2} \iint_{R^2} k_x \tilde{\mathbf{J}}(k_\rho) \tilde{\psi} k_\rho H_0^{(1)}(k_\rho, \rho) \\ & dk_\rho dk_x, \\ \mathbf{E} &= -\frac{i}{8\pi^2 \varepsilon\varepsilon_0\omega} \iint_{R^2} (\varepsilon\mu k_0^2 \mathbf{e}_\rho - \mathbf{k}k_\rho) \tilde{\mathbf{J}}(k_\rho) \\ & \tilde{\psi} k_\rho H_0^{(1)}(k_\rho, \rho) dk_\rho dk_x, \end{aligned} \quad (4)$$

where $J_0(x)$ - Bessel function for the zeroth order, $H_0^{(1)}(x)$ - Henkel function of the first kind of the zeroth order.

3.2. Solving the boundary problem

Using the above relations in (4), refracted and reflected fields are written accordingly as:

$$\begin{aligned} \mathbf{H}^R &= -\frac{ie_\alpha}{8\pi^2} \iint_{R^2} k_x \tilde{\mathbf{J}}_1(k_\rho) \tilde{\psi}_1 k_\rho H_0^{(1)}(k_\rho, \rho) \\ & dk_\rho dk_x, \\ \mathbf{E}^R &= -\frac{i}{8\pi^2 \varepsilon_1 \varepsilon_0 \omega} \iint_{R^2} (k_{01}^2 \mathbf{e}_\rho - \mathbf{k}k_\rho) \tilde{\mathbf{J}}_1(k_\rho) \\ & \tilde{\psi}_1 k_\rho H_0^{(1)}(k_\rho, \rho) dk_\rho dk_x, \\ \mathbf{H}^T &= -\frac{ie_\alpha}{8\pi^2} \iint_{R^2} k_x \tilde{\mathbf{J}}_2(k_\rho) \tilde{\psi}_2 k_\rho H_0^{(1)}(k_\rho, \rho) \\ & dk_\rho dk_x, \\ \mathbf{E}^T &= -\frac{i}{8\pi^2 \varepsilon_2 \varepsilon_0 \omega} \iint_{R^2} (k_{02}^2 \mathbf{e}_\rho - \mathbf{k}k_\rho) \tilde{\mathbf{J}}_2(k_\rho) \\ & \tilde{\psi}_2 k_\rho H_0^{(1)}(k_\rho, \rho) dk_\rho dk_x, \end{aligned} \quad (5)$$

where $k_{01} = \sqrt{\varepsilon_1 \mu_1} k_0$, $k_{02} = \sqrt{\varepsilon_2 \mu_2} k_0$ - wave numbers in the higher and lower half-spaces,

$$\tilde{\psi}_1 = \frac{1}{k_{01}^2 - k_\rho^2 - k_x^2}, \quad \tilde{\psi}_2 = \frac{1}{k_{02}^2 - k_\rho^2 - k_x^2},$$

$\tilde{\mathbf{J}}_1 = \tilde{J}_1(k_\rho) \mathbf{e}_\rho$, $\tilde{\mathbf{J}}_2 = \tilde{J}_2(k_\rho) \mathbf{e}_\rho$ - Fourier component of density of surface current. The field of point dipole is written as:

$$\mathbf{E}^0 = -(\varepsilon_1 \varepsilon_0)^{-1} (\text{grad div} + k_{01}^2) (\psi_1 \mathbf{p}),$$

$$\mathbf{H}^0 = i\omega \text{rot}(\psi_1 \mathbf{p}). \quad (6)$$

Then total solution of electromagnetic field is presented in form:

$$\mathbf{H} = \begin{cases} \mathbf{H}^- = \mathbf{H}^0 + \mathbf{H}^R, & x > 0; \\ \mathbf{H}^T, & x < 0; \end{cases},$$

$$\mathbf{E} = \begin{cases} \mathbf{E}^- = \mathbf{E}^0 + \mathbf{E}^R, & x > 0; \\ \mathbf{E}^T, & x < 0. \end{cases} \quad (7)$$

Calculating integral in (5) by k_x with help of the residue theory we obtain the following relations for \mathbf{H}^- , \mathbf{E}^- , \mathbf{H}^T , \mathbf{E}^T in (7):

in the higher half-space:

$$\mathbf{H}^- = \mathbf{H}^0 - \frac{\mathbf{e}_x}{8\pi} \int_{-\infty}^{\infty} \tilde{J}_1(k_\rho) e^{ik_1 x} \mathbf{H}_0^{(1)}(k_\rho, \rho) k_\rho dk_\rho,$$

$$\mathbf{E}^- = \mathbf{E}^0 - \frac{1}{8\pi^2 \varepsilon_1 \varepsilon_0 \omega} \int_{-\infty}^{\infty} (\mathbf{e}_\rho \kappa_1 - \mathbf{e}_x) \tilde{J}_1(k_\rho) e^{ik_1 x} k_\rho \mathbf{H}_0^{(1)}(k_\rho, \rho), \quad (8)$$

in the lower half-space:

$$\mathbf{H}^T = \frac{\mathbf{e}_x}{8\pi} \int_{-\infty}^{\infty} \tilde{J}_2(k_\rho) e^{-ik_2 x} k_\rho \mathbf{H}_0^{(1)}(k_\rho, \rho) dk_\rho,$$

$$\mathbf{E}^T = -\frac{1}{8\pi^2 \varepsilon_2 \varepsilon_0 \omega} \int_{-\infty}^{\infty} (\mathbf{e}_\rho \kappa_2 + \mathbf{e}_x) \tilde{J}_2(k_\rho) e^{-ik_2 x} k_\rho \mathbf{H}_0^{(1)}(k_\rho, \rho), \quad (9)$$

$$\text{where } \kappa_1 = \sqrt{k_{01}^2 - k_\rho^2}, \quad \kappa_2 = \sqrt{k_{02}^2 - k_\rho^2}.$$

3.3. Boundary conditions

Taking into account nonzero single tangential component of electromagnetic field in (8), (9) we

require satisfaction of boundary condition in form ($x = 0$):

$$\mathbf{H}_\alpha^0 + \mathbf{H}_\alpha^R = \mathbf{H}_\alpha^T, \quad \mathbf{E}_\rho^0 + \mathbf{E}_\rho^R = \mathbf{E}_\rho^T, \quad (10)$$

where

$$\mathbf{H}_\alpha^0 = -\frac{1}{8\pi} \int_{-\infty}^{\infty} \frac{i\omega p k_\rho e^{ik_1 x_0}}{\kappa_1} \mathbf{H}_0^{(1)}(k_\rho, \rho) k_\rho dk_\rho,$$

$$\mathbf{E}_\rho^0 = \frac{i}{8\pi \varepsilon_1 \varepsilon_0} \int_{-\infty}^{\infty} \omega p k_\rho e^{ik_1 x_0} \mathbf{H}_0^{(1)}(k_\rho, \rho) k_\rho dk_\rho,$$

$$\mathbf{H}_\alpha^R = -\frac{1}{8\pi} \int_{-\infty}^{\infty} \tilde{J}_1(k_\rho) k_\rho \mathbf{H}_0^{(1)}(k_\rho, \rho) dk_\rho,$$

$$\mathbf{E}_\rho^R = -\frac{1}{8\pi^2 \varepsilon_1 \varepsilon_0 \omega} \int_{-\infty}^{\infty} \kappa_1 \tilde{J}_1(k_\rho) k_\rho \mathbf{H}_0^{(1)}(k_\rho, \rho) dk_\rho,$$

$$\mathbf{H}_\alpha^T = \frac{1}{8\pi} \int_0^{\infty} \int_0^{2\pi} \tilde{J}_2(k_\rho) k_\rho \mathbf{H}_0^{(1)}(k_\rho, \rho) dk_\rho,$$

$$\mathbf{E}_\rho^T = \frac{-1}{8\pi^2 \varepsilon_2 \varepsilon_0 \omega} \int_{-\infty}^{\infty} \kappa_2 \tilde{J}_2(k_\rho) k_\rho \mathbf{H}_0^{(1)}(k_\rho, \rho) dk_\rho.$$

Then from (10) we derive:

$$\frac{1}{8\pi} \int_{-\infty}^{\infty} \left(\frac{i\omega p k_\rho e^{ik_1 x_0}}{\kappa_1} + \tilde{J}_1(k_\rho) \right) \mathbf{H}_0^{(1)}(k_\rho, \rho)$$

$$k_\rho dk_\rho = -\frac{1}{8\pi} \int_{-\infty}^{\infty} \tilde{J}_2(k_\rho) \mathbf{H}_0^{(1)}(k_\rho, \rho) k_\rho dk_\rho,$$

$$\frac{1}{8\pi \varepsilon_1 \varepsilon_0} \int_{-\infty}^{\infty} \left(-i\omega p k_\rho e^{ik_1 x_0} + \tilde{J}_1(k_\rho) \kappa_1 \right)$$

$$\mathbf{H}_0^{(1)}(k_\rho, \rho) k_\rho dk_\rho = \frac{1}{8\pi \varepsilon_2 \varepsilon_0} \int_{-\infty}^{\infty} \tilde{J}_2(k_\rho) \kappa_2 \mathbf{H}_0^{(1)}(k_\rho, \rho) k_\rho dk_\rho. \quad (11)$$

$$\mathbf{H}_0^{(1)}(k_\rho, \rho) k_\rho dk_\rho.$$

From (11) we obtain the following system of algebraical equations:

$$\begin{cases} \frac{i\omega p k_\rho e^{ik_1 x_0}}{\kappa_1} + \tilde{J}_1(k_\rho) = -\tilde{J}_2(k_\rho), \\ -i\omega p k_\rho e^{ik_1 x_0} + \tilde{J}_1(k_\rho) \kappa_1 = \frac{\varepsilon_1}{\varepsilon_2} \tilde{J}_2(k_\rho) \kappa_2. \end{cases} \quad (12)$$

The solution of system (12) are Fourier component of sought surface current density:

$$\tilde{J}_1(k_\rho) = i\omega p k_\rho e^{ik_1 x_0} \frac{\varepsilon_2 \kappa_1 - \varepsilon_1 \kappa_2}{\kappa_1 (\varepsilon_2 \kappa_1 + \varepsilon_1 \kappa_2)},$$

$$\tilde{J}_2(k_\rho) = -i\omega p k_\rho e^{i\kappa_1 x_0} \frac{2\varepsilon_2}{\varepsilon_2 \kappa_1 + \varepsilon_1 \kappa_2}. \quad (13)$$

3.4. Total solution of boundary problem

Substituting those Fourier components of surface current densities (13) in (8), (9) we derive general solution of problem in form:

in the higher half-space:

$$\begin{aligned} \mathbf{H}^T &= -\frac{i\omega p \mathbf{e}_\alpha}{4\pi} \int_{-\infty}^{\infty} \frac{\varepsilon_2 e^{i(\kappa_1 x_0 - \kappa_2 x)}}{\varepsilon_2 \kappa_1 + \varepsilon_1 \kappa_2} \mathbf{H}_0^{(1)}(k_\rho \rho) \\ &k_\rho^2 dk_\rho, \\ \mathbf{E}^T &= -\frac{ip}{4\pi\varepsilon_0} \int_{-\infty}^{\infty} \left(\mathbf{e}_x \frac{1}{\kappa_2} - \mathbf{e}_\rho \right) \frac{\kappa_2 e^{i(\kappa_1 x_0 - \kappa_2 x)}}{\varepsilon_2 \kappa_1 + \varepsilon_1 \kappa_2} \\ &k_\rho^2 \mathbf{H}_0^{(1)}(k_\rho, \rho) dk_\rho, \end{aligned} \quad (14)$$

in the lower half-space:

$$\begin{aligned} \mathbf{H}^- &= \mathbf{H}^0 - \frac{i\omega p \mathbf{e}_\alpha}{8\pi} \int_{-\infty}^{\infty} \frac{\varepsilon_2 \kappa_1 - \varepsilon_1 \kappa_2}{\kappa_1 (\varepsilon_2 \kappa_1 + \varepsilon_1 \kappa_2)} k_\rho^2 \\ &\mathbf{H}_0^{(1)}(k_\rho \rho) e^{i\kappa_1 (x_0 + x)} dk_\rho, \\ \mathbf{E}^- &= \mathbf{E}^0 - \frac{ip}{8\pi\varepsilon_0} \int_{-\infty}^{\infty} \left(\mathbf{e}_x \frac{1}{\kappa_1} + \mathbf{e}_\rho \right) e^{i\kappa_1 (x + x_0)} \\ &\frac{\varepsilon_2 \kappa_1 - \varepsilon_1 \kappa_2}{\varepsilon_1 (\varepsilon_2 \kappa_1 + \varepsilon_1 \kappa_2)} k_\rho^2 \mathbf{H}_0^{(1)}(k_\rho, \rho) dk_\rho. \end{aligned} \quad (15)$$

4. CONCLUSION

Thus the new rigorous method for solving boundary problem is presented on the basis of Sommerfeld key problem. The physical meaning of the method consists in definition of surface current

density by using the Fourier transformations and Green's functions.

The proposed method can be applied in various boundary problems for anisotropic media.

References

- [1] V.G.Gavrilenko., V.A.Yashnov. "Information transfer on wireless networks in the conditions of a cross-country terrain", N.N. 2007. pp. 26-38.
- [2] R.W.P.King. "New formulas for the electromagnetic field of a vertical electric dipole in the a dielectric or conducting half-space near its horizontal interface", J. Appl. Phys., 53, 1982, P. 8476-8482.
- [3] V.M.Babich., M.A.Ljalinov, V.E.Grikurov. "The method of Sommerfeld-Maljuzhentz in the diffraction theory", CFY, 2003, pp. 23-35.
- [4] F.Collino, F.Millot, and S.Pernet. "Boundary-integral methods for iterative solution of scattering problems with variable impedance surface condition" PIER 80, 2008, pp. 1-28.
- [5] Wait J.R. Image theory of quasi-static magnetic dipole over a dissipative ground. Electr. Letter., 5, 1969, pp. 281-282.
- [6] Lindel I.V., M.E.Ermutlu., K.I.Nicosinen and E. H. Eloranta "Static image principle anisotropic-conducting half-space problems: PEC and PMC boundaries", Geophysics, Vol. 59, No. 12, 1993, pp. 1861-1864.
- [7] J.J.Haninnen, I.V.Lindel, K.I.Nicosinen, "Electrostatic Image Theory For An Anisotropic Boundary Of An Anisotropic Half-Space", Progress In Electromagnetic Research, Vol 47, 2004, pp. 235-262.
- [8] Lindel I.V., M.E.Ermutlu., K.I.Nicosinen and E. H. Eloranta "Static image principle anisotropic-conducting half-space problems: impedance boundary", Geophysics, Vol. 59, No. 12, 1993, pp. 1773-1778.
- [9] J. M. Jarem. "Rapidly-convergent, mixed-partial derivative boundary condition green's function for an anisotropic half-space: perfect conductor case", PIER 67, 2007, pp. 39-112.

UNIFORM RECTANGULAR SMART ANTENNA – MICROSTRIP ELEMENT MODELING AND SIGNAL DIRECTION ESTIMATION

Vyara Yordanova Vasileva

Technical University of Varna, Department of Electrical Engineering
1 Studentska Str., Varna 9010, Bulgaria
E-mail: via_vas@abv.bg

Abstract

This paper focuses on the smart antenna design steps – antenna element and uniform rectangular array modeling, an estimation of the direction of arrival (DOA) and adaptive antenna pattern creation.

For the rectangular patch antenna design is used the transmission line model (TLM). For the design procedure is specified the substrate (its relative dielectric constant and height) and the operating frequency. Numerical results derived by Matlab for patch element radiation pattern are shown.

The DOA estimation method is introduced for the significant improvement in smart antenna resolution. The DOA estimation involves a correlation analysis followed by signal/noise subspace formation and eigenstructure analysis. The 2-D unitary ESPRIT is presented for direction of arrival estimation analysis of the array. Limited numerical examples on the base of Matlab simulations are depicted to illustrate this algorithm.

1. INTRODUCTION

The smart antenna with microstrip (patch) elements is probably the most suitable class antennas for wireless communications. An appropriate adaptive array structure is a rectangular smart antenna with uniformly distributed patch elements because it owns the ability to scan the main beam in any direction of azimuth and elevation in 3-D space [1].

In antenna array modeling, the microstrip antennas are the most widely used class elements on account of their low cost, low profile. These antennas are simple to manufacture, mechanically robust, with a variety of impedance, polarization, and pattern characteristics [2].

In this paper, the direction of arrival (DOA) method is applied to antenna array modeling. The model descriptions are attended by simulation results obtained for a specific uniform rectangular array (URA).

2. THE SMART ANTENNA MODELING

2.1. The Microstrip Element Analysis and Calculation

The rectangular patch element is the most suitable and very easy for mathematical analysis. The microstrip antenna geometry is illustrated in Fig. 1, where the patch with length L ($0.33\lambda_0 \leq L \leq 0.5\lambda_0$,

λ_0 is the wavelength in the free space), consist of a very thin metallic patch with a thickness t ($t \ll \lambda_0$) placed on a dielectric substrate with a thickness h ($0.003\lambda_0 \leq h \leq 0.05\lambda_0$) above a perfectly conducting ground plane [3].

For the analysis and design of the rectangular microstrip element is applied the transmission line model (TLM) which gives accurate enough results with simple calculations. For the antenna modeling, the patch is described as a configuration of two radiating slots with width W , height h , separated by a transmission line with length L into a dielectric with an effective dielectric constant ϵ_{reff} and here is assumed that only the principal mode TM_{010}^x propagates in this line.

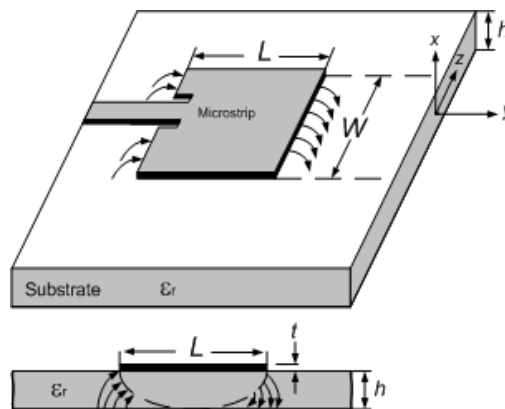


Fig. 1. The rectangular patch element geometry

For the design procedure is necessary to specify the substrate parameters (ϵ_r -relative dielectric constant, h -height) and the resonant (operating) frequency f_r . The procedure steps are:

- width calculation:

$$W = \frac{1}{2f_r \sqrt{\mu_0 \epsilon_0}} \sqrt{\frac{2}{\epsilon_r + 1}} \quad (1)$$

- effective dielectric constant:

$$\epsilon_{r_{eff}} = \frac{\epsilon_r + 1}{2} + \frac{\epsilon_r - 1}{2\sqrt{1 + 12h/W}} \quad (2)$$

- length extension ΔL and effective patch length computations (Figure 2):

$$\Delta L = 0.412h \frac{(\epsilon_{r_{eff}} + 0.3)(W/h + 0.264)}{(\epsilon_{r_{eff}} - 0.258)(W/h + 0.8)} \quad (3)$$

$$L = \frac{1}{2f_r \sqrt{\mu_0 \epsilon_0 \epsilon_{r_{eff}}}}, \quad L_{eff} = L + 2\Delta L \quad (4)$$

The input impedance is determined using the following formulas [4]:

$$R_{in} = \frac{1}{2(G_1 + G_{12})}, \quad R_{in}(y = y_0) = R_{in} \cos^2\left(\frac{\pi}{L} y_0\right) \quad (5)$$

$$G_1 = \frac{-2 + \cos(k_0 W) + (k_0 W) S_i(k_0 W) + \frac{\sin(k_0 W)}{k_0 W}}{120\pi^2} \quad (6)$$

where G_1 is the conductance of a single radiating slot, k_0 is the free space phase constant, $S_i(X)$ is a sine integral, G_{12} is the mutual conductance between the two radiating slots (often neglected in first approximation).

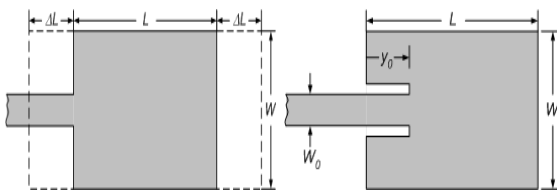


Fig. 2. The microstrip antenna parameters

For the modeling procedure is necessary to calculate the microstrip element directivity [3]

$$D_{patch} = D_0 \frac{2G_1}{G_1 + G_{12}} \quad (7)$$

$$D_0 = \frac{2\pi W / \lambda_0}{-2 + \cos(k_0 W) + (k_0 W) S_i(k_0 W) + \frac{\sin(k_0 W)}{k_0 W}} \quad (8)$$

where D_0 is the directivity of a single slot. In the first approximation after neglecting G_{12} the patch antenna directivity is $D_{patch} \approx 2D_0$.

2.2. The URA Smart Antenna Structure

The URA array with $N \times M$ (M, N – even) equally distributed identical patch elements is located symmetrical in x - y plane (in Figure 3 their center positions are shown by dots). The origin of coordinate system is located at the center of the array. An incoming narrowband signal arrives at the array from elevation angle θ and azimuth angle ϕ .

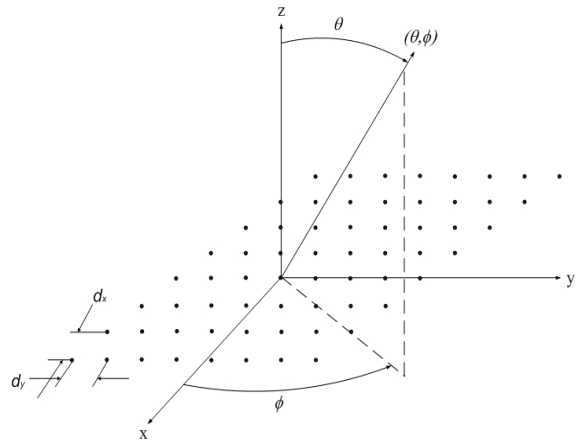


Fig. 3. URA geometry, along with an incoming signal

The *array factor* (AF) of URA with its maximum along (θ_0, ϕ_0) can be calculated using the following expression [3]

$$[AF(\theta, \phi)]_{M \times N} = 4 \sum_{m=1}^{M/2} \sum_{n=1}^{N/2} A_{mn} \cos[(2m-1)u] \cos[(2n-1)v] \quad (9)$$

where

$$u = \frac{\pi d_x}{\lambda} (\sin \theta \cos \phi - \sin \theta_0 \cos \phi_0) \quad (10)$$

$$v = \frac{\pi d_y}{\lambda} (\sin \theta \sin \phi - \sin \theta_0 \sin \phi_0) \quad (11)$$

where A_{mn} is the amplitude excitation of the individual element, and (d_x, d_y) are the inter-element spacing along the x-axis and the y-axis, respectively.

2.3. 2-D Unitary ESPRIT

The DOA algorithm determines the directions of incoming on the URA signals based on the time delays. These delays depend on array geometry, number of elements, and inter-element spacing. The DOA estimation involves a correlation analysis followed by signal/noise subspace formation and eigenstructure analysis.

For the URA of Figure 3, the time delay of the narrowband signal at the (m, n) th element with respect to the origin, is written as [4]

$$\tau_{mn} = \frac{md_x \sin \theta \cos \phi + nd_y \sin \theta \sin \phi}{c} \quad (12)$$

where c is speed of light in free space.

For the significant improvement in smart antenna resolution 2-D Unitary ESPRIT (*Estimation of Signal Parameters via Rotational Invariance Technique*) method is applied. This algorithm is a technique for accurate direction of arrival signal computation in the real time on the base of array matrix analysis. Applying this method under the conditions of a URA structure (Figure 3), the five basic steps of real valued estimation are briefly described [5]:

1. Compute \mathbf{E}_s via d "largest" left singular vectors of $[\text{Re}\{\mathbf{Y}\}, \text{Im}\{\mathbf{Y}\}]$ where $\mathbf{Y} = (\mathbf{Q}_M^H \otimes \mathbf{Q}_N^H) \mathbf{X}$.

2. Calculate $\boldsymbol{\psi}_\mu$ as the solution to the $[(N-1)M \times d]$ $\mathbf{K}_{\mu 1} \mathbf{E}_s \boldsymbol{\psi}_\mu = \mathbf{K}_{\mu 2} \mathbf{E}_s$ matrix equation.

3. Compute $\boldsymbol{\psi}_\nu$ as the solution to the $[(N-1)M \times d]$ $\mathbf{K}_{\nu 1} \mathbf{E}_s \boldsymbol{\psi}_\nu = \mathbf{K}_{\nu 2} \mathbf{E}_s$ matrix equation.

4. Compute $\lambda_i, i=1, \dots, d$, as the eigenvalues of the $(d \times d)$ matrix $\boldsymbol{\psi}_\mu + j\boldsymbol{\psi}_\nu$.

5. Compute spatial frequency estimates

$$\mu_i = 2 \tan^{-1}(\text{Re}\{\lambda_i\}) \text{ and}$$

$$\nu_i = 2 \tan^{-1}(\text{Im}\{\lambda_i\}), i=1, \dots, d.$$

3. SIMULATION RESULTS

Simulation results and numerical examples are based on the theory depicted above. The design

procedure was realized on the base mathematical calculations and Matlab simulations presented in Table 1 and Figure 4 [6]. The modeling smart antenna element was rectangular microstrip antenna operating at frequency 2.4 GHz and using substrate with parameters $\epsilon_r = 2.2$ and $h = 0.1588$.

The DOA estimation is investigated under the conditions of a URA structure with modeling rectangular patch elements described above. The method described in Section 2 is utilized to perform the estimation [4].

Table 1. Modeling results for patch element

Patch parameters	Mathematical calculation	Matlab simulation results
Physical width [cm]	4.9411	4.9411
Physical length [cm]	4.1373	4.1356
Effective length [cm]	4.3047	4.3030
Resonant input resistance [ohms]	244.5795	244.7745
Feed point position [cm]	1.4504	1.4504
Directivity [-]	5.0295	5.2118
Directivity [dB]	7.0152	7.1699

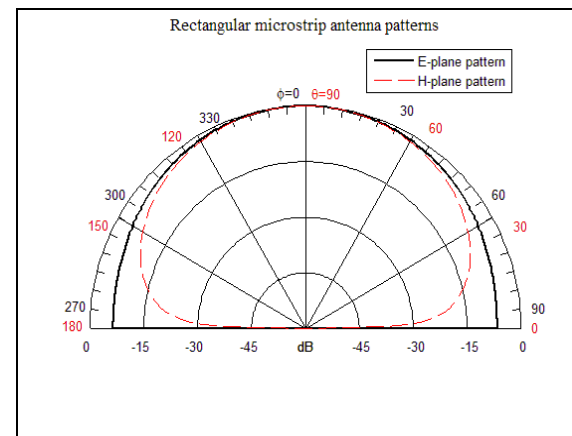


Fig. 4. The rectangular microstrip element radiation pattern

To illustrate the DOA algorithm applicability for URA, is considered the case where the URA with $N=8$ and $M=8$ elements and interelement spacing (the center-to-center separation between elements) $d_x = d_y = 0.45\lambda$ is examined. The *signal of interest* (SOI) incomes from $(\theta = 60^\circ, \phi = 100^\circ)$, while the three *signals not of interest* (SNOI) are directed from $(\theta = 20^\circ, \phi = 70^\circ)$, $(\theta = 40^\circ, \phi = 120^\circ)$ and $(\theta = 90^\circ, \phi = 155^\circ)$ are given in Table 2. Analyzed type of array is investigated in the presence of the *Additive White Gaussian Noise* (AWGN) with the zero mean, and variance 0.1. The results

demonstrate its ability for accurate estimation, great performance, and *robustness*. Simulation results, utilizing the 2-D unitary ESPRIT algorithm give precise data when adapt the smart antenna pattern.

Table 2. The DOA data and estimation obtained utilizing 2-D unitary ESPRIT

URA structure	Data
Number of elements	M=8 ,N=8
Inter-element spacing	0.45 λ
Number of incoming signals	1
Number of data samples	2000
Actual direction data	
SOI	$\theta_1=60^\circ, \varphi_1=100^\circ$
SNOI 1	$\theta_2=20^\circ, \varphi_2=70^\circ$
SNOI 2	$\theta_3=40^\circ, \varphi_3=120^\circ$
SNOI 3	$\theta_1=90^\circ, \varphi_1=155^\circ$
DOA direction estimations	
SOI	$\theta_1=59.9998^\circ, \varphi_1=100.0977^\circ$
SNOI 1	$\theta_2=20.9928^\circ, \varphi_2=69.9951^\circ$
SNOI 2	$\theta_3=40.0031^\circ, \varphi_3=120.0897^\circ$
SNOI 3	$\theta_1=89.9995^\circ, \varphi_1=154.9997^\circ$

4. CONCLUSION

This paper investigates the issues for a single rectangular patch element design procedure and a uniform rectangular smart antenna structure modeling with microstrip elements.

Numerical simulation results are illustrated that the patch element design gives accurate results, and that the antenna geometry configuration with M=N=8 microstrip elements is an optimal scenario, because the DOA estimations are proved to be accurate and stable enough, and the smart antenna pattern creation is affected by the type of elements, size and geometry of the antenna array.

A brief theory of antenna array to distinguish the direction of arrival by 2-D ESPRIT algorithm is considered that is used as a DOA technique.

The rectangular adaptive array with uniformly distributed microstrip elements used here is analyzed based on the TLM method (for a single patch element representation) and the 2-D unitary ESPRIT technique (for the smart array calculation). The influence of different design parameters is explored assuming a monochromatic plane wave excitation coming from a specific direction. Then the specified iterative algorithm is applied to estimate the DOA.

This theory was supported by suitable numerical data (see the Table 2). The direction of arrival estimation for array pattern creation was examined. Matlab programs are used for simulations. The simulations show very good agreement between the assumptions and estimations.

5. ACKNOWLEDGMENT

Project no. 3 in the frames of the Research Program, financed from Ministry of Education of Bulgaria.

References

- [1] L. C. Godara, "Smart Antennas", CRC Press LLC, Florida, 2004.
- [2] J. James, P. Hall, "Handbook of Microstrip Antennas", vols. 1, 2, P.Peregrinus Ltd., London, 1989.
- [3] C. A. Balanis, "Antenna Theory", John Wiley & Sons, New York, 2005.
- [4] R. Roy, T. Kailath, "ESPRIT-Estimation of Signal Parameters via Rotational Invariance Techniques", IEEE Transactions on Acoustics, Speech, and Signal Processing, vol. 37, no. 7, pp. 984-995, 1989.
- [5] M. Zoltowski et al., "Closed-Form 2-D Angle Estimation with Rectangular Arrays in Element Space or BeamSpace via Unitary ESPRIT", IEEE Transactions on Signal Processing, vol. 44, no. 2, pp. 316-328, 1996.
- [6] K. Lonngren, S. Savov, R. Jost, "Fundamentals of Electromagnetics with Matlab", (2nd ed.), SciTech, 2007.

AN AUTOFOCUSING ALGORITHM FOR POST-PROCESSING ISAR IMAGING BASED ON IMAGE ENTROPY MINIMIZATION

E. Kallitsis¹, G. Boultaakis¹, A. Karakasiliotis¹, I. Tseremoglou¹, E. Stergiannis¹,
H. Hristakis¹, E. Grigoratou², A. Vagianou² and P. Frangos¹

¹ National Technical University of Athens

9, Iroon Polytechniou Str., GR 157 73, Zografou, Athens, Greece

Tel: +30 210 772 3694, Fax: +30 210 772 2281, E-Mail : pfrangos@central.ntua.gr

² Hellenic Air Force Academy

Abstract

Fast maneuvering of aircraft targets may be one of possible reasons for Inverse Synthetic Aperture Radar (ISAR) image blurring. This is due to the range bin migration of the target's scatterers during the Radar Coherent Processing Interval (CPI). Traditional ISAR imaging techniques to compensate for this effect include "range tracking" [high resolution range profile (HRRP) alignment] and "Doppler tracking" (phase correction to the HRRP's). Furthermore, a variety of advanced signal processing techniques, which takes into account the time-varying Doppler spectra of the target's scatterers during the CPI, have been proposed in the last decades, including Time-Frequency based ISAR imaging.

In this paper we will present preliminary simulation results based on the proposed autofocusing algorithm, for which the aircraft target exhibits a high angular acceleration, which simulates fast maneuvering. The proposed ISAR imaging post-processing scheme (Section 2), is described as following: for any particular CPI consisting of N range profiles, for which ISAR image entropy exceeds a particular threshold (e.g. due to fast target maneuvering), this CPI is initially divided to two CPI's of equal length, i.e. $N/2$ range profiles in each, and two ISAR images are formed. It is assumed that "Range tracking" and "Doppler tracking", as described above, have already been applied. The entropy values of the above two ISAR images are calculated, and HRRP data corresponding to the worst image, i.e. that corresponding to higher image entropy, are neglected. Instead, a set of $N/2$ HRRP data are borrowed either from the previous or from the next CPI's HRRP data, in order to form a new improved ISAR image in the ISAR image database (i.e. a post-processing scheme). The proposed method may be further improved by subdividing the CPI in four parts of equal length and so on.

Preliminary numerical results, based on simulated radar data are presented in Section 3.1. Finally, preliminary ISAR images obtained by the authors using real radar data ('ORFEO' data from TNO, Netherlands) are presented in Section 3.2. Finally, conclusions and further related research are presented in Section 4.

Keywords: Inverse Synthetic Aperture Radar (ISAR), Range – Doppler (RD) ISAR Imaging, Fast maneuvering of air targets, autofocusing post – processing techniques, raw radar data handling, optimum ISAR data processing, ISAR image entropy, Coherent Processing Interval (CPI).

1. INTRODUCTION

Two – dimensional (2D) ISAR image formation is the process of reconstructing 2D images of radar targets from recorded radar-received complex data [1,2]. The *backscattered radar data*, after initial processing, such as pre-filtering, demodulation, de-chirping etc. [1,2] is obtained in the form of *raw radar data* in the *baseband*. According to *traditional Range – Doppler (RD) ISAR processing*, a *matrix* containing $M \times N$ complex (i.e. *magnitude and phase*) *raw radar data* is obtained, for which traditional Fourier processing is applied to both rows and columns of the matrix, as it will be explained shortly at the beginning of Section 2, below [1,2]. In this way, a 2D ISAR image according to the traditional RD imaging technique is obtained. In this context, we assume in this paper that the radar transmits a *stepped – frequency (SF, [2]) waveform* consisting

of M frequency steps (see Section 2, below). A sequence of M such radar pulses constitutes a radar emitted *burst*. It will be assumed in this paper that N bursts are used at the radar receiver, in order to form a matrix of dimensions $M \times N$ for the raw baseband radar complex data mentioned above. Furthermore, in the context of this paper, as it will also be explained in Section 2 below, the M complex radar data forming any particular row of the data matrix mentioned above, are considered as 'frequency – domain' data, to which an Inverse Fast Fourier Transform (IFFT) is applied, in order to obtain N *range profiles*. According to traditional RD ISAR processing, these range profiles are then 'aligned', before obtaining the final ISAR image through a Fast Fourier Transform (FFT). This alignment usually consists first of 'range *tracking*' [2,3], according to which, roughly to say, the maximum peak in the target radar echo is sought to remain at

the same 'range bin' through the whole 'Coherent Processing Interval (CPI)', or so [2,3]. A possible second step [2,3] consists of the so – called '*phase tracking*' [2], where appropriate phase correction is applied to the $M \times N$ complex data of the 'range profiles', before applying the FFT for obtaining the final 2D ISAR image. After 'range tracking', and possibly 'phase tracking', are applied, then a Fast Fourier Transform (FFT) is applied to the data for each column of the radar data corresponding to the obtained target range profiles, in order to obtain the final 2D ISAR image of the target. This concludes, more or less, the process of *traditional Range – Doppler (RD) ISAR* imaging.

In the context of this paper, the term '*autofocusing*' is related to *post – processing ISAR imaging techniques*, which improve the quality of ISAR images, before further target classification or target identification techniques are applied. This term is used by several authors in different ways (see e.g. [4-11]). Many times autofocusing is applied *through image entropy minimization* [4, 9-11], method that will be adapted also in this paper. Other times it is applied through 'image contrast maximization' (see e.g. [5]), etc. In the present paper, we will mainly focus on how to improve 2D ISAR image quality through a *proposed post – processing scheme*, which neglects raw radar data of poor quality, *due to fast target manoeuvring* (simulated in the present study through high *angular target acceleration*). The criterion for applying the above proposed 'autofocusing' post – processing technique is image entropy minimization. *Ultimately*, our proposed method will lead to a *fully automatic post – processing algorithm of raw radar data handling, for improved 2D ISAR image generation, based on image entropy minimization. Even the problem of optimum number of radar data (number of used radar bursts) will be examined in a systematic way, depending on the target kinematics* (target angular acceleration etc.). Finally, the present study is based on simulated backscattered radar data using stepped – frequency (SF) emitted waveform [12]. However, ISAR imaging is performed in this study also through the use of *real raw radar data* for air civilian targets, provided by TNO, the Netherlands (the so – called 'ORFEO' data, see 'acknowledgement' at the end of this paper). *Ultimately*, optimum radar data handling studies will be provided by the authors for real (experimental) radar data, as well.

2. PROPOSED AUTOFOCUSING POST – processing ISAR imaging technique for a particular fast rotation of the air target simulation scenario

2.1. Raw radar data in matrix form – Simulation scenario for fast manoeuvring of the air target

As we explained in detail in the 'Introduction' Section, above, the backscattered raw radar data in the baseband (i.e. after demodulation etc.), in the frequency – domain, are in the form of a matrix with dimensions $M \times N$, as exactly explained in Section I, above. Traditional 'Range – Doppler' procedure [1-2] for ISAR image generation is applied. Namely we assume here that M transmitted frequencies per burst are used in the transmitted SF waveform, and, furthermore, N bursts are used in order that an ISAR image is formed.

Regarding the simulation of fast maneuvering of the target, in the simulation scenario which will be considered here, this is accomplished through a fast angular acceleration of the target, as shown in Fig. 1, below. Here 2D target geometry is considered, and radar Line-of-Sight (LOS) is considered on this plane. We call this plane 'ISAR image plane' as well, for convenience. Then, in the present simulation scenario, it is assumed, without loss of generality (see e.g. [1-3]), that the axis of target rotation and angular acceleration is perpendicular to the ISAR image plane. Numerical values of these kinematic parameters of the air target will be provided in Section III, below, along with the corresponding radar parameters of the proposed simulation scenario.

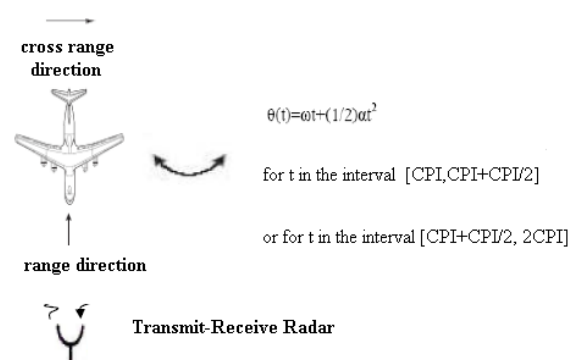


Fig. 1: Simulation of fast maneuvering of the air target in the present simulation scenario through a fast angular acceleration α , as shown in the formula for the aspect angle $\theta(t)$ above, where ω represents the angular velocity of rotation of the target, and t represents time. More details are given in the text.

2.2. Data handling for the proposed 'autofocusing' post – processing algorithm

In the proposed simulation scenario for fast angular acceleration of the air target, we will focus on the process of *deriving a set of ISAR images of 'better quality', as compared to the original set of ISAR images, through the proposed 'autofocusing' post – processing algorithm.* Better image quality means better focused ISAR image of the target, which quantitatively is accomplished through the *'image entropy' concept* [4, 9-10]. For this purpose, in the proposed simulation scenario, we will assume that 3 (three) ISAR images will be produced, corresponding to radar processing time equal to 3 (three) 'Coherent Processing Intervals' (CPI's). Here by 'Coherent Processing Interval' (CPI) we mean, as it is traditional for SAR or ISAR processing [1-3], the radar receiver required processing time in order to form an ISAR image, which, for the SF transmitted waveform considered here is equal to

$$\text{CPI} = N \times T_b \quad (1)$$

where N is the number of bursts in the CPI, as explained above, and T_b is the duration of the burst, given by the formula

$$T_b = M \times T_E \quad (2)$$

where T_E is the pulse repetition interval (or 'period' / PRI) of the radar. Then, in the simulation scenario proposed here, *fast angular acceleration of the target will be assumed to take place only during the 2nd CPI (either during the 1st half or during the 2nd half of the 2nd CPI), during which radar data of inferior quality will be replaced by radar data of superior quality, borrowed from radar data coming from the 1st or 3rd CPI considered here.* This procedure will ultimately result to a better set of derived ISAR images, as already explained above, and as will be quantitatively shown below through a 'proof-of-concept' initial demonstration.

Namely, the proposed 'autofocusing' algorithm is as following: when a particular obtained ISAR image corresponds to a image entropy value [4, 9-10] above a particular (pre-selected) value, and this raise of image entropy value is attributed by the radar user to a temporary target fast maneuvering, then the radar user initiates the proposed algorithm, by keeping only radar data of superior quality. In the proposed simulation scenario we consider the following 2 (two) cases:

(i) Case I: Here we assume that the obtained ISAR image's entropy value (corresponding to the 2nd CPI) exceeds its threshold value due to targets' fast angular acceleration during the 2nd half of the 2nd CPI. Then, as shown in Table 1, below, the radar data of the lower half of the corresponding raw data matrix shown in Table 1 must be replaced by data of better quality, in a suitable way. This proposed way is the following: form the raw radar data matrix corresponding to the 2nd CPI by

- (i) Neglecting the data of inferior quality (marked by the dashed line box of Table 1 / i.e. data corresponding to the *lower* half of the matrix).
- (ii) Shift the data corresponding to the *upper* half of this matrix to the *bottom* part of the matrix (i.e. in the place marked by the dashed line box of Table 1).
- (iii) Fill in the *upper* half of this $M \times N$ matrix with the raw radar data corresponding to the *lower half* of the data matrix of the 1st CPI.

Using the above proposed 'autofocusing' procedure, half of the data corresponding to the 'dangerous' 2nd CPI (i.e. those corresponding to the *upper* half of the matrix) are still preserved for radar processing (i.e. not just 'thrown away'), thus ultimately providing a better set of obtained ISAR images.

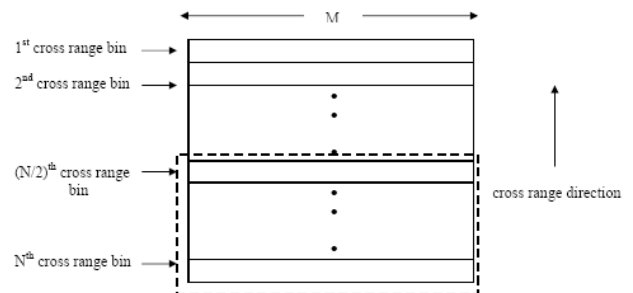


Table 1: Frequency domain raw radar data in the baseband corresponding to the 2nd CPI (out of 3 CPI's) considered in the proposed simulation scenario, which corresponds to an $M \times N$ matrix, as explained in Section IIA. From these $M \times N$ complex data, the data corresponding to the *lower* half of the matrix are considered as data of lower quality due to fast target maneuvering during the 2nd half of the 2nd CPI, and therefore they are replaced suitably for better ISAR image formation, as explained exactly in the text.

(ii) Case II: Here we assume that the obtained ISAR image's entropy value (corresponding to the

2nd CPI) exceeds its threshold value due to targets' fast angular acceleration *during, in this case, the 1st half of the 2nd CPI*. For this case, we follow a procedure analogous to that of Case I, in order to obtain better ISAR image quality (not explained in detail here, for brief).

Numerical results which show 'proof-of-concept', based on the simulation scenario described above, will be provided in the next Section III.A., along with corresponding radar and target kinematics data used in the simulation. Furthermore, preliminary ISAR images based on real radar data provided by TNO, the Netherlands ('ORFEO' data, taken from civilian aircrafts, as mentioned above) will also be provided in Section III.B.

3. NUMERICAL RESULTS

3.1. Preliminary numerical results for the simulation scenario for fast maneuvering of the air target – description of radar and target kinematics parameters

The simulated target geometry is shown in Fig. 2, below, consisting of 22 point scatterers, thus simulating an aircraft target of length equal to 31 m in the range direction (vertical axis of Fig. 2 / from simulated cockpit to rear of the aircraft, in this simplified model), and 11.3 m in the cross – range direction (horizontal axis of Fig. 2 / wingspan of the airplane). The airplane is located 4.5 km away from the monostatic radar, and it rotates about an axis which is perpendicular to the ISAR image plane (which coincides with plane where the 22 point scatterers have been placed, in Fig. 2). Radar and target rotation parameters are appropriately selected [14] (not shown here for brief).

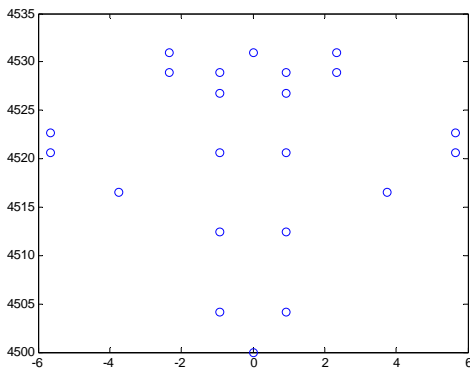


Fig. 2: Geometry of the simulated air target consisting of 22 point scatterers. See text for details.

Following our proposed autofocusing algorithm, as explained in Section II, above, ISAR images of the above simulated target are obtained for three (3) subsequent 'Coherent Processing Intervals' (CPI's). For this purpose, simulated backscattered raw radar data in the baseband are obtained through the following well – known formula [1,3]:

$$x(m,n) = \sum_{k=1}^d s_k \exp(j \frac{4\pi}{c} f_m [x_k \cos \theta_n - y_k \sin \theta_n]) + u(m,n) \quad (3)$$

where d is the number of scatterers ($k=1$ to d / here $d=22$), M ($m=1$ to M) is the number of frequency steps in the SF waveform, N ($n=1$ to N) is the number of bursts in the CPI [equivalently θ_n is the aspect angle of the target at the particular 'slow time' instant $t_n(\theta_n = \omega t_n + \alpha t_n^2/2)$], and $u(m,n)$ is additive white Gaussian noise of mean zero and variance σ^2 . The simulated data derived from Eq. (3), above, correspond to frequency domain raw baseband radar data, from which ISAR images are obtained according to the traditional Range – Doppler (RD) imaging procedure [1,2].

In the particular simulation experiment described here, three (3) subsequent CPI's were considered, according to our proposed autofocusing algorithm, described in Section 2, above. Fast angular acceleration of the target was considered only during the 2nd half of the 2nd CPI, for which our autofocusing algorithm, as explained in Section II, was applied. This resulted in better image focus during the 2nd CPI of fast target maneuvering, thus showing the 'proof-of-concept' for our proposed algorithm. An indicative ISAR imaging result, which corresponds to the 2nd CPI of processing, *after* application of our proposed autofocusing algorithm, is shown in Fig. 3, below (only this ISAR image, for this simulation scenario, is shown here, for brief). Corresponding ISAR image entropy values [9,10] are also calculated [14]. Finally, similar results, also showing the 'proof-of-concept' for our proposed algorithm, were obtained in the case that target's fast angular acceleration occurs in the 1st half of the 2nd CPI, according to our proposed method of Section 2 (these similar results are not shown here, for brief).

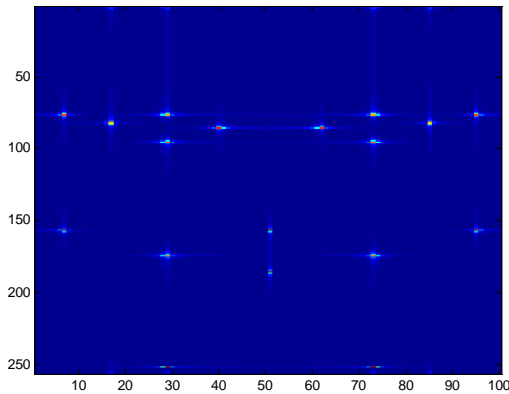


Fig. 3: ISAR image obtained for the simulated target of Fig. 2, for the data obtained during the 2nd CPI of the simulation experiment, for which *target fast maneuvering occurred during the 2nd half of the 2nd CPI*. Here our *proposed autofocusing algorithm was applied*, which reduced the image entropy value to $E=1.44$ (lower than the entropy threshold of 2.3), thus showing the 'proof-of-concept' of our proposed autofocusing algorithm.

3.2. Preliminary ISAR imaging results based on real radar data

In this Section we provide some preliminary ISAR imaging results based on real (experimental) radar data. Namely, these data were provided to us by TNO, the Netherlands ([13], see acknowledgement at the end of this paper), they are called by TNO 'ORFEO' data, and they are concerned with real measurement of civilian aircrafts in flight. TNO provided to us target range profiles, as well as raw baseband radar data in the frequency domain. The transmitted waveform used by TNO during this measurement campaign was 'velocity – tolerant' stepped – frequency (SF) waveform. Related information is given in [13]. Using the ISAR image formation algorithms of our research groups [at this point this is just a traditional inverse Fast Fourier Transform (IFFT) in the cross – range direction] we obtained ISAR images of many civilian aircrafts measured by TNO. A representative example of these ISAR images is shown in Fig. 4, below, concerning Embraer Brasilia EMB-120 aircraft.

In Fig. 4, above, the resolution cell in the range direction (horizontal axis) is again $\Delta R=c/2B=32$ cm, as provided by TNO. The aircraft here consists of about 65 range bins (not shown very clearly here), which corresponds to aircraft length in the range direction (horizontal axis) of about $65 \times 0.32 = 20.8$ m, which compares very well with the length of this aircraft provided by its manufacturers, which is 20.0 m. Regarding the estimation of the 'wing – to – wing' dimension of this aircraft through ISAR ima-

ging, some more precise processing and calculations in the cross – range direction have to be performed by our research group in the near future.

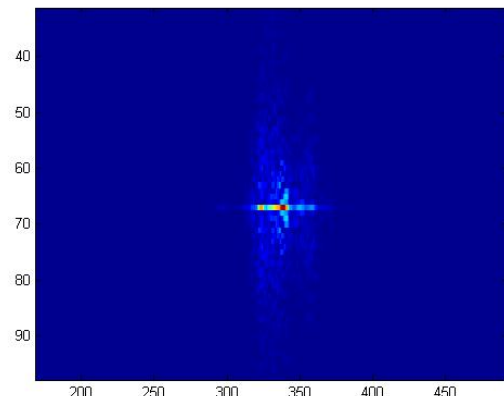


Fig. 4: ISAR image for an Embraer Brasilia EMB-120 civilian aircraft obtained using data from the 'ORFEO' measurement campaign for aircrafts in flight by TNO, the Netherlands [13], by using the ISAR imaging formation algorithm of our research group. Here, again, the horizontal axis corresponds to the 'range' direction, while the vertical axis corresponds to the 'cross – range' direction. See more details in the text.

Concluding this Section, we mention that our research group intends to work in the near future in the direction of applying the proposed autofocusing method, described in this paper, above, for the real 'ORFEO' data described above, as well.

4. CONCLUSION – FUTURE RELATED RESERACH

In this paper we developed, and presented preliminary numerical results, an 'autofocusing' post – processing ISAR imaging method for high maneuvering air targets. The proposed method uses the raw complex radar data in the baseband (in the frequency domain) in a *dynamically optimum way*, so that it uses the string of data coming at the radar receiver in a way such that data leading to ISAR images of poor quality are neglected, and only data leading to ISAR images of superior quality are used. The ultimate goal of this proposed 'autofocusing' post – processing procedure is that the ISAR radar user ends up with a set of ISAR images of superior quality, based on which better image classification will be performed.

At the present stage, presented in this paper, simple point – scatterer air targets were used in the simulation. Furthermore, radar target fast maneuvering was simulated through high angular target acceleration, as explained in the text. Moreover, in the initial simulation scenario described above, we

selected just three (3) 'Coherent – Processing – Intervals' (CPI's) in order to show an initial 'proof – of – concept' of our proposed technique. Finally, preliminary ISAR imaging results, obtained by our research group, and based on real radar data provided by TNO, the Netherlands, were shown above.

Proposed autofocusing technique will be fully automatic, for an arbitrary number of radar observation time, in terms of number of CPI's. Of course, more precise radar target modeling will be used, than the point scatterer model used above, for the proposed simulations, and our technique will be tested against real radar data, as well. Finally, our proposed autofocusing algorithm may be further refined, for example, by dividing the CPI by a factor of four (4), and not by the factor of two (2), as proposed in this paper, in order to use the received data in a possibly even more effective way, as explained above. The counter – effect to this will be, of course, larger processing time, for this proposed 'post – processing' ISAR imaging tool. Then, it is up to this algorithm designer, or to the ISAR radar user, to select the appropriate CPI subdivision factor, for optimum ISAR data processing.

ACKNOWLEDGMENT

The authors would like to express their sincere thanks to Dr. Sjoerd Gelsema, TNO, the Netherlands, for providing to them the 'ORFEO' real radar data for civilian aircrafts (unclassified data), through SET 112 Working Group.

References

[1] D. Wehner, 'High-Resolution Radar', Artech House, 2nd edition, 1995.

[2] V. Chen, H. Ling, 'Time-Frequency Transforms for Radar Imaging and Signal Analysis', Artech House, 2002.

[3] J. Son, G. Thomas, and B. Flores, 'Range-Doppler Radar Imaging and Motion Compensation', Norwood, MA, Artech House, 2001.

[4] A. Lazarov, C. Minchev, 'ISAR Signal Modeling and Image Reconstruction with Entropy Minimization Autofocusing', Proc. DASC, Portland, USA, 2006.

[5] M. Martorella, F. Berizzi and B. Haywood, 'Contrast maximization based technique for 2-D ISAR autofocusing', IEE Proc.-Radar Sonar Navig., Vol. 152, No. 4, Aug. 2005, pp. 253 – 262.

[6] Li Xi, Liu Guosui and Jin Lin Ni, 'Autofocusing of ISAR images based on entropy minimization', IEEE Trans. Aerospace and Electronic Systems, Vol. 35, No. 4, Oct. 1999, pp. 1240 – 1252.

[7] Zhishun She, D.A. Gray and R.E. Bogner, 'Autofocus for inverse synthetic aperture (ISAR) imaging', Signal Processing, 81, 2001, pp. 275 – 291.

[8] H.R. Jeong, H.T. Kim and K.T. Kim, 'Application of subarray averaging and entropy minimization algorithm to stepped – frequency ISAR autofocus', IEEE Trans. Ant. Prop., Vol. 56, No. 4, April 2008, pp. 1144 – 1154.

[9] A. Karakasiliotis, A. Lazarov, P. Frangos, G. Boultadakis, and G. Kalognomos, 'Two-dimensional ISAR model and image reconstruction with stepped frequency-modulated signal', IET Signal Processing, 2008, Vol. 2, No. 3, pp. 277–290.

[10] G. E. Boultadakis, G. K. Kalognomos, L. K. Stergioulas, A. V. Karakasiliotis, and P. V. Frangos, 'A Comparative Study of Bilinear Time–Frequency Transforms of ISAR Signals for Air Target Imaging', 'Electronics and Electrical Engineering' Journal, Vol. 92, Nr. 4, pp. 87 – 92, 2009.

[11] G. K. Kalognomos, G. E. Boultadakis, A. V. Karakasiliotis and P. V. Frangos, 'Performance Analysis of a Parameterized APES (PAPES) Spectrum Estimation Method for ISAR Applications', 'Electronics and Electrical Engineering' Journal, No. 3 (99), March 2010.

[12] A. Karakasiliotis and P. Frangos, 'Comparison of several spectral estimation methods for application to ISAR imaging', RTO/SET 080 International Symposium on 'Target Identification and Recognition Using RF Systems', Oslo, Norway, 11/10/04 – 13/10/04.

[13] TNO report FEL-96-1073, 'The ORFEO measurement campaign', authors: R. van der Heiden, J. de Varies, 25 July 1996 (www.tno.nl).

[14] E. Kallitsis, G. Boultadakis, A. Karakasiliotis, I. Tsereoglou, E. Stergiannis, H. Hristakis, E. Grigoratou, A. Vagianou, P. Frangos, T. Kostis, E. Papkelis and S. Pinzoz, SET 160 Symposium on 'NCTI / ATR in Air-Ground and Maritime Applications based on Radar and Acoustics', Athens, Greece, 11-12/10/2010.

STUDY OF THE INTERACTION OF RADIATED EM FIELDS WITH HUMAN OPERATORS

M.J. Martins, J. F. Rodrigues

DEEC, IST-UTL, Lisbon

Abstract

In the information society, each human being is subjected daily to a significant amount of electromagnetic fields, which comes from power lines, wireless networks, radio transmission and the computers that we use for any aspect of our lives professionally as well as for leisure.

So every human being is immersed nowadays in an ocean of radiofrequency fields, which extend all over the world.

In this paper we present an analysis of the influence of wireless antennas, developed in our department and its effect on human operators.

INTRODUCTION

The exposure of human beings to electromagnetic radiation has been a subject of growing concern over the last decades. The study of the possible effects on human health of EM fields, namely the interaction of low frequency fields associated with power lines goes back to 1979, when a study was conducted, in the state of Colorado (U.S.A.) aiming at proving the connection between the development of child cancer and EM power lines EM fields [1].

Several studies were performed by leading experts, trying to identify a mechanism of cause-effect [2], [3].

A statistical analysis showed some connection concerning the incidence of child leukemia and exposure to EM fields connected to power lines. Despite the intense efforts developed in this field of research, to date no credible mechanism could be identified and no cause-effect relation has been established.

In recent years, other studies have been performed, namely by the European Commission, in order to identify quantitatively the values of magnetic fields which are harmful to human health and also, to investigate if an iterative effect is present leading to long-term consequences.

A study conducted in 2004 [4], identified the value of $100\mu\text{T}$ at 50Hz as a boundary value to be avoided for human exposure.

For long term effects, it was noted that a long exposure to magnetic fields could lead to a substantial reduction at the same frequency for these effects.

In the publication referred above, a value of 0.2 to $0.4\mu\text{T}$, connected to a 24h exposure time was considered potentially harmful.

Another interesting point is the recently appointed connection between EM low-frequency fields and neuro-pathologies such as Alzheimer disease and amyotrophic lateral sclerosis [5].

The study of these effects by our group started in 2002 when some colleagues from the Department have been involved in the project of electrical vehicles for public transportation. Several studies were published on the possible effects for public health of aerial or underground power supply.

Our group is devoted to the design, testing and implementation of antenna systems for telecommunications applications in the radio frequency band, so we had the idea of carrying the same research to higher frequency bands.

SIMULATION AND MEASUREMENT

One of such projects was the development of antennas for wireless communications in laptops. Due to long term exposure of our students to the fields radiated by these antennas, an interesting point was to investigate the influence of the operator nearness on the radiated field, and also the dual effect: how these fields were absorbed by the operator.

The objectives of this project were to obtain a numerical analysis of human-radiated EM fields, considering specifically the following effects:

- how the presence of the user affects the antenna operation,
- how the operating antenna illuminates the human biological tissues,

Dependence of antenna-human EM interaction

on:

- antenna location and laptop screen opening angle,
- antenna type,
- antenna housing type (internal/external),
- position of the operator (typing/ non typing)

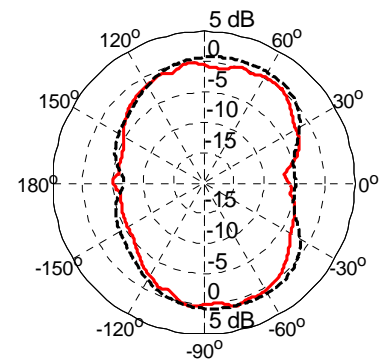
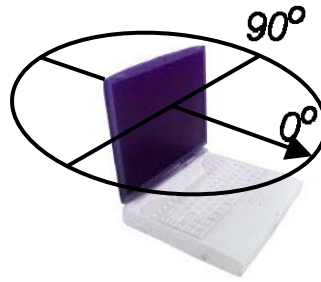
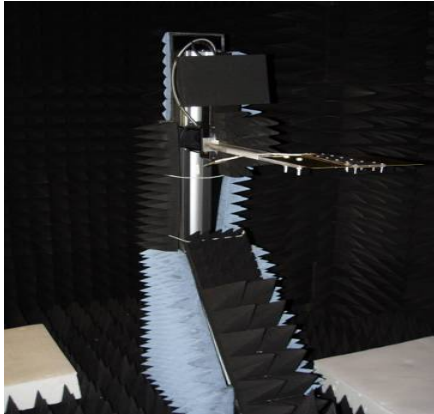


Fig. 1. a) Measurement set-up (transmitter side), b) results obtained by simulation (black lines) and by measurement (red lines), without operator in the H plane.

Figure 1 a) shows the testing of the patch antenna inside the chamber. Figure 1b) shows the measurement scenario, without considering the presence of the operator in the H plane

An important aspect for the simulation of the interaction was the modeling and therefore the parameters attributed to the user.

Simulations were made using a grid method, and measurements were performed in the anechoic chamber of the Department. The dimensions of this chamber which supports tests from 1GHz to 18 GHz are: length- 3.6 m, width-2.4 m and height – 2.4 m.

In this first phase, we have considered an homogeneous distribution of human tissue with a loss angle of 0.16, a relative dielectric permittivity of 40 and a density of 1000kg /m³.

Figure 2 shows the influence on the radiation pattern of the presence of the operator.

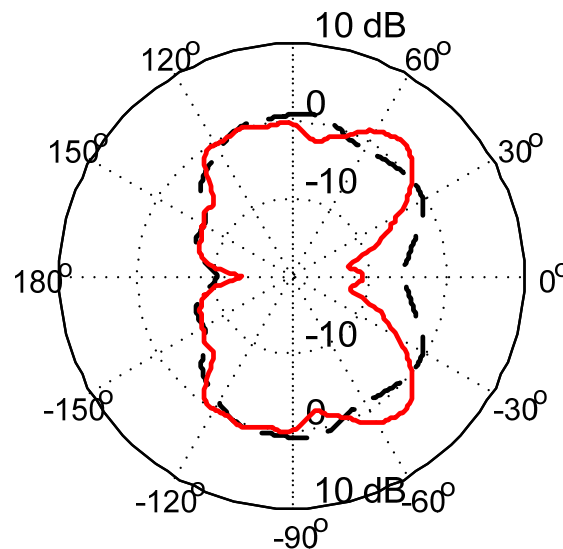
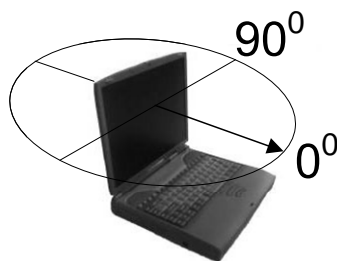


Fig. 2. H-plane Comparison: black lines refer to the simulation without operator. The red line corresponds to the radiation pattern with the operator in the typing position

A significant difference occurs also in human exposure depending on the antenna position and relative position of operator and computer.

In the full paper we will present the different scenarios and the results obtained.

CONCLUSIONS

Computers are nowadays an essential tool of everyday life especially for students. The portability, low weight and wireless access of laptops make them a first choice for most students.

The fields radiated by the wireless antennas inserted in these apparatus interact significantly with the operator. We have computed the influence of the operator in the laptop operation and also the power absorbed by the human operator in different scenarios.

References

- [1] Wertheimer, N., Leeper, E., (1979) – Electrical Wiring Configurations and Childhood Cancer, *Am. J. Epidemiol.* 109(3)
- [2] IARC (2002) – Monograph on the Evaluation of Carcinogenic Risks to Humans, vol 80, part 1, 445 pp.
- [3] Aurengo, A., Clavel, J., de Seze, R. et al, (2004) – Champs EM d'Extremement Basse Fréquence et Santé, DGS, 61 pp.
- [4] Garcia, A.M., Sisternas, A., Hoyos, S.P. (2008) – Exposure to Extremely Low Frequency EM Fields and Alzheimer Disease: a Meta Analysis, *Int J. Epidemiol.* 37(2). 329-40.
- [5] SCENIHR (2009)- health Effects on exposure to EM Fields – European commission, DG health and Consumer, 83 pp.

RANDOM PHASE SPREAD CODING MULTIPLE ACCESS – THE NEW COMPETITOR OF CDMA IN THE BROADBAND WIRELESS NETWORKS

D-r Veselin Demirev

Radio Communications and Video Technologies Department,
TU-Sofia, Kl. Ohridski blv. № 8 , 1756-Sofia,
e-mail:demirev_v@tu-sofia.bg

Abstract

The Radio-communication Sector of ITU is now seeking submissions from industry and governments on various technical, regulatory and economic ideas in order to increase the efficient use of satellite orbits and frequencies. The proposed by the author a year before new mobile access to the satellite segment named RPSC-MA (Random Phase Spread Coding Multiple Access) is based on a reported previously RPSC technology property. It states that close situated RPSC subscriber terminals could communicate with terrestrial or satellite base stations, using the same frequency channel without interference. The isolation between the terminals is provided by their specific random phase spread coding, due to their specific antenna arrays random design. RPSC-MA will be a breakthrough technology, leading to unpredictable increase of the frequency reuse factor in satellite and terrestrial wideband networks, satisfying completely the ITU – R requirements.

Block-schemes of a RPSC-MA satellite system, as well as detailed system principles of operation are given in the report. A comparison of the multiple access properties and the advantages over popular CDMA approach are listed too.

The European Space Policy Institute [ESPI] is arguing for studies to introduce effective counter measures to protect satellites. The most vulnerable components of the space systems are the ground stations and communication links. The ESPI insists the policy makers to reconsider the satellite system architecture as a whole in order to improve the situation. The anti jam characteristics of RPSC-MA are considered in the report in order to satisfy the ESPI anti space terrorism activity. An analysis of up and down links protection principles are given in the report too.

1. INTRODUCTION

The Radio-communication Sector of ITU is now seeking submissions from industry and governments on various technical, regulatory and economic ideas [1,2,3,4] in order to increase the efficient use of satellite orbits and frequencies.

The developed by us SCP-RPSC [5,6,7,8,9] principles could be base of a new breakthrough technology, leading to unpredictable increase of the frequency reuse factor in the satellite and terrestrial wideband networks. This statement is based on the published previously RPSC property, that close situated subscriber terminals could communicate with terrestrial or satellite base stations, using the same frequency channel without interference. The isolation between the terminal up-links will be provided by their specific random phase spread coding, due to their specific random design. Thus, we can consider this way of operation as a new multiple access approach, named by us Random Phase Spread Coding - Multiple Access (RPSC-MA) [10].

2. RPSC MULTIPLE ACCESS TECHNIQUES – THE NEW WAY FOR EFFECTIVE ORBITAL- FREQUENCY REUSE OF THE SATELLITE SEGMENT

A block scheme of a possible RPSC-MA based satellite system is shown in Fig.1. Here I_1, I_2, \dots, I_N are the incoming information streams, C_1, C_2, \dots, C_N are the corresponding pseudo-noise codes, used for pilot access. $VMES_1, VMES_2, \dots, VMES_N$ - the different simultaneous transmitting Vehicle Mounted Earth Stations, equipped with Random Phased Radial Line Slot Antennas (RP-RLSA) with different random design.

In the receiver, equipped with a conventional high gain antenna, the information streams are recovered and separated in several SCP channels. Here I_1, I_2, \dots, I_N are the out coming information streams This principle of operation is similar to the famous CDMA approach. The different RP-RLSA, act as spatial coding devices. As it was shown in [7], the sum of several thousands random phased signals, transmitted by the different slots of the

each RP-RLSA, is Gaussian random process (equivalent to noise) The pilot and information signals, transmitted by same RP-RLSA, will have similar random phase spread in given direction and will correlate in the signal recovery units. The correlators outputs will contain the corresponding recovered information streams at base-band.

The isolation among the different channels of the proposed RPSC-MA system is based on the lack of correlation of the different random phase spread coded signals. The possible numbers of RP-RLSA with different random design and the corresponding frequency reuse factor improvement are not predictable at this stage of research. It is obvious, that similar RP-RLSA, oriented in random way in the space, could work without interference too. The intuitive approach to the problem shows that even similar RP-RLSA, oriented in similar way, could use the RPSC-MA approach. The isolation among them could be result of the random manufacturing and materials tolerances, due to the used cheap materials and technologies.

A block scheme of a RPSC-MA system with QPSK modulation is shown in fig.2. Here the I and Q streams of every single channel will need separate PN – codes for better isolation between them.

3. RPSC TECHNOLOGY – A NEW APPROACH TO PROTECT SATELLITE COMMUNICATIONS FROM SPACE TERRORISM

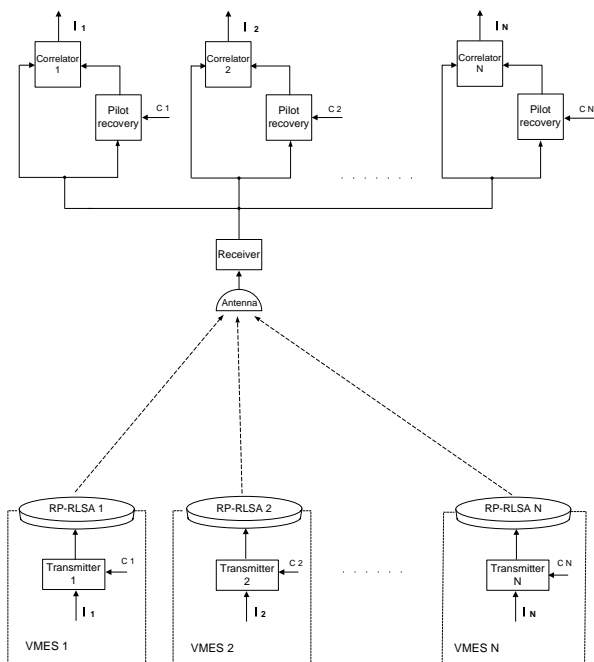


Fig. 1. Block scheme of a RPSC-MA system

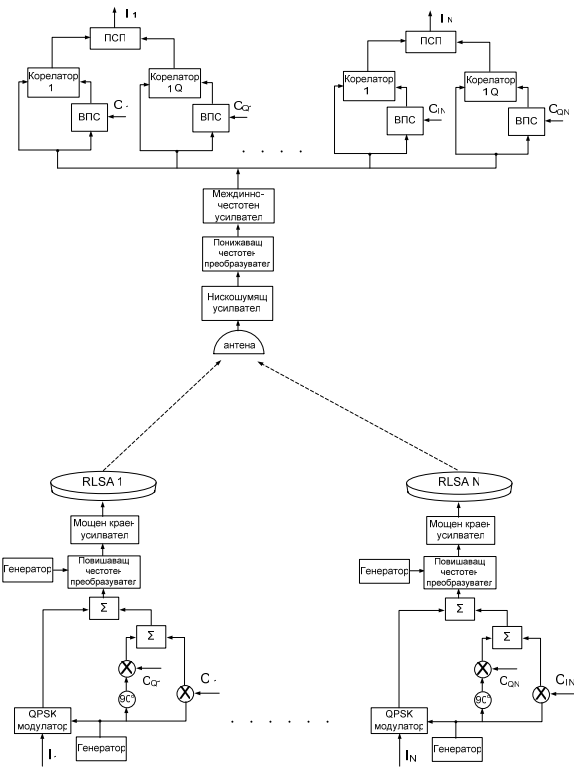


Fig. 2. Block scheme of a RPSC-MA system with QPSK modulation

The European Space Policy Institute [ESPI] issued an article in January, titled “The Need to Counter Space Terrorism - a European Perspective”, arguing for studies to introduce effective counter measures to protect satellites [11]. The article lists several examples of jamming and piracy events that occurred in the commercial satellite sector. One of the conclusions is that the most vulnerable components space systems are the ground stations and communication links. These components are susceptible to attack from widely accessible weapons and technologies. The ESPI agrees with this and says policy makers must consider the system architecture as a whole.

SCP-RPSC technology is one the best technologies, satisfying the above mentioned requirements, as follows:

- *SCP in down-links*

In this particular case the down-links are well protected from jamming, coming from the side-lobes of the Spatial Cross-Correlation Function (SCCF). As it was shown in [6], the level of the side-lobes is very low (in order of -25, -30 dB). It leads to good protection ratios of SCP down-links against ground based terrorist jamming.

- *RPSC in up-links*

In this particular case up-links are protected against jamming, coming even from points, close situated to the earth stations – in the main lobe of the satellite up-link receiving antenna. The receiving SCP units will not recovery the jamming signals because of the lack of correlation between the jamming signals, transmitted by conventional high gain antennas, and the recovered random phase spread pilot signals. Situation is similar to the case of CDMA protection against narrowband interference.

4. CONCLUSION

The practical SCP-RPSC principles implementations in transmit and receive mode will drastically change the existing paradigm in the satellite communication business in general. Many of the existing problems of the proposed LEO, MEO and GEO satellite systems, dealing with frequency and orbital resource sharing, beam pointing, beam shadowing, terrorist jamming etc., will be solved successfully.

References

- [1] G. Oberst, "Efficient Use of satellite Orbits and Frequencies", *Via Satellite*, p.14, February, 2009.
- [2] Question ITU-R 46-3/4, "Preferred multiple-access characteristics in the fixed-satellite service", (1990-1993-2007).
- [3] Question ITU-R 83-5/8, "Efficient use of the radio spectrum and frequency sharing within the mobile-satellite service", (1988-1990-1992-1993-2002-2006).
- [4] Question ITU-R 274/4, "Technical methods for improving the spectrum/orbit utilization" (2008).
- [5] V. Demirev, "SCP technology – the new challenge in broadband satellite communications", *ICEST,04 Conference Proceedings*, pp.159-162, Bitola, Macedonia, 2004.
- [6] V. Demirev, A. Efremov, "SCP-CDMA GSO,s system proposal", *ICEST,04 Conference Proceedings*, pp.163-166, Bitola, Macedonia, 2004.
- [7] V. Demirev, "The Probability Theory with Application in SCP Technology", *ICEST,04 Conference Proceedings*, pp.167-168, Bitola, Macedonia, 2004 .
- [8] V. Demirev, "Review of SCP-RPSC technology", *ICEST,05 Conference Proceedings* , vol. 2, pp.630-633, Nis, Serbia and Montenegro, 2005.
- [9] V. Demirev, "The Probability Theory of SCP-RPSC technology", *Telecom,06*, Varna, 2006 r.(in Bulgarian).
- [10] V. Demirev, A. Angelova, "RPSC-MA – a New Mobile Access to the Satellite Segment", *Telecom,09*, Varna, 2009 r.(in Bulgarian).
- [11] G. Oberst, "Protecting Satellites From Space Terrorism", *Via Satellite*, March, 2009.

THE REGULATORY ASPECTS OF SCP-RPSC TECHNOLOGY – COULD THEY SOLVE THE VMES PROBLEMS

D-r Veselin Demirev

Radio Communications and Video Technologies Department, TU-Sofia, Kl. Ohridski blv. № 8 , 1756-Sofia,
e-mail:demirev_v@tu-sofia.bg

Abstract

The new satellite interactive broadband communication systems use high gain satellite tracking antennas, installed on vehicles. Vehicle-Mounted Earth Stations (VMES) currently can operate on conventional Ku-band frequencies (14 GHz Uplink, 11-12 GHz Downlink) but only on a secondary basis. Regulation on VMES in the co-primary status is not without challenges. There are several primary concerns of allowing VMES to share co-primary status in Ku-band - Ability to maintain pointing accuracy; Danger of using ultra small antennas and Ability to track potential interference.

The unique properties of the SCP-RPSC (Spatial Correlation Processing – Random Phase Spread Coding) technology were demonstrated by the author with examples of co-located same frequency sharing conventional and RPSC satellite systems. In the particular case of total number of antenna array elements 2500, the Protection Ratio of the conventional satellite system will be better than 17 dB for 86,4% of the time and better than 12,2 dB for 99,9% of the time. It means that the transmitted random poly-phase spread signals will not cause significant harmful interference to the conventional satellites, using the same frequency channels.

An analysis of the VMES SCP down links protection from neighbour satellite interferences is given in the report too. It is negligible due to the full electronic principle of operation, pointing the maximum of the Space Cross-Correlation Function (SCCF) to the cooperative satellite without time delay and due to its low side-lobes.

1. INTRODUCTION

Historically, connectivity services for mobile vehicles have been delivered through the use of satellites transmitting in L-band (out of which only a few tens of MHz are assigned to satellite use from regulatory authorities), beginning with Marisat in 1976. Targeted to telephone communication at first, these services have evolved towards IP connectivity and, more recently, the delivery of IP broadband. The use of L-band gives important benefits, such as small onboard antenna size and little or no attenuation due to rain. However, the amount of L-band available, and more specifically the portion allocated to MSS, is limited. Moreover, frequency reuse due to different orbital slots is extremely limited. Broadband applications require a much greater amount of bitrate for the final user than normally available. One technical solution has been to create small spots of coverage, so that the same frequency can be re-used in different spots, thus increasing the total amount of available bandwidth. The lack of the bandwidth in L-band has consequences on the costs to the users. For example, the cost of a minute of Inmarsat communication can range from several Euros to tens of Euros. These costs are hardly compatible with a 'broadband' user experience at reasonable prices. To definitely overcome

the problems due to the scarcity of L-band, the only choice is to move to a higher frequency band [1]. Ku-band (frequencies between 11 and 14 GHz, out of which 2+2 GHz assigned to satellite use) is an ideal candidate to offer broadband services. Although only a part of the overall Ku spectrum is usable in a mobile environment (in particular, only 500 MHz – from 14 to 14.5 GHz – can be used in the uplink direction from a mobile vehicle), bandwidth can be augmented by frequency reuse at different orbital positions.

2. THE VMES REGULATORY PROBLEMS IN KU - BAND

Vehicle-Mounted Earth Stations (VMES) currently can operate on conventional Ku-band frequencies but only on a secondary basis. This means VMES can not claim interference protection from primary services such as fixed satellite systems and Earth Station on Vessels (ESV).

Regulation on VMES in the co-primary status is not without challenges. There are several primary concerns of allowing VMES to share co-primary status in Ku-band [2]:

- *Ability to maintain pointing accuracy:* Vehicles can abruptly accelerate and decelerate

as well as travel in rough terrain. Under these conditions, VMES may find it difficult or impossible to maintain their pointing accuracy. Of greater practicality may be the ability of the antenna systems to automatically mute transmissions upon deviation from the target satellite.

- **Danger of using ultra small antennas:** Vehicles can not accommodate the larger antennas that can be installed on ships. Thus ultra small stabilized antennas are more practical for VMES. However, smaller antennas have greater potential for interference to adjacent satellites because they have wider main and side lobes that can radiate more energy to satellites on either side of the intended satellite.
- **Ability to track potential interference:** Because of the ubiquity of vehicles and their unpredictable driving patterns, a method to identify and correct interference issues is paramount.

3. SCP-RPSC APPROACH

The SCP-RPSC principle of operation [3,4,5,6] is based on the use of random phased antenna arrays and correlation signal processing. It was developed for receive (SCP) and transmit (RPSC) modes. A block scheme of a SCP-RPSC satellite system is shown in fig.1:

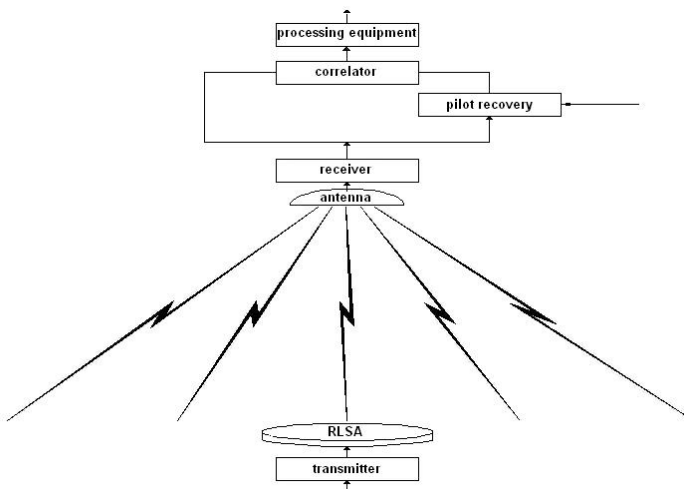


Fig. 1. Block scheme of a SCP-RPSC system

4. POSSIBLE IMPROVEMENTS OF REGULATORY STATUS OF VMES

The unique properties of the SCP-RPSC technology were demonstrated with an example of co-located same frequency sharing conventional and RPSC satellite systems. The case, considered in [6], included a situation, where a conventional antenna, placed near to transmitting random phased antenna array and having the same gain, transmits towards a conventional receiving satellite system with the same parameters as that of the receiving RPSC system. It was shown, that the output signal of the conventional system receiving antenna will be sum of the own signal and the interference from SCP-RPSC system. The Protection Ratio (PR) of the conventional system was defined and calculated by means of the Probability Theory of the Random Gaussian Processes as:

$$PR_{conv}^{86,4\%} = \frac{P_{rec.conv.}}{P_{int.}} = \frac{\sigma_y^2}{\sigma_x^2} = \sqrt{\sigma_y^2} \quad (1)$$

$$PR_{conv}^{99,9\%} = \frac{P_{rec.conv.}}{P_{int.}} = \frac{\sigma_y^2}{3\sigma_x^2} = 0,33\sqrt{\sigma_y^2} \quad (2)$$

Where $\sigma_y^2 = n\sigma_x^2 = n\frac{A^2}{2}$ is the variance of the full interference, caused by the transmitting random phased antenna array and $\sigma_x^2 = \frac{A^2}{2}$ is the variance of the interference, caused by single antenna element.

Bearing in mind that the number of the antenna elements of a random phased antenna array is in order of 2500 [7], the PR will be better than 17 dB for 86,4% of the time and better than 12,2 dB for 99,9% of the time.

The conclusion is that the transmitted random poly-phase spread signals will not cause significant harmful interference to the conventional satellites, using the same frequency channels. The interference will be similar to that, caused by the side-lobes of a circular, phased in another direction antenna array with random inter elements spacing. The transmitted random poly-phase spread signals are uniformly radiated in the space above the antenna. Several satellites, equipped with the same SCP receivers and providing space diversity, could receive them. The knowledge of the receiving satel-

lites positions for the transmitting equipment is not necessary (as it is for a conventional satellite earth station).

Several mitigation techniques have been used until now in order to solve the VMES regulatory problems. One of them uses CDMA techniques to reduce the transmitted spectral power density in order to satisfy ITU transmitting masks. This is a temporally solution for low speed mobile up-links with poor directivity patterns. As it was shown abo-

ve, the interference of RPSC up-links over conventional up-links is in order of that, caused by the side-lobes of random spaced antenna array, phased in another direction. This property is direct result of the principle of operation, so the additional expenditures to realize it are not necessary. To support the above mentioned, in fig.2 the amplitude distribution, and in fig.3 – the phase distribution of a 57 cm in diameter RP-RLSA (Random Phased – Radial Line Slot Antenna) are shown.

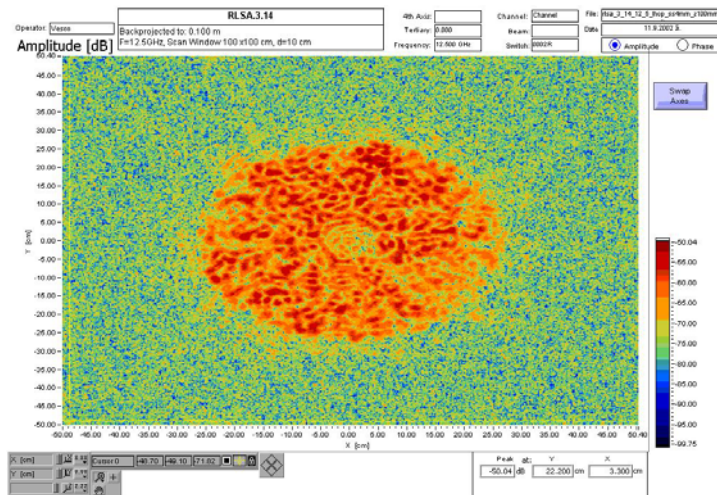


Fig. 2. RP-RLSA amplitude distribution

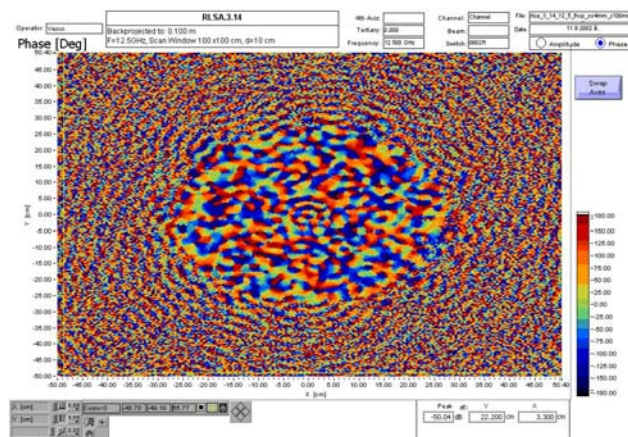


Fig. 3. RP-RLSA phase distribution

The VMES,s SCP down links are protected from neighbor satellite interferences due to the full electronic principle of operation, pointing the maximum of the SCCF to the cooperative satellite without time delay.

5. CONCLUSION

In summary, a co-primary allocation of VMES in the conventional Ku-band would be in the public interest, as it would address a growing commercial demand for on the move services. However, a co-primary allocation would also have to be conditioned on strict adherence to interference avoidance mechanism, which in the best way obviously is satisfied by the RPSC technology.

References

- [1] A. Arcidiacono, D. Finocchiaro, S. Grazzini, "Broadband Mobile Satellite Revolution: the Ku-band Revolution", EUTELSAT SA, Internet, Paris.
- [2] R. Magallanes, "Regulatory Status of Satellite Service Using Vehicle-Mounted Antennas", *Via Satellite*, January, 2009.
- [3] V. Demirev, "SCP technology – the new challenge in broadband satellite communications", *ICEST,04 Conference Proceedings*, pp.159-162, Bitola, Macedonia, 2004.
- [4] V. Demirev, "Review of SCP-RPSC technology", *ICEST,05 Conference Proceedings*, vol. 2, pp.630-633, Nis, Serbia and Montenegro, 2005.
- [5] V. Demirev, "The Probability Theory with Application in SCP Technology", *ICEST,04 Conference Proceedings*, pp.167-168, Bitola, Macedonia, 2004.
- [6] V. Demirev, "The Probability Theory of SCP-RPSC technology", *Telecom,06*, Varna, 2006 r.(in Bulgarian).
- [7] V. Demirev, "SCP-RPSC Technology – a Possible Solution of VMES Regulatory Problems", *Telecom,09*, Varna, 2009 r.(in Bulgarian).

A NEW WIRELESS PRS-OFDM SIMULATION MODEL

Proff. Assis. Stanyo Kolev

Faculty of Communication, TU – Sofia, Kl. Ohridsky str 8, Sofia, Bulgaria, E-mail: skolev@tu-sofia.bg

Abstract

In this paper a new PRS-OFDM model is presented applicable to wireless communication systems from first to fifth class and from second to ninth order. It has been simulated over communication channels with Rayleigh, Rice, and Additive White Gaussian Noise present. The experimental results reveal improved BER and CIR and decreased ICI using high order PRS system in comparison to OFDM system without PRS. This model could be employed into various wireless mobile communication systems, in telemedicine, DVB, optical communication systems, etc.

1. INTRODUCTION

For one OFDM system the correlative coding, known also as PRS will be done in frequency area. The research shows that correlative coding in that are is a simple solution for the ICI interference problem, also makes OFDM systems less sensitive to frequency errors [11]. In addition correlative coding does not reduce the bandwidth efficiency when added to the system. Figure 2.1 shows a simplified block diagram for the proposed correlative coding OFDM system.

2. MAIN TEXT

The source signal before being coded is show with a_k , where k is the carrier $k = 0, 1, \dots, N - 1$, (N is the total carrier count). Having bipolar manipulation BPSK in mind a_k values shifts between -1 and, for which a zero average and independent conditions are accomplished.

Let us have D for k -carrier delay. Then the proposed correlative coding using $F(D) = (1 - D)$ polynomial is realized as:

$$b_k = a_k - a_{k-1}$$

There the coded symbols $b_k, k \in [0, N - 1]$ are modulated on N carriers. b_k accepts three possible values (-2, 0, 2). Equation (2.6) represents correlation between neighboring symbols - b_k, b_{k-1} , that's why independency condition is no longer true. To prevent error multiplication in decoding due to correlative coding a pre modulation bi-phase BPSK encoding (XOR) is performed – similar to single carrier duo-binary signalization. In the OFDM systems carriers' ICI signal is a function of channel deviation and subcarriers modulated signal values. Due to the communication signals random nature ICI is a random process also. It uses CIR to assess systems ICI level by comparing CIR in OFDM systems with and without correlative coding. System with $(1 - D)$ correlative coding evaluates CIR with:

$$CIR = \frac{\sin^2(\pi\epsilon)/(\pi\epsilon)^2}{\sum_{l=1}^{N-1} |S(l)|^2 - \frac{1}{2} \sum_{l=2}^{N-1} [S(l)S^*(l-1) + S(l-1)S^*(l)]} \quad (2.1)$$

To demonstrate the improvements by the proposed system is compared with the CIR values of these correlation OFDM system without coding. Then CIR expression for normal OFDM system:

$$CIR = \frac{\sin^2(\pi\epsilon)/(\pi\epsilon)^2}{\sum_{l=1}^{N-1} |S(l)|^2} \quad (2.2)$$

is:

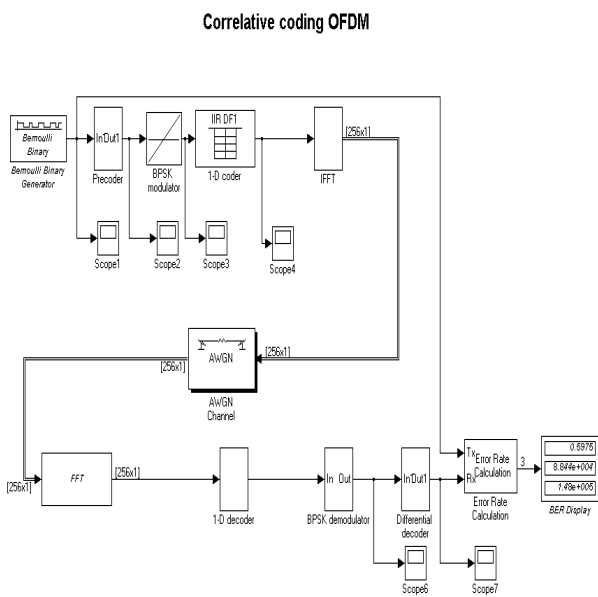


Fig. 2.1

Then to calculate the block error rate Error rate calculation makes the necessary calculations are displayed on irezlutatite display. Received BER results are given in tabl. 1 and fig. 2.2.

SNR, [dB]	BER, [%]
0	20
3	9
4	7
5	4
6	2
7	1
8	0.4
9	0.15
10	0.04
11	0.009
12	0

Tabl. 1

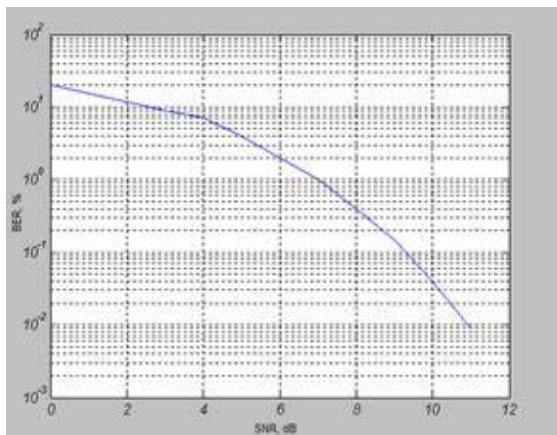


Fig. 2.2

Compared with normal OFDM system, CIR is improved by 3.5 dB (for OFDM system with correlative coding of 1-D polynomial) with no reduction in bandwidth and increase system complexity

3. CONCLUSION

Created a model of OFDM system using correlative coding. Following that simulation are shown graphs of the signals from some points of the system. There are graphs of BER and OFDM system with correlation and without correlative coding.

4. APPENDIX AND ACKNOWLEDGMENTS

This work was supported under UE FP7 INDECT Project: "Intelligent information system supporting observation, searching and detection for security of citizens in urban environment".

References

- [1] J. Armstrong, "Analysis of new and existing methods of reducing intercarrier interference due to carrier frequency offset in OFDM," *IEEE Trans. Commun.*, Mar. 1999, *Trans., Microwave Theory Tech.*, vol. 44, no. 12, pp. 2395-2503, 1996.
- [2] F. Tufvesson, "Design of wireless communication systems issues on synchronization, channel estimation and multi-carrier systems," Ph.D. dissertation, Lund University, Aug. 2000.
- [3] J. Ahn and H. S. Lee, "Frequency domain equalization of OFDM signals over frequency nonselective rayleigh fading channels," *IEE Electron. Lett.*, vol. 29, no. 16, pp. 1476-1477, Aug. 1993.
- [4] Y. Zhao and S.-G. Haggman, "Inter-carrier interference self-cancellation scheme for OFDM mobile communications systems," *IEEE Trans. Commun.*, vol. 49, no. 7, pp. 1185-1191, July 2001.
- [5] "Novel adaptive modulation scheme to reduce both PAR and ICI of an OFDM signal," in *Proc. Int. Symposium on DSP for Commun. Syst.*, Manly-Sydney, Australia, Jan. 2002, pp. 229-233.

AN APPROACH TO INTERACTIVE E-LEARNING: THE COMMUNICATION SYSTEMS IN MEDICINE COURSE

Vicktoria Antonova¹, Dimiter Dimitrov¹, Carlos Vaz de Carvalho²

¹ Technical University of Sofia
8, KlimentOhridski Blvd, Sofia 1000, Bulgaria
v.p.antonova@gmail.com, dcd@tu-sofia.bg

² Instituto Superior de Engenharia do Porto
Rua Dr. António Bernardino de Almeida, 431
P4200-072 Porto, Portugal
cmc@isep.ipp.pt

Abstract

This article presents a project that tried to evaluate if e-learning is interesting for the students and can therefore provide a higher motivation and satisfaction than the traditional modes of teaching.

The study also tried to assess what would be the reaction of teachers when they are confronted with the need to use new educational technologies.

As an initial evaluation of the project, a sample of students and teachers assessed the e-learning contents, course and platform. Most of the students were pleased with the contents and considered the course very rewarding. All the students considered the system user-friendly and said that e-learning exercises are better than the traditional way of teaching.

1. INTRODUCTION

Can the use of e-learning make Technical Higher Education more attractive, more useful and more motivating for students? An answer to those questions was sought through the development of a collaborative project between the Technical University of Sofia and the Engineering Faculty of the Porto Polytechnic, in Portugal. The main research question of this project tried to evaluate if e-learning is interesting for the students and if it can generate a higher motivation than the traditional mode of teaching. But we were also interested in knowing what would be the reaction of the teachers when they use the new technologies applied to education. Could they use the system easily? Would they find e-learning systems user-friendly?

As an initial evaluation of the project, a sample of students and teachers assessed the e-learning contents, the course and the e-learning platform. 60% of the students were pleased with the contents and considered the course very interesting. All the students considered the system user-friendly and they said that e-learning exercises were better than the traditional way of teaching.

On the other side, teachers said that the system was easy to work with and they were pleased to be part of the process of integrating current and future technologies in learning.

2. COURSE CONCEPT

E-learning is characterized by a separation of space / time between teachers and students (but not excluding eventual physical meetings – blended learning) with a pattern of two-way asynchronous or synchronous communication. Normally Internet is used as the means for communication and sharing of knowledge, through the services and tools that this technology provides. The student becomes the centre of an independent and flexible training process, managing his/her own learning, usually with outside tutoring but managing schedules in a completely autonomous way.

E-learning is one of the more frequently used options for continuing education. The generation of professional development programs is growing because there is a strong need that workers are trained and become able to adapt themselves to new production requirements. E-learning, given its characteristics and technological support provides an alternative for those who need to combine work, personal and social schedules and training, as it does not require a permanent presence in a classroom.

Virtual education, another way of designating e-learning, provides an opportunity for the student to choose their hours of study making it a good choice for those who work and want independent study in their spare time. Therefore the use of e-learning for

academic purposes is also being looked upon as an important tool on its own or as a complementary activity to f2f classes.

Especially, and it is important to mention, because e-learning is an excellent tool that can help users learn new concepts but also consolidate knowledge and skills, thereby increasing the autonomy and motivation of students for different subjects.

In [1] Bruffee presented a set of requirements that should exist in exemplary cases of student centred learning environments:

- Students should participate actively in the learning process
- Students are responsible for the acquisition of their knowledge
- The teacher is a moderator and a facilitator rather than a knowledge transmitter
- The environment allows peer interaction and its evaluation

The success of this methodological approach depends on three main factors:

1. The network (Internet and/or Intranet) must be fully functional, allowing instant update, store, retrieval and sharing of instructions, communication and information.

2. The materials are delivered to end users through the use of computers with standard Internet technology.

3. The methodology focuses on a broader vision of learning that goes beyond the traditional paradigms of training.

The advantages offered by online training are:

- Elimination of spatial and temporal barriers (studying from home, work, on a trip through mobile devices, etc.);
- Allows the practice and use of simulation in virtual environments. This would be difficult to get in classroom training, without a big investment.
- Promotes real knowledge management through exchange of ideas, opinions, practices, experiences. Enrichment becomes a collective learning process without boundaries.
- Allows a constant updating of content
- Generates cost reduction (in most cases, methodological and, always, in logistics)

An important aspect of the use of e-learning environments relate to the possibility of practical immersion in a Web 2.0 environment, creating col-

laboration and social opportunities. This methodological approach promotes the communication of ideas, materials, and information, and the interactive creation of documents for learning purposes. This collaborative model of learning is characterized by multiparticipant communication, space and time independent communication, and computer-mediated communication. In [2], Harasim proposes that this is "the process of construction of knowledge by the integration of the student, the teachers, and the specialists in discussions and interactive activities." Several related theories further define this educational phenomenon and scaffold strategies to explore it [3], such as Vygotsky's sociocultural theory, problem-/project-based learning, cognitive flexibility, situated learning, and metacognition.

Computer mediation provides functionalities expressed in the previous points, but it also allows other mechanisms for the educative interactions. It allows revising, archiving, and recovering past interactions. This electronic log with the transcript of past interactions allows a detailed retrospective and critical analysis of the interaction [4]. It also allows collecting further evaluative data either to assess students or even to measure the quality of the course and to extract recommendations for improvement.

3. METHODOLOGY AND IMPLEMENTATION

The project progressed through the following stages:

- Research and comparison of e-learning systems and platforms
- Research and comparison of popular authoring tools for e-learning contents
- Design of an e-learning methodology that enhances interaction, motivation and user-friendliness
- Develop online contents, including exercises for a case study course: Telecommunication systems in medicine
- Test the contents

The pedagogical design assumed that a new educational paradigm was required, focused on the student; adjusted to its characteristics, constraints, and requirements [5]. E-learning platforms together with pedagogical and organizational strategies can support this new way of learning—more personalized, just-in-time, more fitted to individual needs, and more flexible in content and schedules.

A learning management system (LMS) is a software application for the administration, documentation, tracking, and reporting of training programs, classroom and online events, e-learning programs, and training content. Moodle is an LMS that has become very popular among educators around the world as a tool for creating online dynamic web sites for their students. Moodle is designed to support a style of learning called Social Constructionism. This style of learning is interactive. The social constructionist philosophy believes that people learn best when they interact with the learning material, construct new material for others, and interact with other students about the material. The difference between a traditional class and the social constructionist philosophy is the difference between a lecture and a discussion. Therefore Moodle was chosen as the platform for the project as it adjusted very well to the learning philosophy and strategy.

Concerning the course methodology and implementation one of the major ideas was to reuse already existing contents. Therefore all the theoretical material was taken from the book *Medical Information Systems, Handbook for Laboratory Exercises and Selftesting*, Technical University of Sofia, Bulgaria, 2009 written by Prof. Dimiter Tz. Dimitrov. The text in the e-learning exercises was selected in order to address the most important aspects about the subject.

The first step of creating the exercises was designing a template for them. The template is very important for a consistent and coherent view of the whole work. It must be user friendly, pleasant, with the right colours, the best organization of elements, an easy to understand navigation system, etc.

In this particular situation, the chosen colours for development were blue and white.

Blue: The colour of the sky and the ocean, blue is one of the most popular colours. Creates peaceful and tranquil environments and people are more productive in blue rooms. It can be strong or light and friendly. The blue colour doesn't tire the eyes and it is easy for the people to perceive.

White: White is associated with light, goodness, innocence, purity, and virginity. It is considered to be the colour of perfection. White means safety, purity, and cleanliness. White usually has a positive connotation, at least in the Western Society. White can represent a successful beginning. In advertising, white is associated with coolness and cleanliness because it's the colour of snow.

Another important aspect is typography. The chosen font was Arial. It is simple and doesn't draw away attention from the information in the slides.

The theme of the exercises is related to telecommunication systems in medicine. Therefore the template used a background picture that looks like DNA (Deoxyribonucleic acid). The picture was placed in a way that it does not conflict with the text.

The development was accomplished through the collaboration between the universities of ISEP in Porto, Portugal and TU, Sofia, Bulgaria. Because of this the logos of the two universities are on the template, too.

4. RESULTS AND CONCLUSIONS

As an initial evaluation of the project, a sample of students and teachers assessed the e-learning contents, course and platform. A few research questions were placed and answered.

Are the exercises interesting enough for the students? 60% of the students answered that it is enough and 40% answered that there can be some more flash animations and movies to make the contents more interesting.

Is the system user friendly? 100% of the interviewed students answered "Yes".

Is the motivation and interest of students higher than in the traditional modes of teaching? All the students said that e-learning exercises are better than traditional way of teaching. For them it is more interesting and easier to use e-learning exercises. And some of them mention about the advantage of the online lessons that if they miss one it is easy to understand what the colleagues did during the lesson.

What is the reaction of teachers when they meet the new technologies applied to education? and Can the teacher use the system easily? The answers show that teachers think that the system looks easy for work and they were pleased to be part of the future technologies. Some of them mentioned that for them it is easier when it is not necessary to repeat the same thing in several lessons.

In conclusion, we created an e-learning methodology, implemented through an e-learning platform

using interactive exercises, for the course "Telecommunication systems in medicine".

The online exercises are the beginning of the project in Technical University Sofia. In a few years all the Telecommunications courses in Medicine will be accessible through the Internet.

In that moment more animated and interactive contents must be produced to make it more interesting for the students.

References

- [1] Bruffee, K. (1983). Collaborative learning: Higher education, interdependence, and the authority of knowledge. Baltimore, MD: Johns Hopkins, University Press.
- [2] Harasim, L. (1989). On-line education: A new domain. In R. Mason & A. Kaye (Eds.), *Mindweave: Communication, computers and distance education* (pp. 50-62). Oxford: Pergamon Press.
- [3] Hsiao, J. (1995). Computer supported collaborative learning theories. Retrieved from <http://www.edb.utexas.edu/csclstudent/Dhsiao/theories.html>
- [4] Harasim, L. (1990). Online education: An environment for collaboration and intellectual amplification. In *Online education: Perspectives on a new environment* (pp. 39-66). New York: Praeger.
- [5] Vaz de Carvalho, C. (2005). Systematic approach to advanced training through e-learning in higher education institutions. Proceedings of the CATE 2005 8th Conference on Computers and Advanced Technology in Education, Oranjestad, Aruba.

The authors wish to thank the European Commission for the grant in the Lifelong Learning Programme, the Executive Agency for its help and all the partners of the project for their contribution.

*Project Number: 142814-LLP-1-2008-FR-ERASMUS-ENW
Instrument type: ERASMUS NETWORK*

KEEPING UP-TO-DATE IN THE MEDICAL FIELD AT NO COST

Nuno Escudeiro¹, Paula Escudeiro²

^{1,2}Instituto Superior de Engenharia do Porto
Rua Dr António Bernardino de Almeida, 431, 4200-072 Porto

¹LIAAD-INESC Porto L.A.
Rua de Ceuta 118, 6º, 4050-190 Porto

²GILT
Rua Dr António Bernardino de Almeida, 431, 4200-072 Porto
T. +351 228 340 500; F. +351 228 321 159; E. ¹nfe@isep.ipp.pt; ²pmo@isep.ipp.pt.

Abstract

Medical information is available from many distinct sources in the web such as resources' hubs and medical news services. Being aware of constant advances and innovation in the medical field is necessary to achieve a good work performance. However, keeping up to date in the medical field requires significant effort, and consequently a large cost.

This effort might be largely reduced by automating part of the process required to gather relevant information.

In the current paper we propose an automatic process to assist users to keep up to date in medical information. This process retrieves medical information from the web and organizes it in a taxonomy that is especially tailored towards users' specific needs.

Our results led us to conclude that it is possible to achieve a very significant reduction in the user work load and still have high quality content.

1. INTRODUCTION

Topic focused web portals reduce users' effort in the task of finding the right information at the right time and keeping up-to-date in their area of expertise. This reduction is achieved mainly by transferring part of that effort to an editor that works on behalf of all the portal users which are assumed to have common needs. However, creating and maintaining attractive and functional thematic web resources still demands for a high effort from web site editors.

This effort can be largely reduced by semi-automating some of the editor's tasks, mainly those related to content gathering and organization.

Having a medical resource focused on a specific area, that automatically gathers and organizes only the relevant information on a given area, seems valuable since it might present a permanently updated view of the advances and innovations in that specific area while requiring no effort from its users once it has been setup.

In the present work we propose a process that automates most of the hard working tasks that are required to keep a resource on medical information up-to-date and valuable.

In this process, editors are just required to: (1) set the web address of the sites that they usually visit when looking for fresh information on their area of expertise, the *seeds*; (2) define the taxonomy of topics representing the ontological structure re-

quired for the resource and (3) provide a few text paragraphs, previously collected from the seeds, that are representative of the topics in the taxonomy.

From these inputs, we apply text mining techniques to learn a classification model for the resource taxonomy and to extract text snippets from the seeds. These text snippets are then automatically classified and placed in the right topic on the taxonomy.

This process provides a huge reduction of the editor workload producing a resource with a quality that is close to that of the resource compiled by the editor without being assisted by our prototype.

2. AUTOMATIC RESOURCE HARVESTING

Our proposal may be seen as an automatic resource compiler, i.e., a system that seeks and retrieves a list of the most authoritative documents for a given topic [1]. In our work we are interested in collecting and organizing medical information, in a continuous effort to keep a web page up-to-date and organized according to a specific need.

Many automatic resource compilation systems have been proposed in the past.

With Thesus [6], users search documents in a previously fetched and classified document collection. Documents are classified on their content and link semantics. The system includes four compo-

nents: acquisition, information extraction, clustering and query.

WebLearn [8] retrieves documents related to a topic, specified through a set of keywords, and then automatically identifies a set of salient topics, by analyzing the most relevant documents retrieved in response to the user query. The identification of these salient topics is fully automatic.

iVia [9] is an open source virtual library system that collects and manages resources, starting with an expert-created collection that is augmented by a large collection automatically retrieved from the web. iVia identifies relevant internet resources through focused crawling [4] and topic distillation approaches.

Personal View Agent [5] is another personalization system that learns user profiles to assist them when searching for information in the web. This system organizes documents in a taxonomy, which is user dependent and dynamic.

Metiore [2] is a search engine that ranks documents according to user preferences, which are learned from user historical feedback depending on the user objective.

Personal WebWatcher [10] is a system that observes users' behaviour – by analyzing page requests and learning a user model – and suggests potentially interesting pages.

The ARC system [3] compiles a list of authoritative web resources on any topic. The algorithm has three phases: retrieval of root and expanded set, analysis of anchor text and relevance inferring, compute authority and hub measures in the expanded set.

Letizia [7] is a user interface agent that assists a user browsing the web, suggesting potentially interesting links. Interest in a document is learned through several heuristics that explore user actions and current context.

In our work users' interests are specified by the web site editor through a taxonomy and by specifying the topics in the taxonomy through examples. From there on, the system learns the topic, periodically inspects the seeds identifying and retrieving text paragraphs that are assigned to the topics of interest.

3. METHODOLOGY

The main goal of the current work is to reduce the work load that is required from the website editor to keep the content of the medical information resource up-to-date.

This reduction is achieved by automating the tasks that are required to update the resource.

To harvest the relevant information, according to user interests, we have devised a methodology with four stages (Figure 1):

Acquisition: in this stage we download the seeds previously specified by the editor and stored in a database. These are URL for valuable sources of information usually visited by the editor when looking for information to update the web site on an unassisted mode.

Pre-processing: the content of these web pages, downloaded from the seeds, are split into text paragraphs. Extracted paragraphs are stored in text files and registered in the resource database. Each of these paragraphs is then pre-processed and indexed to build a doc-term matrix representing the corpus. After this, the database is updated on the number of extracted paragraphs per seed; this will serve as a measure of the seed relevance.

Learning: in this stage we use Support Vector Machines to learn a classification model for the taxonomy which has been previously provided by the resource editor. This classification model is learned from a set of exemplary text paragraphs – that are representative of all the classes in the taxonomy to learn – also provided by the editor. The classification model will henceforth be used to classify new incoming text paragraphs. The learning stage can be skipped if the current classification model is accurate; if it is not, the editor may manually label additional paragraphs and then use them to rebuild the classification model which is expected to be more accurate.

Organization: the final stage. The classification model, generated in the previous stage, is applied to new incoming text paragraphs assigning them to a given topic. This information is used to build the html code for the resource's web page.

3.1. Architecture

Our methodology includes five core functions to ensure its goals:

Download seeds: connects to the database to get the seeds URLs and then downloads them.

Split into paragraphs: splits web pages into separate paragraphs and saves each paragraph as a text file. Then, it indexes all the saved paragraphs building a weights matrix (TFxIDF coding) [1] of the terms in the paragraphs that will be used in the classification process – and in the learning process as well, if needed.

Update model: rebuild the TFxIDF weights matrix from the exemplary paragraphs and their corresponding labels – that have both been provided by the editor; these will be used to build a new classification model. The classification model is rebuilt only when the editor has new exemplary documents that can eventually generate a more accurate model.

Manually classify paragraph: when selecting a paragraph, the editor can choose to select a label for that paragraph. This label represents the topic in the resource taxonomy to which the paragraph belongs.

Make webpage: goes through the labels – manually assigned by the editor or automatically assigned by the classification model – to select paragraphs grouped by label – topics in the resource taxonomy. When it comes to sorting the labels, the prototype first looks at the manual classification, explicitly set by the editor. If that is not specified, we use the label automatically assigned by the classification model to that paragraph.

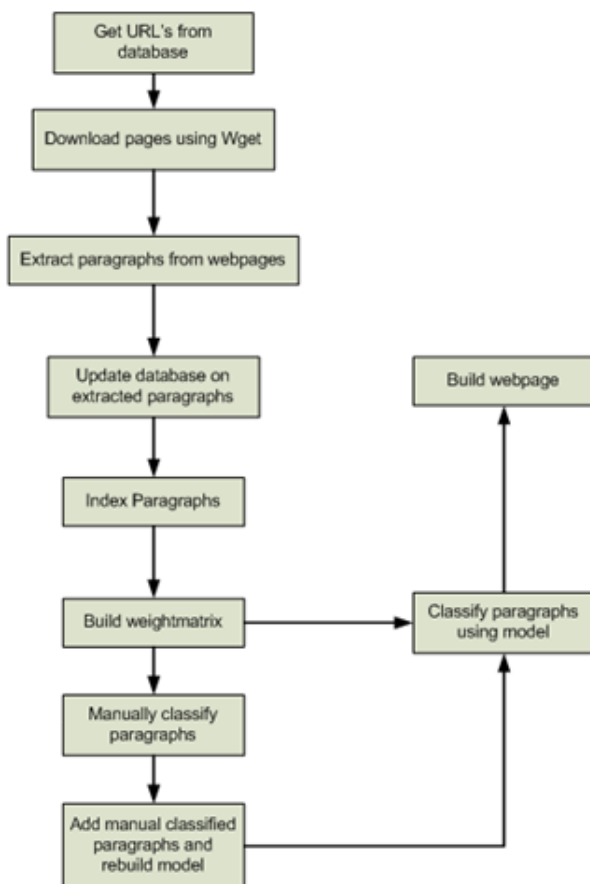


Fig. 1. Methodology

3.2. Prototype

Some preliminary work was necessary in order to automate the harvesting task. Initially we had to identify and catalogue the seeds to crawl. In the current work we have relied on three seeds: the Science Daily [15], a provider of the latest research news on Health and Medicine among other fields, the National Institutes Health [13], a medical research agency from the US Department of Health and Human Services and on the Medical Application web page of the On Semiconductors company [14].

The content in each of these seeds has been analyzed to define a model for representing relevant objects appearing in it.

The crawling process, allowing the download of potentially interesting web pages, was designed and tested. In our prototype we are using wget [12] to download seeds.

A method for pre-processing web pages, generating relevant documents (text paragraphs) and representing them on the previously defined model – a TFxIDF document-term matrix – has also been deployed. Text processing is done using the Lucene library [11].

To determine whether recently gathered text paragraphs are relevant or not, we apply a text classifier – based on a classification model that has been previously learned for the resource's taxonomy. Relevant paragraphs are then catalogued on this taxonomy.

These fresh objects are placed in the resource's web page which is automatically updated according to the topic taxonomy.

4. EVALUATION

A preliminary evaluation procedure was carried out based on a taxonomy with three distinct topics (*Medical devices*, *Infectious diseases* and *Chronic illness*) and 100 text paragraphs, previously extracted from the seed web pages. All these documents have been previously labelled by the resource editor so we can compare these manual labels to those automatically generated by the classifier.

We have observed an average accuracy, over these three topics, of 88%. This performance is achieved with a very big reduction in the workload that is required from the resource editor to keep the resource updated. Building a classification model

with this accuracy (88% on average) requires the editor to label an average of 32 text paragraphs, a gain of 68 labels that are no longer required. Once the classification model is available the site is continuously updated at no extra cost, i.e., without requiring the editor to label any new text paragraph.

5. CONCLUSIONS AND FUTURE WORK

Our evaluation plan relies on a single experiment with a small dataset with 100 text documents. Additional experiments are required to provide more robust conclusions. However, we should notice that this is a real dataset, composed by text snippets directly extracted from real web pages. This brings more realism to our experiment than if it has been performed on a repository dataset.

Our prototype is able to retrieve and organize the content of a web resource, keeping its quality high – close to 90% that of a resource that is kept by the website editor without any automatic assistance – with a very significant reduction in the workload required from the editor.

We are now working on more complex taxonomies and evaluating this methodology against bigger corpora. In another line of work we try to devise algorithms that can reduce further the label complexity – the number of labels that are required to learn the taxonomy.

References

- [1] Baeza-Yate, R., Ribeiro-Neto, B., *Modern Information Retrieval*, Addison Wesley, 1999
- [2] Bueno, D., David, A.A., "METIORE: A Personalized Information Retrieval System", *Proceedings of the 8th International Conference on User Modeling*, Springer-Verlag, 2001
- [3] Chakrabarti, S., Dom, B., Raghavan, P., Rajagopalan, S., Gibson, D., Kleinberg, J., "Automatic Resource Compilation by Analyzing Hyperlink Structure and Associated Text", *Proceedings of the 7th International World Wide Web Conference*, 1998
- [4] Chakrabarti, S., Berg, M., Dom, B., "Focused crawling: a new approach to topic-specific resource discovery", *Proceedings of the 8th World Wide Web Conference*, 1999
- [5] Chen, C., Chen, M., Sun, Y., "PVA: A Self-Adaptive Personal View Agent System", *Proceedings of the SIGKDD Conference*, 2001
- [6] Halkidi, M., Nguyen, B., Varlamis, I., Vazirgiannis, M., "Thesus: Organizing Web document collections based on link semantics", *The VLDB Journal*, 12, pp 320-332, 2003
- [7] Lieberman, H., "Letizia: an Agent That Assists Web Browsing", *Proceedings of the International Joint Conference on AI*, 1995
- [8] Liu, B., Chin, C.W., Ng, H. T. , "Mining Topic-Specific Concepts and Definitions on the Web", *Proceedings of the WWW Conference*, 2003
- [9] Mitchell, S., Mooney, M., Mason, J., Paynter, G.W., Ruschewski, J., Kedzierski, A., Humphreys, K., "iVia Open Source Virtual Library System", *D-Lib Magazine*, Vol. 9, No. 1, 2003
- [10] Mladenic, D., *Personal WebWatcher: design and implementation*, Technical Report IJS-DP-7472, SI, 1999
- [11] <http://lucene.apache.org/java/docs/>, accessed on September 2010
- [12] <http://www.gnu.org/software/wget/>, accessed on September 2010
- [13] <http://health.nih.gov>, accessed on September 2010
- [14] <http://www.onsemi.com/PowerSolutions>, accessed on September 2010
- [15] <http://www.sciencedaily.com>; accessed on September 2010

THE INVESTIGATION OF ULTRASONIC PREAMPLIFIER COMPLEX PERFORMANCE

L. Svilainis, A. Chaziachmetovas, V. Dumbrava

Signal processing department, Kaunas University of Technology
Studentu str. 50, LT-51368 Kaunas, Lithuania
T, +370 37 300532; F, +370 37 753998;
E, linas.svilainis@ktu.lt / andrius.chaziachmetovas@ktu.lt / vytautas.dumbrava@ktu.lt

Abstract

Ultrasonic preamplifier operating in a pulse-echo mode is analyzed. Due to the presence of high energy excitation pulses at the preamplifier input a protection circuit is required. The noise, bandwidth, input impedance and protection superiority for various preamplifiers is analyzed. The input impedance, insertion gain and noise AC response were analyzed and are presented over 20kHz to 40MHz frequency range. Essential protection circuit requirements, such as protection efficiency, recovery time are discussed and experimental results presented. Brief description and explanations on equipment and techniques used are presented.

1. INTRODUCTION

Expansion of air-coupled ultrasonics [1] is raising special demands for electronics used. Because of the large difference of acoustic impedances of solid body under investigation and air, loss can reach 100dB so powerful transmitters and low noise receivers are demanded. Since conventional ultrasound equipment is not suitable here, the development of dedicated equipment was needed.

Ultrasound transmitted power is limited to certain limits in case of medical applications for the sake of tissue protection. But transmission performance improvement is important in portable equipment [2,3].

When it comes to the preamplifier operating in a pulse-echo mode [4] input circuits become more complex and design of a low noise input stage requires of a special investigation. This type of operation assumes the presence of high energy excitation pulses at the preamplifier input. Therefore the preamplifier should contain a protection circuits. The protection circuit de-rates the preamplifier noise and bandwidth performance. Proper balance should be achieved. In this paper we analyze the preamplifier performance in the presence of such protection circuitry.

2. PERFORMANCE PARAMETERS

Amplifier input impedance interacts with the source (ultrasonic transducer) electrical impedance and affects the power available at transducer transfer to amplifier. Amplifiers used in ultrasound elec-

tronics usually are voltage-sensing (operational amplifier in non-inverting topology) or current-sensing (inverting) only. As it was indicated in [5, 6], in such case amplifier input impedance should be significantly higher than the ultrasonic transducer output impedance. But when it comes to application of transmission line (usually the coaxial cable) to connect the transducer and the preamplifier the signal reflection can occur due to receiving part impedance mismatch [7]. This can be the case in transmission line length is above one tenth of the wavelength. Most popular ultrasonic transducers operate at 20kHz to 20MHz frequency range. Then maximum cable length should not exceed 1 m which is almost always the case.

The impedance, acting at amplifier input, determines the noise level. Operational amplifier intrinsic noise is modelled using voltage source e_n and current noise sources i_{n+} and i_{n-} . refer to Figure 1 for essential noise model components (full noise model is presented in [6]).

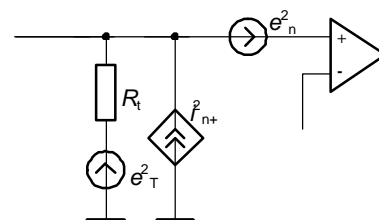


Fig. 1. Simplified noise model

If impedance can be modified using transformer then optimal impedance, acting at amplifier input, R_{opt} exists [8]:

$$R_{opt} = \frac{e_n}{i_{n+}} \quad (1)$$

For instance, R_{opt} is $3.7M\Omega$ for OPA657 and 400Ω for LMH6624 [9]. Contribution of various noise sources for LMH6624 at noise model [9] is presented in Figure 2. Impedance, acting at operational amplifier non-inverting input noise is labelled as NR+, impedance noise at inverting input is labelled as NR-, noise voltage source e_n contribution is labelled Nen and current noise sources i_{n+} and i_{n-} contributions is referred as Nin+ and Nin- respectively.

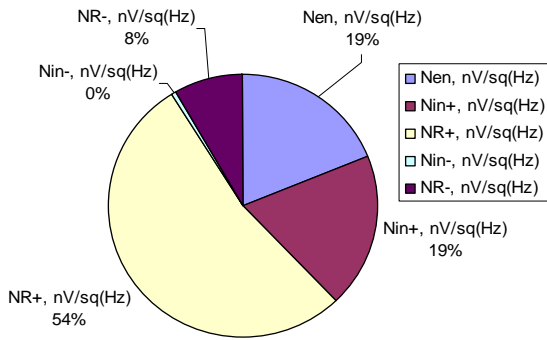


Fig. 2. Noise sources' contribution

It can be seen that contribution of source impedance thermal noise is most significant even for the case when source impedance equals R_{opt} . Otherwise it must be kept as low as possible (Figure 3).

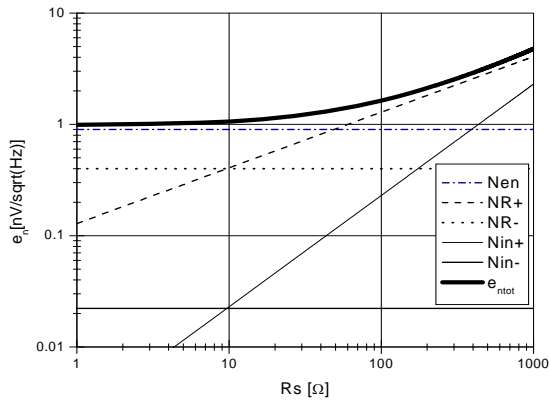


Fig. 3. Noise vs. source resistance

Analysis above indicates that preamplifier input impedance is important performance parameter. The auto-balancing bridge technique with measurement compensation using Open/Short/Load conditions [10] was chosen for impedance measurement.

The noise was obtained from amplifier gain and output noise measurement results. Sine wave [10] correlation technique was used to extract the complex signal amplitude.

To counter the high power transmission signal which is present in systems operating in a pulse-echo mode preamplifier input contains a protection circuit. The protection circuit's recovery time is important in near-field imaging. The recovery time investigation circuit is presented in Figure 4.

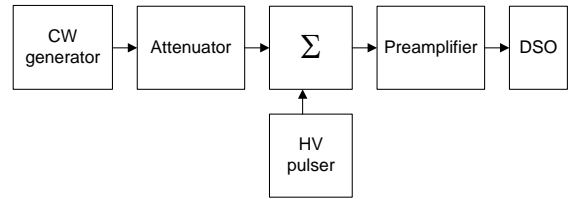


Fig. 4. Recovery time measurement

Continuous wave (CW) generator with attenuator in series is simulating the received signal. Thanks to continuous nature of CW the recovery dynamics of the preamplifier output can be evaluated by monitoring output signal magnitude. By measuring the time when signal reaches its initial level the recovery time can be estimated.

Following parameters have been chosen for performance evaluation: amplifier input equivalent noise, AC response shape, bandwidth, recovery time, input impedance.

3. PERFORMANCE EVALUATION

Olympus 5682 preamplifier (labeled Olympus), Ultratek (labeled Ultratek) and two preamplifiers of our own design (labeled LSLMH and LSAD) were evaluated. The results for gain and phase measurement are presented in Figure 5.

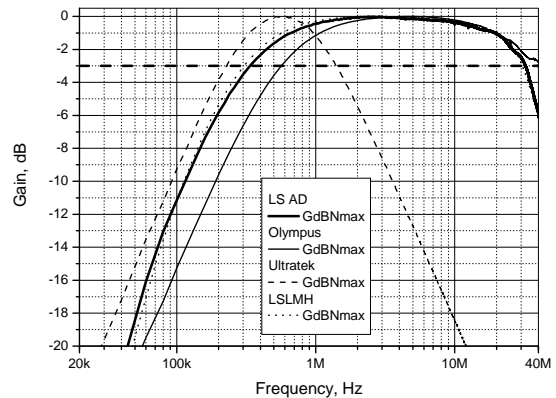


Fig. 5. Preamplifier gain curves

It could be noted that LSLMH and LSAD preamplifiers have same AC response shapes. Ultratek's bandwidth varies with gain – only maximum bandwidth curve is shown. Olympus AC response in HF end is not as sharp as LSLMH and LSAD amplifiers.

Noise measurement results are presented in Figure 6 (infinite source impedance, internal impedance present) and Figure 7 (zero source impedance).

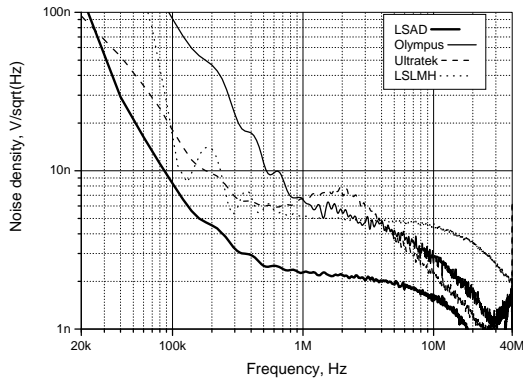


Fig. 6. Preamplifier noise curves with input circuit open

It can be seen that LSAD has lower noise density than LSLMH, Olympus and Ultratek by noise for high source impedance (Figure 6). Similar results were obtained for source with low impedance (Figure 7).

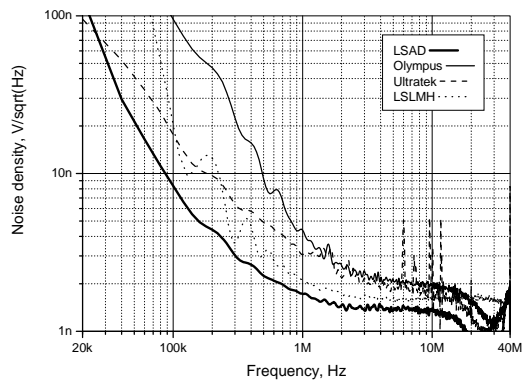


Fig. 7. Preamplifier noise curves with input shorted

Input impedance of the preamplifier is the only impedance acting at preamplifier input in case of open circuit. Measurement results are presented Figure 8.

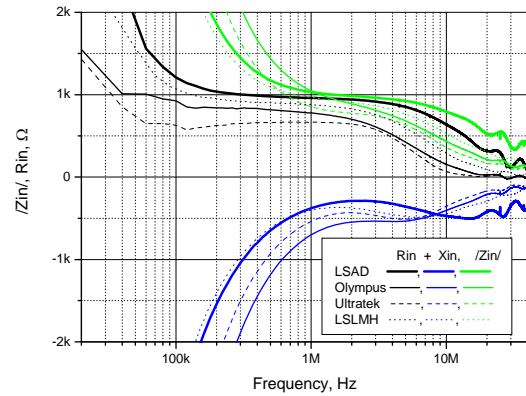


Fig. 8. Preamplifier input impedance

Investigation indicates that input impedance is stable within a passband.

The recovery time measurement results for LSLMH amplifier are in Figure 9.

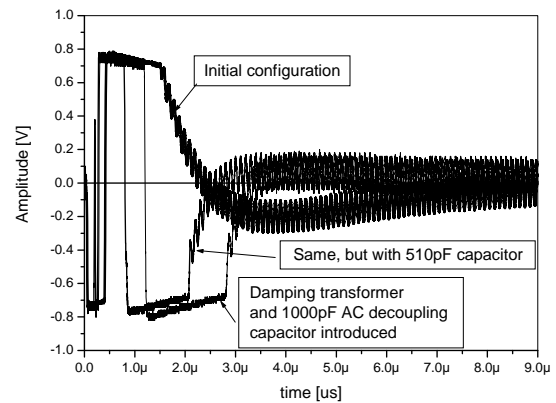


Fig. 9. Preamplifier recovery

Measured recovery times at -400V 200ns pulse were 3us for LSLMH design and 5us for LSAD preamplifier. Investigation has revealed that Ultratek preamplifier has tendency to turn into oscillations at low gains. Olympus has 1us recovery when excited from galvanically coupled pulser.

6. CONCLUSIONS

The input impedance, insertion gain and noise AC response analysis over 20kHz to 40MHz frequency range is presented. Brief description and explanations on equipment and techniques for ultrasonic preamplifier's performance evaluation is given and different manufacturers' products comparison has been established.

Results show that the noise performance is achieved with LSAD. Best recovery performance is for Olympus equipment.

References

- [1] R. Kazys, R. Raisutis, E. Zukauskas, et al. "Air-coupled ultrasonic testing of CFRP rods by means of guided waves", *Physics Procedia*, 2010, vol. 3(1), pp 185-192.
- [2] G. J. He, L. Zhang, H. L. Zhang. "Development of the Portable Ultrasonic Testing Device for Hoisting Equipment", 8th International Symposium on Test Measure, AUG 23-26, 2009 Chongqing, PRC, vol. 1-6, pp 1909-1911.
- [3] S. Meyer, D. Todd, B. Shadboldt. "Assessment of portable continuous wave Doppler ultrasound (ultrasonic cardiac output monitor) for cardiac output measurements in neonates", *Journal of paediatrics and child health*, 2009, vol. 45 (7-8), pp. 464-468.
- [4] R. Raisutis, R. Kazys, L. Mazeika. "Application of the ultrasonic pulse-echo technique for quality control of the multi-layered plastic materials" *NDT&E international*, 2008, vol. 41(4), pp. 300-311.
- [5] Y. Yanez, M. J. Garcia – Hernandez, J. Salazar, A. Turo, J. A. Chavez. "Designing amplifiers with very low output noise for high impedance piezoelectric transducers", *NDT&E International*, 2005, vol.38, pp. 491-496.
- [6] L. Svilainis, V. Dumbrava, "Investigation of a preamplifier noise in a pulse-echo mode", *Ultragarsas*, 2005, vol.56, pp. 26-29.
- [7] T. L. Rhyne, "Characterizing Ultrasonic Transducers Using Radiation Efficiency and Reception Noise Figure", *IEEE trans. UFFC*, 1998, vol.45, pp. 559- 566.
- [8] C. D. Motchenbacher, J.A. Connelly, "Low noise electronic system design", John Willey & Sons Inc., 1993.
- [9] L. Svilainis V. Dumbrava, "Design of a low noise preamplifier for ultrasonic transducer", *Ultragarsas*, 2005, vol. 55, pp. 28-32.
- [10] L.Svilainis, V.Dumbrava, "Test fixture compensation techniques in impedance analysis", *Electronics and Electrical Engineering*, 2008, vol. 7(87), pp. 37-40.

THE INVESTIGATION OF FILTERS FOR REAL-TIME DATA ACQUISITION

L. Svilainis, S. Kitov, V. Dumbrava

Signal processing department, Kaunas University of Technology,
Studentu str. 50, LT-51368 Kaunas, Lithuania

T, +370 37 300532; F, +370 37 753998; E, linas.svilainis@ktu.lt / serzhj@gmail.com / vytautas.dumbrava@ktu.lt

Abstract

Application of the real time digital filters in ultrasonic data acquisition system has been investigated. The work compares the digital filters (both programmable logic (CPLD/FPGA) both real time processing carried in PC) effectiveness when applied on ultrasonic signals. The investigation is cover filter, rounding noise and amplitude estimation performance. The acquisition system has been developed, including Xilinx Spartan 3E FPGA, high speed 10bit ADC and USB2 high speed interface. FIR filters have been developed and investigated experimentally.

Experimental results are documented and presented in tables and figures. Description and grounding of experimental techniques are presented.

1. INTRODUCTION

Development of ultrasonic inspection is raising demands for signal filtering since fields of application require higher dynamic range of the reception channel. Along with conventional, analog filter circuits, digital filtering is being extensively used. High gain values used, use of switched mode power supplies gives rise for electromagnetic interference (EMI). Ultrasound equipment should contain filters for EMI reduction [1].

Application of real time digital and/or analog filters in ultrasonic data acquisition system allows to have required processing immediately, during data acquisition process. The work will compare the digital (both programmable logic (CPLD/FPGA) both real time processing carried in PC) [2]. The investigation will cover filter rounding noise and AC response performance.

2. EXPERIMENTAL SYSTEM

The acquisition system has been developed for experimental purposes, including Xilinx Spartan 3E FPGA, high speed 10bit analog-to-digit converter (ADC) and USB2 high speed interface (Figure 1).

The core of the system is Spartan 3E Starter Board [3], obtained from Digilent, Inc. The Board is a self-contained development platform for designs targeting the Spartan 3E FPGA from Xilinx. It features a 500K gate Spartan 3E XC3S500E FPGA with a 32 bit RISC processor and DDR interfaces. A Xilinx Platform Flash for storing FPGA configurations, JTAG interface, 32MB Micron DDR SDRAM,

16MB Numonyx StrataFlash, 2MB ST Microelectronics Serial Flash, necessary Power Supplies regulators. For FPGA development in VHDL [4], Xilinx ISE web pack was used. Simulation was run on Aldec software Active HDL. Filter design and some simulations were run on MATLAB.

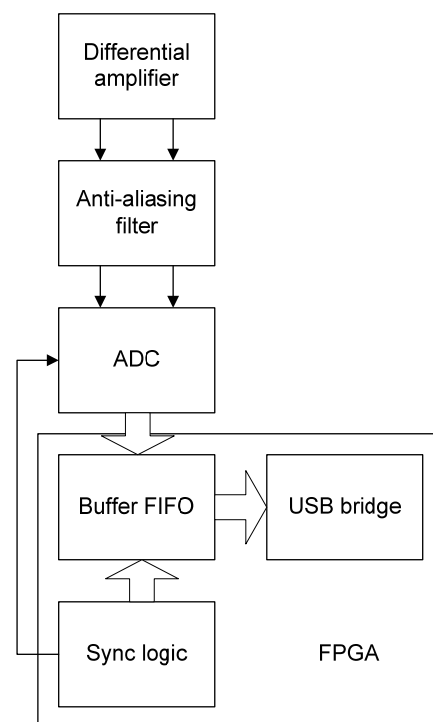


Fig. 1. Simplified system structure

The 100-pin Hirose FX2 connector is used for daughter board connection (Figure 2).

Daughter board contains coaxial connectors for analog signals supply, asymmetric to differential

converter and differential amplifier, anti-aliasing filter, high speed 10 bit ADC and USB2 high speed interface. Refer Figure 3 for daughter board circuit diagram.



Fig. 2. FPGA board with daughter board attached

3. DIGITAL NOISE INVESTIGATION

Sampled continuous wave (CW) amplitude extraction error standard deviation was used as noise evaluation. Sine wave correlation (SWC) [5] technique was used to extract the signal amplitude from acquired data set.

It was suggested to use common reference frequency source for excitation generator and sampling. Then frequency instability errors can be dis-

regarded. In such case non-iterative fitting is used [5]:

$$U_c = \frac{\sum_{m=1}^M [\cos(2\pi f t_m) \cdot y_m]}{\sum_{m=1}^M [\cos(2\pi f t_m)]^2}, \quad (1)$$

$$U_s = \frac{\sum_{m=1}^M [\sin(2\pi f t_m) \cdot y_m]}{\sum_{m=1}^M [\sin(2\pi f t_m)]^2}, \quad (2)$$

$$U_{DC} = \frac{\sum_{m=1}^M y_m}{M}. \quad (3)$$

Then the magnitude and phase:

$$U = \sqrt{U_c^2 + U_s^2}, \quad \varphi = \arctan\left(\frac{U_s}{U_c}\right). \quad (4)$$

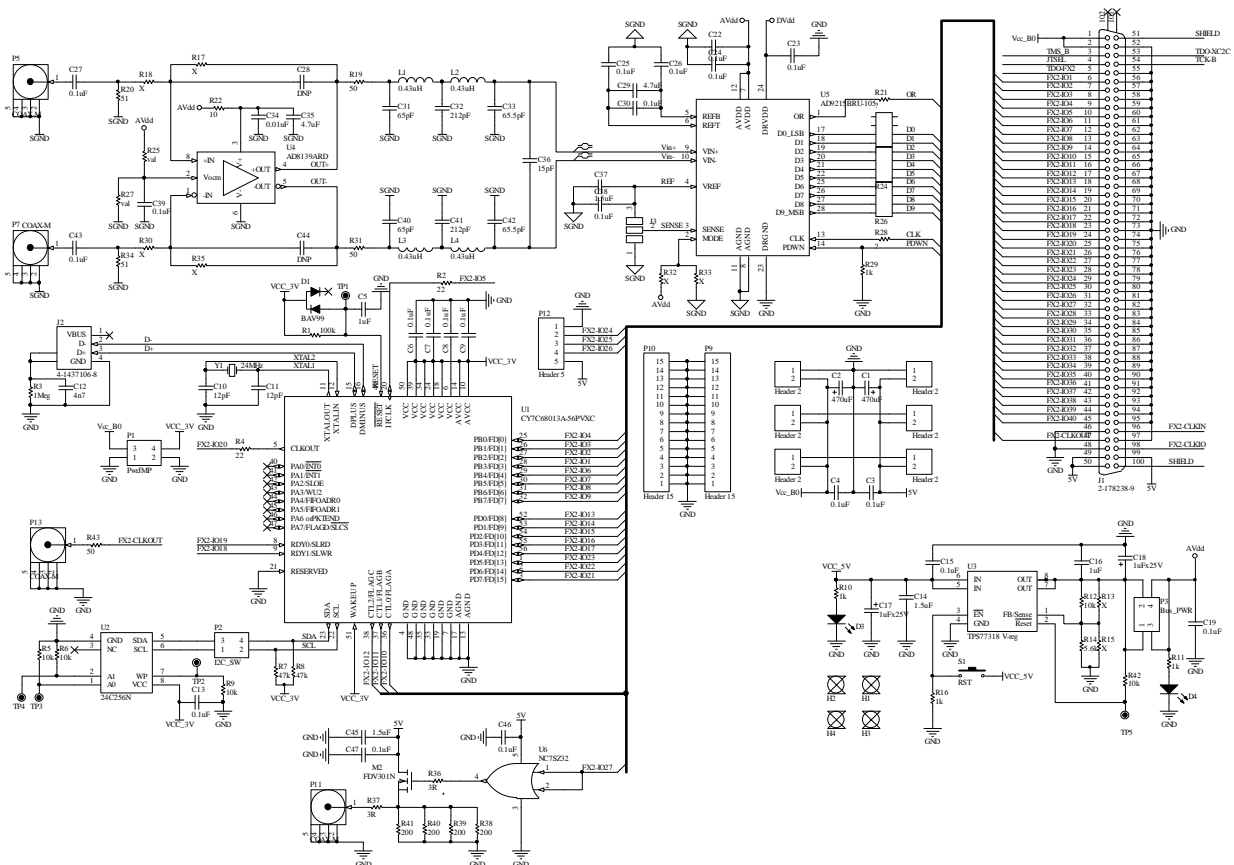


Fig. 3. Daughter board circuit diagram

The SWC technique has been implemented for measured signal amplitude and phase estimation in data acquisition module. Experiments were repeated 1000 times and amplitude obtained in every cycle was accumulated and then standard deviation calculated.

Following system operation modes were investigated:

1. 1 MHz CW signal acquired using 100 MHz sampling frequency and 10 bit ADC. Analog signal was passed through anti-aliasing filter. Signal stored in 8k memory.

2. Same 1 MHz CW signal acquired using at 100 Ms/s sampling frequency and 10 bit ADC with preceding anti-aliasing filter. But then was decimated to 10 Ms/s and stored in 8k memory. Anti-aliasing filter is used during decimation and stored as 10 bit.

3. Same 1 MHz CW signal acquired using at 10 Ms/s sampling frequency, 10 bit ADC with preceding anti-aliasing filter and stored in 8k.

Experiments were carried out in MATLAB. System input noise density was varied. Results where quantisation error was not taken into account are presented in Figure 4.

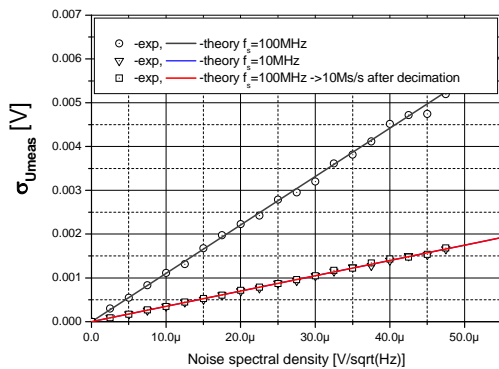


Fig. 4. Measured voltage standard deviation vs. electronics noise spectral density

It can be concluded that only filter bandwidth is influencing errors obtained. Therefore, keeping record length 8k gives same filter bandwidth for 10 Ms/s case and wider bandwidth for 100 Ms/s case.

Then quantisation was applied to evaluate the quantisation noise influence. In order to keep the quantisation noise as much random, carrier frequency was varied and kept as a fractional number of sampling frequency. Also, small amount (10 nV/sqrt(Hz)) of electronics noise was injected to simulate the real case. Results are presented in Figure 5.

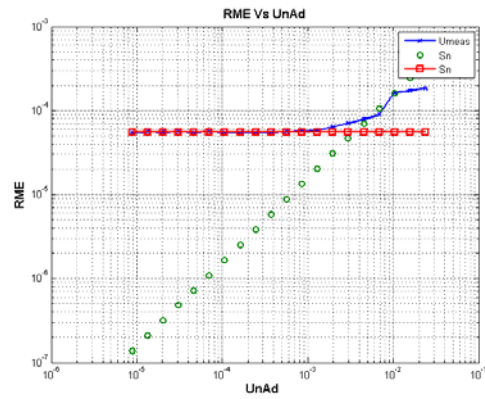


Fig. 5. Measured voltage standard deviation vs. quantisation noise standard deviation

ADC resolution was varied from 4 to 16bits and resulting quantisation noise standard deviation evaluated as:

$$U_{ADCnRMS} = \frac{U_{FS}}{2^K \sqrt{12}}, \quad (5)$$

where K is ADC bits number, U_{FS} is the ADC full-scale range.

It can be concluded that ADC quantisation noise should match the electronics noise: otherwise noise statistics is distorted (see the upper part of the curve on Figure 5); also, there no need for further increase of ADC resolution since electronic noise starts to dominate (see the lower part of the curve on Figure 5 – there is no improvement in noise performance).

4. DIGITAL FILTERS INVESTIGATION

Digital filters were implemented in FPGA and testing signals acquired using acquisition system developed. Filter AC response was measured passing chirp signal through the filter. Using the spectra of signal supplied to filter and at the filter output filter AC response was obtained:

$$T_{filt}(j\omega) = \frac{S_{out}(j\omega)}{S_{in}(j\omega)}. \quad (6)$$

Refer Figure 6 for signal magnitude spectrum used for testing.

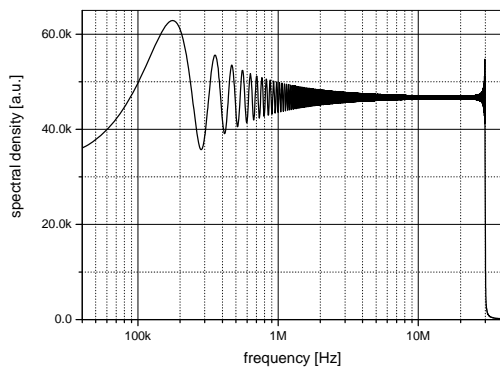


Fig. 6. Test signal spectrum

AC response for 39 taps FIR equiripple filter is in Figure 7.

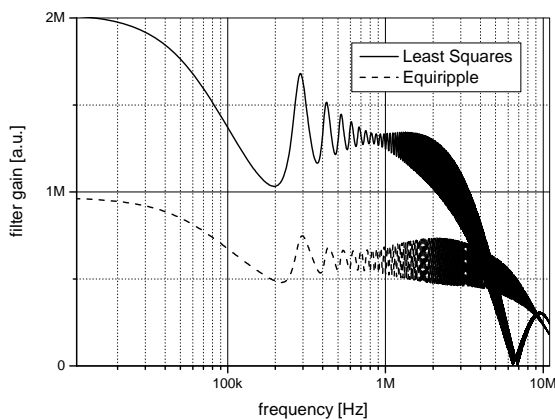


Fig. 7. FIR filters AC response

Filter cutoff frequency was 4.4MHz and stopband frequency was 9MHz with stopband attenua-

tion 64dB (demanded by 10bit decimation from 100Ms/s to 10Ms/s) and it had 42 taps.

Another filter (Figure 7) had same cut-off frequency and stopband frequencies and attenuation but it was designed as least squares filter.

5. CONCLUSIONS

Application of digital filters in real time non-destructive testing ultrasonic systems is favoured nowadays. But possible artefacts are the penalty for digital processing advantages. Design of the filters require both high designer qualification both efforts in fighting such issues as saturation, abrupt degradation of the signal.

References

- [1] C.Fritsch, R.Giacchetta, R.Gonzalez, et al. "A Full Featured Ultrasound NDE System in a Standard FPGA", ECNDT Proceedings 2006 pp.1-10.
- [2] J.Brizuela, A. Ibañeza and C. Fritscha, "NDE System for Railway Wheel Inspection in a Standard FPGA", Journal of Systems Architecture, article in press, doi: 10.1016/j.sysarc.2010.07.015.
- [3] Spartan 3E Starter Board, Digilent, Inc. 2010: <http://www.digilentinc.com/Products>
- [4] C. Maxfield. "The Design Warrior's Guide to FPGAs", Elsevier 2004.
- [5] L. Svilainis, V. Dumbrava, "Amplitude and phase measurement in acquisition systems," Matavimai, 2006, vol. 38, pp. 21-25.

THE ELECTROMAGNETIC INTERFERENCE OF ULTRASONIC PULSER – PREAMPLIFIER

A. Chaziachmetovas¹, A.Citavicius², L. Svilainis¹

*1 Signal processing department, Kaunas University of Technology,
2 Electronics and measurement systems department, Kaunas University of Technology,
Studentu str. 50, LT-51368 Kaunas, Lithuania
T, +370 37 300532; F, +370 37 753998;
E, andrius.chaziachmetovas@ktu.lt / algimantas.citavicius@ktu.lt / linas.svilainis@ktu.lt*

Abstract

Electromagnetic interference inside the standalone ultrasonic pulser – receiver is investigated. Simulation of EMI situation inside the extruded aluminum case using several electromagnetic simulation software was done.

1. INTRODUCTION

Development of ultrasonics non-destructive testing (NDT) [1] has transformed the configuration and demands for ultrasound electronics: system usually is spread over large area; signal cable length can reach hundreds of meters. Along with high gain, wide bandwidth and large excitation powers these long distances are increasing the electromagnetic interference (EMI) coupling to signal path. Therefore EMI immunity performance is important here [2,3].

Ultrasonic pulser is using high voltage power supply. This high voltage is produced by step-up DC-DC converter from relatively low 5-12V power supply which is available in portable equipment. If pulser is combined with reception circuitry in one case, then DC-DC converter presence creates significant EMI. This was the case in our standalone ultrasonic pulser – receiver design. Design is placed inside of extruded aluminium case. Electromagnetic interference inside the case is investigated.

2. ULTRASONIC NDT SYSTEM

The ultrasonic non-destructive testing system (Figure 1) contains at least the excitation channels (usually square wave) for the generation of ultrasonic signal. Application of pulse or bursts with the square pulses excites the ultrasonic transducer.

Low noise amplifier (LNA) is used at the input to ensure a wide dynamic range of the input. Transmission-reception switch (can be only limiter) is used to prevent the receiving circuitry damage during excitation. These two units can be placed in

separate box, located close to the ultrasonic transducer and received signals relayed to acquisition unit.

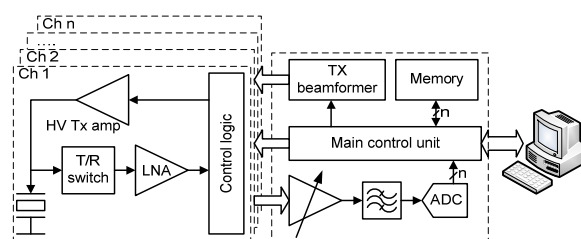


Fig. 1. Simplified system structure

The main acquisition unit contains control, excitation beam former, time variable gain amplifier (TVG), a band pass filter and analog-to-digital converter (ADC) with a corresponding memory and glue logic. Signal decay with distance is compensated by TVG. This unit includes variable (usually linear-in-dB) amplifiers.

3. PULSER

Piezoceramic ultrasonic transducers usually have high input impedance. Therefore, high voltage excitation is necessary to supply sufficient power for excitation. The most convenient way to get high voltage pulse [4] is two switches connected in totem-pole (Figure 2) topology.

Switches are commuting the high voltage power, produced by DC/DC step-up converter. To produce the high voltage on transducer terminals the switch S_1 is turned on and S_2 stays off. To remove this high voltage from the transducer terminals the S_2 is turned on and S_1 off. This is done after time interval

defined by ultrasonic transducer operation frequency. To repeat, the pulse S_1 is turned on again and S_2 is off so we get another high voltage pulse.

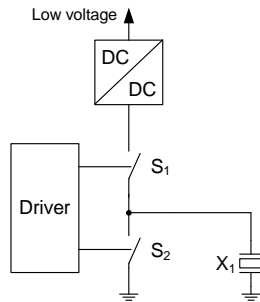


Fig. 2. Pulser circuit

Such excitation pulses penetrate to reception channel as EMI. But this EMI is not essential since can be separated in time by acquisition timing.

4. HIGH VOLTAGE CONVERTER

In addition to high voltage pulses DC-DC converter is producing additional EMI. Figure 3 present simple DC-DC converter to produce 200 V from 12 V input.

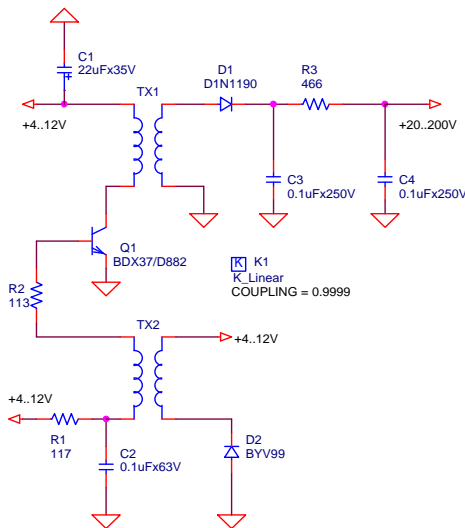


Fig. 3. HV DC-DC converter

Circuit above was used in simulation using P-SPICE to investigate the transistor Q1 current. Figure 4 present the simulation result for output voltage on capacitor C3.

Figure 5 is for Q1 simulated collector current spectrum presentation.

It can be seen that current is covering significant part of spectrum, so it will not be easy to get rid of it.

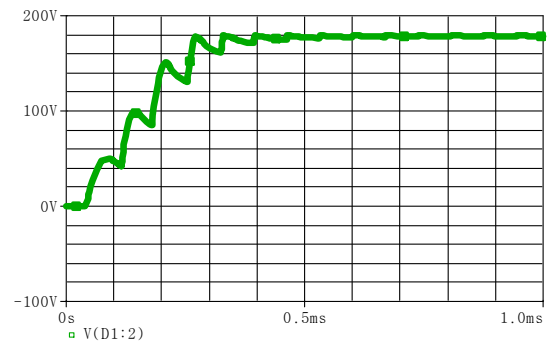


Fig. 4. HV output signal at startup

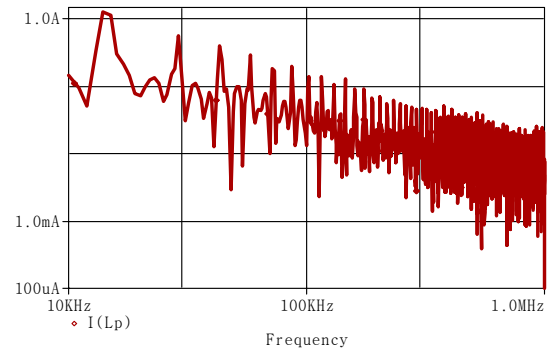


Fig. 5. Q1 collector current spectrum

5. PREAMPLIFIER

Amplifiers used in ultrasound reception should be low noise. Also the impedance, acting at amplifier input, should be accounted since it determines the noise level. Usually input impedance varies in range 50Ω to few $k\Omega$ [6,7]. This creates perfect reception path for induced EMI pickup and amplification.

In systems operating in a pulse-echo mode the preamplifier is connected to high voltage pulser output. Of course, there is a protection circuit at the input (Figure 6).

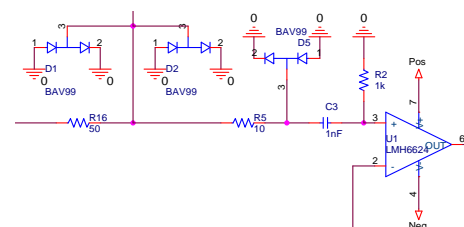


Fig. 6. Input protection circuit

But this circuit creates a local loop (R16-R5-C3-R2) which picks up the high current induced by Q1. Only 1uA induced in R2 circuit creates 1mV signal which is amplified further.

In order to decide what measures should be taken internal eigenmode analysis was done in high frequency structure simulator (HFSS). Decision was inspired by [8].

Three dimensional pulser-amplifier model was developed in SolidWorks (Figure 7).

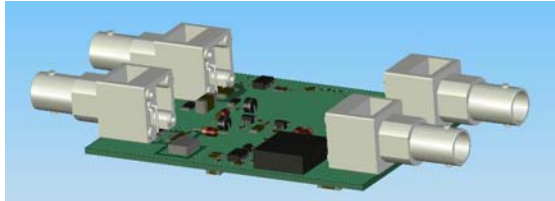


Fig. 7. PCB model in SolidWorks

Model was imported into HFSS environment. DC-DC converter power supply PCB track was assigned as excitation port. Unfortunately, due to multiple elements simulation time was too long to converge and memory limit was exceeded. Therefore simpler model of the box and the PCB was applied to investigate the fields in 0.1-2 GHz range. Results at 1.5 GHz are presented in Figure 8.

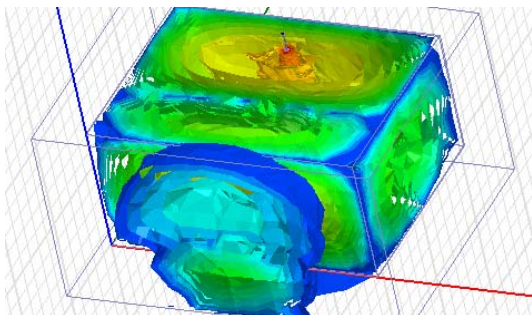


Fig. 8. E-field simulation result

The box front panel gap was simulated by placing the slot beneath coaxial connectors. It can be

seen in Figure 8 that E-field is leaking out through the slot.

6. CONCLUSIONS

Simulation of electromagnetic interference of standalone ultrasonic pulser – receiver placed inside the extruded aluminium case has indicated, that presence of high voltage DC-DC converter in close proximity of receiving preamplifier creates significant EMI in reception channel. Application of simulation software can be of much help in problem location.

References

- [1] R Kažys, "A review of NDT activities in Lithuania", *Insight*, June 2001, Vol 43, No 6, pp. 369-371.
- [2] Standard EN 61326-1:2006 Electrical Equipment for Measurement, Control and Laboratory use: General requirements.
- [3] Standard EN61326-2-3:2006 Electrical Equipment for Measurement, Control and Laboratory use: Transducers with integrated or remote signal conditioning.
- [4] L. Svilainis, V.Dumbrava, G.Motiejūnas. "Optimization of the ultrasonic excitation stage", *proceedings IEEE ITI 2008, Cavtat, Croatia, 2008*, pp. 791-796.
- [5] HV DCDC
- [6] Y. Yanez, M. J. Garcia – Hernandez, J. Salazar, A.Turo, J. A. Chavez. "Designing amplifiers with very low output noise for high impedance piezoelectric transducers", *NDT&E International*, 2005, vol.38, pp. 491-496.
- [7] L.Svilainis, V. Dumbrava, "Investigation of a preamplifier noise in a pulse-echo mode", *Ultragarsas*, 2005, vol.56, pp. 26-29.
- [8] D.Thompson"PCB Radiated Emissions With Linked Enclosure", *Ansoft 2007*.

SIMULATION OF SELECTIVE REPEAT AUTOMATIC RETRANSMISSION REQUEST SCHEME

Valentin Hristov

*Department of Computer Systems and Technology at South West University
66, Iv. Mihajlov, 2700 Blagoevgrad, Bulgaria
E-mail: v_hristov@swu.bg*

Abstract

The present paper presents a simulator to evaluate the impact of burstness both in the channel errors and in the arrival process on the SR ARQ statistics. The simulations then used to show and discuss some results which are explained. In this investigation GPSS- General Purpose Simulation System is used to create the simulation model

Keywords – Selective Repeat Automatic Retransmission Request, GPSS Simulations.

1. INTRODUCTION

The Selective Repeat Automatic Repeat re-Quest (SR ARQ) protocol is a general strategy for handling frame transmission errors when the round-trip time for frame transmission and reception of the acknowledgment is comparable to or larger than frame transmission time, e.g. TCP. In this protocol, the transmitter groups the frames into windows so that each window contains N frames. When the sender sends frames within a window, the receiver stores the frames of the current window and checks for errors. After a complete window has been received, or after the proper timeout period, the receiver instructs the transmitter to resend only the frames that contained errors.

The investigations of delay performance and other related issues of different ARQ schemes has been subject of many papers [1]–[7].

In [1], Badia presents an extended analysis, with two Markov chains describing arrival and channel error processes. However, he assumes error-free ACK/NACKs and unlimited transmitter and receiver buffers as well as omits the constant propagation delay term.

Seo et al., in [4], derive the delay statistics of Hybrid ARQ also through Markov chains.

A matrix geometric approach [7] has been used by Le et al. to evaluate the performance of ARQ schemes in a radio link with adaptive modulation and coding. To derive the queueing statistics it is observed that the process is Quasi-Birth and Death (QBD), which holds also for the system studied in [5]. Finally, in [6], Luo et al. discuss the ARQ delivery delay by focusing on the impact of the link layer

ARQ on the performance of upper layers, i.e., the service data unit (SDU) delay. Though their focus is different, they obtain some results by means of simulation, which in what follows will be derived analytically.

The purpose of present paper is to present a simulator to evaluate the impact of burstness both in the channel errors and in the arrival process on the SR ARQ statistics. The simulations then used to show and discuss some results which emerge in the statistics and which are non intuitive.

2. SIMULATION MODEL

Figure 1 shows the delay between the first transmission of a frame and its release from the receiver buffer, we will call delivery delay- T_D . Total delay- T_t experienced by a frame also comprises the time spent in the transmitter's queue, which we denote as queueing delay- T_Q . Because round-trip delay is larger than the frame transmission time, frames are not always transmitted in numerical increasing order, and this forces the receiver to keep the received frames in a buffer, from where they can be released only when all frames with lower identifiers have been acknowledged. The delay between the first transmission of a frame and its release from the receiver buffer can not be computed trivially [1], since it also depends on the outcome of the transmission of all frames with lower identifiers. In this paper General Purpose Simulation System (GPSS) is used to create the simulation model and to estimate the delay terms. Q- system of this model is depicted on fig. 2.

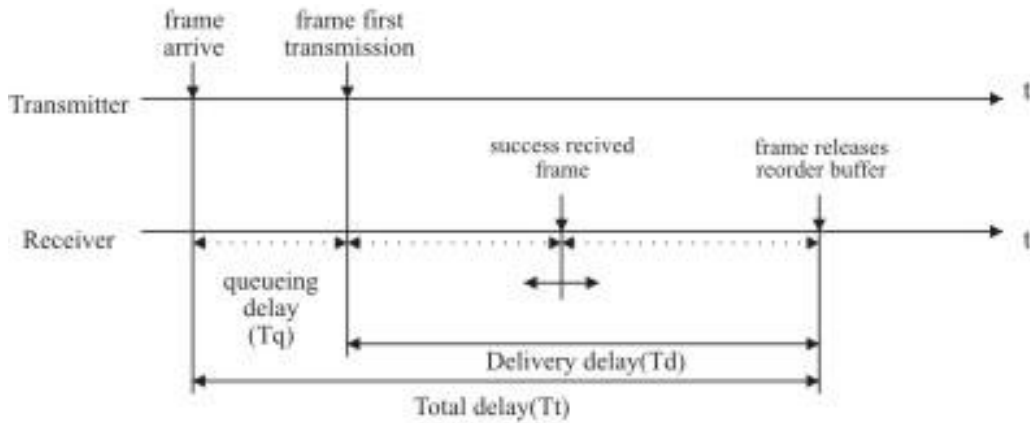


Fig. 1. Frames delivery in Selective Repeat Automatic Retransmission Request Scheme

The transmitter transfers frames after that receiver answers with positive or negative acknowledgement (ACK/NACK) according to the correct/erroneous reception of these frames, respectively. After a full round-trip time ACK/NACKs arrive at the transmitter's side, and either a new frame or a retransmission is sent over the channel. We assume that the value of the ARQ window size is m , i.e. the round-trip time equals m transmitted frames. Frames arrive at the transmitter's queuing buffer from an ON- OFF source with two states, referred in the following as "OFF"=no frame arrival and "ON"=frame arrival.

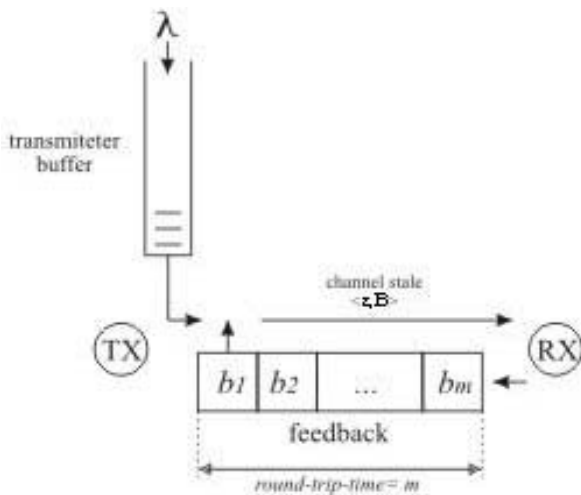


Fig. 2. Q- system of simulation model

The ON- OFF source is characterized by means of two independent parameters, the average arrival rate- λ , and the average arrival burst length- A .

The data sent from the transmitter's queue arrive at the receiver through a noisy channel. This is modeled through "good" state corresponding to error-free transmission and "bad" state where the frame is always in error.

The channel in proposed model is characterized again by two parameters, the error probability ϵ , and the average error burst length B .

3. SIMULATION RESULTS

In this section we present some interesting results given from the proposed above GPSS Simulator. For all of the reported results, m and ϵ are taken to be equal to 10 and 0.1, respectively, even though other values have been tested and the results agree with the ones shown here.

Fig. 3 shows the queuing delay and the delivery delay as functions of A in the case $B = 3$ (a mildly correlated channel), $m=10$, and $\epsilon=0.1$, for various values of $\lambda = \{0.4, 0.6\}$. The delivery delay curves show that the value of T_D does not significantly change when λ and/or A varies. The queuing delay, instead, is shown to increase with λ , which maybe somehow expected, but also it exhibits a linearly increasing behavior in A .

This can be explained by considering that the frames arrive in bursts and therefore are likely to find many other frames ahead in the queue, which results in a higher T_Q and total delay.

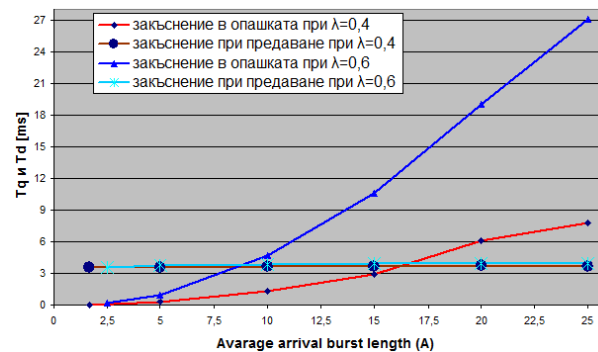


Fig. 3. Queuing and delivery delay vs. A , for various values of λ

Fig. 4 shows average values of the delivery delay for $m=10$, $\epsilon=0.1$, $A=2.5$ as a function of arrival rate λ , for various values of B .

In this figure, a counterintuitive behavior is emphasized: one might expect that the delay increases with λ , since the system is more heavily loaded. This reasoning is correct for the queuing delay, but not for the delivery delay.

However, for more realistic cases where the average burst length is moderate or higher, the delivery delay is almost independent of the frame arrival rate or may decrease with increasing λ . This phenomenon can be explained by appearance of long sequences of slots where the channel is in a good state, thus it is easier to solve an entire sequence of frames directly. It is more acute for large values of burst error length B .

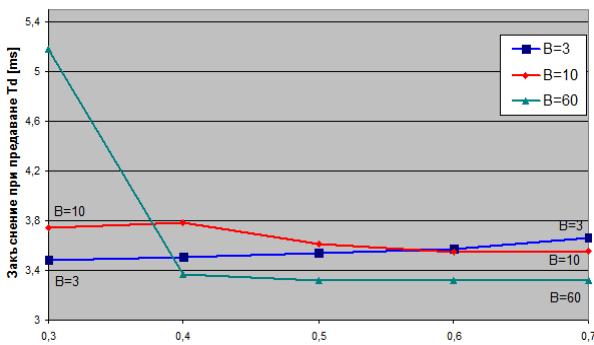


Fig. 4. Delivery delay vs. λ , for various values of B

Fig. 5 shows average values of the total delay for $m=10$, $\epsilon=0.1$, $\lambda=0.6$ as a function of burst error length B , for various values of arrival burst length $A=\{2.5, 7\}$.

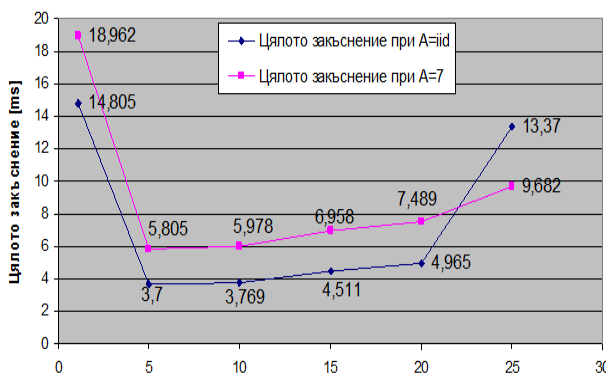


Fig. 5. Total delay vs. B , for various values of $A=\{2.5, 7\}$.

As can be seen total delay decreases at first and then increases linearly, i.e. the moderate channel burstiness achieves lower delay than one at the lower or higher channel burstiness.

Finally, comparison between the queuing delay, the delivery delay, and the total delay for $m=10$, $\epsilon=0.1$, $\lambda=0.6$, as a function of B , for $A=2.5$ is shown in Fig. 6. This figure explains the fact that moderate channel burstiness achieves a lower total delay than one at the lower or higher channel burstiness: By looking at the figure, we are now able to recognize that total delay depends on the dominant delay term being either the delivery or the queuing delay. In fact, while T_D is decreasing when the channel burstiness increases around moderate values, T_Q is linearly increasing, which becomes the prominent term for high B .

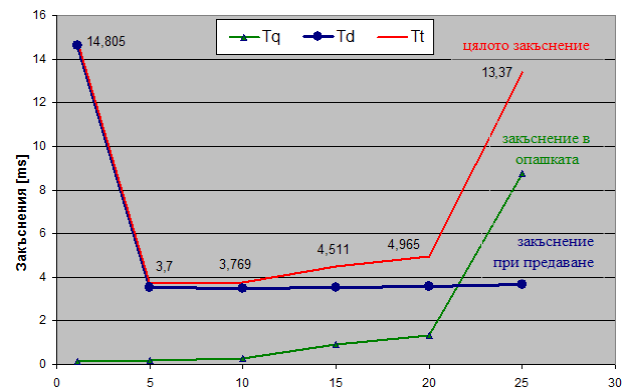


Fig. 6. Queuing, delivery, and total delay vs. error length B

Similar curves have been given in [1], which are derived analytically, and this fact can be presented as the kind of verification of proposed in present paper simulation model and results.

4. CONCLUSION

In present paper, we compare the SR ARQ delays with various intensities of the arrival rate and the arrival burstiness at the transmitter's queue as well as investigate the effect of the error burstiness in the channel. We show that the delivery delay may actually decrease for an increasing arrival rate when the channel is moderately burst, and in certain cases error burstiness may imply a general decrease of the total delay. These aspects are remarkable to achieve correct delay estimation in real time multimedia services over wireless channels, e.g. video-streaming applications.

5. ACKNOWLEDGEMENTS

This paper is sponsored by Research project No SRP-B4 at South West University- Blagoevgrad, Bulgaria.

References

- [1] Badia, L. On the Impact of Correlated Arrivals and Errors on ARQ Delay Terms, IEEE TRANSACTIONS ON COMMUNICATIONS, VOL. 57, NO. 2, FEBRUARY 2009, pp.334-337.
- [2] Hristov, V., SIMULATION OF TRANSPORT LAYER PROTOCOLS, Proc. of the Conference Computer Science'2006, Instambul, Turkey, 30 September – 2 October, 2005, Part I, pp. 114- 119.
- [3] J. G. Kim and M. M. Krunz, "Delay analysis of selective repeat ARQ for a Markovian source over a wireless channel," IEEE Trans. Veh. Technol. , vol. 49, no. 5, 2000, pp. 1968-1981.
- [4] J.-B. Seo, Y.-S. Choi, S.-Q. Lee, N.-H. Park, and H.-W. Lee, "Performance analysis of a type-II hybrid-ARQ in a TDMA system with correlated arrival over a non-stationary channel," in Proc. ISWCS,Siena, Italy, 2005, pp. 59-63.
- [5] L. B. Le, E. Hossain, and A. S. Alfa, "Radio link level performance evaluation in wireless networks using multi-rate transmission with ARQ– based error control," IEEE Trans. Wireless Commun.,vol.5,no.10, Oct. 2006, pp. 2647-2653.
- [6] W. Luo, K. Balachandran, S. Nanda, and K. Chang, "Delay analysis of selective-repeat ARQ with applications to link adaptation in wireless frame data systems," IEEE Trans. Wireless Commun., vol. 4, no. 3, May 2005, pp. 1017-1029.
- [7] M. F. Neuts,Matrix-Geometric Solutions in Stochastic Models.New

ARCHIVING AND CONTENT PROTECTION OF VISUAL MEDICAL INFORMATION WITH INVERSE PYRAMID DECOMPOSITION

Roumen Kountchev

Technical University of Sofia
Bul. Kl. Ohridsky 8, Sofia 1000
Phone: +3592 965 3283;
E: rkountch@tu-sofia.bg

Roumiana Kountcheva

T&K Engineering Co.
Mladost 3, Sofia 1712, POB 12
Phone: +3592 983 4541
E: kountcheva_r@yahoo.com

Abstract

The paper presents new technique for archiving and content protection of visual medical information. For this is developed a special format based on new decomposition, named Inverse Pyramid. The images are archived with highest quality, but their restoration is performed in accordance with the application. The method permits the regions of interest to be visualized with lossless visual quality. The image content is protected by inserting multiple fragile watermarks, which could be extracted by authorized users only. The fragile watermark is inserted as additional decomposition layer and does not influence the image quality. This approach permits the creation of archiving systems with hierarchical access control.

1. INTRODUCTION

Hospitals and other healthcare institutions have recently to maintain significant number of electronic files: images, ECGs, EEGs, scanned documents, and many others. Two main problems exist when this information is archived and stored: how to archive it efficiently so that to create databases of size as small as possible, retaining the visual quality unchanged, and how to ensure the needed confidentiality. The first problem is solved using some kind of image and data compression. Images are usually compressed using some kind of lossy compression [1-3]. The most famous standard, used for medical images, is DICOM [4] (based on the JPEG standard). This is a high-efficient compression, which offers restored images with retained visual quality, but it does not involve watermarking tools.

The second problem (the image content protection) is based on some kind of watermarking, encryption, etc. The watermark insertion is usually performed in the frequency domain, but this results in lower quality of the restored images [5,6].

In this paper is presented a method for image content protection based on new decomposition (Inverse Pyramid Decomposition, IPD), which permits fragile watermark insertion without image quality deterioration.

The paper is arranged as follows: in Section 2 are given the basic principles of the IPD and the method for multi-layer watermark insertion; Section 3 presents the structure of a database with hierarchical access control, based on the new decomposition, and Section 4 is the Conclusion.

2. BASIC PRINCIPLES OF IPD AND MULTI-LAYER FRAGILE WATERMARK INSERTION

The IPD essence is presented here in brief for 8-bit grayscale images as follows. First, the digital image (B) is processed with two-dimensional (2D) direct Orthogonal Transform (OT) using limited number of low-frequency coefficients only. The values of these coefficients build the lowest pyramid level (S). The image is then restored, performing Inverse Orthogonal Transform (IOT) for the retained coefficients' values only. In result is obtained the first, coarse approximation of the original image, which is then subtracted pixel by pixel from the original. The difference image (E), which is of same size as the original, is divided into 4 sub-images and each is processed with 2D OT again. The values of the retained coefficients build the second pyramid level. The processing continues in similar way with the next (higher) pyramid layers. The set of coefficients of the orthogonal transform, retained in every pyramid layer, can be different and defines the restored image quality (more coefficients naturally give higher image quality). The image decomposition is stopped when the needed quality of the approximating image is obtained – usually earlier than the last possible pyramid layer. The values of the coefficients got in result of the orthogonal transform from all pyramid layers are then quantized, sorted in accordance with their spatial frequency, arranged as one-dimensional sequence, and losslessly compressed. For practical applications the decomposition is usually “truncated”, i.e. it does not start from the lowest possible layer but from some

The example image in the lowest layer is overlapped by the visible WM of size 256 x 256 pixels, shown in Fig. 4. After using the special lossless compression, developed by the authors [7], the size of the compressed file is 751 B only. In the proposed IPD compression the additional information, added to the metadata is this of the compressed

WM image (i.e. 751 B). The WM image from Fig. 4 is just an example - in principle, any image could be used as a fragile WM. The basic requirements are the image to be relatively simple and to consist of comparatively large areas, which to resist the basic compression standards (JPEG, etc.).

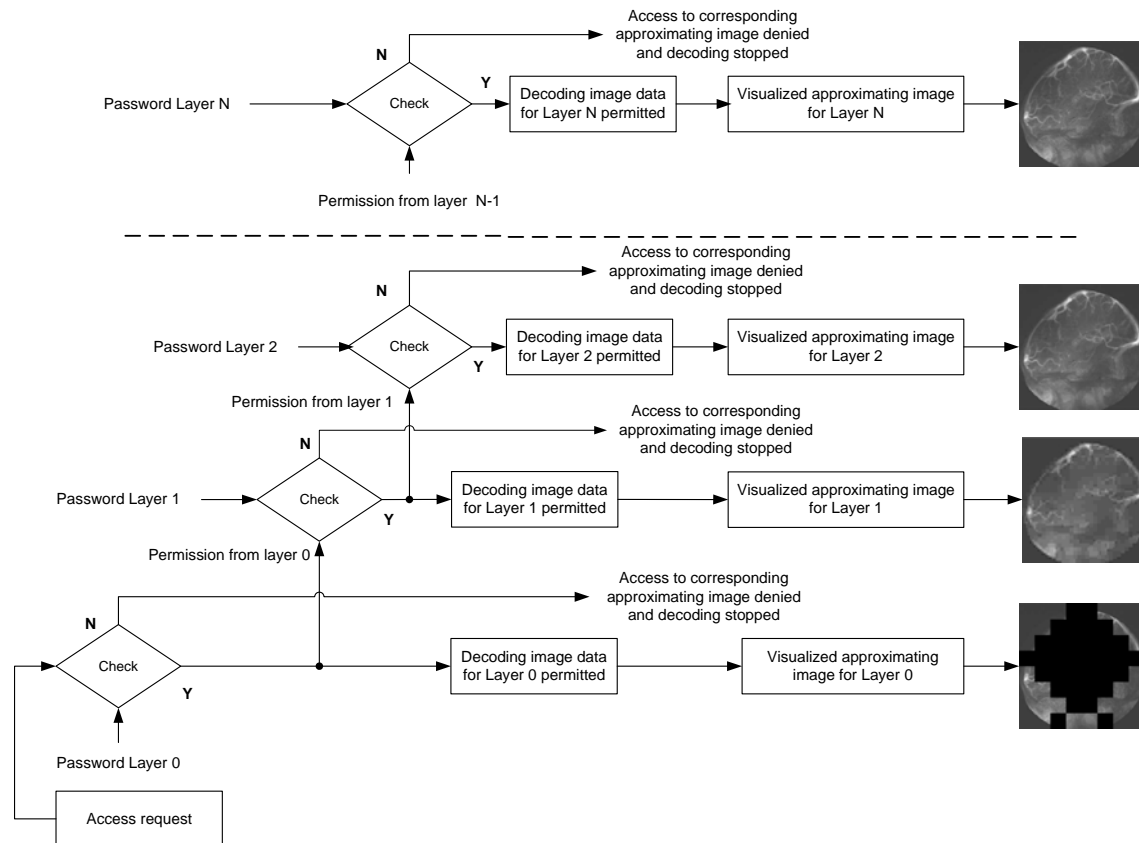


Fig. 2. Block diagram of a system with hierarchical access control

4. CONCLUSIONS

The main advantages of the IPD method are:

- It permits the processed images to be transferred layer by layer, with increasing quality. In result, the image transfer could be stopped any time, when required image quality is obtained;
- It permits the insertion of fragile and resistant watermarks in the processed visual information, on the basis of which to be developed special tools for data access management;

The main *application areas* of the method are:

- Creation of medical databases which to contain the global patients' information.

- Creation of tools for hierarchical access control in image databases.

ACKNOWLEDGMENTS

This work was supported by the National Fund for Scientific Research of the Bulgarian Ministry of Education, Youth and Science, Contract VU-I 305.

References

- [1] G. Menegaz, Trends in Model-based coding of Multidimensional Medical Data. Ch. 14 in: *Document and Image Compression*. Ed. M. Barni, CRC Press, 2006, pp. 351-388.
- [2] S. Tai, Y. Wu, C. Lin, "An Adaptive 3D Discrete Cosine Transform Coder for Medical Image compression", *IEE Trans. Inform. Tech. Biomed*, v. 4, 2000, pp. 259-263.

- [3] Z. Xiong, H. Wu, D. Yun, W. Pearlman, "Progressive Coding of Medical Volumetric Data Using 3D Integer Wavelet Packet Transform". *IEEE Second Workshop on Multimedia SP*, NJ, USA, 1998, pp. 553-558.
- [4] ACR-NEMA, DICOM Digital Imaging and Communications in Medicine, 2003.
- [5] Tefas, N. Nikolaidis, I. Pitas, Image Watermarking: Techniques and Applications. Ch. 22. In: *The Essential Guide to Image Processing*, Ed. Bovic, A. Elsevier, 2009, pp. 597-648.
- [6] F. Cayre, C. Fontaine, T. Furon, "Watermarking Security: Theory and Practice", *IEEE Trans. Signal Processing*, 53 (10), 2005, pp. 3976-3987.
- [7] R. Kountchev, M. Milanova, C. Ford, R. Kountcheva, Multi-layer Image Transmission with Inverse Pyramidal Decomposition. Ch. 13 in *Computational Intelligence for Modeling and Predictions*, S. Halgamuge, L. Wang (Eds.), Vol. 2, Springer-Verlag, 2005, pp. 179-196.
- [8] R. Kountchev, Vi. Todorov, R. Kountcheva. "Fragile and Resistant Image Watermarking Based on Inverse Difference Pyramid Decomposition". *WSEAS Trans. on Signal Processing*. Issue 3, Vol. 6, July 2010, pp. 101-112.

METHOD FOR WATERMARKING OF MEDICAL IMAGES BASED ON FAST COMPLEX HADAMARD TRANSFORM

Rumen Parvanov Mironov

Assistant Professor

*Technical University of Sofia, Faculty of Telecommunications,
Boul. Kl. Ohridsky 8, Sofia 1000, Bulgaria
Phone: 00359-2-965-22-74, E-mail: rmironov@tu-sofia.bg*

Roumen Kirilov Kountchev

Professor, D.Sc.

*Technical University of Sofia, Faculty of Telecommunications,
Boul. Kl. Ohridsky 8, Sofia 1000, Bulgaria
Phone: 00359-2-965-22-74, E-mail: rkountch@tu-sofia.bg*

Abstract

In this article a new method for digital watermarking of medical images is proposed. The used approach is based on the modification of selected coefficients phases of their discrete spectrum obtained by applying of the developed by the authors' discrete 2D Fast Complex Hadamard Transform algorithm. The halftone image is divided into 16x16 sub-blocks and selected parts introduces digital watermark. The main advantages of the proposed approach to tagging images are the practical invisibility of watermarks in place, their resistance to change, compression with loss of information, affine transformations, trimming, contrasting, linear and nonlinear filtering, noising, and implementing other effects and manipulations.

The obtained results show that the developed method is especially suitable for medical imaging and databases, where information announces to be reliable, protected from external access and to reproduce with high accuracy.

1. INTRODUCTION

As a result of the widespread use of information and communication technologies, archiving and secure storage of large quantities documents in digital form is integral part of the modern life. For this reason, electronic archiving and authenticity protection of digital content is an important task for society in a number of priority areas such as administrative services to the population, health, financial and police service, judiciary, distance education, preserving cultural heritage, and others.

Usually the medical documents and images are stored in one of the popular formats such as JPEG, BMP, TIFF, PDF, PNG and others. Basic compression methods and algorithms used in these formats are associated with maintaining the visual quality of the images and their reproduction without losses. A disadvantage of this approach for storing of documents is that they may be edited, in result of which their authenticity is distorted. For important documents, the problems with their reliable storage in ensuring their authenticity are particularly significant. Typically, this protection is done using special methods and use of codes with high resistance,

which can lead to a considerable increase in the volume of stored data. Therefore, the problems associated with archiving of medical documents are of particular relevance in the world and attract to a significant proportion of applied research in this area.

One possible solution is the use of digital watermarking, as a means of integrating hidden information in halftone images [1]-[6]. The watermark should be invisible to the viewer, resistant to attempts to delete it, have a large information capacity, can be read using a passkey on several levels, to introduce a minimum number of computing operations and extracted without the use of original product.

2. MATHEMATICAL DESCRIPTION

The coefficients of Complex Hadamard Transform matrix $[CH_N]$ with dimension N by N can be represented by the following equations [7], [8], [9]:

$$\begin{cases} c(u, v) = j^{uv} s(u, v) \\ c^*(u, v) = (-j)^{uv} s(u, v) \end{cases}, \quad (1)$$

where: $N = 2^n$, $j = \sqrt{-1}$, $u, v = 0, 1, \dots, 2^n - 1$ and

$$s(u, v) = \begin{cases} 1 & \text{for } n = 2 \\ (-1)^{\sum_{r=3}^n \lfloor u/2^{r-1} \rfloor \lfloor v/2^{r-1} \rfloor} & \text{for } n = 3, 4, \dots \end{cases}, \quad (2)$$

is the sign function. Here $\lfloor \cdot \rfloor$ is an operator, which represents the integer part of the result, obtained after the division.

From the equations (1) and (2) the CHT basis matrix of order 2^n calculated for $n=2$ and $u, v = 1, 2, 3, 4$ is presented as follows:

$$[CH_4] = \begin{bmatrix} 1 & 1 & 1 & 1 \\ 1 & j & -1 & -j \\ 1 & -1 & 1 & -1 \\ 1 & -j & -1 & j \end{bmatrix}. \quad (3)$$

The basis complex Hadamard matrices of order 2^n ($n > 2$) can be received as the Kronecker product of a number of identical "core" matrices of order 2^{n-1} in the following way:

$$[CH_{2^n}] = \begin{bmatrix} [CH_{2^{n-1}}] & [CH_{2^{n-1}}] \\ [CH_{2^{n-1}}] & -[CH_{2^{n-1}}] \end{bmatrix}. \quad (4)$$

The developed by the author's algorithm for Fast Complex Hadamard Transform (FCHT) use factorization of basis CHT matrices by the sparse matrices [10]. The complex Hadamard matrix $[CH_N]$ of order $N=2^n$ can be presented by the equation:

$$[CH_N] = [CHJ_N] \prod_{r=1}^{n-1} [G_r(N)], \quad (5)$$

where: $n = \log_2 N$, $[G_r(N)]$ are the sparse matrices with two non-zero elements in each row, which have the following block-diagonal structure:

$$[G_r(N)] = \begin{bmatrix} [A(r)] & 0 & \dots & 0 \\ 0 & [A(r)] & \dots & 0 \\ \dots & \dots & \dots & \dots \\ 0 & 0 & \dots & [A(r)] \end{bmatrix}.$$

The sub-matrices $[A(r)]$ are defined as Kronecker product of the matrices:

$$[A(r)] = [H_2] \otimes [I_{2^r}], \quad (6)$$

where: $[I_{2^r}]$ is identity matrix of size $2^r \times 2^r$, and $[H_2]$ is real basic Hadamard matrix of order 2.

Using definitions in (1) and equations (2)-(6) the fast forward one-dimensional CHT from the N -components input signal vector $\vec{A} = [a_1, a_2, \dots, a_{N-1}, a_N]$, the output spectral vector $\vec{B} = [b_1, b_2, \dots, b_{N-1}, b_N]$ is received by the equations [7]:

$$\vec{B} = [CHJ_N][G_1(N)][G_2(N)] \dots [G_{n-1}(N)]\vec{A}$$

or as a sequence of elementary transformations:

$$\begin{aligned} \vec{C}_1 &= [G_{n-1}(N)]\vec{A} \\ \vec{C}_2 &= [G_{n-2}(N)]\vec{C}_1, \\ &\dots \\ \vec{B} &= [CHJ_N]\vec{C}_{n-1} \end{aligned}, \quad (7)$$

where: $\vec{C}_1, \vec{C}_2, \dots, \vec{C}_{n-1}$ is the sequence of "intermediated" vector-iterations, which are received by the transformations with sparse matrices.

The developed FCHT algorithm can be illustrated by the signal flow graph for $N=4$, shown on Fig.1.

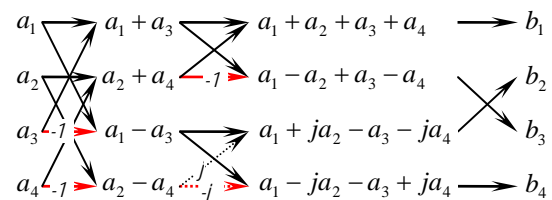


Fig. 1. FCHT signal flow graph of order 4.

The first matrix $[CHI_4]$ is presented with a first sub-graph and the second matrix $[CHJ_4]$ is presented with a second one in the generalized CHT signal flow graph. The third sub-graph presents reordering of spectrum elements. Multipliers are $+1$ and -1 as indicated by the black and red solid lines in real parts of sub-graphs and $+j$ and $-j$ as indicated by the black and red dashed lines in complex parts, respectively.

The described algorithm can be used for the reverse Fast Complex Hadamard Transformation. The flow graphs are identical and all output components must be divided on the N .

The FCHT algorithm is similar with the real FHT algorithm, which leads to considerable decreasing of mathematical computations. The difference be-

tween FCHT and FHT is entirely into the last iteration, which includes all complex operations.

3. EXPERIMENTAL RESULTS

The developed one-dimensional FCHT algorithm requires $N \cdot \log_2 N$ additions or subtractions and $N/2$ complex operations in the last iteration. Using the matrix descriptions for the 2D Complex Hadamard Transform in [8], the 2D FCHT algorithm can be realized by applying of 1D FCHT on the rows of the input image matrix and after then applying the 1D FCHT on the columns of the obtained matrix. The calculation complexity of 2D FCHT can be evaluated from the complexity of 1D FCHT and require: $2 \cdot N^2 \cdot \log_2 N$ additions or subtractions and N^2 complex operations.

The developed method for watermarking of medical images includes:

- viding of input image into sub-blocks of size 16x16;
- caulation of complex spectrum of each sub-block by the using of 2D FCHT;
- modification of the phase of some chosen complex-conjugated couple of spectrum coefficients by the approaches, described in [14].
- calculation of inverse 2D FCHT of each sub-block and writing the real part into the output image.

The developed method for watermarking of medical images by the using of FCHT was simulated on Matlab 6.5 environment for one X-Ray test image.

As a criteria for the watermark quality, evaluation for every image, could be used the signal to noise ration (SNR) of the watermarked image in respect to the original.

The obtained results proved the high efficiency of the watermarking with $SNR > 50$ dB when the values of the watermark elements are in the range $\pm 3^0$ and are coded with 5 bits per element, missing the code 00000. In this case the maximum speed for watermark data transmission is approximately 860 bps.

To protect the digital content of medical images can be used scrambling of image elements in each sub-block and a law scan of scrambling to be recorded in the involved watermark. This leads to the practical impossibility of using the medical imaging from unauthorized persons.

As a sample on Fig.2 is shown one test image "Spine.tif", with watermark sequence "13 9 5 1 1 5 9

13 29 25 21 1 1 21 25 29", written in each sub-block and on Fig.3 is shown the same image with scrambling.



Fig. 2. Watermarked X-Ray test image

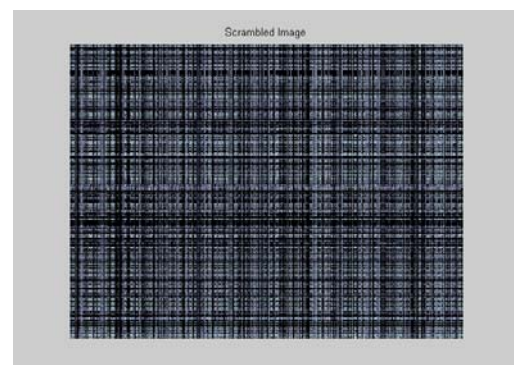


Fig. 3. Scrambled X-Ray test image

The scrambling was accomplished by the pseudo random reordering of rows and columns of each sub-block.

4. CONCLUSION

A new method for watermarking of medical images in the phase spectrum was developed. The method uses the developed Fast Complex Hadamard Transform algorithm. Advantage of the method is the fact that there is no quantization of the transform coefficients, the method has relatively low computational complexity and permits the insertion of different watermark with high information capacity in every sub-block of the images.

The method offers exact watermark extraction, high resistance against pirates' attacks with multiple lossy compression or different kinds of image transforms. The insertion of different watermarks in every sub-blocks makes the identification of the manufacturers and of the authorized distributors of multimedia production much easier.

The obtained results show that the developed method is especially suitable for medical imaging and databases, where information announces to be reliable, protected from external access and to reproduce with high accuracy.

5. ACKNOWLEDGMENTS

The authors thank the National Fund for Scientific Research of the Bulgarian Ministry of Education and Science for the financial support by the contract VU-I-305/2007.

References

- [1] B. M. Planitz, A. J. Maeder. "Medical Image Watermarking: A Study on Image Degradation". *Proceedings of the Australian Pattern Recognition Society (APRS) Workshop on Digital Image Computing (WDIC 2005)*, Brisbane, Australia, 12 February 2005, pp.3-8.
- [2] K. A. Navas, M. Sasikumar. "Survey of Medical Image Watermarking Algorithms", *4th International conference: Sciences of Electronic, Technologies of Information and Telecommunications*, Tunisia, March 25-29, 2007
- [3] M. Kallel, M. S. Bouhlej, J. C. Lapayre. "A multiple Watermarking Scheme for Medical Image in Spatial Field". *ICGST International Journal on Graphics, Vision and Image Processing*, GVIP, 2007, vol.7, No.1, pp.37-42.
- [4] C. Chemak, J. C. Lapayre, M.S. Bouhlej. "A new scheme of image watermarking based on 5/3 wavelet decomposition and Turbo-Code". *European Computing Conference (ECC'07)*, WSEAS Transactions on Biology and Biomedicine, Vol.4, No.4, 2007, pp.45-52.
- [5] C. Chemak, J. C. Lapayre, M. S. Bouhlej. "New Watermarking Scheme for Security and Transmission of Medical Images for Pocket Neuro Project". *Radioengineering*, Vol. 16, No. 4, December 2007, pp.58-63.
- [6] Hui-fen Huang, "Perceptual Image Watermarking Algorithm Based on Magic Squares Scrambling in DWT", *2009 Fifth International Joint Conference on INC, IMS and IDC*, 2009, pp.1819-1822.
- [7] B. Falkowski, S. Rahardja. "Complex Hadamard Transforms: Properties, Relations and Architecture", *IEICE Trans. Fundamentals*. Vol. E87-A, No.8, August 2004.
- [8] R. Mironov, R. Kountchev. "Analysis of Complex Hadamard Transform Properties", *XLI International Scientific Conference on Information, Communication and Energy Systems and Technologies*, ICEST 2006, 26 June – 1st July, Sofia, Bulgaria, 2006, pp.173-176.
- [9] R. Mironov, R. Kountchev, V. Mirchev "Ordered Complex Hadamard Transform of Images", *XL International Scientific Conference on Information, Communication and Energy Systems and Technologies*, ICEST 2007, Ohrid, Macedonia, June 24-27, 2007, pp.123-126.
- [10] R. Mironov, R. Kountchev. "Algorithm for Fast Complex Hadamard Transform", *XLV International Scientific Conference on Information, Communication and Energy Systems and Technologies*, ICEST 2010, Ohrid, Republic of Macedonia, 23-26 June 2010.

VOLUMETRIC IMAGE PROCESSING BY THREE-DIMENSIONAL FILTERS

Dimitar G. Valchev

Technical University of Varna
1 Studentska St, 9010 Varna, Bulgaria
Phone: +359 52 383 596; E-mail: dvalchev@ece.neu.edu

Abstract

This paper develops filter derivation for volumetric image processing both for the cases of separable and non-separable three-dimensional filters. Such filters find major applications in the fields of computed tomography and magnetic resonance imaging systems, as well as in other subsurface sensing techniques.

1. INTRODUCTION

Volumetric images arise in many applications such as computer tomography imaging and subsurface sensing of various hidden spaces. Volumetric images are represented as three-dimensional (3-D) arrays of voxel values. They provide realistic representations of real world solids as true 3-D images, not just 2-D projections onto a planar display. Being 3-D signals, volumetric images are subject to 3-D signal processing. The various filtering techniques from 2-D signal processing may be extended to three dimensions.

Basic to the filter characterization methodology is the derivation of the impulse response of an ideal lowpass 3-D filter. Based on that response, various highpass, bandpass and bandstop filters can be developed.

The paper is organized as follows. Section 2 gives the impulse responses of a separable filter with an ideal rectangular passband and of a non-separable filter with an ideal spherical passband. Section 3 summarizes the results and a separate Appendix section outlines the derivation of the results in Section 2.

2. IDEAL LOWPASS FILTER

The starting point for designing a filter is the ideal lowpass filter spectral characteristic from which different highpass, bandpass and bandstop filter configurations can be derived. Similarly to the digital filters in 2-D signal and image processing [1, 2], the 3-D image filters can also be separable with rectangular support and non-separable. The non-separable 3-D filter considered in this paper has a circular support.

The performance difference between a separable and a non-separable filter lies in the spectral characteristics along different directions in 3-D space. On the one hand, the separable filter is simply designed; its impulse response is equal to the product of the marginal impulse responses along the three spatial axes which determines independent spectral characteristics along the three axes. Its passband is rectangular which means that this kind of filter would pass higher frequencies along the diagonal directions of the rectangle, compared to the frequencies along each frequency axis.

On the other hand, the non-separable filter offers spectral characteristics along the different directions which are no longer independent. In particular, the non-separable filter with spherical passband offers equal spectral characteristics along any direction in 3-D space. This may be very important especially in computed tomography and magnetic resonance imaging where the data details are equally important in all directions.

Those observations give grounds to develop filter characterizations for both separable and non-separable 3-D filters. The particular use of one of them is determined by such factors as complexity, speed, reliability in all directions and, of course, the particular intended application.

2.1. Rectangular passband

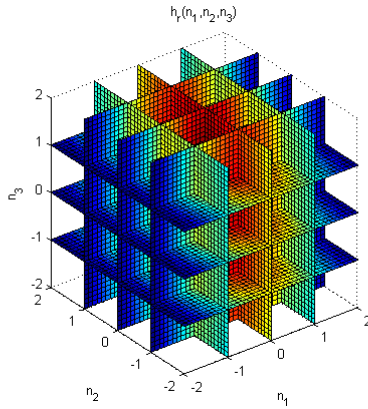
The rectangular passband defines a separable 3-D filter. The impulse response of such a filter is given by (details in Appendix A)

$$h_r(n_1, n_2, n_3) = \frac{\sin \omega_{c_1} n_1}{\pi n_1} \frac{\sin \omega_{c_2} n_2}{\pi n_2} \frac{\sin \omega_{c_3} n_3}{\pi n_3} \quad (1)$$

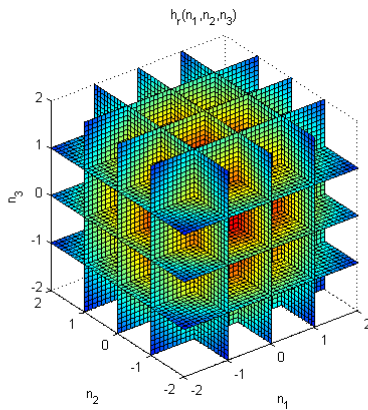
for $-\infty < n_1, n_2, n_3 < \infty$, where $\omega_{c_1}, \omega_{c_2}$ and ω_{c_3} are the cut-off spatial frequencies along the corresponding three frequency axes.

For $\omega_{c_1} = \omega_{c_2} = \omega_{c_3} = \omega_c$, the filter's passband becomes cubic.

Fig. 1 shows pseudocolor slice plots of the impulse response of the separable 3-D filter in (1). Fig. 1a shows the rectangular passband 3-D filter with $\omega_{c_1} = \pi/2$, $\omega_{c_2} = \pi/4$ and $\omega_{c_3} = \pi/8$. Fig. 1b shows the cubic passband 3-D filter with the cut-off spatial frequency $\omega_c = \pi/4$.



a) Rectangular passband with $\omega_{c_1} = \pi/2$, $\omega_{c_2} = \pi/4$ and $\omega_{c_3} = \pi/8$



b) Cubic passband with $\omega_c = \pi/4$

Fig. 1. Impulse response of a separable 3-D filter with a rectangular passband

2.2. Spherical passband

The spherical passband defines a non-separable 3-D filter. The impulse response of such a filter is given by (details in Appendix B)

$$h_s(n_1, n_2, n_3) = \frac{\omega_c j_1(\omega_c \sqrt{n_1^2 + n_2^2 + n_3^2})}{4\pi(n_1^2 + n_2^2 + n_3^2)} \quad (2)$$

with $j_1(\bullet)$ being the first-order spherical Bessel function of the first kind and ω_c being the cut-off spatial frequency.

Fig. 2 shows a pseudocolor slice plot of the impulse response of the non-separable 3-D filter with spherical passband in (2) with cut-off spatial frequency $\omega_c = \pi/4$.

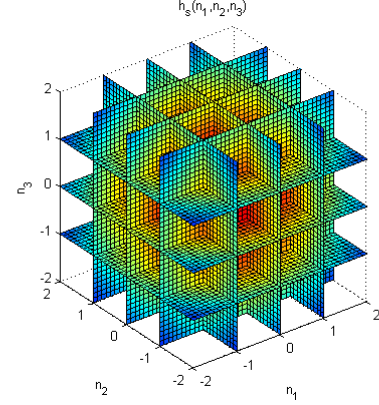


Fig. 2. Impulse response of a non-separable 3-D filter with a spherical passband

3. CONCLUSION

This paper develops derivation of the impulse responses for a separable and a non-separable 3-D filters. The separable filter naturally has a rectangular passband while the non-separable filter considered here is with spherical passband. Such filters are applicable in 3-D and 4-D computed tomography imaging, as well as in various volumetric subsurface sensing and imaging applications. Further work will report various performance measures of those filters applied to different real-world captured data sets.

4. APPENDIX

A. Ideal lowpass filter with a rectangular passband

The frequency response of such a filter is given by

$$H_r(\omega_1, \omega_2, \omega_3) = I_{\omega_{c_1}}(\omega_1) I_{\omega_{c_2}}(\omega_2) I_{\omega_{c_3}}(\omega_3) \quad (3)$$

in the frequency cube $[-\pi, +\pi]^3$, where the indicator function $I_{\omega_{c_i}}$ is defined as

$$I_{\omega_{c_i}} \triangleq \begin{cases} 1, & |\omega| \leq \omega_{c_i}, \\ 0, & \text{else,} \end{cases} \quad (4)$$

for $l = 1, 2, 3$, and with ω_{c_l} being the filter's cut-off frequency with $|\omega_{c_l}| \leq \pi$. The ideal impulse response of the filter is derived by taking the inverse 3-D Fourier transform of this separable function in the frequency domain:

$$\begin{aligned} h_r &= \frac{1}{(2\pi)^3} \int_{-\pi}^{\pi} \int_{-\pi}^{\pi} \int_{-\pi}^{\pi} 1 e^{j(\omega_1 n_1 + \omega_2 n_2 + \omega_3 n_3)} d\omega_1 d\omega_2 d\omega_3 \\ &= \left[\frac{1}{2\pi} \int_{-\pi}^{\pi} I_{\omega_{c_1}}(\omega_1) e^{j\omega_1 n_1} d\omega_1 \right] \\ &\quad \times \left[\frac{1}{2\pi} \int_{-\pi}^{\pi} I_{\omega_{c_2}}(\omega_2) e^{j\omega_2 n_2} d\omega_2 \right] \\ &\quad \times \left[\frac{1}{2\pi} \int_{-\pi}^{\pi} I_{\omega_{c_3}}(\omega_3) e^{j\omega_3 n_3} d\omega_3 \right] \\ &= \frac{\sin \omega_{c_1} n_1}{\pi n_1} \frac{\sin \omega_{c_2} n_2}{\pi n_2} \frac{\sin \omega_{c_3} n_3}{\pi n_3}, \quad (5) \end{aligned}$$

for $-\infty < n_1, n_2, n_3 < \infty$.

B. Ideal lowpass filter with a spherical passband

The frequency response of such a filter is given by

$$H_s(\omega_1, \omega_2, \omega_3) = \begin{cases} 1, & \sqrt{\omega_1^2 + \omega_2^2 + \omega_3^2} \leq \omega_c, \\ 0, & \text{else,} \end{cases} \quad (6)$$

in the frequency cube $[-\pi, +\pi]^3$. The ideal impulse response of the filter is derived by taking the inverse 3-D Fourier transform of this function in the frequency domain:

$$\begin{aligned} h_s &= \frac{1}{(2\pi)^3} \iiint_{\sqrt{\omega_1^2 + \omega_2^2 + \omega_3^2} \leq \omega_c} 1 e^{j(\omega_1 n_1 + \omega_2 n_2 + \omega_3 n_3)} d\omega_1 d\omega_2 d\omega_3 \\ &= \frac{1}{(2\pi)^3} \int_0^{\omega_c} \int_0^{2\pi} \int_0^{2\pi} e^{jur \begin{pmatrix} \sin \psi \sin \phi \cos \theta \\ + \sin \psi \sin \phi \sin \theta \\ + \cos \psi \end{pmatrix} \cdot \begin{pmatrix} n_1 \\ n_2 \\ n_3 \end{pmatrix}} u^2 \sin \phi du d\theta d\phi \\ &= \frac{1}{(2\pi)^3} \int_0^{\omega_c} \int_0^{2\pi} \int_0^{2\pi} e^{jur \begin{pmatrix} \sin \psi \sin \phi \cos(\theta - \phi) \\ + \sin \psi \sin \phi \sin \theta \\ + \cos \psi \end{pmatrix} \cdot \begin{pmatrix} n_1 \\ n_2 \\ n_3 \end{pmatrix}} u^2 \sin \phi du d\theta d\phi \\ &= \frac{1}{(2\pi)^2} \int_0^{\omega_c} u^2 \int_0^{2\pi} e^{jur \cos \phi} \sin \phi d\phi du \\ &= \frac{1}{4\pi} \int_0^{\omega_c} u^2 j_0(ur) du = \frac{\omega_c j_1(\omega_c \sqrt{n_1^2 + n_2^2 + n_3^2})}{4\pi \sqrt{n_1^2 + n_2^2 + n_3^2}} \quad (7) \end{aligned}$$

where $j_0(\bullet)$ and $j_1(\bullet)$ are the zero-order and the first-order spherical Bessel functions of the first kind [3].

In order to carry out the integration, the following substitutions have been made. First, polar coordinates in frequency are used for $\omega_1 = u \sin \psi \cos \theta$, $\omega_2 = u \sin \psi \sin \theta$ and $\omega_3 = u \cos \psi$. Then, polar coordinates in space are used for $n_1 = r \sin \phi \cos \phi$, $n_2 = r \sin \phi \sin \phi$ and $n_3 = r \cos \phi$.

References

- [1] J. Woods, Multidimensional signal, image and video processing and coding, Elsevier Academic Press, 2006.
- [2] D. Dudgeon, R. Mersereau, Multidimensional digital signal processing, Prentice Hall, 1990.
- [3] M. Abramowitz, I. Stegun, Handbook of mathematical functions with formulas, graphs and mathematical tables, Dover, 1972.

ASYMPTOTIC STATE OF ONE-DIMENSIONAL SOM AT RAYLEIGH POINT DENSITY INPUT

Ivo R. Draganov, Antoaneta A. Popova

Radiocommunications and Videotechnologies Dept.
Technical University - Sofia
8 Kliment Ohridski Blvd., 1000 Sofia, Bulgaria
Tel.: +359 2 965 2274; E-mail.: {idraganov, antoaneta.popova}@tu-sofia.bg

Abstract

In this paper an analysis is presented concerning the asymptotic state of the one-dimensional self-organizing map (SOM) with finite grid in the case of Rayleigh point distribution input. The main goal is to find the diversion of the neurons' location after a certain number of epochs. The SOM distortion measure is analyzed with its value found approximately using Taylor series. The stationary values of the statistical expectations covered by the neurons are found solving a set of non-linear equations. Also the objective function of the SOM is found along with its gradient and using gradient-descent approach the minimum of the distortion measure is calculated. Based on the values obtained useful tips for proper initialization of the SOM in this case are given. The results are considered useful enough in wide variety of practical cases in telemedicine, image processing, optical communications and other areas.

1. INTRODUCTION

It is well known fact that the area allocated for storing the most important feature set inside a self-organizing map (SOM) is proportional to the frequency of occurrence of that very same feature in the observations [1].

So far an investigation of the point density for the linear map is led in the presence of a very large number of codebook vectors over a finite area for linear, linear-quadratic and quadratic distributions [2], [3]. It is revealed that the asymptotic point density is proportional to the probability of a certain feature vector occurring raised to some exponent depending on the number of neighbors including the winning neuron and some scalar factor. Similar research on the change of this power is done in [4] when the neighbor function is Gaussian kernel and its normalized second moment is independent variable. The resulting range for the power value in this case is from 1/3 to 2/3. Similar results are presented in [5].

Some more recent researches concern the asymptotic state of the SOM at normal [6] and distorted normal distributions when the input passes at first through non-linear channel [7] where the power value range is found to be wider.

Here the influence of the Rayleigh point density of the input over the asymptotic state of a finite one-dimensional SOM is investigated with its distortion measure. In part 2 theoretical analysis is presented and in part 3 some experimental results are given. In part 4 a conclusion is made.

2. SOM ANALYSIS WITH RAYLEIGH POINT DENSITY INPUT

Let one-dimensional feature space of x is considered. The number of points must be large enough (e.g. by criteria given in [1]) and they must be stochastic variables so their probability density $p(x)$ could be defined. The codebook vectors m_i usually form regular optimal configuration and thus can not be stochastic. Their number is typically low in any cluster as well.

2.1. Asymptotic State of the One-Dimensional Finite-Grid SOM

Let suppose m_i and m_{i+1} are two neighboring points. A way of defining the point density is as $(m_{i+1} - m_i)^{-1}$ but it does not cover the samples around the boundaries of the clusters for which this density does not have meaning. So a better way of defining it is as the inverse of the width of the Voronoi set $[(m_{i+1} - m_i)/2]^{-1}$. The input consists of samples $x(t) \in \mathfrak{R}, t = 0, 1, 2, \dots$ while the codebook is $m_i(t) \in \mathfrak{R}, t = 0, 1, 2, \dots, i = 1, \dots, k$. The one-dimensional SOM algorithm with at least one neighbor at each side is given by [1]:

$$\begin{aligned} m_i(t+1) &= m_i(t) + \varepsilon(t)[x(t) - m_i(t)], \text{ for } i \in N_c \\ m_i(t+1) &= m_i(t) \text{ for } i \notin N_c \\ c &= \arg \min_i \{ |x(t) - m_i(t)| \} \\ N_c &= \{ \max(L, c-1), c, \min(k, c+1) \} \end{aligned} \quad (1)$$

where N_c is the neighbor set around node c and $\varepsilon(l)$ is the learning-rate factor. The Voronoi set V_i around m_i is defined as:

$$V_i = \left[\frac{m_{i-1} + m_i}{2}, \frac{m_i + m_{i+1}}{2} \right], V_1 = \left[0, \frac{m_1 + m_2}{2} \right],$$

$$V_k = \left[\frac{m_{k-1} + m_k}{2}, 1 \right], \text{ for } 1 < i < k, \quad (2)$$

$$U_i = V_{i-1} \cup V_i \cup V_{i+1}, U_1 = V_1 \cup V_2,$$

$$U_k = V_{k-1} \cup V_k, \text{ for } 1 < i < k$$

In this case U_i is the set of such $x(t)$ which provoke changes in $m_i(t)$ during one learning step. Following (1) and (2) we get to the well known stationary equilibrium for m_i coinciding for the general case [1]:

$$m_i = E\{x \mid x \in U_i\}, \forall i \quad (3)$$

In other words every m_i becomes centroid of the probability mass for each U_i and then for $2 < i < (k-1)$ the limits for U_i are:

$$A_i = \frac{1}{2}(m_{i-2} + m_{i-1}),$$

$$B_i = \frac{1}{2}(m_{i+1} + m_{i+2}) \quad (4)$$

For $i=1$ and $i=2$, $A_i = 0$, and for $i=k-1$ and $i=k$, $B_i = 1$.

The case investigated here concerns input data with the following distribution:

$$p(x) = \frac{x}{\sigma^2} e^{-x^2/2\sigma^2}. \quad (5)$$

As (5) is too complex to be used in finding the centroids of the probability masses, Taylor series are used instead:

$$p(x) = \sum_{i=0}^{\infty} \frac{p^{(i)}(0)}{i!} x^i. \quad (6)$$

We find the absolute difference between the third and second order approximations:

$$\Delta p_{32}(x) = \sum_{i=0}^3 \frac{p^{(i)}(0)}{i!} x^i - \sum_{i=0}^2 \frac{p^{(i)}(0)}{i!} x^i =$$

$$= \frac{x^3 p^{(3)}(0)}{6} \quad (7)$$

Since:

$$p'(x) = \frac{e^{-x^2/2\sigma^2}}{\sigma^2} \left(1 - \frac{x^2}{\sigma^2} \right),$$

$$p''(x) = -\frac{x e^{-x^2/2\sigma^2}}{\sigma^4} \left(3 + \frac{x^2}{\sigma^2} \right), \quad (8)$$

$$p'''(x) = \frac{e^{-x^2/2\sigma^2}}{\sigma^4} \left(\frac{x^4}{\sigma^4} - 3 \right)$$

then $p(0) = 0$, $p'(0) = 1/\sigma^2$, $p''(0) = 0$, $p'''(0) = -3/\sigma^4$, and $\Delta p_{32}(x) = -x^3/2\sigma^4$.

Now for 5 typical cases of σ the error Δp_{32} is found and the results are presented in Fig. 1. It is visible that only for $\sigma = 0.5$ the error between the second and third approximation exceeds considerably 1 by module and this in such a wide range for x from 0 to 10. So it is reasonable to use approximation for the original distribution of second order that is $p(x) \approx x/\sigma^2$.

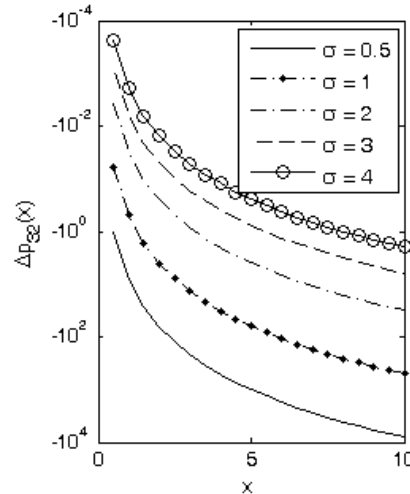


Fig. 1. The absolute error between approximations of second and third order

The stationary values of the m_i are defined by:

$$m_i = E\{x \mid x \in U_i\} = \frac{\int_{A_i}^{B_i} xp(x)dx}{\int_{A_i}^{B_i} p(x)dx} =$$

$$= \frac{2(B_i^3 - A_i^3)}{3(B_i^2 - A_i^2)}, \forall i \quad (9)$$

But they could be expressed in even simpler way - it consists of defining the point density q_i around m_i as the inverse of the length of the Voronoi set - $q_i = [(m_{i+1} - m_{i-1})/2]^{-1}$. As a result of that q_i can be expressed in the form $const.[p(m_i)]^\alpha$. Then passing from m_i to m_j it is true:

$$\alpha = \frac{\log(m_{i+1} - m_{i-1}) - \log(m_{j+1} - m_{j-1})}{\log[p(m_j)] - \log[p(m_i)]}. \quad (10)$$

For improved accuracy more values of the m_i are needed as we shall see in the next section.

2.2. Finding the One-Dimensional SOM Distortion Measure with Finite Grids

The objective function of the SOM is given by [1]:

$$E = \sum_i \sum_j \int_{x \in V_i} h_{ij} \|x - m_j\|^2 p(x) dx, \quad (11)$$

where V_i is the Voronoi set around m_i and h_{ij} is defined as:

$$h_{ij} = \begin{cases} 1, & \text{if } |i - j| < 2 \\ 0, & \text{otherwise} \end{cases} \quad (12)$$

and i and j run over all the values defining h_{ij} .

Then (11) becomes:

$$\begin{aligned} E &= \sum_i \sum_j \int_{C_i}^{D_i} (x - m_j)^2 p(x) dx = \\ &= \sum_i \sum_j \frac{1}{\sigma^2} \left[\frac{(D_i^4 - C_i^4)}{4} - \right. \\ &\quad \left. - \frac{2m_j(D_i^3 - C_i^3)}{3} + \frac{m_j^2(D_i^2 - C_i^2)}{2} \right] \end{aligned} \quad (13)$$

where N_i is defined in (1) and the borders C_i and D_i of the Voronoi set V_i are:

$$\begin{aligned} C_1 &= 0, \\ C_i &= \frac{m_{i-1} + m_i}{2} \quad \text{for } 2 \leq i \leq k, \\ D_i &= \frac{m_i + m_{i+1}}{2} \quad \text{for } 1 \leq i \leq k-1, \\ D_k &= 1. \end{aligned} \quad (14)$$

3. EXPERIMENTAL RESULTS

As a simulation environment we use Matlab® R2009B over MS® Windows® XP® Pro SP3.

First α from (10) is found for different number of grid points. The more m_i are used the more accurate are the results. For $i = 4$ and $j = k - 3$ assuring negligible border effects 10, 25, 50, and 100 grid

points are used. The same experiment is done with normally distributed input points in [6], so here a direct comparison can be made. The results are given in Table 1.

Table 1. Experimentally estimated α for two different distributions of the input

Grid points	Exponent α	
	Normal, [6]	Rayleigh
10	0.2989	0.3480
25	0.3330	0.3495
50	0.3331	0.3501
100	0.3330	0.3509

It is clearly seen that the exponent approximation is presented here by higher α which is actually expected because of the steeper left slope of the Rayleigh curve in comparison to the symmetric Gaussian one.

Obviously the values obtained for the Rayleigh distribution almost do not depend on the number of grids. Now when we have the real case m_i found it is seen that the exponent of the approximated state of the SOM is close to 1/3. This is actually a case strongly related with the optimal vector quantization [1].

Graphically the results from Table 1 are given in Fig. 2.

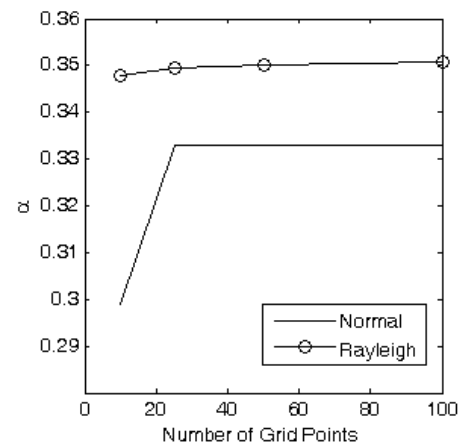


Fig. 2. Experimentally derived α as a function of the number of grid points for two different distributions of the input for the SOM

4. CONCLUSION

In this paper an approach for finding the stationary positions of the nodes of one-dimensional SOM has been presented in the case of Rayleigh density point input. The results are precise enough taking

the advantage of very fast computation. Furthermore the distortion measure of the SOM using finite grid is calculated in the general case and it is shown that the positions of the nodes could be optimized at the stage of initialization.

The results achieved prove the correctness of the suggested approach which is considered useful in a large number of practical cases where the input data poses Rayleigh point density distribution.

5. ACKNOWLEDGMENT

This work is supported by Research and Development Sector (R&DS) with TU-Sofia under Grant № 102pd177-7 "Creation of models and object segmentation, applied to medicine and education".

References

- [1] T. Kohonen, *Self-Organizing Maps*, 3 ed., Springer, New York, 2001.
- [2] H. Ritter and K. Schulten, "On the Stationary State of Kohonen's Self-Organizing Sensory Mapping", *Biological Cybernetics*, Vol. 54, Issue 2, June 1986, pp. 99-106.
- [3] H. Ritter, "Asymptotic Level Density for a Class of Vector Quantization Processes", *IEEE Transactions on Neural Networks*, No. 2, 1991, pp. 173-175.
- [4] D. Dersch and P. Tavan, "Asymptotic Level Density in Topological Feature Maps", *IEEE Transactions on Neural Networks*, Vol. 6, No. 1, 1995, pp. 230-236.
- [5] S. Luttrell, "Code Vector Density in Topographic Mappings: Scalar Case", *IEEE Transactions on Neural Networks*, Vol. 2, No.4, 1991, pp. 427-436.
- [6] Draganov, "Normal Point Density Input Influence over a Finite One-Dimensional SOM", *Proc. of ICEST'2010*, Ohrid, Macedonia, June 23-26, 2010, pp. SP.II.17-20.
- [7] Draganov, A. Popova, and N. Neshov, "Asymptotic State of One-Dimensional SOM at Normal Point Density Input Passed Through Non-Linear Channel", *Proc. 14th WSEAS Conf. on Computers*, Vol. 2, Corfu Island, Greece, July 23-25, 2010, pp. 761-765.

DISSIMILARITY-BASED METRIC FOR MEDICAL DATA CLASSIFICATION

Agata Manolova

Technical University
8 ave Kliment Ohridski, Sofia 1000, Bulgaria
amanolova@tu-sofia.bg

Abstract

Data mining techniques have been applied to medical services in several areas, including prediction of effectiveness of surgical procedures, medical tests, medication, and the discovery of relationships among clinical and diagnosis data. In our study we use a dissimilarity-based metric for the classification of different types of medical data for diagnostics such as breast cancer, heart disease, diabetes etc.

Dissimilarity-based pattern recognition offers new possibilities for building classifiers on a distance representation such as kernel methods or the k nearest neighbors (kNN) rule. The goal of this work is to expand the advantageous and rapid adaptive approach to learn only from dissimilarity representations by using the effectiveness of the Support Vector Machines algorithm for real-world classification tasks for medical data. This method can be an alternative approach to the well known methods based on dissimilarity representations and can be as effective as them in terms of accuracy for classification. Practical examples on real medical data show interesting behavior compared to other dissimilarity-based methods.

1. INTRODUCTION

Pattern recognition techniques play a critical role when applied to medical databases by fully automating the process of abnormality detection and thus supporting the development of computer-aided diagnosis (CAD) systems. Often this involves identifying structures such as tumors or lesions, but it can also include monitoring present structures such as the size of the heart in chest X-rays. In most cases, CAD systems are designed to be used for screening purposes, in which large numbers of medical data needs to be examined. They are adopted as an alternative "second opinion" that can assist for example a radiologist in detecting lesions and in making diagnostic decisions. The computerized schemes combine detection and classification of malignancies. The importance of these CAD systems in almost all telemedicine applications is evident and is expected to increase dramatically over the coming years [1], [2].

The goal of this work is to test the advantageous and rapid adaptive approach to learn only from dissimilarity representations by using the effectiveness of the Support Vector Machines algorithm developed by Manolova and Guerin [3] for real-world classification tasks for medical data of different types. This method can be an alternative approach to the known methods based on dissimilarity representations such as Pekalska's dissimilarity classifier [4], Haasdonk's kernel-based SVM classifier [3] and to classic kNN classifier.

The paper is organized as follows: in Section 2 we introduce the motivation of the approach, in Section 3 we describe the theoretical basis of this approach; in Section 4 we provide experimental results on real-life medical data sets. Finally, Section 5 concludes the paper.

2. MOTIVATION OF THE APPROACH

The motivation for the development of a dissimilarity-based classifier is the following: if we assume that "similar" objects can be grouped together to form a class, a "class" is nothing more than a set of these "similar" objects. Based on this idea, it is possible that the notion of proximity (similarity or dissimilarity) is actually more fundamental than that of a feature. Thus, the dissimilarity-based classifiers are a way of defining classifiers between the classes, which are not based on the feature measurements of the individual patterns, but rather on a suitable dissimilarity measure between them. The advantage of this methodology is that since it does not operate on the class-conditional distributions, the accuracy can exceed theoretically the Bayes' error bound. Another salient advantage of such a paradigm is that it does not have to confront the problems associated with feature spaces such as the "curse of dimensionality", and the issue of estimating a large number of parameters.

The distance representation is most commonly used as dissimilarity because is usually the simplest measure. A dissimilarity value expresses a magni-

tude of difference between two objects and becomes zero only when they are identical.

This paper focuses on the incorporation of SVM in to the dissimilarity-based classifier "Shape Coefficient" described in [5], [6]. The Shape Coefficient (Cs) is defined from simple statistics (mean and variance) on the dissimilarity data. The proposed decision rules are based on this Shape Coefficient description and on optimal separating hyper plane with Support Vector Classifier (SVC), using the Cs coefficient as dissimilarity on the input space. This provides a decision rule with a limited number of parameters per class.

3. DESCRIPTION OF THE "SHAPE COEFFICIENT"

Let us consider a two-class classification problem where ω_1 is the first class and ω_2 the second class. Let N be a set of objects o_i to be classified, D is the dissimilarity ($N \times N$) table between each object such as: $D = [d(o_i, o_j) : 1 \leq i, j \leq N]$. Following [5] and [6], the Shape Coefficient describes the proximity of an object to a given class (for example for ω_1 , eq. 1):

$$Cs(o_i, \omega_1) = \frac{\overline{[d^2(o_i, \omega_1) - I(\omega_1)]^2}}{[\text{var}(d^2(o_i, \omega_1))]^{\delta_1}} \quad (1)$$

where $\overline{d(o_i, \omega_1)^2}$ is the empirical average of the dissimilarity between object o_i and all the observations in class ω_1 , $\text{var}(d(o_i, \omega_1))$ is the empirical variance, and $I(\omega_1)$ is the class inertia computed as the empirical mean of all the squared dissimilarities between objects in class ω_1 . The numerator deals with the "position" of the observation o_i relatively the class center. The denominator interpretation is more complex, taking into account the "structure" (orientation, shape, intrinsic dimension...) of the observations distribution in the class. Then the parameters γ_1 and δ_1 are learning parameters to best fit this data structure. The equation for $Cs(o_i, \omega_2)$ with the class ω_2 is equivalent to (1) and has two fitting parameters γ_2 and δ_2 . The decision rule for a two-class classification problem for an object o_i is given then by the following equation:

$$Cs(o_i, \omega_1) \underset{2}{\overset{1}{<}} Cs(o_i, \omega_2) \quad (2)$$

3.1. Decision rule using SVC optimization

The quantities $Cs(o_i, \omega_1)$ and $Cs(o_i, \omega_2)$ being positive, we can transform (2) using the logarithmic function as follows:

$$\begin{aligned} & \log\left(\frac{\gamma_1}{\gamma_2}\right) + 2 \log(\overline{d^2(o_i, \omega_1) - I(\omega_1)}) - \\ & - 2 \log(\overline{d^2(o_i, \omega_2) - I(\omega_2)}) - \\ & - \delta_1 \log(\text{var}(d^2(o_i, \omega_1))) + \\ & + \delta_2 \log(\text{var}(d^2(o_i, \omega_2))) \underset{2}{\overset{1}{<}} 0 \end{aligned} \quad (3)$$

This is in fact, a linear decision rule in a 4-dimensional input space. Following (3), we can represent each object o_i using a vector x_i with 4 features, $x_i = [x_{i1} \ x_{i2} \ x_{i3} \ x_{i4}]^T$:

$$\begin{aligned} x_{i1} &= 2 \log(\overline{d^2(o_i, \omega_1) - I(\omega_1)}) \\ x_{i2} &= -2 \log(\overline{d^2(o_i, \omega_2) - I(\omega_2)}) \\ x_{i3} &= -\log(\text{var}(d^2(o_i, \omega_1))) \\ x_{i4} &= \log(\text{var}(d^2(o_i, \omega_2))) \end{aligned} \quad (4)$$

So now, the decision rule (3) becomes:

$$\beta^T x_i + \beta_0 \underset{2}{\overset{1}{<}} 0 \quad (5)$$

with $\beta = [1 \ 1 \ \delta_1 \ \delta_2]^T$ be the normal to the optimal separating hyper plane and $\beta_0 = \log\left(\frac{\gamma_1}{\gamma_2}\right)$ be the bias from the hyper plane to the origin. Labeling the objects with the auxiliary variables per class, such as $y_i = -1$ for $o_i \in \omega_1$ and $y_i = 1$ for $o_i \in \omega_2$, we have the following classical linear decision rule:

$$y_i = \text{sign}(\beta^T x_i + \beta_0) \quad (6)$$

This is the standard decision rule for SVC. Here, the difference is the vector β normal to the optimal hyper plane: it is constraint to have the same two first components: $\beta_1 = \beta_2$. Thus finding the optimal hyper plane when the 2 classes are inseparable consists of this optimization problem solved by using the Lagrange multipliers [BUR98]:

$$\begin{aligned} \min_{\beta, \beta_0} \quad & \frac{1}{2} \|\beta\|^2 + C \sum_{i=1}^N \zeta_i \\ \text{subject to} \quad & y_i (\beta^T x_i + \beta_0) \geq 1 - \zeta_i, \quad (7) \\ & \zeta_i \geq 0, i = 0, \dots, N \end{aligned}$$

where ζ_i are the slack variables, associated with all the objects. If the object o_i is classified in the wrong class then $\zeta_i > 1$. The parameter C corresponds to the penalty for errors and it is chosen by the user. In order to introduce the constraints on the β vector, we consider the observations x_i into two orthogonal subspaces such as:

$x_i = [x_{i1} \ x_{i2}]^T$, $x_i' = [x_{i1} \ x_{i2}]^T$, $x_i'' = [x_{i3} \ x_{i4}]^T$ and also:

$$\begin{aligned} \beta &= [\beta' \ \beta'']^T, \\ \beta' &= \|\beta'\| \cdot [1 \ 1]^T / \sqrt{2}, \quad (8) \\ \beta'' &= [\beta_3 \ \beta_4]^T \end{aligned}$$

The optimization problem is then transformed such as:

$$\begin{aligned} \min_{\|\beta'\|, \beta_3, \beta_4} \quad & \frac{1}{2} \|\beta'\|^2 + \frac{1}{2} \|\beta''\|^2 + C \sum_{i=1}^N \zeta_i \\ \text{subject to} \quad & y_i (\|\beta'\| u_i' + \beta''^T \cdot x_i'' + \beta_0) \geq 1 - \zeta_i, \quad (9) \\ & \zeta_i \geq 0, i = 0, \dots, N \end{aligned}$$

with u_i' the scalar product such as:

$$u_i' = \langle [1 \ 1]^T, x_i' \rangle / \sqrt{2} \quad (10)$$

4. EXPERIMENTAL RESULTS

All the experiments are done using SVM^{Light}, an implementation of Support Vector Machines in C by Thorsten Joachims (<http://svmlight.joachims.org>) and Matlab. We have made source modifications in order to implement the supplementary constraints on the β vector.

The medical datasets come from the UCI Machine Learning Repository (<http://archive.ics.uci.edu/ml/>). The information of the medical dataset used in our experiments is gathered in Table 1.

The information is collected from real world patients or microbiological laboratories and consists of mixed types of data: continuous, dichotomous and categorical variables (ex. age, sex, chest pain type, blood sugar, heart condition, proteins, blood pres-

sure etc.). There are also datasets with missing values (ex. the Heart dataset). For the multi class SVC optimization procedure we use “one versus all” method.

Table 1. Medical Datasets used in the experiments

Data	Class	Class sizes	Dissimilarity
Heart	2	139/164	Gower's distance
Proteins	5	72/72/ 39/30/13	Evolutionary Distance
Cat Cortex	4	18/10/ 18/19	Determined by Expert

Table 2 summarizes the results for the average classification error for these datasets with the classifier “Shape Coefficient” and the classifiers 1-NN (Nearest Neighbor), K-NN (K Nearest Neighbors), the SVM with 3 different kernels (linear, polynomial and Gaussian) from [3] and [4].

Table 2. Average classification error [in %] for the medical datasets in LOO

Data	Heart	Proteins	Cat Cortex
1-NN	26.8	1.66	5
K-NN	22.6	1.66	3.84
Cs	22.6	1.11	3.46
SVM	21.5	0.89	3.09

5. CONCLUSION

We have proposed a new way of optimizing the parameters of the proximity index “Shape Coefficient”. It used the SVM decision rules which allow us to find the optimal solution for our classification problem. With only two parameters per class, the model for class description is compact and parsimonious. The model is flexible, effective and fast in different classification tasks as already proven in [5] and [6]. The result of the comparison with the K-NN and 1-NN shows better results for the classification error. The Cs with SVC optimization procedure is a global method with adjustable parameters according to the properties of the class so it performs better than the K-NN rule in case of (1-NN or 3-NN). The good performance the SVM with linear kernel on proteins and cat-cortex data is a hint on the linear separability of these two datasets. The result is confirmed by the Cs classifier. Indeed, the polynomial and Gaussian kernel improve the results of the linear kernel for most datasets. The Gaussian ker-

nel even slightly outperforms the polynomial in most cases so in Table 2 only the best results are shown.

The results with the real-world medical datasets encourage us to propose this metric as a good alternative to other dissimilarity-based classifiers for this kind of tasks – assisting the medical personnel to take decisions about the condition of a patient for example. Because the metric uses only 2 parameters per class and a linear kernel, data classification is very fast (0.07 seconds in SVM^{Light} for 200 points).

6. ACKNOWLEDGEMENTS

This work was financed by a project grant of the National Fund for Scientific Research of the Bulgarian Ministry of Education and Science by the contract VU-I-305.

References

- [1] Anke Meyer-Base, *Pattern Recognition for Medical Imaging*, Elsevier Academic Press, 2004.
- [2] G. Dougherty, *Digital Image Processing for Medical Applications*, Cambridge University Press, 2009.
- [3] B. Haasdonk, C. Balhmann, "Learning with Distance Substitution Kernels", *Pattern Recognition -Proc. of the 26th DAGM Symposium*, Tubingen, Germany, August/September 2004.
- [4] R.P.W. Duin, E. Pekalska, *Object representation, sample size and dataset complexity*, Springer-Verlag, pp. 25-58, 2006.
- [5] Manolova, A. Guerin-Dugue, *Classification of dissimilarity data with a new flexible Mahalanobis-like metric*. *Pattern Anal. Appl.* 11(3-4): 337-351 (2008), Springer Link.
- [6] Manolova, A. Guerin-Gugue, "Dissimilarity-based metric for data classification using Support Vector Classifiers", RSFC, Grenoble, France, 2009, pp. 37-41.

PRACTICAL ADAPTIVE FILTERING ON FPGA

Spirov R. P.

Technical University- Varna
1, Studentska str., 9010 Varna, Bulgaria
Tel: +359 52383618; E-mail: rosexel@abv.bg

Abstract

In this paper the author is presented the hardware application of the adaptive Kalman filter algorithm for pattern recognition with the FPGA. The adaptive temporal filter is proposed that lend itself to hardware implementation for real-time temporal processing of image sequences. Adaptation in this case is with respect to motion in the image sequence as well as variation of noise statistics. The project is used the Altera DE2 board to implement a simple hardware design. For describing its behavior use the VHDL language and the Altera's Quartus tools to synthesize and Altera DE2 board to implement a simple hardware FPGA design

1. INTRODUCTION

In this paper is presented basic hardware architecture, using extended Kalman filter-based method for calculating a trajectory by tracking features at an unknown location on Earth's surface, provided the topography is known, is given in [1]. The proposed model is implemented using VHDL and simulated and synthesized into an FPGA. The hardware design was implemented on an Altera Quartus II board. The practical method for using FPGA to realize VHDL implementation of the developed algorithm using Altera De2 FPGA. The board is shown in fig. 1.

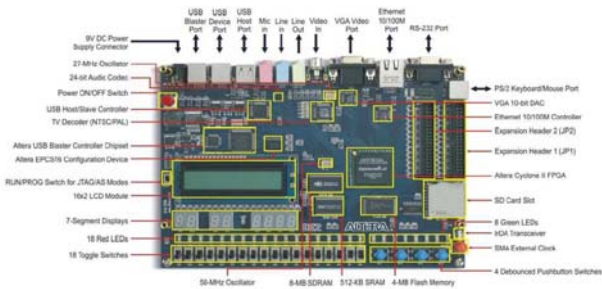


Fig. 1. The Altera DE2 board

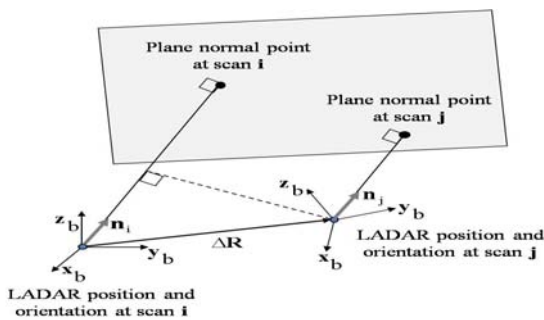


Fig. 2. Navigation-changes in perceived location of the normal point between scan I and scan j are applied to estimate position changes

In Fig. 2 ΔR is the delta position vector (displacement vector between scans i , at time t_i , and scan j , at time t_j , in this case); n_i is the plane normal vector whose components are resolved in the Ladar body frame at scan epoch t_i ; n_j is the plane normal vector whose components are. Note that in the navigation frame, the planar surface normal vectors at epoch's t_i and t_j are equal since resolved in the Ladar body frame at scan epoch t_j ; and, ρ_i and ρ_j are the shortest distances from the Ladar to the plane at epochs t_i and t_j , respectively. stationary planar surfaces are assumed. However, expressed in the Ladar body frame both normal vectors are likely to be unequal due to the body frame rotation between epoch's t_i and t_j . From the geometry presented in Fig.1, a relationship can be derived between the projection of the displacement vector (between epoch's t_i and t_j) onto the planar surface normal vector and the change in the normal point range between scans i and j is shown in Eq.1:

$$\Delta \mathbf{R} \cdot \mathbf{n}_i = \rho_i - \rho_j \quad (1)$$

Given M associated planar surfaces, a set of linear equations like (7) can be set up in matrix form is given in Eq.2:

$$\mathbf{H} \cdot \Delta \mathbf{R} = \Delta \rho \quad (2)$$

Were:

$$\mathbf{H} = \begin{bmatrix} \mathbf{n}_{i,1}^T \\ \mathbf{M} \\ \mathbf{n}_{i,M}^T \end{bmatrix}, \quad \Delta \mathbf{r} = \begin{bmatrix} \rho_{i,1} - \rho_{j,1} \\ \mathbf{M} \\ \rho_{i,M} - \rho_{j,M} \end{bmatrix} \quad (3)$$

Note that a minimum of three non-collinear planar surfaces is required for the observation matrix, \mathbf{H} , to be non-singular and thus allowing for a unique solution of Eq.2. The estimation process is based on a complementary Kalman filter methodology [2] which employs differences between INS and laser scanner observables as filter measurements. Changes in planar surface ranges between consecutive scans are used as laser observables. Correspondingly, laser scanner observables of the Kalman filter are formulated as follows for the scan at time epoch t_m in Eq.4:

$$\Delta \mathbf{p}_{LS}(t_m) = \begin{bmatrix} \rho_1(t_{m-1}) - \rho_1(t_m) \\ \dots \\ \rho_N(t_{m-1}) - \rho_N(t_m) \end{bmatrix} \quad (4)$$

where N is the number of features for which a match is found time epoch t_m and t_{m-1} . Equivalent observables can be synthesized from INS measurements by transformation of the INS displacement vector into the range domain as follows in Eq.5 and Eq.6:

$$\Delta \mathbf{p}_{INS}(t_m) = \mathbf{H}(t_{m-1})(\Delta \mathbf{R}_{INS}(t_m) + \Delta \mathbf{C}_b^n(t_m) \mathbf{l}_b) \quad (5)$$

$$\Delta \mathbf{C}_b^n(t_m) = \mathbf{C}_b^n(t_m) - \mathbf{C}_b^n(t_{m-1}) \quad (6)$$

The differences between inertial and laser scanner observables Eq.7:

$$\mathbf{y}_{Kalman}(t_m) = \Delta \mathbf{p}_{INS}(t_m) - \Delta \mathbf{p}_{LS}(t_m) \quad (7)$$

Particular filter states include: errors in position changes between consecutive scans, velocity errors, attitude errors, gyro biases, and accelerometer biases in Eq.8:

$$\delta \mathbf{x} = [\delta \Delta \mathbf{R}_n^T \quad \delta \mathbf{v}_n^T \quad \boldsymbol{\psi}^T \quad \mathbf{a}_b^T \quad \mathbf{b}_b^T]^T \quad (8)$$

For this state vector, the observation matrix \mathbf{H}_{Kalman} can be derived directly by augmenting the geometry matrix of Eq.3 with zero elements is shown in Eq.9:

$$\mathbf{H}_{Kalman}(t_m) = \begin{bmatrix} \mathbf{n}_1^T(t_{m-1}) & 0 & \mathbf{L} & 0 \\ \mathbf{M} & \mathbf{M} & \mathbf{O} & \mathbf{M} \\ \mathbf{n}_M^T(t_{m-1}) & 0 & \mathbf{L} & 0 \end{bmatrix} \quad (9)$$

The measurement noise matrix \mathbf{R}_{Kalman} is derived from the line and planar surface estimation processes performing a comprehensive covariance analysis of the feature extraction method. Derivation of the filter state transition matrix and the system noise matrix for the filter states chosen employs a standard Kalman filter formulation. Errors in the position estimate are thus transformed into errors in line parameters and add up to line extraction errors. As a result, the current position error contributes to the position error for the next scan where the new line is used for navigation.

2. ADAPTIVE FILTERING

The Adaptive filters are based on dynamically adjusting the parameters of the supposedly optimum filter based on the estimates of the unknown parameters. Adaptive Kalman filter can be based on an on-line estimation of motion as well as the signal and noise statistics available data. Let $x(k)$ represent a pixel grayscale on frame k . The ideal noise-free pixel value is represented by $s(k)$ which is assumed to be a first-order AR model. This is a more realistic and simple model that is usually used to represent the temporal behavior of pixels in video signals[3]. Under this assumption, the process and measurement equations:

1. The process model is $s(k+1) = as(k) + w(k)$, in which a is a constant that depends on the signal statistics and $w(k)$ is the process noise (assumed to be a white independent zero mean Gaussian random process with variance of σ_w^2).

2. The measurement signal is $x(k) = s(k) + v(k)$ in which $v(k)$ is the independent additive zero mean Gaussian white noise with variance of σ_v^2 .

The noise and signal are stationary random processes that are fully determined by their second-order statistics. The recursive Kalman filter is developed based on the following definitions:

1. The filter output is $y(k)$ which is the estimate of the signal, at time k .

2. The estimation error is defined by:

$\sigma^2(k) = E\{[y(k) - s(k)]^2\}$, which is initially unknown.

3. Kalman filter gain is presented by $K(k)$.

The overall Kalman filter algorithm is then given as follows:

Algorithm A

```

Let  $y(-1)=0$ , and  $\sigma^2(-1)=\sigma_v^2$ , and start by
setting  $k=0$ 
LOOP: for  $k$  do the following operations:

$$K(k) = \frac{\alpha^2 \sigma^2(k-1) + \sigma_w^2}{\alpha^2 \sigma^2(k-1) + \sigma_w^2 + \sigma_v^2}$$


$$y(k) = K(k) \cdot x(k) + \alpha \cdot [1 - K(k)] \cdot y(k-1)$$


$$\sigma^2(k) = \alpha^2 [1 - K(k)] \cdot \sigma^2(k-1) + \sigma_w^2$$

Increment  $k$ ,  $k=(k+1)$ , and go back to
LOOP
END
    
```

In this algorithm, there are several parameters, which are unknown in practice. These parameters are σ_v^2 , σ_w^2 and α . Based on the aforementioned assumptions, the following instantaneous estimates can be used to achieve fast and simple implementation:

1. Parameter α , defined by

$E\{x(k)x(k-1)\} - E\{x^2(k)\}$, can be estimated by using $\hat{\alpha} = x(k)x(k-1) - (x^2(k) + x^2(k-1))$. For stability reasons it is suggested to use some a priori information about the signal and keep this parameter constant.

2. Simple estimates of:

$\sigma_v^2 = E\{[x(k) - \hat{\alpha}y(k-1)]^2\}$ well as

$\sigma_w^2 = E\{[y(k) - \hat{\alpha}y(k-1)]^2\}$, are calculated, in turn by

$\hat{\sigma}_v^2 = [x(k) - \hat{\alpha}y(k-1)]^2$ and

$\hat{\sigma}_w^2 = [y(k) - \hat{\alpha}y(k-1)]^2 = K^2 \hat{\sigma}_v^2$

Assuming there is a motion, estimates of the noise and process variances, $\hat{\sigma}_v^2$ and $\hat{\sigma}_w^2$, increase which results in less filtering of the signal. This will reduce the noise filtering so that it can better follow the motion with minimal lagging effect. Selection of the threshold Γ is very important. In this case, it can be shown that γ^2 has χ^2 distribution with one degree of freedom [4]. Kalman filter by simulating a sudden change in the signal to represent motion [5]. In this case the SNR is set to 20dB, highest level, namely 99,9% ($\Gamma = 3.29$). One approach to motion estimation is to compare two consecutive temporal samples and use their magnitude difference to infer existence or non existence of motion. When there is a sudden change in the signal, the difference between $\alpha y(k-1)$ and $x(k)$, with a given confidence level, goes beyond its statistical variation. Assuming that σ_v^2 represents the vari-

ance of the aforementioned differences, then based on Gaussian noise [4] distribution, it can be said that a motion is present if $\gamma = \{[x(k) - \alpha y(k-1)]/\sigma_v\} < \Gamma$. If the test is positive, then the gain calculation in the Kalman filter can be reinitiated by assuming $\sigma^2(k) = \sigma_v^2$. The new gain value significantly reduces the lagging effect while improves the noise filtering. Or set both $\sigma^2(k)$ and σ_w^2 equal to σ_v^2 and initiate the Kalman gain to $K(k) = (\alpha^2+1)/(\alpha^2+2)$ right after the motion. The overall algorithm is Algorithm B.

Algorithm B

```

Let  $y(-1)=0$ ,  $\sigma_w^2 = \sigma_v^2$ , and  $\sigma^2 = \sigma_v^2$ , and start the
loop by setting  $k=0$ 
LOOP: for  $k$  do the following operations:

$$K = \frac{\sigma^2 + \sigma_w^2}{\sigma^2 + \sigma_w^2 + \sigma_v^2}$$


$$y(k) = K \cdot x(k) + (1 - K) \cdot y(k-1)$$
; or

$$y(k) = y(k-1) + K [x(k) - y(k-1)]$$
;
if  $D = \frac{|x(k) - y(k-1)|}{\sigma_v} < \Gamma$ ,

$$\sigma_w^2 = \sigma_v^2$$
;

$$\sigma^2 = \sigma_v^2$$
;
else

$$\sigma_w^2 = K \sigma_v^2$$
;

$$\sigma^2 = (1 - K) \cdot \sigma^2 + \sigma_w^2$$
;
end-if
Increment  $k$ ,  $k=(k+1)$ , and go back to LOOP
END
    
```

3. FPGA IMPLEMENTATION

Memory components are used for frame and parameter buffers while the FPGA is used for pixel and parameter calculations. The system architecture shown in Fig.3 illustrates 3 input buffers holding $y(k-1)$, and σ^2, σ_w^2 and a Altera implementation to calculate updated values for these buffers in addition to generating the output $y(k)$.

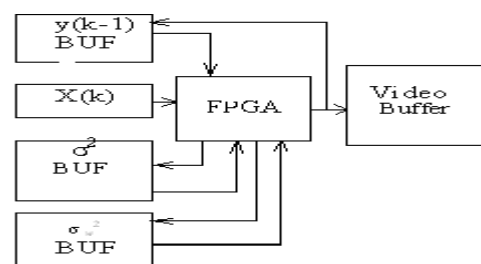


Fig. 3. Levels of implementation for Kalman filtering

The system can easily operate at 66 MHz clock enabling 1024 X 1024 60 Frames operation. System clock rates of 80 MHz and 100 MHz can also be achieved for more aggressive system bandwidth requirements. The pixel calculation data path for $y(k)$ is straight forward once the K parameter is calculated. The parallel pipelined structure used for the sample processing algorithm involves pre-subtractions, two input variable multiplier and post-addition as shown in Fig.4.

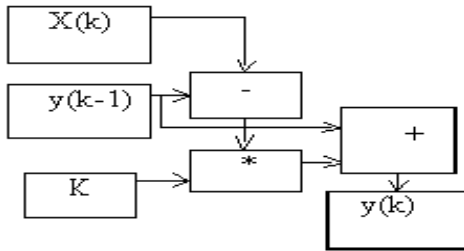


Fig. 4. Pixel Calculation

After the initial latency a sample $y(k)$ is output every system clock. Hardware resources to perform this data path operation are approximately 458 Logic Cells. The parameter calculation is more involved and also requires a parallel pipelined structure for sample processing since each pixel in the frame also has parameters σ^2 and σu^2 .

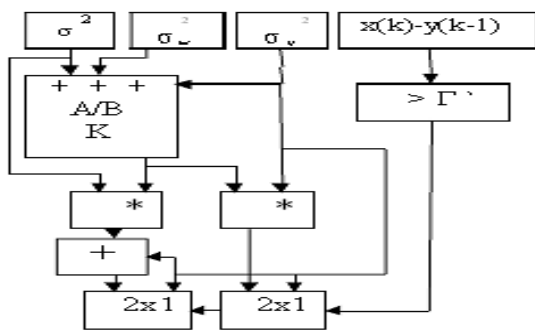


Fig. 5. Implementation for filtering

The algorithm requires pre-addition and division for the K parameter calculation. To perform the comparison for the in quality it can requires pre-addition and division for the K parameter calculation. To perform the comparison for the in quality it can normalize for σ , define D' and Γ' . Using second compliment function on $x(k) - y(k - 1)$ from the pixel calculation, we derive the necessary signal for the 2×1 mux parameter selection. The calculation of new parameters involves an adder, subtract-

er, variable multiplier and loadable constant coefficient multiplier as shown in Fig. 6.

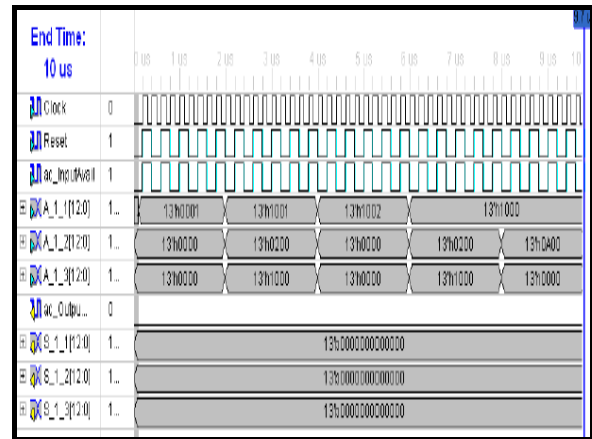


Fig. 6. Behavioral simulation of the Kalman Filter

After initial latency a new updated parameter is given every system clock. The pixel and parameter calculation blocks are latency synchronized such that K and $x(k) - y(k - 1)$ are property aligned.

The output and parameters are aligner such that one memory controller can handle reads and writes to input buffers. Hardware resources for the parameter calculation is approximately 1664 Logic Cells.

Table 1. Synthesis Results

No.	Information	Count	% use
1	No of slice	2145 of 32640	7%
2	Slice LUTs	3626 of 32640	14%
3	Slice LUTs Used as logic	3626 of 32640	14%
4	LUT Flip-FI.pair used	4168	
5	LUT Flip-FI. pairs withan unused FF	2023 of 4168	49%
6	LUT flip-flop an unused LUT	542 of 4168	17%
7	Fully used FF pairs	1603 of 4168	41%
8	Bonded IOBs	82 of 480	21%
9	DSP48Es	16 of 288	7%

The project includes the creation of parallel models respectively Matlab environment and secondly in Quartus tools. The Altera Cyclone II FPGA connected to a variety of peripherals including 512K of SRAM, 4MB of Flash, 8MB of SDRAM, VGA output Ethernet, audio input and output, and USB ports.

4. CONCLUSION

The performance of this implementation can be attributed to the parallel hardware blocks used in performing the necessary calculations for the algorithm [7]. Further to this, the design can be scaled for larger databases by simply adding more processing elements in parallel. The above hardware design was implemented on an Altera Quartus II board (clocked at 100 MHz) and was able to operation time is about 60 clock cycle, which about 0.6us at 100MHz clock pulse, so the operation speed can be up to 1.5MHz. The whole design requires 4168 ALUTs and 241 registers (occupancy of resources is about 49%). The advantage of parallel processing in FPGA leads to a substantial increase in performance and accuracy in processing, extraction of information than in the simulation in Matlab. It should be understood that if there is an impulsive noise in the image sequence, this Kalman filter algorithm should be used in conjunction with pre-spatially non-linear filtered frames. The main contribution of the work is design and implementation of a physically feasible hardware system to accelerate the processing speed of the operations required for real time face recognition. The proposed models are implemented using VHDL, and simulated and synthesized into a single FPGA. It is demonstrated that this technology can produce effective and powerful applications systems.

References

- [1] Hagen, E., Navigation by Optical Flow, In Proc. of IAPR Intern.Conf.-Patt. Recgn.. Vol.1, 1992, pp. 700–703.
- [2] Maybeck, Peter S. *Stochastic Models Estimation and Control, Vol I.* Academic Press, Inc., Orlando, 32887.
- [3] Lazarov, A. D. *Spatial correlation algorithm for ISAR image reconstruction-* 2000 IEEE - Rad.Conf. Virginia, USA, 7-12
- [4] S. Haykin, *Adaptive Filter Theory*, 3rd Ed., Jersey, 1996
- [5] Brown and P. Y. C. Hwang, *Introduction to Random Signals and Applied Kalman Filtering*, 3rd Ed. 2006.
- [6] Pellerin D. and S. Thibault. *Practical FPGA programming in C.* Prentice Hall PTR, ISBN: 0-13-154318-0.
- [7] Wang Y., Osterman J. and Zhang Y. *Video Processing and Communications.* C.Prentice Hall PTR, ISBN: 0-13-017547-1.
- [8] Parhi K. *VLSI Digital Signal Processing System Design and Implementation* Wiley Inter Since 0471241865.

TEXTURE RECOGNITION AS A QUANTITATIVE ANALYSIS OF UNDERDOSES IN PHARMACOLOGY AND MEDICINE

Natalia Ampilova

*St. Petersburg State University, Dept. Computer Science
Universitetsky pr.28, Faculty of Math. & Mech., Starii Peterhof, SPb, 198504,
E-mail nataly@is1483.spb.edu*

Evgeny Gurevich

*Sofia & Jacobs Foundation, Italyanskaya str. 10/5, St.Petersburg, 191186
E-mail info@organicproduct.ru*

Igor Soloviev

*St. Petersburg State University, Dept. Computer Science
Universitetsky pr.28, Faculty of Math. & Mech., Starii Peterhof, SPb, 198504,
E-mail solo@is1483.spb.edu*

Abstract

When obtaining histological preparats or compounds containing underdoses of a matter, the problem on analysis of their specimens arises. Electron microscope and special software allows us to obtain images of such patterns and save them as files in graphic formats. The images may be considered as textural ones, i.e. images consisting of elements (or several classes such elements) which may be identified on perception. The authors have implemented a method based on texture analysis and expert knowledge, which allows us to classify patterns using their graphical representations. The method was applied to distinguish among three classes of brain tumours (astrocytoma, oligodendroglioma and nevrinoma) and classify compounds containing underdoses of a matter.

1. INTRODUCTION

The analysis of histological preparations and compounds containing underdoses of a matter concerns to the problem of pattern recognition that is crucial issue in many applications. To solve the problem neural networks [1] and texture analysis [2] are often used.

It is well known that textual and visual information happens to be redundant: one may delete as stable words combinations from a text as inconsequential details from a visual image without loss of meaning.

From geometrical point of view one can consider both metric and topological properties of an object. Metric properties usually vary when the object is transformed by a continuous mapping that changes its size and form, whereas topological properties are main invariant properties of the object.

It looks like our perception at first fixes topological properties (visual invariants) adding to them minor details afterwards. Many of pattern recognition methods are based on finding visual invariants of an object.

Invariance of a sign or a value means that it is the same for a class of systems (objects). So, to find an invariant means to classify systems (objects) according to this sign (or value).

It should be noted that there are widely used numerical invariants of processes that are applied to investigation of dynamical systems behaviour: correlation dimension of restored attractor and entropy. In [3] correlation dimension of restored attractor was used to reveal α -synchronization phenomenon in EEG records.

Experienced people (professional experts included) mostly give accurate solutions for recognition and diagnostic problems using neither the objects features revealed by classic mathematical techniques nor morphometry. While working with the experts analysing both EEG records to diagnose the evoked potentials and histological preparations, we have realised them to *perceive a record as a picture, an image*. Accumulating a clinical experience in reading and analysing EEG and tumour recognition the experts have shown to form mentally visual invariant underlying their solution of a diagnostic problem.

Basing on our own experience in research into human information processing in perception and thinking we have developed a *mimetic* approach to an automated image analysis and processing aimed at duplicating, quantitating, and extending of human analysis process [4].

2. MAIN NOTIONS

Image (pattern) is a group in a classification system uniting a set of objects in accordance with a feature. Image perception of the world is one of the properties of the brain that allows it to investigate and sort endless information flow. When perceiving external world we classify an information, i.e. quantize it such that any group consists of similar but not identical objects.

Images have a feature: if you acquainted with a finite number of objects from a group you can recognize a great deal of representatives of the group. Moreover, images have objective properties in that different people which use different data of observation for the most part classify the common objects in the same manner and independently of one another.

To recognize a pattern means to identify an object or obtain some of its properties using visual image or audiorecord.

Texture is a structure of a pattern. In this work we assume that texture is a regular (in a way) structure of a pattern.

There are various methods to reveal features in a pattern using its structure (texture analysis).

3. METHOD OF ANALYSIS

The recognizing algorithm uses both an expert knowledge in the correspondent subject area and the texture analysis. The expert knowledge is formalized as a generalized feature that is significant for patterns recognition and classification. For example, it may be the ratio of areas with high and low brightness. The method we realised lies in construction of associative image series. By this series we mean the sequence of images, each of them is the coded input image and depicts some information sign. Solving our problem we coded this sign by a colour according to some scale.

The images of histological preparations were obtained with the help of special software of electronic microscope. The images of compounds with differ-

ent doses of Ag were obtained with the help of software for atomic-force microscope.

An input image (*associative series 1*) of a preparation is transformed to a brightness matrix with 256-by-256 pixels (the pixel brightness being measured in 256 gradations: 0–255). According to the developed algorithm an input matrix is partitioned into equal parts, being the part size depends on the microscope magnifying power. In our experiments we select part size equal 16. The generalised normalised brightness is calculated for each part; its value is determined as a natural number from the row 1, 2, ..., 8. It appeared enough to represent the part brightness range by only eight gradations.

We obtain a simplified variant of the input image (*associative series 2*). By applying to this image the program implementing formalized expert knowledge we obtain *associative series 3*.

So, we impose the input preparation image and two coded pictures together. Simultaneous presentation of all images allows originating the associative series with desired directionality. Thus, a visual invariant of a texture is formalized as some numerical value and used for classification process.

In what follows figures 1-3 show associative series for nevrinoma.

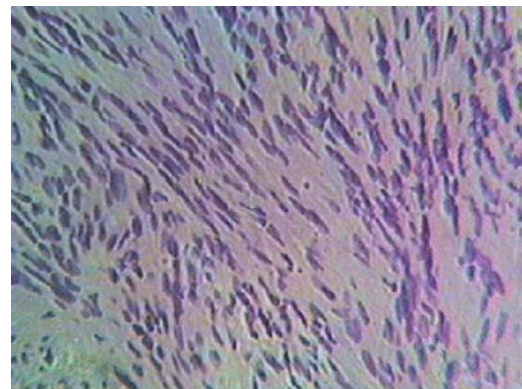


Fig. 1. Input histological preparation

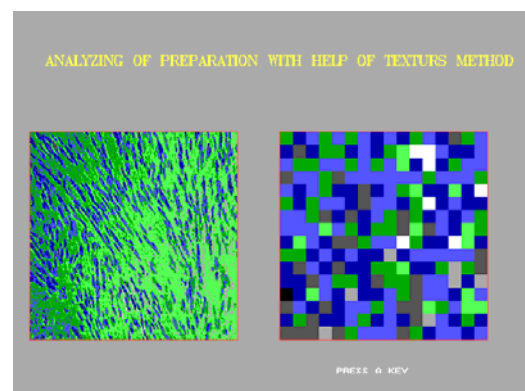


Fig. 2. The result of texture analysis

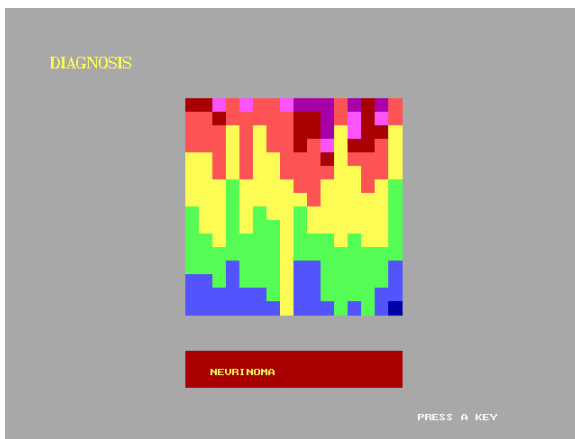


Fig. 3. The final result of analysis

Figures 4-6 demonstrate compounds with different underdoses of Ag. Dimensions are given in μm . The histogram in right side of a figure shows a saturation and is used for construction of the image in 3D-format. In this work we use only images in 2D-format, but we have for an object to apply the described method for images in 3D-format, which may lead to more detailed analysis. For each pattern numerical characteristics that allowed classifying compounds with respect to a dose were obtained.

Numerous experiments show that adding Ag to a solution results in appearing a set of organized structures. One can say about processes of self-organization. Such processes on atomic-molecular level indicate rather complex system behaviour on a higher level.

In solutions with small concentration of Ag there are no complex structures. The solution not containing Ag do not demonstrate any self-organization at all.

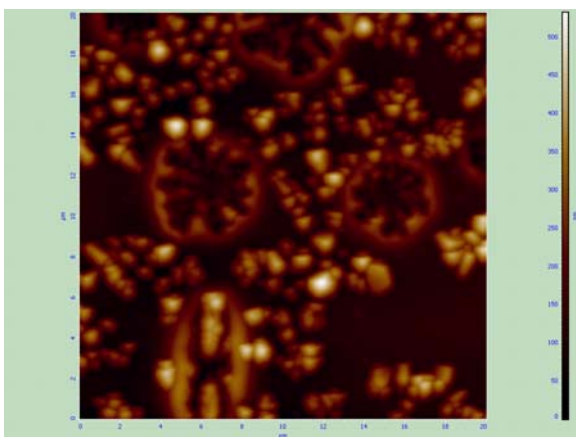


Fig. 4. Large dose of Ag. There is fractal structure of the pattern

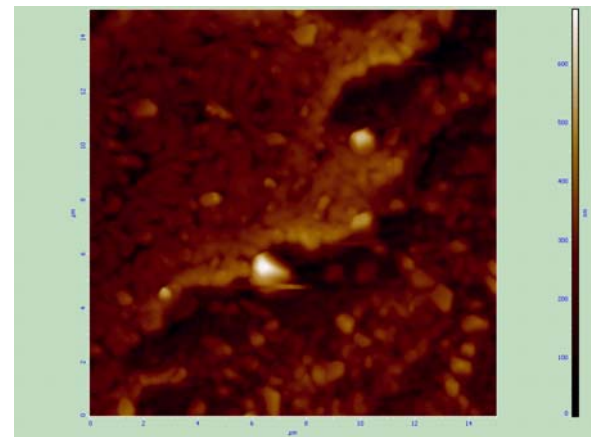


Fig. 5. Small dose of Ag. There is no regularity

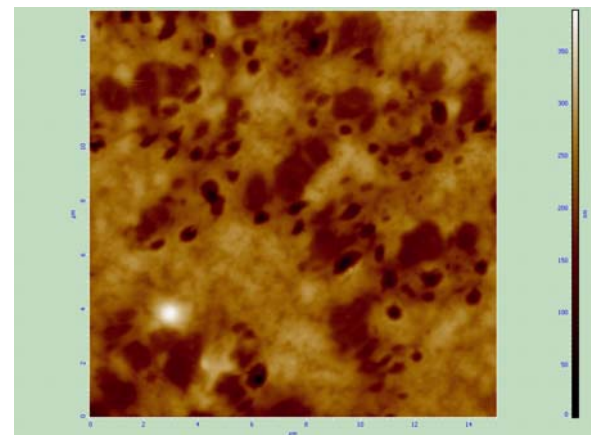


Fig. 6. Zero concentration of Ag

4. RESULTS

The developed algorithm allowed us to classify the brain tumors of three types: astrocytoma, oligodendroglioma and nervrinoma. This method may be also applied to classify other types of brain histological preparations. The patterns of pharmacological compounds whose graphic images are two-dimensional pictures were studied. The results show that such an approach allows us to recognize specimens of different classes as having different texture characteristics.

5. CONCLUSIONS

Our algorithms may be slightly modified and applied to classify patterns where a regular structure is found out. They may be applied to classify the compounds containing underdose of a matter depending on the dose. One of perspective application of described method of the classification of compounds with underdose is homeopathy.

6. ACKNOWLEDGEMENTS

Authors wish to express their thanks to Neurosurgical Institute by A. Polenov and Institute Silicate Chemistry for given data.

References

- [1] Freeman J., Skapura D. Neural Networks. Algorithms, Applications and Programming Techniques. – Addison-Wesley, 1991. – P. 373-392
- [2] Haralick R., Shanmugam K., Dinstein I. Textural features for image classification // IEEE Trans.Syst.Man Cybern. 1973. V.3. P. 610-621.
- [3] N. Ampilova, D. Nikolaeva. On application of correlation dimension for EEG analysis of patients with epilepsy. Proc. 4 Conf. CEMA09 Sofia, 8-10 Oct.2009, p.99-101.
- [4] Ampilova N. B., Gurevich E. Y., Strakhovich E. V. Knowledge based medical training systems. Proceedings of 9 International conference ED-Media and ED-telecom 97, June 14-19,1997, Calgary, Canada, v.2, p. 1437.

EXPERIMENTAL AND NUMERICAL ASSESSMENT OF TISSUE TEMPERATURE ELEVATION DUE TO MOBILE PHONE USE

Maria Christopoulou¹, Irene Karanasiou², Konstantina S. Nikita¹ and Nikolaos K. Uzunoglu²

¹Biomedical Simulations and Imaging Unit, ²Microwave and Fiber Optics Lab
School of Electrical and Computer Engineering, National Technical University of Athens
9 Iroon Polytechniou Str., 15780, Zografou Campus, Athens
Tel: +30 210 772 2968, +30 210 772 2289, FAX: +30 210 772 3557, +30 210 772 2320
Emails: mchrist@biosim.ntua.gr; ikaran@esd.ece.ntua.gr; knikita@cc.ece.ntua.gr; nuzu@cc.ece.ntua.gr

Abstract

The electromagnetic and thermal exposure of users to commercially available mobile phones, operating at GSM 900 MHz and DCS 1800 MHz are studied. Simulated data, using Finite Difference Time Domain Method and Bio-heat Equation, are combined with non invasive temperature elevation measurements in healthy adult volunteers, using a prototype Microwave Radiometry-based Imaging System (MiRaIS). Specific Absorption Rate (SAR) and temperature elevation (ΔT) are computed in a three layered spherical head model, radiated by a linear dipole and a generic phone, at both frequencies. The maximum peak temperature increase due to electromagnetic power absorption is 0.402°C, computed in skin for the case of linear dipole operated at 1800 MHz, placed at $d_1 = 2$ mm, in room temperature of 30°C. Radiometry measurements concluded to temperature increase of 0.8-1°C.

1. INTRODUCTION

Mobile phone use has dramatically increased over the last decade, but doubts remain over its safety. One of the many electromagnetic field induced effects on tissues is the tangible temperature elevation. According to epidemiological investigations, mobile phone users report symptoms of discomfort feeling, warmth behind/around or on the ear and heat sensation of the cheek [1]. The heat sensation may be due to power absorption by the tissues, thermal insulation and phone battery currents. Obviously, the symptoms become intense, as the duration of mobile phone use increases.

This study assesses numerically and experimentally the tissue temperature elevation, combined with the electromagnetic absorbed power, due to mobile phone usage. A preliminary numerical computation of the electromagnetic absorbed power and the thermal distribution in tissues is combined with measurements of temperature elevation in healthy adult volunteers, using a radiometry experimental set-up.

2. MATERIALS AND METHODS

2.1. Simulation

In order to numerically assess the absorbed power and the temperature elevation in biological tissue, electromagnetic [2] and thermodynamic [3] computations are respectively conducted. A three

layered spherical adult head model is considered, consisting of skin, skull (cortical bone) and brain (grey matter) tissue. Head diameter is 20 cm, while the thicknesses of the skin and skull layers are both assumed to be 0.5 cm [4]. Head model is radiated by (a) a $\lambda_0/2$ linear dipole and (b) a generic phone [5] operating at GSM $f_0 = 900$ MHz and DCS $f_0 = 1800$ MHz. The linear dipole is placed at distance $d_1 = 2$ mm (feed point at (3,0,0)) and $d_2 = 10.5$ mm from the spherical surface, while the plastic cover of the generic phone is placed in touch with the sphere resulting to distance $d = 10.5$ mm between antenna feed point and head surface. The Finite Difference Time Domain (FDTD)-based platform SEMCAD-X (SPEAG, Zurich) is used. Both electromagnetic and thermodynamic computations are carried out with the same FDTD grid (up to ~20 million FDTD cells). Tissue dielectric properties are assigned according to [6], while the thermal properties are derived by literature (e.g. [7]). At the thermal boundary between the head model and the ambient, a heat transfer of 5 W/(m²K) at a nominal ambient temperature of 25°C is assumed. Room temperature of 30°C is also taken into consideration. Initial temperature of all tissues is set to 37°C.

2.2. Measurement

2.2.1. System Description

Based on the focused microwave radiometry method, a prototype system (MiRaIS), including an

ellipsoidal conductive wall cavity, which provides the required beamforming and focusing, has been developed for the imaging of biological tissues via remote passive contactless measurements. The measurement is realized by placing the human head in the region of the first focus and collecting the radiation converged at the second by an almost isotropic dipole antenna connected to a sensitive total power radiometer operating at the range 1-4 GHz. The system has already shown in previously performed research work [8] the capability to provide temperature and/or conductivity variations in phantoms and biological tissue. Theoretical and experimental results conclude that with the appropriate combination of operation frequencies and dielectric matching layers placed around the human head, it is possible to monitor areas of interest with a variety of detection depths and spatial resolutions [9].

2.2.2. Participants and Measurement procedure

Initial measurements were performed with the participation of five healthy volunteers. The measurements were performed using MiRals at 3.5 GHz operation frequency before and after usage of

commercial mobile phones, three at 1800 MHz and two at 900 MHz, in sessions of 30 min duration. Each one of the participants was appropriately placed with the area of the ear lateral to the mobile phone at the ellipsoid's focus point and steady state measurements were acquired before and after mobile usage. In all cases of mobile use, all participants were instructed to keep the phone in normal usage ("cheek") position.

3. RESULTS

3.1. Numerical

Tissue peak temperature elevation (ΔT) is related to the peak spatial average Specific Absorption Rate ($\text{psSAR}_{1\text{g}/10\text{g}} = 2 \text{ W/kg}$) with reference tissue mass of 1g and 10g, as defined by [10] and [11] respectively. Additionally, ΔT is scaled to average emitted power of 0.25 W (900 MHz) and 0.125 W (1800 MHz) for typical commercial equipment. Thermal steady state is achieved in less than 20 min. Numerical results are presented in Table 1.

Table 1. Peak temperature elevation ΔT ($^{\circ}\text{C}$) in tissue for 900 MHz and (1800 MHz)

EM source	distance (mm)	$P_{\text{in}} = 0.25 \text{ W (0.125 W)}$ at room temperature		$\text{psSAR} = 2 \text{ W/kg}$	
		25 $^{\circ}\text{C}$	30 $^{\circ}\text{C}$	$\text{psSAR}_{1\text{g}}$ [10]	$\text{psSAR}_{10\text{g}}$ [11]
linear dipole	$d_1 = 2$	0.173 (0.173)	0.210 (0.402)	0.159 (0.153)	0.171 (0.161)
	$d_2 = 10.5$	0.165 (0.162)	0.168 (0.168)	0.167 (0.160)	0.179 (0.168)
generic phone	$d = 10.5$	0.162 (0.158)	0.164 (0.161)	0.170 (0.161)	0.184 (0.170)

The maximum peak temperature elevation is 0.402 $^{\circ}\text{C}$ and it is computed in skin for the case of linear dipole operated at 1800 MHz, placed at $d_1 = 2$ mm, in room temperature of 30 $^{\circ}\text{C}$. The corresponding peak temperature elevation in brain tissue is 0.375 $^{\circ}\text{C}$. Temperature distribution is indicatively illustrated in Figure 1 for the case of linear dipole operated at 900 MHz, placed at $d_1 = 2$ mm, in room temperature of 30 $^{\circ}\text{C}$. Temperature distribution has been extracted for xz plane ($y = -0.45$ mm) where the peak temperature elevation has been calculated (0.210 $^{\circ}\text{C}$).

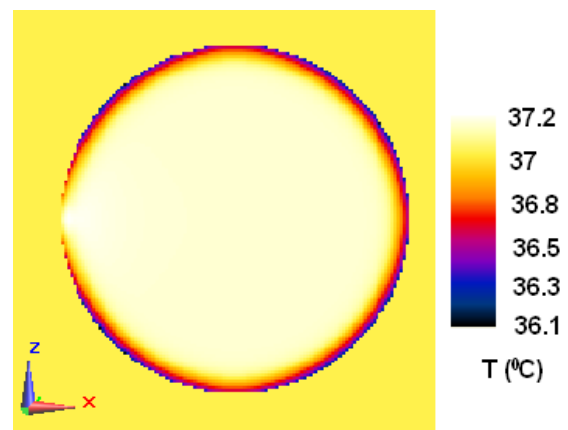


Fig. 1. Temperature distribution in ($^{\circ}\text{C}$) for the case of linear dipole operated at 900 MHz, placed at $d_1 = 2$ mm, in room temperature of 30 $^{\circ}\text{C}$. xz plane ($y = -0.45$ mm) where peak ΔT is illustrated.

Figure 2 illustrates temperature values along the x-axis, for $(y,z) = (-0.45, 0)$ mm. The peak ΔT is computed in skin at $x = 9.6$ mm, i.e. in depth 4.6 mm from the surface.

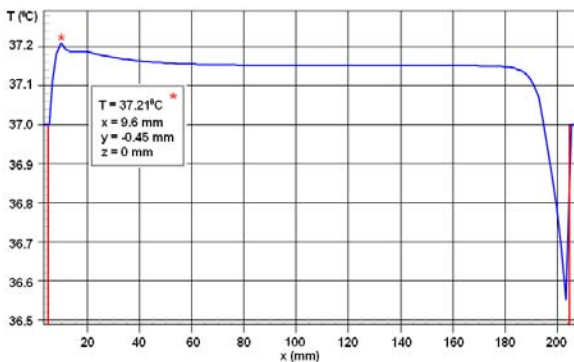


Fig. 2. Temperature in ($^{\circ}\text{C}$) for the case of Figure 1 along the x-axis for $(y,z) = (-0.45, 0)$ mm. Red vertical lines indicate the sphere diameter

3.2. Experimental

Radiometric output voltage differences before phone usage compared to measurements made after using the mobile phones were in the order of 1.5 mV-2 mV which according to the system's temperature resolution with the receiver setup described above corresponds to a temperature difference of 0.8-1 $^{\circ}\text{C}$ [8]. The spatial resolution is less than 1 cm and detection depth inside the human head up to 2 cm.

4. DISCUSSION

Due to electromagnetic power absorption, the peak temperature increase is 0.402 $^{\circ}\text{C}$ and 0.375 $^{\circ}\text{C}$ in skin and brain, respectively at 1800 MHz, scaled to average emitted power of 0.125 W, for 30 $^{\circ}\text{C}$ room temperature. The values of temperature elevation are in good agreement with already published simulated data (e.g. [12]). Radiometry measurements concluded to additional temperature increase, which is probably due to i) the contact between the phone and the skin (thermal insulation) and ii) conduction of the heat produced in the phone by the battery currents and running of the radiofrequency electronic circuits transmitted to the tissue.

Future investigations will include the use of several anatomically correct head models in order to take into consideration i) the efficient heat transfer mechanisms taking place in the tissues and ii) the computation uncertainty and inter-subject variability.

5. CONCLUSION

Nowadays the number of cell phone users is increasing rapidly while the technology is constantly evolving. Numerous studies are carried out to investigate the effects of RF energy from cell phones on the human body. In the present paper an effort to numerically and experimentally assess the tissue temperature elevation due to mobile phone usage is made. The maximum peak temperature increase in brain tissue theoretically computed is in the order of 0.4 $^{\circ}\text{C}$ whereas preliminary radiometry measurements concluded to temperature increase of 0.8-1 $^{\circ}\text{C}$.

References

- [1] M. Sandström, J. Wilen, G. Oftedal, and K. Hansson Mild, "Mobile phone use and subjective symptoms. Comparison of symptoms experienced by users of analogue and digital mobile phones", *Occup Med (Lond)*, vol. 51, 2001, pp. 25-35.
- [2] Taflove, and S. C. Hagness, *Computational Electromagnetics: The Finite-Difference Time-Domain Method*, MA: Artech House Publishers, Boston, 2nd edn, 2000.
- [3] H. H. Pennes, "Analysis of tissue and arterial blood temperatures in resting forearm," *J. Appl. Physiol.*, vol. 1, 1948, pp. 93-122.
- [4] M. Christopoulou, S. Koulouridis, and K. S. Nikita, "Parametric study of power absorption patterns induced in adult and child head models by small helical antennas", *Progress in Electromagnetics Research-PIER*, vol. 94, 2009, pp. 49-67.
- [5] B. Beard *et al*, "Comparisons of computed mobile phone induced SAR in the SAM phantom to that in anatomically correct models of the human head," *IEEE Trans. Electromagn. Compat.*, vol. 48, 2006, pp. 397-407.
- [6] S. Gabriel, R. W. Lau, and C. Gabriel, "The dielectric properties of biological tissues: III. Parametric models for the dielectric spectrum of tissues," *Phys. Med. Biol.*, vol. 41, 1996, pp. 2271-93.
- [7] F. A. Duck, *Physical properties of tissue*, A comprehensive reference book Academic Press Ltd, London, 1990.
- [8] S. Karanasiou, N. K. Uzunoglu, and Ch. Papageorgiou, "Towards functional non-invasive imaging of excitable tissues inside the human body using Focused Microwave Radiometry", *IEEE T Microw Theory*, vol. 52, 2004, pp. 1898-1908.
- [9] A. Gouzouasis, K. T. Karathanasis, I. S. Karanasiou, and N. K. Uzunoglu, "Contactless Passive Diagnosis for Brain Intracranial Applications: a Study using Dielectric Matching Materials", *Bioelectromagnetics*, vol.31(5), 2010, pp.335-49.
- [10] ICNIRP, "Guidelines for limiting exposure to time-varying electric, magnetic and electromagnetic fields (up to 300 GHz)", *Health Phys.*, vol. 74, 1998, pp. 494-522.
- [11] IEEE Std C95.1-2005, IEEE standard for safety levels with respect to human exposure to radio frequency electromagnetic fields, 3 kHz to 300 GHz, IEEE, New York, 2005.
- [12] G. Schmid, R. Überbacher, and T. Samaras, "Radio frequency-induced temperature elevations in the human head considering small anatomical structures, *Radiation Protection Dosimetry*, vol. 124, 2007, pp. 15-20.

TRAINING OF PERCEPTRON NEURAL NETWORK USING PIECEWISE LINEAR ACTIVATION FUNCTION

Maria P. Barbarosou¹ and Nicholas G. Maratos²

¹M. P. Barbarosou is with the Technological Educational Institute of Piraeus, 250 Thivon and P. Ralli Ave., GR 12244, Egaleo, Greece, and also with the Hellenic Air-Force Academy, Dekelia Air Force Base, GR 1010, Tatoi, Greece, Fax:+302105450962, E-mail: mbarbar@teipir.gr.

²N.G. Maratos is with the School of Electrical and Computer Engineering, National Technical University of Athens, 9 Iroon Polytechniou St., GR 15773, Athens, Greece, Fax:+302107722281, E-mail: maratos@ece.ntua.gr.

Abstract

A new Perceptron training algorithm is presented, which employs the piecewise linear activation function and the sum of squared differences error function over the entire training set.

The most commonly used activation functions are continuously differentiable such as the logistic sigmoid function, the hyperbolic-tangent and the arc-tangent. The differentiable activation functions allow gradient-based optimization algorithms to be applied to the minimization of the error. This algorithm is based on the following approach: the activation function is approximated by its linearization near the current point, hence the error function becomes quadratic and the corresponding constraint quadratic program is solved by an active set method.

The performance of the new algorithm was compared with recently reported methods. Numerical results indicate that the proposed algorithm is more efficient in terms of both, its convergence properties and the residual value of the error function.

1. INTRODUCTION

Neural network (NN) models are of board interest to researchers in the recent years, as its applications have flooded many areas.

The activation function is a key factor in the NN structure [1]. The most fuzzy applications use a piecewise linear function (PLF) [2] for activation of neurons, because of its easy handling from their limited computational resources. NNs that use PLFs as activation function is known as piecewise linear NNs (PWL NNs). These cannot be trained by a gradient based optimization method because the lack of continuous derivatives. Hence several training algorithms of PWL NNs have been developed. For example the algorithm presented in [3] is used to NNs that employs the absolute value as activation function. In addition, in [4] is proposed a basis exchange algorithm.

In this paper a new algorithm for training a PWL NN is proposed. The main stage of the method is the modification of the training problem to a quadratic programming. This process is briefly described in Section 2. The main steps of the algorithm are presented in Section 3. Section 4 contains numerical results. The paper is concluded in Section 5.

2. MODIFICATION OF PERCEPTRON TRAINING TO A CONSTRAINED QUADRATIC OPTIMIZATION PROBLEM

A graphical representation of a single hidden layer Perceptron with a single output is shown in Figure 1. The hidden layer consists of n neurons.

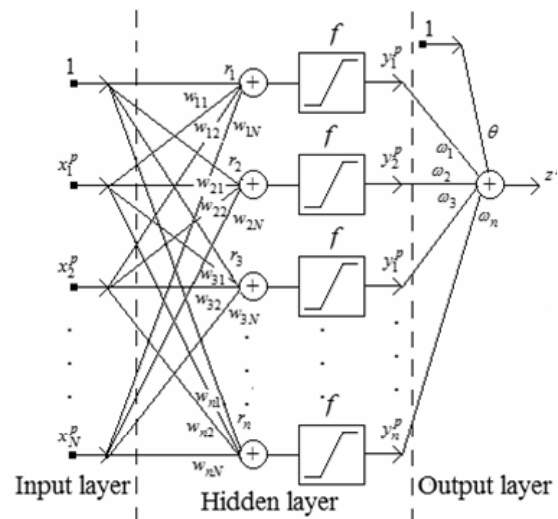


Fig. 1. Graphical depiction of a single hidden layer Perceptron

In Fig. 1 each neuron passes its input which is the weighted sum of the inputs of the network plus the input bias term, through its activation function f and presents the result to its output. The pro-

posed method adopts the 1-dim piecewise linear function (PLF) as activation of neurons:

$$f: R \rightarrow [-L, L], f(y, L) = \begin{cases} L & y \geq L \\ y & |y| < L \\ -L & y \leq -L \end{cases} \quad (1)$$

where $L = 1$, its threshold. Obviously, it is nondifferentiable and bounded between -1 and 1. Its graph is given in Fig. 2. It has three linear pieces which are locally differentiable and two corners. This form of the activation function may be viewed as an approximation to a nonlinear amplifier.

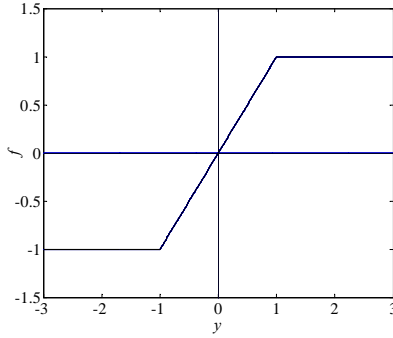


Fig. 2. 1-dim PLF bounded between -1 and 1

Hence the output of the i th neuron, y_i^p , corresponding to the input of the p th training data x^p , is computed as:

$$y_i^p = f\left(\sum_{j=1}^N w_{ij} x_j^p + r_i, 1\right), \text{ for } i = [1, \dots, n] \quad (2)$$

where n is the number of neurons, x_j^p is the j th element of the N -dim vector x^p , that is $x^p = [x_1^p, \dots, x_j^p, \dots, x_N^p]^T$, r_i the input bias of the i th neuron and w_{ij} the weight connecting the j th input to the i th neuron. By considering $w_i = [w_{i1}, \dots, w_{iN}]^T$, (2) is written equivalently as: $y_i^p = f(w_i^T x^p + r_i, 1)$ for $i = [1, \dots, n]$.

The output of the network, z^p , corresponding to the x^p , is the weighted linear combination of the outputs of the neurons plus the output bias:

$$z^p = \sum_{i=1}^n \omega_i f(w_i^T x^p + r_i, 1) + \theta = \sum_{i=1}^n \omega_i y_i^p + \theta \quad (3)$$

where θ is the output bias and ω_i the weight connecting the i th neuron to the output layer.

For every given training sample, let the p th one, the output of the network, z^p , differs from the target (desired) value, t^p , by $(t^p - z^p)$. The purpose of the proposed method is to determine the coefficients w_{ij} , ω_i , r_i , and θ in such a way that the summed over all training samples squared error, between the actual and the target output, to be minimized. Hence the total error is selected to be

$$E = \frac{1}{2} \sum_{p=1}^M (t^p - z^p)^2 \text{ which since (3) becomes:}$$

$$E(\theta, r, W, \omega) = \frac{1}{2} \sum_{p=1}^M \left(t^p - \theta - \sum_{i=1}^n \omega_i f(w_i^T x^p + r_i, 1) \right)^2 \quad (4)$$

where M is the number of training samples, r is the vector of input bias, that is $r = [r_1, \dots, r_n]$, W is the $n \times N$ matrix of the weights connecting the inputs to the neurons that is $W = [w_{ij}]_{i=1, \dots, n}^{j=1, \dots, N}$ and ω is the vector of weights connecting the outputs of neurons and the output layer of the network, that is $\omega = [\omega_1, \dots, \omega_n]$.

The following property of the PLF is an easy consequence of its definition given by (1):

$$af(y, L) = f(ay, |a|L), \quad \forall a \in R \quad (5)$$

Take into account (5), (4) becomes:

$$E(\theta, r, W, \omega) = \frac{1}{2} \sum_{p=1}^M \left(t^p - \theta - \sum_{i=1}^n f(\omega_i w_i^T x^p + \omega_i r_i, |\omega_i|) \right)^2 \quad (6)$$

To simplify the formula (6), the following transformation is applied:

$$\zeta_i = |\omega_i|, \quad b_i^T = \omega_i w_i^T, \quad q_i = \omega_i r_i, \quad \forall i = 1, \dots, n \quad (7)$$

Hence the error function (6) is written:

$$\hat{E}(\theta, q, B, \zeta) = \frac{1}{2} \sum_{p=1}^M \left(t^p - \theta - \sum_{i=1}^n f(b_i^T x^p + q_i, \zeta_i) \right)^2 \quad (8)$$

where $\zeta = [\zeta_1, \dots, \zeta_n]$, $B = [b_1, \dots, b_n]$ and $q = [q_1, \dots, q_n]$. So the training of NN whose layout is pictured in Figure 1, is modified to the following optimization problem with inequalities constraints:

$$\min_{\theta, q, B, \zeta} \left\{ \hat{E}(\theta, q, B, \zeta): \zeta_i \geq 0, i = 1, \dots, n \right\} \quad (9)$$

The basic idea of the proposed approach to carry out the optimization process for the problem (9) is the following: At each algorithm iteration and $\forall(i, p)$ the PWF in problem (9) is approximated by its linearization at the current point. In doing so the problem (9) is modified to a constrained quadratic optimization problem. It is remarked that, to be valid the linearization has to be restricted within the linear piece of the PWF where its current value belongs. The validity of the linearization, is assured by setting extra constrains. The resulting quadratic problem is solved via an active set method [5]. The original weights and bias of NN can be obtained by applying the inverse of the transformation (7) on the solution.

3. OVERVIEW OF THE ALGORITHM

The outline of the proposed algorithm is as follows:

Initialization

Input:

- 1) $\{(x^1, t^1), \dots, (x^M, t^M)\}$, the training set,
- 2) n : the number of neurons,
- 3) ε : the threshold for stopping criterion,
- 4) $u^o \stackrel{\text{def}}{=} (\theta^o, q^o, B^o, \zeta^o)$, the initial point such that $b_i^{oT} x^p + q_i^o \neq \pm \zeta_i^o, \forall \{i, p\}$.

k iteration

Step 1. Let $u^k = (\theta^k, q^k, B^k, \zeta^k)$ be the current point. Compute $f\left(b_i^{kT} x^p + q_i^k, \zeta_i^k\right), \forall \{i, p\}$.

Step 2. Modify the problem (9) to the corresponding quadratic substituting $\forall(i, p)$ the PLF for its linearization and setting the proper extra constraints, so that the linearizations to be valid.

Step 3. Apply the active set quadratic programming algorithm. Firstly, determine the feasible descent direction, d^* . If $\|d^*\| < \varepsilon$ the algorithm ends, otherwise determine the maximum step length a ,

in this direction, for point $u^{k+1} = u^k + a \times d^*$ to be feasible.

Step 4. Set $k = k + 1$ and go back to Step 1. (For some $\{i, p\}$ at the new point u^k the PLF attains a corner of its graph. In these cases the linearization consider the other linear piece. As a result both the objective function and the extra constraints of the quadratic problem change at each iteration of the algorithm).

[6] provides a detailed description of both the modification process and the relative algorithm.

4. SIMULATION RESULTS

Two benchmark problems were selected from [7]. The simulation results confirm the effectiveness of the algorithm in terms of both accuracy and speed. The algorithm was developed using Matlab.

4.1. 1-dim Function approximation

The desired function is the following:

$$g(x) = 0.5 \sin \frac{2\pi x}{10} + 0.5 \left(\sin \frac{2\pi x}{10} \right)^2$$

As in [7], it was used 20 $(x, f(x))$ -samples with x in $(0, 1)$ randomly chosen, as the training set of two neurons NN. The new algorithm run 50 times using each time different random starting weights and bias in $(0, 1)$. All times the algorithm was reaching the termination after 4 iterations and the final sum squared error $SSE = \sum_{p=1}^{20} (g(x^p) - z^p)^2$

was 6×10^{-4} . These are better performances than most in [7].

Furthermore, the algorithm is tested to approximate g over a larger domain. So, the algorithm used 20 random samples within $(0, 9)$, as the training set of 3 neurons NN and is tested for 50 different random starting weights and bias, in $(0, 1)$. The final SSE fluctuated between 1.9×10^{-4} and 2.3×10^{-2} after 19 and 39 iterations correspondingly. In Figure 1 it is shown the approximation of g from the output of NN with the best performance.

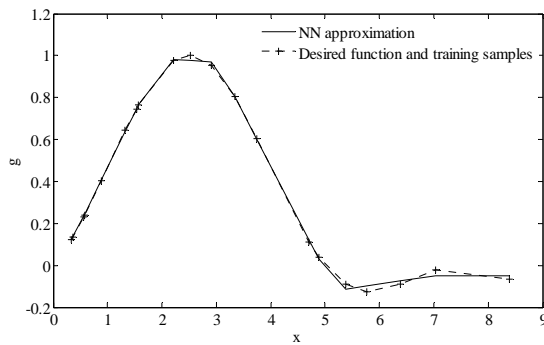


Fig. 3. The output of NN after training with the new algorithm

4.2. 2-dim Exclusive OR problem

In this example a two neurons NN is trained to output a 1, when its input is (0,0) or (1,1), and a 0, when its input is (0,1) or (1,0). The new algorithm run 50 times using each time different random starting weights and bias in (0, 1). All times the algorithm was reaching the termination after 10 iterations and the final SSE was 2.5×10^{-5} . These are by far better performances than most in [7].

5. CONCLUSION

A new training algorithm for a single layer NN with a single layer output is introduced in this work. Making use of PLF as activation of neurons, it modifies the training problem to a constrained quadratic optimization problem. Numerical results confirm its effectiveness compared to other algorithms.

References

- [1] A. Ngaopitakaul and A. Kunakorn "Selection of proper activation functions in backpropagation neural networks algorithm for transformer internal fault locations", International Journal of Computer and Network Security (IJCNS), vol. 1, 2009, pp. 47-55.
- [2] W. Eppler, "Piecewise linear networks (PLN) for process control, Proceedings of the 2001 IEEE Systems, Man, and Cybernetics Conference, 2001.
- [3] J. Lin and R. Unbehauen, "Canonical piecewise-linear networks", IEEE Trans. On Neural Networks, vol.6, 1995, pp. 43-50.
- [4] E. F. Gad, et al., "A new Algorithm for learning in piecewise-linear neural network", Neural Networks, vol. 13, 2000, pp. 485-505.
- [5] D. G. Luenberger, "Linear and Nonlinear Programming", Addison Wesley Publishing Company, Canada, 1989.
- [6] Μ. Π. Μπαρμπάρσους, "Νέα αναλογικά νευρωνικά δίκτυα και νέες μέθοδοι εκπαίδευσης νευρωνικών δικτύων», Διδακτορική Διατριβή, ΕΜΠ, 2005.
- [7] A. Bortoletti, et al. "A new class of quasi-Newtonian methods for optimal learning in MLP-networks", IEEE Trans. On Neural Networks, vol. 14, 2003, pp. 263-273.

THE MEASURE OF ECG COMPLEXITY BY MATRIX ANALYSIS

Liepa Bikulciene^{1,3}, Zenonas Navickas¹, Alfonsas Vainoras², Rasa Šmidkaitė¹

(1) Kaunas University of Technology, (2) Kaunas University of Medicine, Institute of Cardiology,

(3) Lithuanian Academy of Physical Education

(1) Studentu 50-326, Kaunas, Lithuania, LT- 51368, (2) Sukilėlių av. 17, Kaunas, Lithuania, LT-50009,

(3) Sporto 6, Kaunas, Lithuania, LT-44221

T.0037068217227; F.0037037456472;

E. liepa.bikulciene@ktu.lt, zenavi@ktu.lt, alfavain@gmail.com, rasa.smidkaite@ktu.lt.

Abstract

The subject of this paper is intensive extraction of information from ECG signals and using it in diagnostics and assessment status of heart function. The aim of this study is presentation of the analytical methods designed for analysis of dynamic interrelations between different ECG parameters. The main idea of this paper is adaptation of Hankel matrix ranks and second order coherence matrices to describe complexity of ECG and relationship between parameters of ECG. The results show that expressing of cardiac signals with Hankel and coherence matrix could be useful for diagnostic purposes.

1. INTRODUCTION

Over the last years there has been growing interest in problems of complexity analysis. There are very interesting research fields including the wide spectrum of tackled problems - from software development to analysis of medical information. The complexity can be described as strength connection between different parts of complex system. It is obvious that human organism is a complex system. There are many excellent methods describing the complexity measure of various physiologic signals. The complexity of electrocardiogram (ECG) signal may reflect the physiological function and healthy status of the heart. For the purpose to characterize the nonlinear complexity of ECG signal the power spectrum, fractal dimensions, wavelet transformation, phase portrait, correlation dimension, the largest Lyapunov exponent, time-dependent divergence exponent, mass exponent spectrum and complexity measure can be used, [1]. The methods verifies the fact that ECG dynamics are dominated by an underlying multi dimensional non-linear chaotic system, whose complexity measure is about 0,7.

Usually in system identification Hankel matrices are formed when is a sequence of output data and realization of an underlying state-space given or hidden Markov model is desired, but in this paper the ranks of the Hankel matrix will be used as features for the system identification purposes.

The ECG signals were recorded and analyzed by means of multi cardio signal analysis system developed in the Kaunas Institute of Cardiology and

produced by "Kardiosignalas" Ltd. (Kaunas, Lithuania). All signal analysis techniques used in this paper are implemented on a PC using custom software developed in Matlab R2007b.

The work is divided into three sections. In the first theoretical section the mathematical reasoning of H ranks evaluation and complexity measure estimation are described. In the second section the method for investigation of intro concatenation between two elements of dynamical system based by second order matrix analysis is presented, and conclusions are delivered in the last section.

2. COMPLEXITY FROM THE MATHEMATICAL POINT OF VIEW

In this section the mathematical characterization of complexity will be presented.

Let a dynamical system S be given. This system can be characterized in this way: it consists of m components K_1, K_2, \dots, K_m and these components $K_r, r = 1, 2, \dots, m$ are related by algebraic relations. Usually these relationships are composed of ordinary sum and product operations, i.e. $S = \alpha_1 K_1 + \alpha_2 K_2 + \dots + \alpha_m K_m$. In this case measure of complexity of dynamical system S is noted $cmpl S$.

Having proposed interpretation of complexity it is possible to compose the mathematical algorithm of complexity estimation. Suppose that time series (y_0, y_1, y_2, \dots) describes dynamical system S . Here $y_k, k = 0, 1, 2, \dots$ measures are describing the state

of dynamical system S in time moment n . It can be either scalar, or function, or matrix etc.

Then the concept of Hankel rank for these series can be defined. Let a series (y_0, y_1, y_2, \dots) be a sequence of real or complex numbers. Then the sequence (H_1, H_2, H_3, \dots) of Hankel matrices $H_m, m = 1, 2, 3, \dots$ can be formed:

$$H_1 := [y_0], H_2 := \begin{bmatrix} y_0 & y_1 \\ y_1 & y_2 \end{bmatrix}, \dots$$

and from values of its determinants

$\det H_1 := d_1, \det H_2 := d_2, \dots$ the sequence of determinants (d_1, d_2, d_3, \dots) can be formed.

Frequently the elements $d_r, r = 1, 2, 3, \dots$ of this sequence with fixed $\varepsilon > 0$ satisfy special constructed estimation. There exists fixed natural number $m, m \in \mathbb{N}$ and such number satisfies inequalities

$$|d_m| \geq \varepsilon, |d_{m+n}| \leq \varepsilon, n = 1, 2, 3, \dots \quad (1)$$

If the system of inequalities (1) hold true for sequence of determinants then the series has ε -Hankel rank equal to natural number m . Besides, this is noted by this way:

$$H_\varepsilon(y_0, y_1, y_2, \dots) = m \quad (2)$$

Then exists a function $f(x)$ which is described by relation

$$f(x) = \sum_{r=1}^m Q_r(x) e^{\lambda_r x} \quad (3)$$

when $Q_r(x)$ is a polynomial and

$$f(j) \approx y_j, j = 0, 1, 2, \dots$$

The primary concepts for Hankel matrices analysis in finding exact, periodic and chaotic solutions of ordinary differential equations were presented in [2].

If the dynamical system S is described by time series with has ε -Hankel rank, then the components K_r can be the functions $Q_r(x) e^{\lambda_r x}, r = 1, 2, \dots, m$ it means that complexity of dynamical system S is outlined this way:

$$cmpl S = (Q_1(x) e^{\lambda_1 x}, \dots, Q_m(x) e^{\lambda_m x}) \quad (4)$$

The accuracy of expression depends on choose level of ε .

Proposed analysis of time series using Hankel matrices is an alternative method for Fourier analysis which is widely developed. But in proposed method the expression for dynamical systems are finite functions and in most cases it needs less parameters to describe the evaluation of dynamical systems than Fourier methods. For fast classification of dynamical systems and its complexity measure the convolution of Mealy and Moore automaton is practiced [3].

3. INVESTIGATION OF INTERNAL LINKS OF DYNAMICAL SYSTEM

Let a dynamical system S be given. Suppose that this system can be described by two (or more) synchronous time series $(y_0, y_1, y_2, \dots), (z_0, z_1, z_2, \dots)$. Then it is considered that internal links of dynamical system S are relations between two synchronous time series described by mathematical expressions. It must be noticed that usually the couple of series are investigated using statistical methods and there are widely developed analysis of correlation of two series which describes tendency of variation of these series (global type features). But statistical methods are not convenient for investigation of instantaneous features of series variation. The knowledge of such characteristics is none the less important than correlation type properties.

Experience shows that for description of instantaneous features of two time series the algebraic matrix analysis is convenient. In this case the elements y_n and $z_n, n = 0, 1, 2, \dots$ are considered as determined. The basis of algebraic matrix analysis is algebraic arrangement of matrices. The discriminant of matrix A or difference of eigen values is outlined by this formula:

$$|\lambda_1 - \lambda_2| = \sqrt{|\text{dsk } A|} \quad (5)$$

and it shows the „informative degree“ of matrix, [4].

The smaller value of $\sqrt{|\text{dsk } A|}$ implies simplicity of dynamical system described by matrix A . When two time series describing dynamical system are given then it is possible to relate to these series one matrix time sequence: (A_1, A_2, A_3, \dots) when

$$A_n = \begin{bmatrix} y_n & y_{n+1} - z_{n+1} \\ y_{n-1} - z_{n-1} & z_n \end{bmatrix} \quad (6)$$

Then the features of matrix series sufficiently reflect the interdependence of two series. It shows the variation of discriminates series ($\text{dsk } A_1, \text{dsk } A_2, \dots$). Besides, these series can be considered as analogue of correlation characteristic if the statistical methods in some cases for couple of initial series would be used.

4. THE EXPERIMENTAL RESULTS

The primary step of investigation of physiological systems requires the development of appropriate sensors and instrumentation to transduce the phenomenon of interest in a measurable electrical signal. The next step of the signals analysis, however, is not always an easy task for a physician or life-sciences specialist. The clinically relevant information in the signal is often masked by noise and interference, and the signal features may not be readily comprehensible by visual or auditory systems of a human observer. Processing of biomedical signals is not only directed toward filtering for removal of noise and power-line interference; spectral analysis to understand the frequency characteristics of signals; and modelling for feature representation and parameterization. Recent trends have been toward quantitative or objective analysis of physiological systems and phenomena via signal analysis [1].

Analysis of ECG complexity is implemented by scientific group which contains employees of Kaunas University of Technology, Kaunas University of Medicine and Lithuanian Academy of Physical Education. The physiological state of persons with cardiovascular diseases, elite sportsmen's, elderly people (project GUARANTEE) during various physical tasks is investigating.

The expressing of cardiac signals with Hankel matrix could be useful for diagnostic purposes, because averaged ranks in each RR interval and normalized in one scale separate the "healthy" and "sick" persons groups, [5]. In Fig. 1 the example of these ranks (red line) is presented, when initial data is divided to RR intervals (blue lines).

The higher rank value describes the higher signal complexity in certain interval. It is clearly observable that from numerical relations between ranks and the computation step for describing the higher variation of the signal, the higher rank is needed [6].

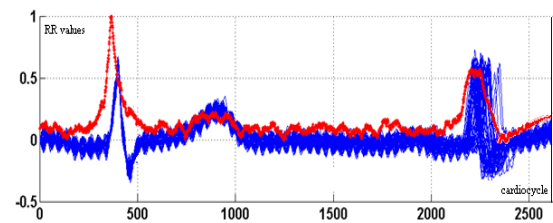


Fig. 1. Example of Hankel matrix analysis

Discriminates for healthy people in normal conditions fluctuate between 0 and 0.2 and grow if physical load is applied, [7]. Results for three different sportsmen (wrestle, stage 10-12 years, 11- 13 place in Europe championship) are shown Fig. 2 (I Rest – 1 min; II – physical load - Rouffier test (30 squats per 45 s); IIIa Recovery (1st minute); IIIb – recovery (2nd minute)).

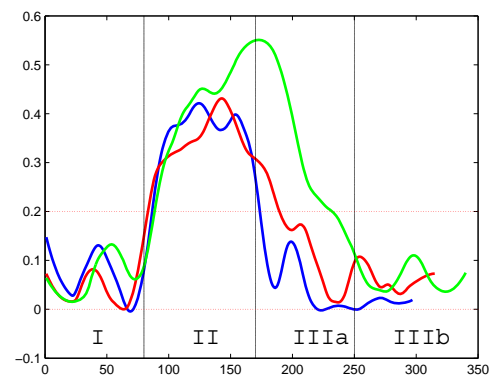


Fig. 2. Example of coherence matrix analysis

5. CONCLUSION

The Hankel matrix ranks and second order coherence matrices for describing complexity of ECG and relationship between parameters of ECG were presented. Such type analysis was applied in evaluation of physiological state for different persons. The increasing amount of studies in this area and application of complex system theory into medicine it is hope to have more detailed and motivated interpretation of intra and interpersonal concatenation and complexity itself.

6. ACKNOWLEDGMENTS

The study was supported by Agency for International Science and Technology Development Programs in Lithuania, project ITEA2 08018 GUARANTEE.

References

- [1] S. Rangayyan, Rangaraj M. Biomedical Signal Analysis - A Case-Study Approach, John Wiley & Sons, 2002, pp. 533.
- [2] Z.Navickas, L.Bikulčienė. Expressions of solutions of ordinary differential equations by standard functions // *Mathematical Modelling and Analysis*. Vilnius : Technika. 2006, Vol. 11, no. 4, p. 399-412.
- [3] A.Sliupaitė, Z.Navickas, L.Gargasas. "Data stream control in e-medicine using the convolution of Mealy and Moore automata". *Biomedical engineering: proceedings of the conference*. Kaunas : Technologija, 2006. p. 288-293.
- [4] Z.Navickas, L. Bikulčienė. "Informative structures for second order matrices". *Mathematics and mathematical modelling Kaunas University of Technology / Kaunas : Technologija*. T. 4 ,2008, p. 26-33.
- [5] G. Kersulytė, Z. Navickas, A. Vainoras, L. Gargasas. "Calculation of the Hankel matrix ranks of electric and haemodynamic processes in the heart" *Electronics and Electrical Engineering*. Kaunas: Technologija. 2009, 3(91), p. 43-48.
- [6] G.Keršulytė, Z.Navickas, V.Raudonis. "Investigation of complexity of extraction accuracy modelling cardio signals in two ways". *IDAACS'2009 : proceedings of the 5th International Workshop on Intelligent Data Acquisition and Advanced Computing Systems: Technology and Applications*, September 21-23, 2009, Rende, Italy. Piscataway: IEEE, 2009. p. 462-467.
- [7] L.Bikulčienė, Z.Navickas, A.Vainoras, J.Poderys, R.Ruseckas. "Matrix analysis of human physiologic data". *ITI 2009: proceedings of the ITI 2009 31st International Conference on Information Technology Interfaces*, June 22-25, 2009, Cavtat/Dubrovnik, Croatia / University of Zagreb. Zagreb: University of Zagreb, 2009. p.41-46.

THE DYNAMIC INTERRELATIONS OF THREE ECG SIGNAL PARAMETERS

Kristina Berškienė¹, Alfonsas Vainoras², Gediminas Jaruševičius², Zenonas Navickas³

¹Lithuanian University of Health Sciences, Medical Academy

M. Jankaus str. 2, Kaunas, Lithuania, LT-50275, e-mail: k.berskiene@gmail.com

²Institute of Cardiology, Lithuanian University of Health Sciences, Medical Academy
Sukilėlių str. 17, Kaunas, Lithuania, LT-50009, e-mails: alfavain@gmail.com, gedijaru@takas.lt

³Kaunas University of Technology

Studentų str. 50, Kaunas, Lithuania, LT-51368, e-mail: zenonas.navickas@ktu.lt

Abstract

The rapid development of counting techniques and technology make it possible to collect increasing amounts of information and perform modern data analysis. The complexity of the problems often stimulates the use of innovative mathematical techniques that are able to capture accurately processes that occur at multiple scales in time and space. The purpose was to present the analytical method for the analysis of dynamic interrelations of ECG, cointegrating data to matrixes by each cardio - cycle. The dynamic interrelations were compared between healthy persons and persons with MI, during coronary angiography. The results showed that a short and quick reciprocity of the signals could be observed using matrix analysis. The values of dynamic interrelations were significant higher ($p < 0.05$) in healthy persons. The new algorithm required just three signal points for the evaluation of dynamic interrelations – it was practical to use in monitoring systems for real time analysis.

1. INTRODUCTION

Recently, the rapid development of counting techniques and technology make it possible to collect increasing amounts of information and perform modern data analysis. New problems of processing of signals and their inherent information emerge that are particularly acute in areas where signal sources are very complex. One of the most actual and complex information storage and signal processing areas is human physiology [1]. Basically, the majority of complex adaptive systems were defined as complex as well as the signals characterizing these systems. The processing of these signals in terms of complex systems provides the possibilities to perceive the system components and dynamic interrelations [2], [3]. Currently, timely diagnosis of cardiovascular diseases is one of the most important problems not only in medical but also in social terms. The basic cardiovascular research, widely used in clinical practice is an ECG recording. The new electronic technologies allowed automatically to record the characteristic points of ECG signal during each cardio-cycle time, and to use them for examining of the different dynamic processes on different time scales. Moreover, it provided a selection of combinations of the parameters that reflected best different processes occurring in the heart and the detailed analysis of the level of these processes. However, the fragmental, disinte-

grated methods that are used in the modern analysis systems of ECG parameters still lack a unifying methodology and processing techniques of holistic signals and information that allow to combine and synthesize information into cardiac organically integrated whole. Small and fast changes occurring may have significant consequences.

In view of these problems, the aim of the study is to analyse the ECG signals using the complex system theory approach based on integral analysis, which embraces holism of the systems analysed, as well as interrelations of their components. So the main aim of this paper was to present the analytical method for the analysis of dynamic interrelations of three ECG parameters.

2. THEORETICAL BACKGROUND

The classical methods for data set interrelation – the correlation analysis, the crosscorrelation analysis, the coherence analysis require big sets of data. Their results are generalized. The complex system adapts to different conditions, the relations between its elements (complex system consists of at least three elements) are shifting. So the main was to present the new analytical method for the analysis of dynamic interrelations of three signals, which require only three points of each signal.

Suppose we have three synchronous signals $(x_n; n=0,1,2,\dots)$, $(y_n; n=0,1,2,\dots)$ and $(z_n; n=0,1,2,\dots)$, the following elements x_n , y_n and z_n are determined. For the cointegration of three signals to series of third order matrixes can be constructed as follows:

$$A_n = \begin{pmatrix} a_{11}^{(n)} & a_{12}^{(n)} & a_{13}^{(n)} \\ a_{21}^{(n)} & a_{22}^{(n)} & a_{23}^{(n)} \\ a_{31}^{(n)} & a_{32}^{(n)} & a_{33}^{(n)} \end{pmatrix},$$

here $a_{11}^{(n)} = x_n$, $a_{12}^{(n)} = x_{n+1} - y_{n+1}$, $a_{13}^{(n)} = x_{n+1} - z_{n+1}$,
 $a_{21}^{(n)} = y_{n-1} - x_{n-1}$, $a_{22}^{(n)} = y_n$, $a_{23}^{(n)} = y_{n+1} - z_{n+1}$,
 $a_{31}^{(n)} = z_{n-1} - x_{n-1}$, $a_{32}^{(n)} = z_{n-1} - y_{n-1}$, $a_{33}^{(n)} = z_n$.

The invariants of matrix A_n :

$$\begin{aligned} Inv_1(A_n) &:= a_{11}^{(n)} + a_{22}^{(n)} + a_{33}^{(n)} ; \\ Inv_2(A_n) &:= a_{22}^{(n)} \cdot a_{33}^{(n)} + a_{11}^{(n)} \cdot a_{22}^{(n)} + \\ &+ a_{11}^{(n)} \cdot a_{33}^{(n)} - a_{13}^{(n)} \cdot a_{31}^{(n)} - a_{21}^{(n)} \cdot a_{12}^{(n)} - a_{32}^{(n)} \cdot a_{23}^{(n)} ; \\ Inv_3 A_n &= \det A_n . \end{aligned}$$

If $Inv_1 A_n = a$, $Inv_2 A_n = b$, $Inv_3 A_n = c$, then the symmetry coefficients can be defined:

$$\begin{aligned} \rho_{23} &= \text{dsk}_2(A_n) = a^2 - 3b ; \\ \rho_{12} &= \left(a - \sqrt{a^2 - 3 \cdot b} \right)^2 \cdot \left(a + \sqrt{a^2 - 3 \cdot b} \right) - 27c ; \\ \rho_{13} &= \left(a + \sqrt{a^2 - 3 \cdot b} \right)^2 \cdot \left(a - \sqrt{a^2 - 3 \cdot b} \right) - 27c . \end{aligned}$$

The large discriminant of matrix A_n :

$$\text{dsk}_1 A_n = \rho_{12} \cdot \rho_{13} .$$

According to these expressions, hypothesis can be formulated: if discriminants of matrixes become close to zero, then numeric time series become similar, i.e., their interrelation is high [4].

Interrelations of the signal series can be labeled as „ \circ “. According to the previous expressions, the value of interrelations can be defined as follows:

$$\varepsilon(x_n \circ y_n \circ z_n) = \frac{1}{l \cdot \text{dsk}_1 A_n} ,$$

here l – real number, ε – the value of interrelations.

Assuming that $l=1$, dynamic interrelationship of each cardio-cycle was calculated for ECG parameters.

3. MATERIALS AND METHODS

For the synchronous registered ECG parameters series the matrix analysis was applied. The automated ECG analysis system “Kaunas – Load W01”, developed at the Institute of Cardiology was used [5]. From ECG signals some parameters during every cardio – cycle were calculated: RR interval in ms (RR), JT interval duration in ms (DJT), R wave amplitude in μV (AR), QRS complex duration in ms ($DQRS$) and T wave amplitude in μV (AT).

Data of ECG parameters series of 30 persons were analyzed. All persons were divided into three groups: healthy persons ($N=10$, 40-60 years old, average age 43.16 ± 1.17), 2 groups of patients with acute myocardial infarction (one group patients of 30-60 years old, $N=9$, average age 42.44 ± 3.91 ; another group - patients of 60-90 years old, $N=11$, average age 72.55 ± 3.78). For all patients the coronary angiography was performed and occlusion of at least of the one coronary artery was diagnosed. For all of them percutaneous transluminal coronary angioplasty reconstructing TIMI3 flow in damaged artery was successfully performed [6], [7].

For the analysis of different complexity levels of the heart [8] some triad were selected:

$$RR \circ DJT \circ AR \text{ for the system level,}$$

$$RR \circ DJT \circ DQRS \text{ for the subsystem (heart regulation) level and}$$

$RR \circ DJT \circ AT$ for the subsystem (heart metabolism) level. For the correct interrelations analysis and comparison all the data were normalized to interval [0; 1] as follows:

$$x = \frac{x_0 - x_{\min}}{x_{\max} - x_{\min}} ,$$

here x_0 - the original value, x – normalized value x_{\min} and x_{\max} minimal and maximal physiological value [4].

4. RESULTS AND DISCUSSION

It was hypothesized, that if a person was healthy, the values of ECG parameter interrelations were high, if ischemic heart disease was diagnosed – values were low. All mentioned dynamic interrelations for each person were calculated and analyzed individually. The examples of initial ECG parameters and their dynamic interrelations before, during and after coronary angiography of patient with acute myocardial infarction are given in the Figure 1 and Figure 2.

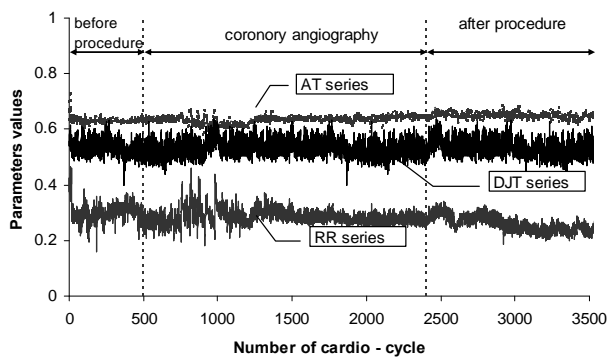


Fig. 1. An example of one investigation, initial ECG parameters RR, DJT and AT sequences

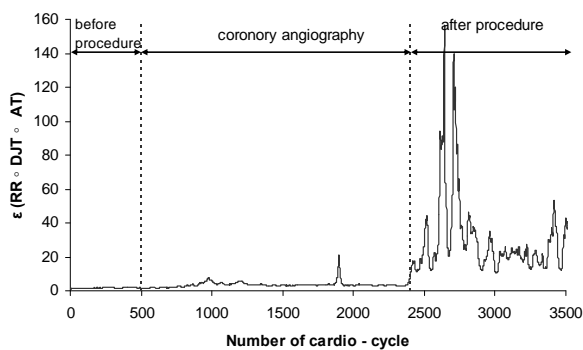


Fig. 2. An example of dynamic interrelations of one investigative ECG parameters RR, DJT and AT

For the results comparison the average value of was calculated. Non – parametric Man – Whitney – U test for the independent samples was applied. For the comparison of results before and after coronary angiography for ischemic patients non – parametric Wilcoxon test for two related samples was applied. The significance level 95 % was selected. The dynamic interrelations after coronary angiography were significant ($p < 0.05$) higher for both groups. The comparison between groups is given in Figure. 3.

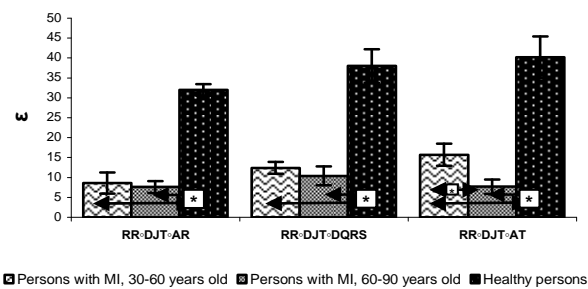


Fig. 3. Comparison of different ECG parameters dynamical interrelations average values for between different groups (* - the difference is statistically significant, $p < 0.05$)

It was estimated that the values of dynamic interrelations of ECG signal parameters were significant higher ($p < 0.05$) in healthy persons and better physical state (younger group). But in both situations the initial data didn't differ ($p < 0.05$).

Non-invasive diagnosis of ischemic heart disease (IHD) is the main objective of cardiologists. However at rest accuracy of usual ECG, using only common, widely used diagnostic parameters is only about 45%. It increases using stress test [9], but also in this case accuracy and specificity is too low. If to take human body as a complex system [1], [10], important features of its complex function is assessment of dynamic interrelations between investigative parameters. There is still unknown the form of changes of any ECG parameters, during coronary artery revascularization procedures, when there is changing ischemic situation in the heart [11]. In this work it was hypothesized, that if person is healthy, ECG parameters interrelations values are high, if an ischemic heart disease is diagnosed – values are low [4]. The results confirm the hypothesis and illustrate, that dynamic interrelations are more informative for clinical practice than initial ECG parameters series [4],[10].

5. CONCLUSIONS

The results showed that a short and quick reciprocity of the signals could be observed using matrix analysis. Moreover, the new algorithm required just three signal points for the evaluation of dynamic relations – it was practical to use in monitoring systems for real time analysis.

It was observed, that dynamic interrelations are different to each person and it is better to analyze them individually.

All results should be tested with more data from ECG signals, registered for different age, gender and functional state persons.

6. ACKNOWLEDGMENTS

The study was supported by Agency for International Science and Technology Development Programs in Lithuania, project ITEA2 08018 GUARANTEE.

References

- [1] Quarteroni, L. Fornaggia, A. Veneziani, *Complex Systems in Biomedicine*, Springer, Milan, 2006.
- [2] G. Kersulyte, Z. Navickas, A. Vainoras, L. Gargasas, G. Jarusevicius, "Analysis of Cardiosignals Cohesion based on Hankel Matrix", *Electronics and Electrical Engineering*, Vol. 8(88), Technology, Kaunas, 2008, pp. 55-58.
- [3] J. West Bruce, *Where Medicine Went Wrong. Rediscovering the Path to Complexity. Studies of Nonlinear Phenomena in Life Science*, World Scientific, 2006.
- [4] K. Berškienė, A. Vainoras, A. Lukoševičius, Z. Navickas, L. Bikulčienė, "The analysis of the interactions of nonlinear physiological systems", *Biomedical engineering: Proceedings of International Conference*, Technologija, Kaunas, 2008, pp. 38-41.
- [5] Vainoras, L. Gargasas, R. Jurkonienė, V. Jurkonis, G. Jaruševičius, K. Berškienė, Z. Navickas, "Analysis of Electric Cardiac Signals – Methods and Application Results", *Electronics and Electrical Engineering*, Vol. 5(85), Technology, Kaunas, 2008, pp. 81-84.
- [6] M. C. De Bruyne, A. W. Hoes, J. A. Kors, A. Hofman, J. H. Van Bommel, D. E. Grobbee, "QTc dispersion predicts cardiac mortality in the elderly. The Rotterdam Study", *Circulation*, Vol. 97, 1998, pp.467 - 472.
- [7] R. Yilmaz, R. Demirbag, M. Gur, "The Association of QT Dispersion and QT Dispersion Ratio with Extent and Severity of Coronary Artery Disease", *Annals of Noninvasive Electrocardiology*, Vol. 11, 2006, pp. 43 - 51.
- [8] B. Y. Yaneer, *Complexity Rising: From Human Beings to Human Civilization, a Complexity Profile*, EOLSS Publishers, Oxford, 2002.
- [9] Vainoras, L. Gargasas, G. Jarusevicius, "The bicycle ergometry and the possibility of complex evaluation", *Lithuanian Journal of Cardiology*, Vol. 6(4), Kaunas, 1999, pp. 760-763.
- [10] W. T. Myers, *Anatomy trains*. – Edinburgh, Churchill Livingstone, 2001. - 281 P.
- [11] H. V. Huikuri, T. H. Mäkikallio, J. Perkiömäki, "Measurement of Heart Rate Variability by Methods Based on Nonlinear Dynamics", *Journal of Electrocardiology*, Vol. 36, 2003, pp. 95–99

EHEALTH INFORMATION AND SIMULATION MODELING

Roumiana Yossifova Ilieva,

*Dept. Economics, Industrial Engineering and Management, Faculty of Management, Technical University of Sofia,
Sofia 1000, Bulgaria, 8 "Kliment Ohridski" boul., bl.3
Phone: +359 893690233, E-mail: rilieva@tu-sofia.bg*

Abstract

Various aspects of simulation modeling using Matlab Simulink are considered in this study. Attention is focused on simulating the procedure for issuing European Health Insurance Card from the competent authorities. The presented simulation model is developed on the basis of the regulations describing the procedure for issuing such a card in Bulgaria. The study ends with an analysis of the results of the simulation and identification of the opportunities for optimization of the procedure. The results are obtained in the project "Simulation Modelling of Administrative Services and Processes for e-Serving and Management", funded by the grant for research at the Technical University of Sofia. The author is leader of the team of the scientific project.

1. INTRODUCTION

The improvement of the automated electronic services requires application of a systematic approach for simulation modeling to test and evaluate the parameters of the service quality. The service quality requirements must be combined with the level of service from input to output, taking causation so as to ensure the network characteristics that define the communications between separate administrative units.

2. SIMULATION TOOLS

A few stages of simulating the procedure for issuing European Health Insurance Card (EHIC) using Matlab Simulink are considered in this study. The presented simulation model is based on the regulations describing the procedure for issuing such a card from the competent authorities in Bulgaria.

The capabilities of MATLAB Simulink [1] - [7] for modeling dynamic systems are demonstrated, which enables the realization of the relevant principles in other areas. Only standard blocks are used for portability and compatibility of the model with older versions on other workstations. Matlab programming environment was chosen because of the superb opportunities it provides for the simulation of models from all areas of science and technology and its wide distribution among researchers in these areas.

3. Ehealth SIMULATION PROCEDURE

Decision Scheme in the MATLAB Simulink environment is built of subsystems, each of which presents institutions through which the documents are passed (Figure 1). To start the procedure documents are submitted in the subsystem „Customer” (Figure 2). The subsystems “Current number verification”, “Appeal against refusal” and “Issue of EHIC” are joined to this subsystem.

Block “Registering with an incoming number and classification” presents RHIF register, which brought the documents submitted for the EHIC. Block “Check for paid health insurance contributions” in the real system is confirmation of continued health insurance rights of the client. “Issue of EHIC” subsystem is under the jurisdiction of the NHIF. The block “Archive” is a virtual model of the archive of the NHIF.

3.1. Subsystem „Customer”

The documents are divided into two blocks (Figure 2):

1) Medical epicrisis and photos that are made by step generators having in mind the accessibility of these documents and in most cases a single issue.

2) Copy of Birth certificate, copy of identity card or passport and document for paid taxes are generated by pulse generators in view of the frequent need for issuing such documents.

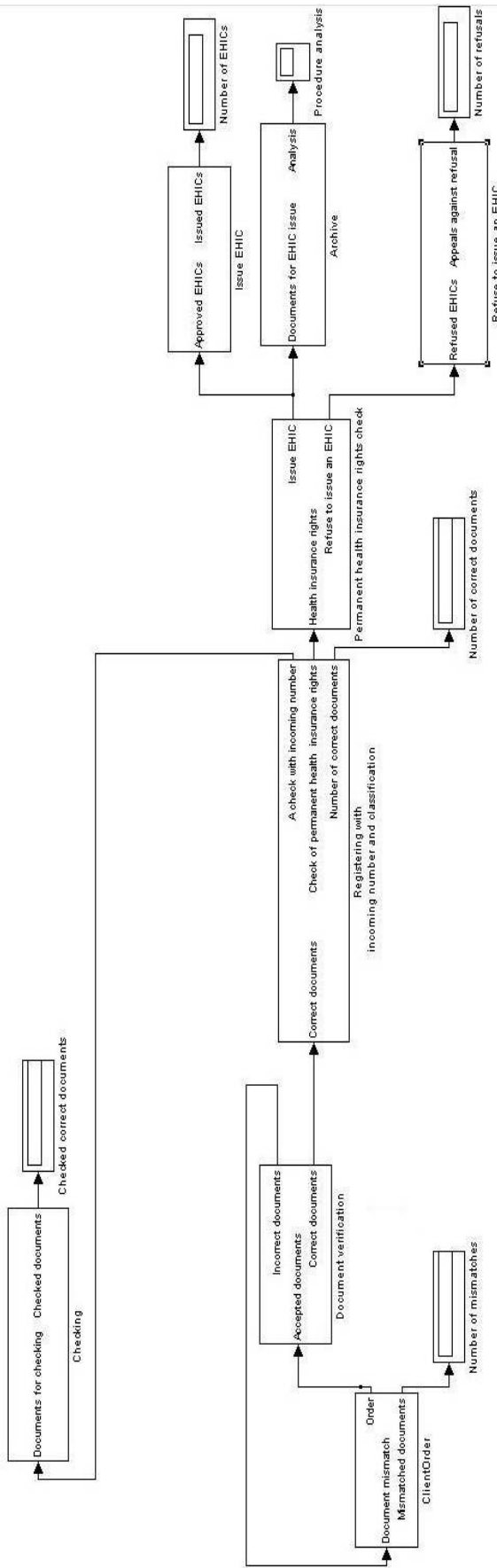


Fig. 1. Overall Simulation scheme

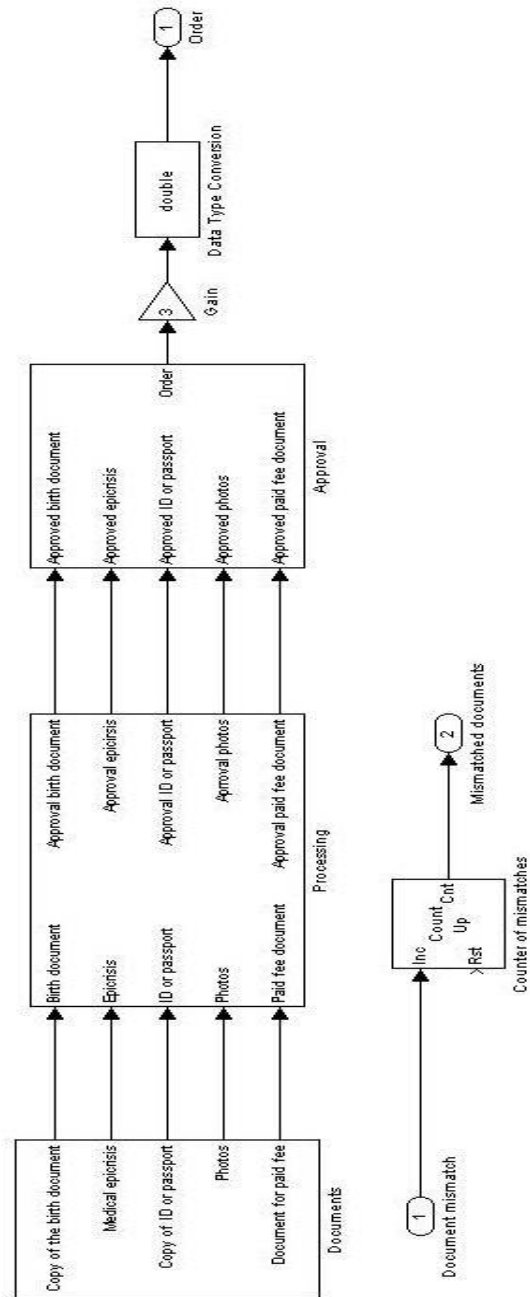


Fig. 2. Subsystem „Customer”

3.2. Subsystem “Documents confirmation”

In order to prevent interference the amplitude of the output signal is increased before the output of the upper subsystem. The same subsystem contains a feedback block "Documents confirmation" (Figure 3), which is connected to counter considering the number of unfair documents.

The verification of the correctness of the documents is conducted in accordance with the above logic. Each amplitude of the signal with a value other than zero is a correct document and vice

versa. For the purposes of the functions performed by this block are used two standard blocks to check the amplitude of the input signal. Any incorrect set of documents is returned to the subsystem „Customer” to be processed there.

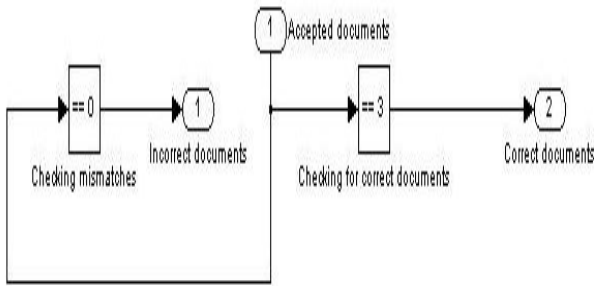


Fig. 3. Subsystem “Documents confirmation”

3.3. Subsystem “Registering with an incoming number and classification”

Once the documents are adopted by employees of the regional health insurance fund, they are registered with the registration number and classified. During the process of classification documents are sent to be checked on incoming number in the subsystem "Verification of incoming number" (Figure 4) and to check the insurance status of the sender in subsystem "Check for paid health insurance". Additional functionality of the subsystem is added by finding the number of correct documents.

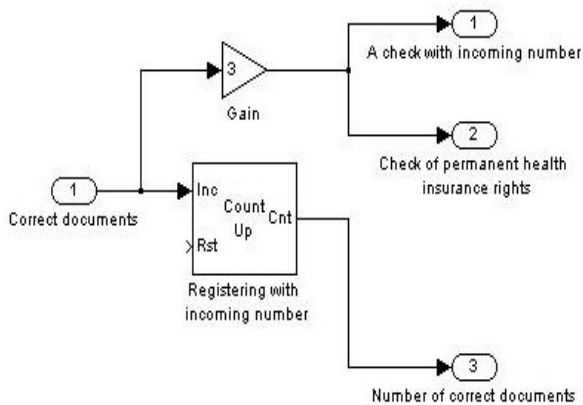


Fig. 4. Subsystem “Registering with an incoming number and classification”

4. SIMULATION RESULTS ANALYSIS

The simulation procedure for issuing EHIC was carried out throughout 480 units with the assump-

tion that this is the duration of a working day in minutes. For the other studies the duration of the simulation can be changed as the duration and time unit.

A "right" logic is used in the whole scheme (Figure 5). Each signal amplitude value of zero can be interpreted as an incorrectly filed document, incomplete set of documents or lack of documents for processing. If the amplitude value of any signal from the scheme is different from zero, it is interpreted as a complete set of submitted papers, documents or correct processing of documents.

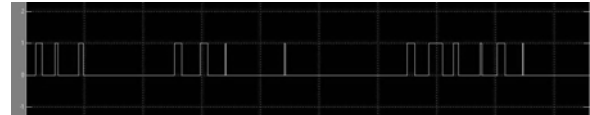


Fig. 5. Simulation results

After a careful analysis the percentage of incorrect documents, lack of full set of documents, the senders with unpaid health insurance contributions or discrepancy between the number of incoming documents may be determined. This analysis would be used to determine the reasons for the shorter and longer processing applications. It can take information to serve as a basis for further optimization of the procedure at its various stages.

5. CONCLUSION

This simulation model is widely applicable in the field of eGovernment, because of the potential for fast modification of the model for other procedures. After deposition of modifications on the model, it can be used for determining the bottlenecks in the information flow and to optimize the processing of documents in local or global plan of any e-service.

The advantages of the simulation model are easiness to work with the model, the opportunities to regulate the duration of the simulation, model portability between computer systems with different software and/or hardware and compatibility with older versions of the programming environment. Unlike other abstractions of the procedure for issuing the EHIC this model allows rapid and significant changes in amendments to the regulations describing the card issue. This model is applicable for both an employee and the department or the whole system. Quick and visually easily distinguished analysis is to be made by changing the input parameters.

6. APPENDIX AND ACKNOWLEDGMENTS

The research results presented in this publication are funded by the Internal competition of Technical University of Sofia -2010 [8].

The author expresses her deep gratitude to the student Zafer Shishkov, member of the above project for the priceless enthusiastic support in the process of simulation modelling.

References

- [1] Barnes, B., G. Fulford. *Mathematical Modeling with Case Studies: A Differential Equations Approach using Maple and MATLAB*, 2ed., CRC Press Inc., 2009
- [2] Karris, S. *Introduction to Simulink with Engineering Applications*, Second Edition, Orchard Publ., 2008
- [3] Halpin, T., T. Morgan, A. Morgan, "Information modeling and relational databases". 2nd ed. Morgan Kaufmann, 2008,
- [4] Hanselman, D., B. Littlefield. *Mastering Simulink 7*. Prentice Hall, 2005
- [5] Цисарь, И. Ф. *MATLAB Simulink. Компьютерное моделирование экономики*. Серия: Библиотека профессионала, М., Солон-пресс, 2008
- [6] Гультяев А. *Визуальное моделирование в среде MATLAB*. Питер, 2000
- [7] Дьяконов, В., В. Круглов. *MATLAB. Анализ, идентификация и моделирование систем*. Питер, 2001
- [8] Проект № 102 НИ 221-15 /26.02.2010 на тема „Симуляционно моделиране на административни услуги и процеси за целите на електронното обслужване и мениджмънт”

MODIFIED MIND MAPPING FOR EHEALTH MODELING

Roumiana Yossifova Ilieva

*Dept. Economics, Industrial Engineering and Management, Faculty of Management, Technical University of Sofia, Sofia 1000, Bulgaria, 8 "Kliment Ohridski" boul., bl.3
Phone: +359 893690233, E-mail: rilieva@tu-sofia.bg*

Abstract

eHealth Mind Map is derived through Busan's iMind Mapping software. Analysing and combining the advantages of the Dialectical Spiral, Boehm's Spiral Model and Spiral Iterative Development the eHealth Mind Map model is modified into a spiral one. It is widely applicable in the field of eGovernment, because of the potential for fast modification of the model for other procedures. The results are obtained in the project "Simulation Modelling of Administrative Services and Processes for e-Serving and Management", funded by the grant for research at the Technical University of Sofia. The author is a leader of the team of the scientific project and creator of this innovative approach.

1. INTRODUCTION

eHealth is a brand new area which needs a lot of innovative knowledge-based modelling techniques to be well understood, modelled and simulated. The improvement of the automated electronic services requires application of new approaches for the stages of service procedures. The service quality requirements must be combined with the level of service from input to output, taking causation so as to ensure the network characteristics that define the communications between separate administrative units.

2. BUSAN'S MIND MAPPING

Visual thinking is our brain's natural way to solve problems creatively [3]. A mind map is a normal way of organizing information that is both rational and artistic. It uses visual thinking to create an organized display of the problem. It is typically an organic multicoloured chart, containing words and drawings for the mind's images and associations by arranging them around a central theme. It utilizes analytical left brain functions such as key words, sequencing, and associative links combined with spatial right brain functions like symbols, colour, images, links, attachments, dimension, and connective lines [2]. It leads to harmonious whole brain thinking that brings together the left and right brain thinking parts which is greater than the simple sum of them.

3. Ehealth MIND MAP

An eHealth Mind map model is proposed on Figure 1. In its centre is the core idea – eHealth

(symbolically shaped in red heart). After the central idea is set, then modifying the eHealth mind map begins with creating of main branches. These main branches represent the most important aspects of eHealth - Health knowledge management, mHealth, Telemedicine, Virtual Physiological Human, national eHealth, ePharmacy, Internet, Virtual Care Teams, Electronic Medical Record, Personal Health Systems, ICT for Patients Safety.

Mind map development continues with identifying topics connected to mentioned main branches. These topics are parent nodes of eHealth mind map. If information labeled on a parent node should be expanded, then child node is created with specific description. The process goes further in order to completely uncover all the important events or data concerned with the core idea. The last thing to do when modifying a mind map is to draw feed back connections between communicating nodes.

Health knowledge management is a design of a customizable prototype public health knowledge management repository system and interface with optimal interoperability and the capability to provide timely access to public health information in support of decision making at the point and time of need.

mHealth includes the use of mobile devices in collecting aggregate and patient level health data, providing healthcare information to practitioners, researchers, and patients, real-time monitoring of patient vitals, and direct provision of care (via mobile telemedicine) [7].

Telemedicine is a rapidly developing application of clinical medicine where medical information is transferred through interactive audiovisual media for the purpose of consulting, and sometimes remote medical procedures or examinations [8].

The Virtual Physiological Human (VPH) is a methodological and technological framework that, once established, will enable collaborative investigation of the human body as a single complex system [7]. The collective framework will make it possible to share resources and observations formed by institutions and organizations creating disparate, but integrated computer models of the mechanical, physical and biochemical functions of a living human body. The VPH is a framework which aims to be descriptive, integrative and predictive.

Connections are data bases store information for computer models.

Parent nodes are:

- Fields of research – bioinformatics, genomics, neuron-informatics;
- Aims – personalized care solutions; reduced need for experiments on animals; more holistic approach to medicine; preventive approach to treatment

Virtual healthcare teams consist of healthcare professionals who collaborate and share information on patients through digital equipment. ePharmacy and Virtual Care Teams imply the use of Internet to provide connections [7].

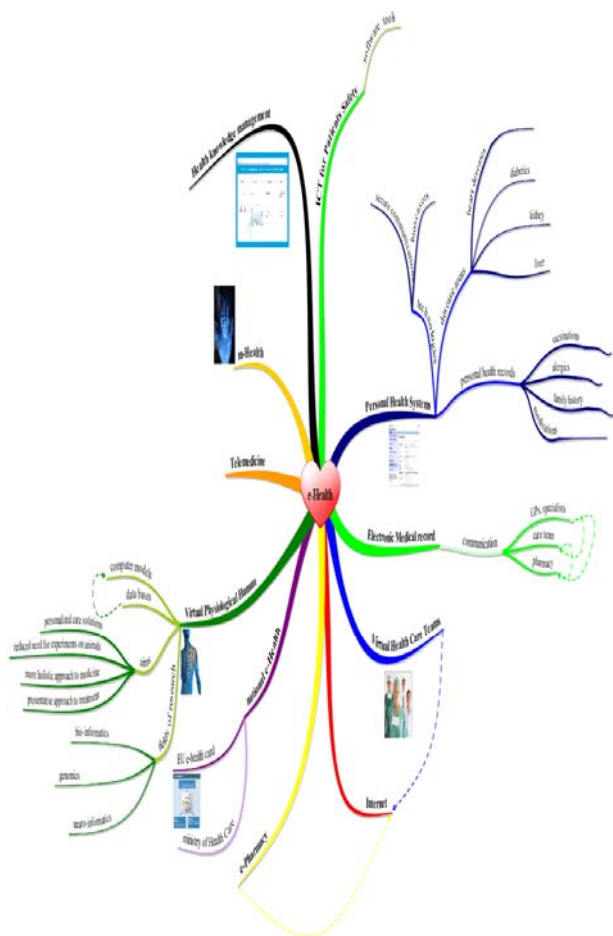


Fig. 1. eHealth Mind Map

3.1. Dialectical Spiral of the eHealth development

The systemic pattern of eHealth evolution can be visualized as an ascending spiral (Figure 2) where its first convolution reflects the conflict (theses vs. antitheses), the second convolution - the conflict resolution (synthesis), and the third convolution -its transcendence [4]. This model assumes that we will be able to learn how to ascend the dialectical staircase and build a better security governed e-Society free of bureaucracy and corruption for all.

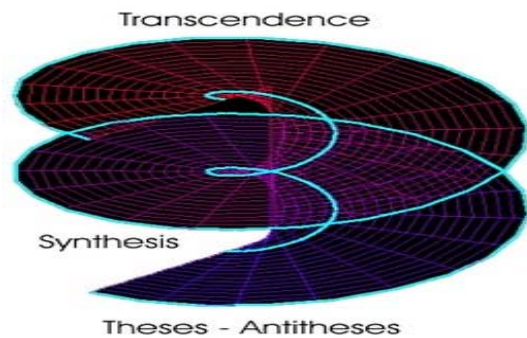


Fig. 2. Dialectical Spiral

3.2. Boehm's Spiral Model

Boehm's Spiral Model (Figure 3) [1], [5] is a 2D variant of the "dialectical spiral" and as such provides useful insights into the life cycle of the system. It can be considered as a generalization of the prototyping model with the first iteration being a prototype.

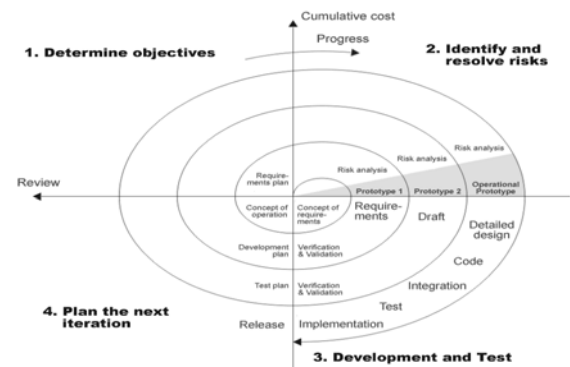


Fig. 3. Boehm's Spiral Model

3.3. Spiral Iterative Development

Spiral Iterative Development (Figure 4) [6] is an approach to building software in which the overall project life cycle is composed of several sequential

A SIMPLE AND ACCURATE METHOD FOR ACHIEVEMENT OF A UNIFORM ON-AXIS MAGNETIC FIELD OF LONG SOLENOID

Sava Vasilev Savov

Department of Electrical Engineering, Technical University of Varna,
Varna 9010, Bulgaria
e-mail: savovsv@yahoo.com
phone: +359 52 383 408
fax: +359 52 302 442

Abstract

A uniform and strong magnetic field is required for application in the magnetic resonance imaging (MRI). There are two main approaches to achieve a uniform enough DC magnetic field: a) using a permanent magnet; b) using a resistive magnet (coil). Here the second approach is considered.

Coils of different shapes can be applied to achieve such a uniform DC magnetic field over the vicinity of its center. Here a long solenoid is chosen and analyzed. Another two systems of coils inside one MRI device are: a) gradient coil; b) RF coil, but they are out of our scope here.

In this paper a simple analytical algorithm for improving the uniformity of magnetic field's distribution of solenoid, is presented. The on-axis magnetic flux density is improved by using a variable winding's density.

Suitable numerical results are included in the paper to demonstrate the efficiency of proposed method for improvement of the uniform on-axis magnetic field distribution.

1. INTRODUCTION

Magnetic resonance imaging (MRI) is an efficient nonionizing medical imaging technique used in radiology to visualize the structure of the body by providing detailed images of it in any plane [1 -7]. A strong DC magnetic field *aligns* the nuclear spins of the hydrogen protons of the water contained in the body, while a perpendicular RF magnetic field *alters* the alignment of these protons following prescribed pulse sequences. This is very similar to the phenomenon of gyrotropy in a ferrite where an RF field perpendicular to the *DC magnetic field* modulates the magnetic dipole moments (to provide an anisotropic macroscopic response).

After each pulse, the protons drift back into alignment with the DC field, thereby emitting a detectable RF signal, which is picked up by coils and recorded. The MRI images with spatially varying contrast can then be constructed by various *digital signal processing (DSP) techniques* based on the fact that protons in different tissues of the body (e.g. fat vs. muscle) realign at different speeds. A critical issue for high-resolution imaging in MRI is the capability to generate an extremely *uniform DC magnetic field* across the field of view [8 -11]. In principle, it can be also applied for the off-axis magnetic flux density, but there much more complicated expressions in terms of special functions (elliptic inte-

grals) appear [12]. Because of that, such an opportunity is not further explored in the paper.

Another possible method to solve this problem is, for example, to use a genetic algorithm in order to find the position of every turn of the coil, but this stochastic optimization method is rather time-consuming (because of the big number of parameters involved).

The design of resistive and superconducting magnets is usually based on two well-known coils in electromagnetics. The first one is the so-called *Helmholtz pair* [9], which consists of *two adjacent loops of the same radius carrying same current I in same direction*, as illustrated in Fig. 1. It can be shown easily that when the distance between the two loops *equals* the radius of the loops ($d = R$), the magnetic field B_z is *uniform around* $z = 0$ through the third power of z :

$$B_z(z) = B_z(0) + O((z/d)^4) \quad (1)$$

where

$$B_z(0) = \frac{4\mu_0 I}{5\sqrt{5}R} \quad (2)$$

One can achieve even a *higher degree of homogeneity* for B_z by using two or more symmetrical pairs of loops but then it is difficult to find the optimum distance analytically. This multiple case yields to the second important coil considered below.

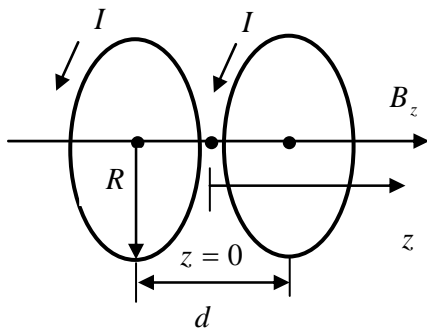


Fig. 1. Geometry of the Helmholtz pair

Another symmetrical source of a relatively *uniform* magnetic field is the cylindrical coil (*solenoid*) [10] with a length L and a radius R (Fig.2), but with a *length greater than the radius* ($L \gg R$). The classical result for the uniform magnetic flux density of such a coil is obtained approximately by Ampere's law application

$$B_z(z) = \mu_0 N_0 I \quad (3)$$

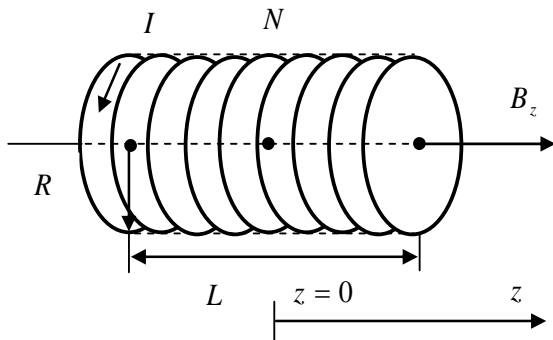


Fig. 2. Geometry of the long solenoid

where $N_0 = N / L = \text{const}$ is the *number of windings per unit length* and N is the total number of windings. In this paper we propose a *method to improve the uniformity of the axial magnetic field* $B_z(z)$ by exploring a more general case with a *variable winding's density*. Because of the geometrical symmetry in magnetic field distribution it is natural to assume that the last function is an *even function*. Let us assume that N_0 is replaced by a simple polynomial of second order

$$M_0(z) = N_0(1 + b_2' z^2) \quad (4)$$

where b_2' is a unknown coefficient that *has to be determined* in such a way so the corresponding magnetic field to be *uniform as much as possible*. Here $M_0(z) = N_0$ is the particular case when

$b_2' = 0$ (uniform density). In the next section a more general expression for the on-axis magnetic field of a solenoid with non-uniform winding's density $M_0(z)$ is derived.

2. MAGNETIC FIELD OF NON-UNIFORM SOLENOID

The on-axis magnetic field of a solenoid, represented in Fig.2, can be obtained by the solution of the following superposition integral [11]

$$B_z(z) = \frac{\mu_0 I R^2 N_0}{2} \int_{-L/2}^{L/2} \frac{(1 + b_2' z'^2) dz'}{[R^2 + (z - z')^2]^{3/2}} \quad (5)$$

where z' is the integral variable. It is convenient to introduce new *relative variables*: $\varsigma = 2z / L$, $\eta = 2z' / L$ and new *relative parameter*: $\rho = 2R / L$. It is clear that for a long solenoid the interest region of the last parameter is $\rho < 1$ or $L > 2R$. A substitution with the new variables into (5) yields

$$B_z(\varsigma) = \mu_0 N_0 I \frac{\rho^2}{2} \int_{-1}^1 \frac{(1 + b_2 \eta^2) d\eta}{[\rho^2 + (\eta - \varsigma)^2]^{3/2}} \quad (6)$$

where new coefficient $b_2 = b_2' L^2 / 4$ is involved. The particular case of $b_2 = 0$ can be solved by setting: $\eta = \varsigma + \rho \tan \varphi$ and by direct integration - this gives the well-known magnetic field of a uniform coil. Taking into account that $d\eta = \rho \frac{d\varphi}{\cos^2 \varphi}$ for the non-uniform coil is obtained

$$B_z(\varsigma) = \frac{\mu_0 N_0 I}{2} \left\{ D_0(\varsigma) + \left[b_2 \left[\varsigma^2 D_0(\varsigma) + 2\varsigma D_1(\varsigma) + \rho^2 D_2(\varsigma) \right] \right] \right\} \quad (7)$$

where new auxiliary integrals are introduced

$$D_k(\varsigma) = \int_{\varphi_1(\varsigma)}^{\varphi_2(\varsigma)} \tan^k \varphi \cos \varphi d\varphi \quad (k=0,1,2) \quad (8)$$

with the following integration limits

$$\varphi_1(\varsigma) = a \tan \left(\frac{-1 - \varsigma}{\rho} \right); \quad \varphi_2(\varsigma) = a \tan \left(\frac{1 - \varsigma}{\rho} \right) \quad (9)$$

For the uniform case ($b_2 = 0$) only the first integral $D_0(\zeta)$ survives and for an *infinite long* coil $L \rightarrow \infty$, $D_0(\zeta) \rightarrow 2$, that yields the *uniform* field (3).

After lengthy but straightforward calculations (omitted here) the following final expressions *in terms of elementary functions* are obtained for the three integrals above

$$D_0(\zeta) = \frac{\alpha_2(\zeta)}{\sqrt{1+\alpha_2^2(\zeta)}} - \frac{\alpha_1(\zeta)}{\sqrt{1+\alpha_1^2(\zeta)}} \quad (10)$$

with parameters

$$\alpha_1(\zeta) = -\frac{1+\zeta}{\rho}; \quad \alpha_2(\zeta) = \frac{1-\zeta}{\rho} \quad (11)$$

Similarly:

$$D_1(\zeta) = \frac{1}{\sqrt{1+\alpha_1^2(\zeta)}} - \frac{1}{\sqrt{1+\alpha_2^2(\zeta)}}, \quad (12)$$

and

$$D_2(\zeta) = D_3(\zeta) - D_0(\zeta) \quad (13)$$

Here new auxiliary integral is introduced

$$D_3(\zeta) = \int_{\varphi_1(\zeta)}^{\varphi_2(\zeta)} \frac{d\varphi}{\cos \varphi} \quad (14)$$

which leads to the following final expression

$$D_3(\zeta) = \ln \left| \frac{(1+t_2(\zeta))(1-t_1(\zeta))}{(1-t_2(\zeta))(1+t_1(\zeta))} \right| \quad (15)$$

where

$$t_1(\zeta) = \tan \left(\frac{\varphi_1(\zeta)}{2} \right); \quad t_2(\zeta) = \tan \left(\frac{\varphi_2(\zeta)}{2} \right) \quad (16)$$

is set.

The magnetic field of the solenoid with non-uniform winding's density can be found by *closed-term expression* (7), where the three auxiliary integrals are defined by expressions (10), (12), (13) and (15).

3. NUMERICAL RESULTS

Good enough results are obtained for the case of a long solenoid (when $\rho < 1$) – here the parameter b_2 is in the range $0 < b_2 < 1$. Several results of simulations in the special case $\rho = 0.2$ and with

different values of the parameter b_2 are shown in Figs. 3 – 5. For this particular case very uniform on-axis magnetic field is obtained for the value $b_2 = 0.12$ which may be considered as an *optimum* here (Fig. 4). The real range of the coordinate z is $0 \leq z < 0.5L$ ($0 \leq \zeta < 1$). However, we will explore the magnetic flux density $B_z(z)$ in the interval $0 \leq z < 0.3L$. For this particular choice *the magnetic field is very uniform*. For every value of the shape parameter ρ a suitable optimum value of the other polynomial parameter b_2 could be found. The corresponding winding's density for these three cases is shown in Fig. 6. It is obvious that to *compensate* the decreasing of the on-axis magnetic flux density near the ends a *suitable increasing* of the winding's density of the coil there has to be applied (see the curve for the optimal case $b_2 = 0.12$ with a dashed line).

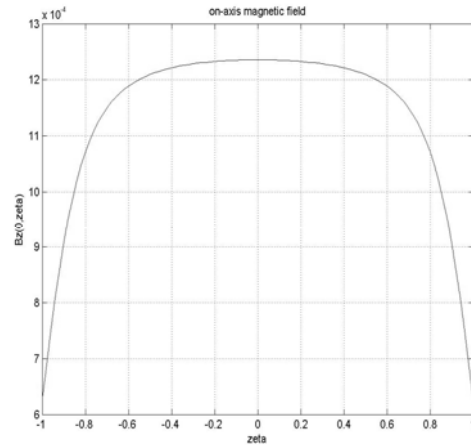


Fig. 3. Magnetic field for the case $b_2 = 0$ (uniform winding's density).

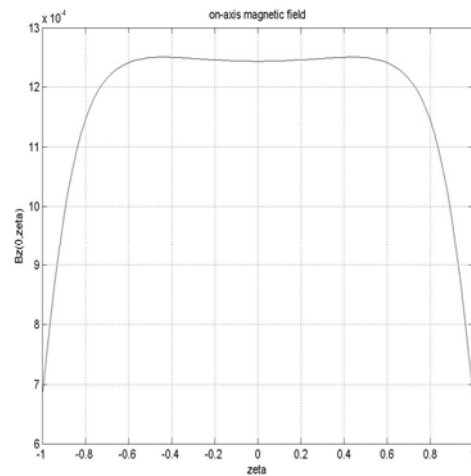


Fig. 4. Magnetic field for the case $b_2 = 0.12$ (optimal case)

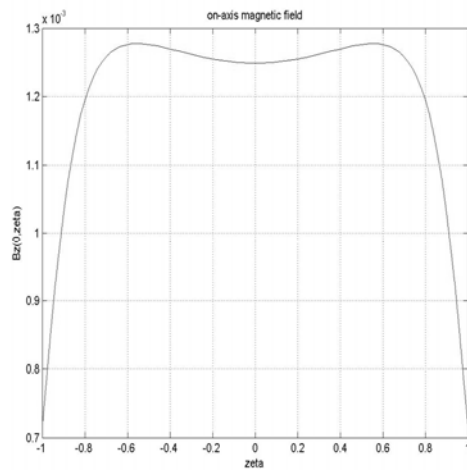


Fig. 5. Magnetic field for the case $b_2 = 0.20$

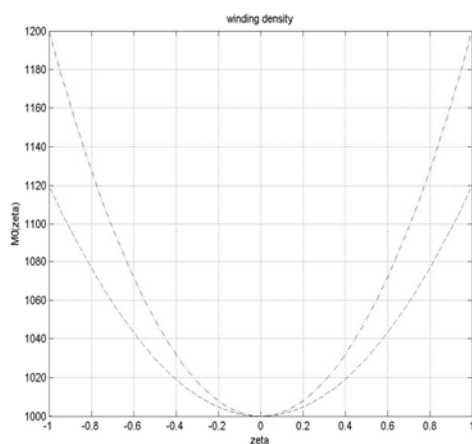


Fig. 6. Winding's density for the case $N_0 = 1000$
($b_2 = 0$ – solid line; $b_2 = 0.12$ - dashed line;
 $b_2 = 0.20$ - dash-dotted line)

4. CONCLUSION

In this paper one simple method of *improving the homogeneity* of the axial magnetic field of solenoid is considered. We have analyzed the case of variable winding's density – the numerical calculations are based on the derived equation (7) which involves *elementary functions only* for the integrals (8). They show that for every shape parameter $\rho = 2R/L$ a specific *optimum value* for the coefficient $b_2' = b_2 4/L^2$ of the polynomial (4) exists. The problem with achieving a *uniform magnetic flux density* B_z on the z-axis of a permanent magnet is important in the case of MRI and also in other medical applications [13 – 16].

5. ACKNOWLEDGMENT

Project no. 3 in the frames of the Research Program, financed from Ministry of Education of Bulgaria.

References

- [1] A. Podolski, "Design Procedure for Permanent Magnet Assemblies With Uniform Magnetic Fields For MRI Devices", *IEEE Trans. Magnetics*, vol. 36, no. 2, pp. 484 – 490, 2000.
- [2] L. Chu et al., "Efficiency Of Permanent Magnet For MRI Devices", *IEEE Trans. Magnetics*, vol. 41, no. 10, pp. 3835 – 3837, 2005.
- [3] M. Fuentes et al., "Analysis and Measurements of Magnetic Field Exposures For Healthcare in Selecting MR Environments", *IEEE Trans. Biomed. Engineering*, vol. 55, no. 4, pp. 1335 – 1346, 2008.
- [4] J. Jensen, "Minimum Volume Coil Arrangements For Generation Of Uniform Magnetic Fields", *IEEE Trans. Magnetics*, vol. 38, no. 6, pp. 3579 – 3588, 2002.
- [5] R. Guillemaud et al., "Estimating the Bias Field Of MR Images", *IEEE Trans. Medical Imaging*, vol. 16, no. 3, pp. 238 – 251, 1997.
- [6] C. Akgun et al., "Novel Multi-Channel Transmission Line Coil for High Field MRI", *IEEE Microwave Symposium Digest*, vol. 2, pp. 1425 – 1428, 2009.
- [7] J. Vaughan et al., "Current And Future Trends in MRI", *IEEE Microwave Symposium Digest*, pp. 211– 212, 2006.
- [8] F. Mohamed et al., "Image Nonuniformity Correction In High Field (1.5 T) MRI", *IEEE Proc. Engineering in Medicine and Biology Society Conference*, vol. 1, pp. 471 – 472, 1995.
- [9] B. Joonhan et al., "The Analysis Of the Initial Magnetic Field Decay In the Persistent Current Mode", *IEEE Trans. Applied Superconductivity*, vol. 10, no. 1, pp. 740 – 743, 2000.
- [10] R. Rojas et al., "Numerical Study of SNR and SAR of MRI Coil Arrays", *Proc. IEEE EMB International Conference*, pp. 1196 – 1199, 2007.
- [11] L. Chu et al., "Efficiency Of Permanent Magnet Assemblies For MRI Devices", *Magnetic Conference Intermag Asia Digest*, vol. 3, pp. 1959 – 1960, 2005.
- [12] R. Jackson, "Off-Axis Expansion Solution Of Laplace's Equation Application To Accurate And Rapid Calculation Of Coil Magnetic Field", *IEEE Trans. Electron Devices*, vol. 46, no. 5, pp. 1050 – 1062, 1999.
- [13] E. Zastrow et al., "Development Of Anatomically Realistic Numerical Breast Phantoms With Accurate Dielectric Properties For Modeling Microwave Interactions With Human Breast", *IEEE Trans. Biomed. Engineering*, vol. 55, no. 12, pp. 2792 – 2800, 2008.
- [14] Y. Gao et al., "Reduction of Artifact of Metallic Implant in MRI by Coating of Diamagnetic Material", *IEEE Trans. Magnetics*, vol. 45, no. 10, pp. 4837 – 4840, 2009.
- [15] I. Khalidov et al., "BSLIM: Spectral Localization By Imaging With Explicit B_0 Field Inhomogeneity Compensation", *IEEE Trans. Medical Imaging*, vol. 26, no. 7, pp. 990 – 1000, 2007.
- [16] S. Kazan et al., "Modeling the Effects Of Flow Dispersion In Arterial Spin Labeling", *IEEE Trans. Biomed. Engineering*, vol. 56, no. 6, pp. 1635 – 1643, 2003.

EDGE DETECTION IN ULTRASOUND MEDICAL IMAGES USING WAVELET DECOMPOSITION

Veska M. Georgieva

Faculty of Telecommunications, Technical University of Sofia, Bulgaria
1000 Sofia, "Kl. Ohridsky" str.8
T. (+359 2) 965-3998; E-mail: vesg@tu-sofia.bg

Abstract

In the paper is presented a new approach to edge detection using wavelet packet decomposition. The proposed wavelet based edge detection algorithm combines noise reduction with edge detection on a series of scales to achieve better results for shape and contours of different objects in the ultrasound (US) image. To reduce the specific noise, the input US image is decomposed on the base of wavelet packet transformation (WPT) by using soft threshold on all highpass subbands. The wavelet transform characterizes the local regularity of signals by their decomposing into elementary building blocks that are well localized both in space and frequency. This not only explains the underlying mechanism of classical edge detectors, but also indicates a way of constructing optimal edge detectors under specific working conditions. Then the wavelet model is applied for Canny edge detector to develop a multiscale wavelet model for edge detection.

In the paper are presented some results obtained by using the proposed algorithm. They are compared with results obtained by using of classical Canny edge detector and multiscale edge detector based on discrete wavelet transformation (DWT).

1. INTRODUCTION

Edge detection is a fundamental issue in image analysis. The classical edge detectors work fine with high-quality images, but often are not good enough for noisy medical images (especially in case of ultrasound images) because they cannot distinguish edges of different significance. There are two kinds of noise typically for US images: speckle noise and white noise [1]. Due to the presence of speckle, which can be modeled as a strong multiplicative noise and white noise can be modeled as an additive noise, edge detection in US images is difficult and methods developed for optical images are generally applied after a process of noise reduction. On the other hand approaches based on wavelet transform has been proposed separately for noise reduction and edge detection. Many existing methods for multiscale edge detection are based on DWT [2], [3].

In the paper is proposed to incorporate noise reduction and multiscale edge detection in US medical images as a single process. To reduce the specific noise, the input US image is decomposed on the base of WPT by using soft threshold on all highpass subbands. Then the wavelet model is applied for Canny edge detector to develop a multiscale wavelet model for edge detection.

2. STAGES FOR US IMAGES EDGE DETECTION

In this paragraph are presented the basic stages of the algorithm, used to improve image edge detection, shown in Figure1.

2.1. Noise model and preprocessing stage

In an image contained additive Gaussian white noise the basic model for each pixel is as follows (1):

$$s(x, y) = f(x, y) + n(x, y) \quad (1)$$

where $f(x, y)$ is the desired image, without noise, $n(x, y)$ is $N(0,1)$ noise.

As speckle noise is proportional to the desired signal it is generally modeled as multiplicative noise (2):

$$s(x, y) = f(x, y).n(x, y) \quad (2)$$

where $f(x, y)$ is the desired image, without noise, $n(x, y)$ is the noise.

Logarithmic transformation of a US image converts the multiplicative noise model to an additive noise model (3):

$$\log(s) = \log(f) + \log(n) \quad (3)$$

Our goal is to extract f and reduce the noise n .

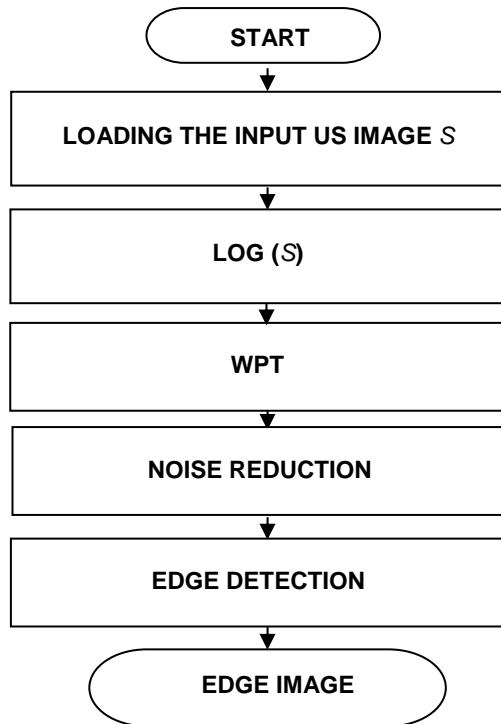


Fig. 1. Block diagram of the algorithm

2.2. Noise reduction

The next stage of the algorithm is noise reduction. It is based on the wavelet packet transform [4]. The wavelet packet analysis is a generalization of wavelet decomposition that offers a richer image analysis [5]. Based on the organization of the wavelet packet library, it can be determine the decomposition issued from a given orthogonal wavelets. As this number may be very large, it is interesting to find an optimal decomposition with respect to a conventional criterion. The classical entropy-based criterion is a common concept. It's looking for minimum of the criterion from three different entropy criteria: the energy of the transformed in wavelet domain image, entropy by Shannon and the logarithm of the entropy by Shannon [6]. By looking for best shrinkage decomposition to noise reduction two important conditions must be realized together [7]. They are the conditions (4) and (5):

$$E_K(S) = \min, \quad \text{for } K = 1, 2, 3 \dots n \quad (4)$$

where E_K is the entropy in the level K for the best tree decomposition of the image s

$$s_{ij} \geq T \quad (5)$$

where s_{ij} are the wavelet coefficients of s in an orthonormal basis, T is the threshold of the coefficients.

By determination of the threshold it is used the strategy of Birge-Massart. This strategy is flexibility and used spatial adapted threshold that allows to determine the threshold in three directions: horizontal, vertical and diagonally. It is focused on soft thresholding technique which consists in putting to zero all detail wavelet coefficients of amplitude smaller than T , reducing the amplitude of the other coefficients by the quantity T [5].

2.3. Edge detection

Wavelet filters of large scale are more effective for noise reduction, but at the same time increase the uncertainty of the location of edges. Canny edge detection method is optimal for step edges corrupted by white noise, with application of additive noise model. It is used three criteria to design edge detector. The first requirement is reliable detection of edges with low probability of missing true edges, and a low probability of detecting false edges. Second, the detected edges should be close to the true location of the edge. Third, there should be only one response to a single edge. Canny edge detection uses the first derivative of a Gaussian as its filter. The choice of the standard deviation σ for the Gaussian filter depends on the size, or scale, of the objects contained in the image. From the point of wavelet transforms, it can be used more effective approach to adjust the scale of the filters. So the wavelet best shrinkage decomposition to noise reduction of the US image can be used as wavelet model for Canny edge detection. The level of decomposition can be selected in depending on the requirement of details desired in the edges.

3. EXPERIMENTAL RESULTS

The formulated stages of processing are realized by computer simulation in MATLAB environment by using IMAGE PROCESSING TOOLBOX and WAVELET TOOLBOX. In analysis are used 20 grayscale US images from cardiology with size 640X 480 pixels.

Errors as "missed detection" and "false alarm" in edge detection are minimized when the SNR of the detection filter is maximized. In the paper are analyzed some quantitative estimation parameters:

Coefficient of noise reduction (CNR), Signal to noise ratio in the noised image (SNR_Y), Signal to noise ratio in the filtered image (SNR_F), Effectiveness of filtration (E_{FF}), PSNR [8]. In Table 1 are presented the obtained average results from simulation by using the proposed algorithm. They are compared with results obtained by using of classical Canny edge detector and multiscale edge detector based on discrete wavelet transformation (DWT).

Table1. Simulations results

Method of edge detection	Estimations Parameters				
	PSNR [dB]	CNR	SNR_Y [dB]	SNR_F [dB]	E_{FF} [dB]
Canny edge detection (CED)	21.963	0.857	4.515	7.463	3.947
Noise reduction with DWT+CED	23.812	0.533	6.949	12.116	5.167
Noise reduction with WPT+CED	23.855	0.255	11.518	16.739	5.862

The best results are obtained by proposed approach including noise reduction on the base of WP transformation. The CNR is minimum (0.25) and shows that the noise is four times reduced. The values of SNR_F , E_{FF} and PSNR are more sufficient.

On Figure 2 is illustrated the original grayscale US image of size 640x480 pixels. On Figure 3 is shown its edge map image, obtained from Canny edge detection method. On Figure 4 is illustrated the edge map image after noise reduction on the base of DWT and Canny edge detection.

Figure 5 presents the edge map image for the proposed approach. The best shrinkage decomposition to noise reduction is obtained by Shannon entropy criterion. In depending on the requirement of details desired in the edges the selected level of decomposition is 3.



Fig. 2. Original US image

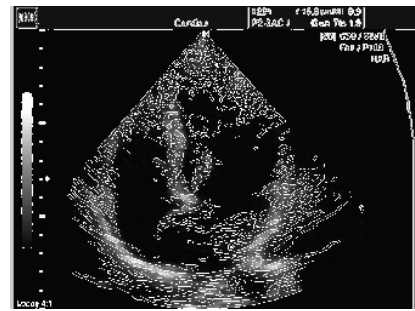


Fig. 3. Edge map of US image, obtained by Canny edge operator

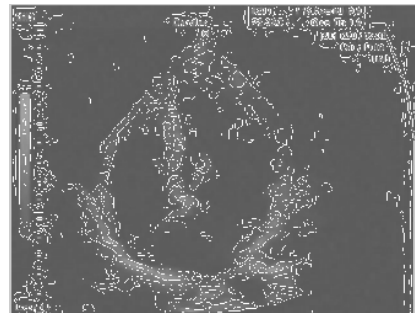


Fig. 4. Edge map of US image, obtained by noise reduction on the base of DWT and Canny edge operator

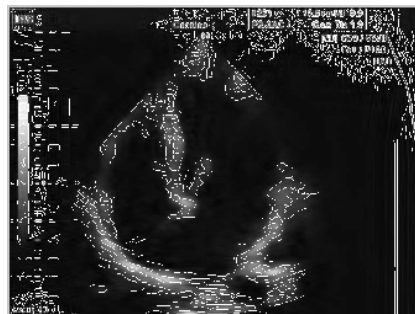


Fig. 5. Edge map of US image, obtained by proposed approach

4. CONCLUSION

In the paper is presented a new approach to edge detection using wavelet packet decomposition. The proposed wavelet based edge detection algorithm combines noise reduction with edge detection on a series of scales to achieve better results for shape and contours of different objects in the ultrasound images. The implemented studying and obtained results by using of real images attempt to make diagnostic more precise.

The proposed approach can be demonstrated by studying of medical image processing in engineering and medical education.

References

- [1] M. Smith, A. Docef, "Transforms in telemedicine applications", Kluwer Academic Publishers, 1999.
- [2] S. Mallat, S. Zhong, "Characterization of signals from multiscale edges", IEEE Trans. PAMI, 14 (7), pp.2207-2232, 1992.
- [3] S. Madchakham, P. Thitimajshima, P. Rakprathanporn, "Edge detection in speckled SAR images using wavelet decomposition", Proceedings of the 22nd Asian Conference on Remote Sensing, pp. 325-328, 2001.
- [4] V. Georgieva, "An application of wavelet transforms for ultrasound images enhancement," *Journal of Electrical Engineering and Elelectronics*, vol. 42, pp. 78-83, May, 2007.
- [5] D. Donoho, I. Johnston, "Adapting to unknown smoothness via wavelet shrinkage", Am. Stat. Assoc., 1995, 90:1200-1224
- [6] R. Coifmann, M. Wickerhauser, "Entropy based Algorithms for best basis selection", IEEE Transaction on information theory, Vol.38, 1992, pp.713-718.
- [7] V. Georgieva, R. Kountchev, "An influence of the wavelet packet decomposition on noise reduction in ultrasound images", Proceedings of ICEST'06, Sofia, Bulgaria, 2006, pp.185-188.
- [8] R. Gonzalez, R. Woods, Digital Image Processing, Addison Wesley Publishing, 1992.

GUI FOR EDGE DETECTION IN MEDICAL IMAGES

Veska M. Georgieva

Faculty of Telecommunications, Technical University of Sofia, Bulgaria
1000 Sofia, "Kl. Ohridsky" str.8
T. (+359 2) 965-3998; E-mail: vesg@tu-sofia.bg

Sofiya P. Shtarbova

Faculty of Computer Systems and Control, Technical University of Sofia, Bulgaria
1000 Sofia, "Kl. Ohridsky" str.8
E-Mail: sofiya_psht@abv.bg

Abstract

In the paper is presented software for edge detection and contour segmentation of objects in medical images and its graphic user interface (GUI). It works in the MATLAB environment and uses IMAGE TOOLBOXES defined functions. Different operators for edge detection and contour segmentation with different parameters can be used, regarding to process different medical modalities of the images. The GUI proposes also an interactive option to choose the type of the edge detection operator and also its parameters.

The aim of algorithms, based on edge detection, is detail preservation abilities of the different objects in medical images or in their selected region of interest (ROI). The quality of the edge detection and his stability of noises can be also estimated.

The proposed GUI can be applied to real medical images attempt to make diagnostic more precise. The presented GUI is suitable also to engineering education for studying of this processing.

1. INTRODUCTION

Edge detection is an important task in medical image processing [1]. It is a main tool in pattern recognition, image segmentation and scene analysis. An edge detector is basically a high pass filter that can be applied to extract the edge points in an image. It is realized by the convolution with a set of directional derivative masks [2], [3].

The aim of algorithms, based on edge detection, is detail preservation abilities of the different objects in medical images. By properly choosing of different type of classical operators for edge detection such as: Roberts, Sobel, Prewitt, Laplacian of Gaussian, Zerocross, Canny and their parameters different medical modalities of the images can be processed.

The software is created in MATLAB 6.5 environment by using IMAGE PROCESSING TOOLBOX.

The graphic user interface consists of checkboxes, buttons, edit boxes, pop-up controls, which make it easy to use. Users enter or choose input data in a single form, because input information changes and visualizations are easier and faster in this way.

The processed image can be saved on the disk and so can be used to another processing or its visualization.

2. THE GUI FOR EDGE DETECTION IN MEDICAL IMAGES

The GUI for edge detection in medical images is shown on Fig.1. It is divided in several areas, where the user applies different settings, concerning edge detection operators and theirs parameters.

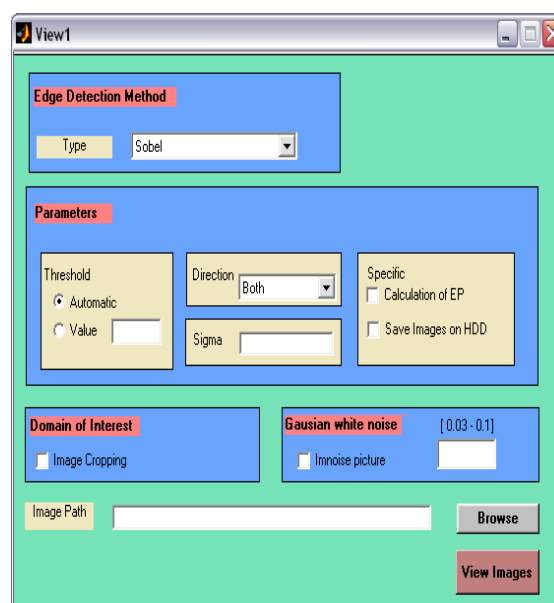


Fig. 1. GUI for edge detection of medical images

The area "Image Path" is for entering an image file name with an image file extension. The image

file for edge detection must be in the same directory (folder), where the main program and the rest modules are. The user can navigate among the folders in the work folder and choose image by using "Browse" button. The edge detection operator can be selected in area "Edge Detection Method", shown in Fig. 2.



Fig. 2. Area "Edge Detection Method"

The selection is realized through drop-down menu and it contains the following operators: Sobel, Prewitt, Roberts, Laplacian of Gaussian, Zerocross and Canny [5]. Selecting appropriate parameters is an important part in edge detection of medical images. It can be selected in area "Parameters", shown in Fig. 3.

The first parameter is the Threshold. There are two options: Automatic generation of the threshold (Automatic) or manual input of the threshold (Value). When "Automatic" radio button is selected the generated value for the threshold is visualized at the bottom of the GUI in red color.

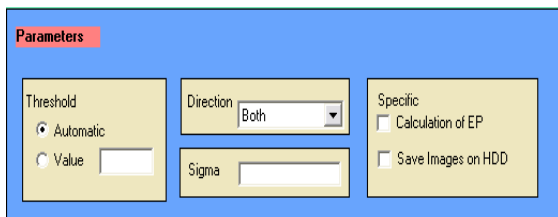


Fig. 3. Area "Parameters"

The second parameter is the Direction, shown in Fig.4. This is a drop-down menu with three values: Both, Horizontal and Vertical.

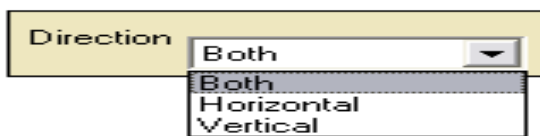


Fig. 4. Area "Direction"

Another parameter is standard deviation σ ("sigma"), which has to be manually filled in. The

choice of the standard deviation for the Gaussian filter depends on the size of the objects in the image.

The area "Specific" gives an opportunity to save results in image files in 'jpg' format if 'Save Image on HDD' is checked and estimate edge detection quantitative estimation parameters if "Calculation of EP" is checked, as shown in Fig.5.



Fig. 5. Area "Specific"

Selecting check box "Image Cropping" located in area "Domain of Interest" or "Region of Interest" (ROI) is shown in Fig. 6. It gives the opportunity to process only part of the image.



Fig. 6. Area "ROI"

It is possible to apply additive white Gaussian noise on the image by selecting the check box "Imnoise picture" located in area "Gaussian white noise", shown in Fig. 7. This option requires standard deviation parameter σ for the Gaussian white noise, which has to be manually filled in and the value has to be between 0.001 and 0.1.



Fig. 7. Area "Gaussian white noise"

After choosing all input information the procedure of edge detection processing begins, when the user clicks on button 'View images'. Then the final result is shown – original image, and processed images.

3. TASKS CARRIED OUT FROM THE MAIN PROGRAM

By acting of component from GUI can be implemented a callback-function from the main program. Every graphic component can be treated to object. Every object can be referred to handle. The objects

referred a complex of attributes, which can be manipulated from the software. The multifarious attributes can be left for using in MATLAB environment, such as "Enabled", "Value", "Visible", "On", "Off" etc.. Every attribute can be enabling in the presence of corresponding handle or reference to the object. Every graphic component can be reiterated to a cycle of events for the MATLAB environment by initialization of the graphic application. It submits addresses of the callback-functions, associated to a given event, which are important. By its identification can be called out a corresponding callback-function. One of the important tasks that the main program has is input data validation. The execution is canceled if an error concerned with wrong information occurs. Another essential purpose of the main program is presenting the input information in appropriate data structures. It is necessary for the next steps in the processing strategy, in this step the processing is made with appropriate input data. Wrong information prevents edge detection from carrying out or may lead to wrong output.

Some of the classical edge detectors do not work well with noisy images, because their SNR is not maximized through the detection filter [3]. The applied algorithm calculates also some objective quantitative estimation parameters as: CNR, Signal to noise ratio in the noised image (SNR_Y), Signal to noise ratio in the filtered image (SNR_F), Effectiveness of filtration (E_{FF}), PSNR [4]. On the base of their analysis the quality of the edge detection and his stability of noises can be also estimated.

In Fig. 8 is shown an original gray scale ultrasound image (US) with size 640x480 pixels from urethra. In Fig. 9 are shown respectively the visualizations of its original and noised ROI images with size 210x150 pixels and their modifications by processing of three different classical edge operations: Sobel, Zerocross and Canny operator. The thresholds for all operators are automatic selected from the program. The noise is additive Gaussian white noise with standard deviation $\sigma = 0.03$.



Fig. 8. The original US Image

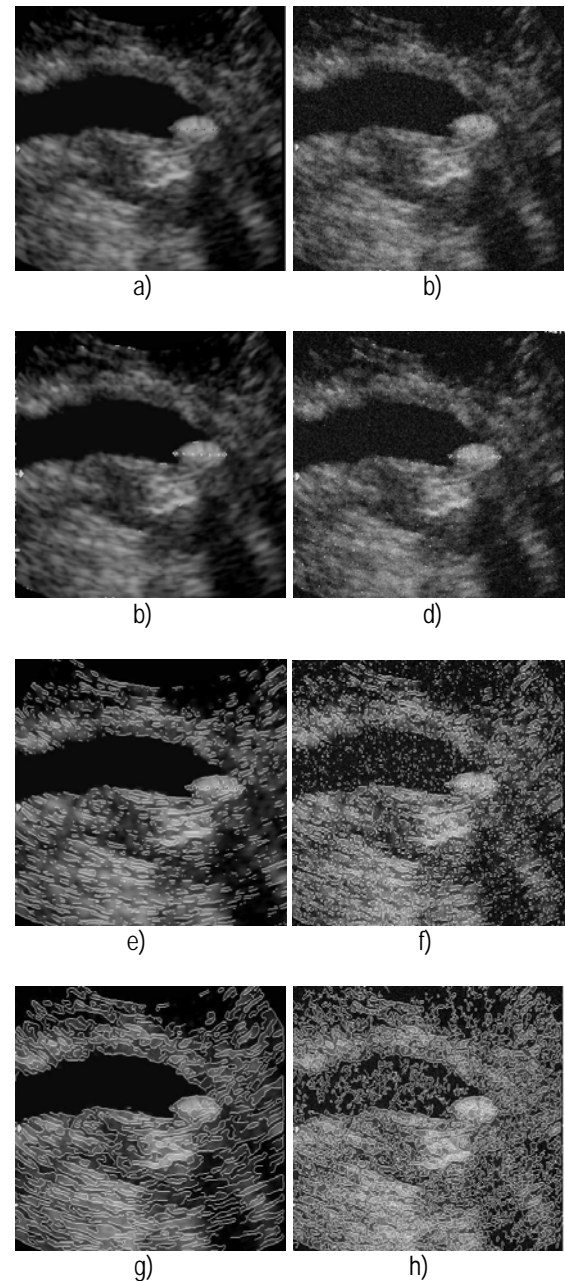


Fig. 9. US ROI Images: a) original; b) noised; c) original image by processing with Sobel operator; d) noised image by processing with Sobel operator; e) original image by processing with Zerocross operator; f) noised image by processing with Zerocross operator; g) original image by processing with Canny operator; h) noised image by processing with Canny operator

4. CONCLUSION

In the paper is presented a GUI for edge detection in medical images. It uses MATLAB defined function and works in MATLAB 6.5 environment. The pre-processing can realize a contour segmentation by using of different classical type of edge detection operators and its parameters. The GUI can be used in engineering education for studying this process. It can be used also in real time to pro-

vide important anatomical information in medical images to physicians and specialist upon which can be made diagnoses of different diseases.

References

- [1] M. Smith, A. Docef, "Transforms in telemedicine applications", Kluwer Academic Publishers, 1999.
- [2] R.M.Haralik, "Digital step edges from zero crossing of second directional derivatives", IEEE trans. Pattern Anal. Machine Intell., Vol.PAMI-6,No.1, pp.58-68, 1984
- [3] J.Canny," A computational approach to edge detection", IEEE trans. Pattern Anal. Machine Intell., Vol.PAMI-8, pp.679-698, 1986
- [4] R.Gonzalez, R. Woods, Digital Image Processing, Addison Wesley Publishing, 1992.
- [5] W.Pratt, Digital Image Processing. New York: John Wiley and Sons, 2001
- [6] MATLAB, User's Guide, www.mathwork.com

DEVELOPMENT OF A MOBILE TELEMEDICINE SYSTEM WITH MULTI COMMUNICATION LINKS FOR URBAN AND RURAL AREAS IN BULGARIA

Deyan M. Milev

*Radiocommunications and Videotechnologies Department
Technical University – Sofia
8 Kliment Ohridski Blvd., 1000 Sofia
BULGARIA
E-mail: dmilev@tu-sofia.bg*

Abstract

Telemedicine, the use of information technology to deliver health care from one location to another, has the potential to increase the quality and access to health care and to lower costs. Telemedicine besides facilitating the delivery of quality healthcare to the remotest regions, can also prove to be useful to increase the efficiency of urban physicians whose main target is the urban masses.

This software system offers a telemedicine platform with the ability to create a clinical analysis with textual information and data from biomedical peripherals, and send data for consultation. Health care professionals are able to view the data and respond to the case using a Personal Computer from remote.

Since the delay is the enemy for patients, so the integrated and high-speed telecommunication is an optimal option for Telemedicine systems.

Index Terms: Telemedicine, telehealth Internet, Java

1. INTRODUCTION

Application of electronics, computer and telecommunication technology for medical information exchange from one site to another, to facilitate the improvement of health care delivery.

Lessons learned from other developing countries indicated that usage for community purpose would face problems in operations and cultural sustainability, even with the relatively low-cost internet-based system. Computer networks have made it possible to share electronic medical records and to deliver medical expertise via remote consultation. Web-based telemedicine systems have been attempted by many researchers, and the most approaches are experimented with the use of videoconferencing for remote consultation [1].

Prevention and treatment interventions on this scale require efficient information management, which is critical as clinical care must increasingly be entrusted to less skilled providers. To help them, we need to find a way not only to improve management tools, but also to reduce unnecessary, duplicate efforts[2]. To overcome the problems, proposed development of internet-based community telemedicine in Bulgaria should be based on the concept of initially focusing on the essentials. In this paper, we developed telemedicine system to promote the idea of E-medicine.

Characteristics in the system

- Provides the efficient and convenient methods for patients and doctors to communicate with each other and allows patients to send their medical data/image through the Internet;
- Build computer-based patient records and other electronic information systems that provide relatively easy and fast access to large databases and that permit the application of powerful statistical methods for analysing and displaying those data;
- Potentially allows easier access to more information about a patient than the user either requests or needs.

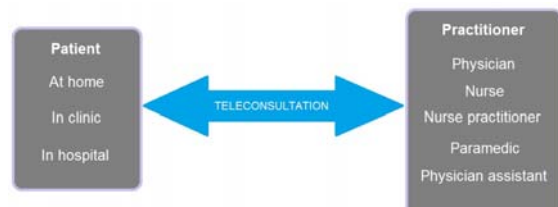


Fig. 1. Real-time video conferencing between a practitioner and a patient or between a practitioner and patient and another specialist practitioner.

Fig. 1 show ways in which telehealth can be used in determining the problem and making a diagnosis.

The inability to examine a patient directly is frequently raised as a criticism of telehealth's capacity

to discover patients' problems and make a correct clinical diagnosis. The fact that face-to-face consultations the correct clinical diagnosis is usually made in 60%-80% of cases from the clinical history alone suggests that telehealth should be able to make a correct diagnosis in the majority of cases as long as a detailed clinical history is taken[3].

Clinical research comparing telehealth with conventional methods of clinical examination and interpreting investigations suggests that telehealth is a reliable way of making clinical diagnosis remotely. The diagnostic accuracy of telehealth consultations does not have to be 100% equivalent to conventional methods of clinical practice to make telehealth a workable proposition. If a telehealth application is consistently reliable in a sufficient percentage of cases and is of high quality and lower cost, it can safely replace some, but not all, elements of conventional clinical practice.

Types of telemedicine information.

In a face-to-face consultation, a physician might use some combination of all five senses-sight, sound, touch, smell and taste-to assess a patient's condition. In telemedicine, however, the sensory data are first converted into electrical impulses for transmission to the remote physician.

Methods to convert smell and taste stimuli into electrical signals are still in the experimental stage and, while the sense of touch can be translated successfully into an electrical equivalent, the reverse process is more difficult and not well understood.

Hence, a consultation relies primarily on the two senses of sight and sound[6].

The information (useful data) derived from these senses can be divided into four types:

- text and data;
- audio;
- still (single) images;
- video (sequential images).

Table 1 gives telemedicine examples of these types along with their typical file size in kilo- or megabytes following digitization [4].

Table 1. Typical examples of telemedicine information

Source	Type	File size
Patient notes	Text	< 10KB
Stethoscope	Audio	100 KB
Chest X-ray	Still image	1 MB
Ultrasound	Video	10 MB

2. MAIN TEXT

Telemedicine in Bulgaria is a new, seductive, and superficially easy-to-use technology, there tends to be a belief among health service managers that it can simply be made available to clinicians who will automatically accept and use the telemedicine systems.

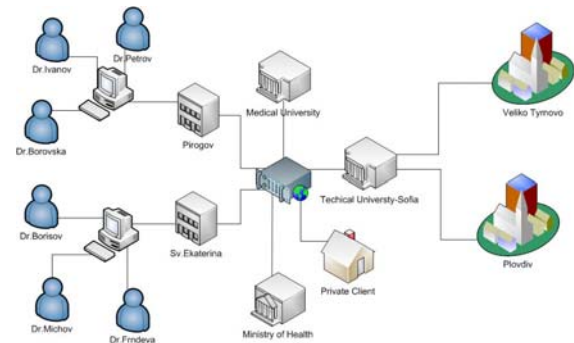


Fig. 2. TU-Sofia Telemedicine Network

Every developed nation throughout the world, whatever the political persuasion of its government, is facing serious difficulties with the delivery of healthcare to its citizens[5].

The USA and the countries of Europe exhibit the full diversity of these different systems but they face the same daunting problems, particularly:

- the increasing age of the population;
- the increasing cost of medical technology;
- patient expectations;
- economic and social change

These and other factors drive up the cost of healthcare and reduce equity of access. [7]

These advantages are difficult to factor into the cost-benefit equation but they are attractive to countries such as Australia, Canada, Sweden, Norway and Finland where distance and/or climate prevent rural communities from experiencing the same provision of services as their urban counterparts.

The priorities in underdeveloped countries are very different. Often finance, organization, culture and/or distance do not allow the authorities to provide even basic healthcare[8].

While underdeveloped countries are unable to finance these programmes themselves, a surprising amount of progress can be made with small clinics, voluntary organizations and satellite links to specialists in industrialised countries.

3. SYSTEM ARCHITECTURE

In this system, JBoss server maintains the whole system, which includes Seam Framework, RichFaces, Hibernate, and PostgreSQL object-relational database system. JBoss, by Red Hat, is the leader in enterprise-class open source middleware. JBoss Enterprise Middleware is comprised of certified, supported platform and framework distributions that are based on JBoss Community projects.

Seam is a powerful open source development platform for building rich Internet applications in Java. RichFaces is an open source framework that adds Ajax capability into existing JSF applications without resorting to JavaScript. Hibernate is concerned with data persistence as it applies to relational databases.

System Management can be specified as a combination of Service System, Information System, Entertainment System, Security System and Department Administration System. And every system performs particular functions.

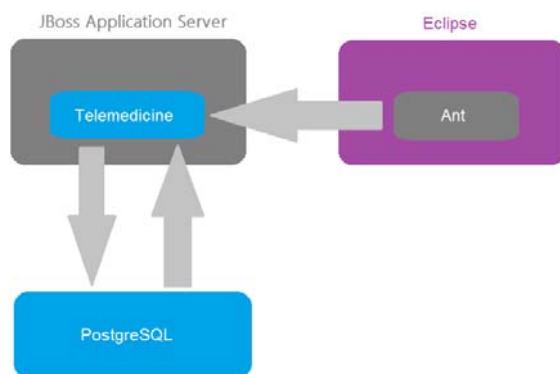


Fig. 3. System Architecture

The approaches to home monitoring range from low-cost and easy to use touch-tone telephone systems to more expensive systems that mimic the real-time videoconferencing approach in traditional telemedicine and web-based systems that allow access to patient data from anywhere an Internet connection is available[9].

These systems are different from web interfaces to medical records systems at hospitals. In the hospital systems, only care providers can view and add information to records. In the patient-targeted systems, patients can access their records. One of the advantages of current database systems is the capability to enforce global integrity constraints on a large amount of data. Input of contradicting data will be rejected by database systems in order to maintain correctness. On the other hand, in medical

information systems it may be necessary to realize two or more databases in one system, where there are some controlled contradictions among these databases.

Data sharing and data security are important functions required for medical information systems. There are, however, cases when we need to show non-real data to some users. Security mechanisms usually prevent a user from retrieving critical data. If a request for retrieval of some data is rejected by the system, a user may find there is something secret being kept from him. Using PostgreSQL rule system in medical information systems, doctors can make a smooth explanation of a patient's condition in serious cases, when hiding real data is required [10].

I believe that PostgreSQL rule system can be applied to many fields in medical data processing.

CONCLUSION

The goal of this E-Medicine system was to demonstrate that an asynchronous web-based telemedicine system could be successfully implemented with low-cost components that are available off the shelf.

Even novice computer users were able to operate the system, although the web browser user interface may be too complex for some.

A larger trial with a patient population that has a greater need for telemedicine support is needed to comprehensively test the clinical impact of E-Medicine systems.

In conclusion, after painting a brief picture of some of the interests affecting telehealth, we see a rosy future. The unifying point of contact among government, professional groups in health care, and the telecommunications industry is a focus on consumers. The interest of the telecommunications companies is in providing the pipeline for services into the home. It is interesting to see the interest of consumer IT companies in health care on the Internet as a major area of growth potential.

References

- [1] MARILYN J., "Telemedicine". Committee on Evaluating Clinical Application of Telemedicine, National Academy Press, Washington, D.C. pp. 20-52, 1996.
- [2] H.K. HUANG, D.Sc., "PACS", A John Wiley & Sons, Inc., publication, pp.449-467, 1999.

- [3] XIN LI, DANIE J. VALETINO, George J., " A world wide web telemedicine System" ,SPIE Proceedings of Medical Imagine1996. PACS: design and Evaluation, vol.2711,pp.427-439,1996.
- [4] MOUKHEIBIR NW, "The digital clinical diagnostic process: An application for telemedicine over the Internet." *Telemedicine Today*, Jun/Jul, 2000.
- [5] Charles, B. L., "Telemedicine can lower costs and improve access", *Healthcare Financial Management*, 54(4), The Healthcare Financial Management Association, Oak Brook, Ill., 2000, pp. 66-69.
- [6] Field, Marilyn J. (Eds.), *Telemedicine: A Guide to Assessing Telecommunications in Health Care*, National Academy Press, Washington, D.C., 1996, pp. 26.
- [7] Bashshur, Rasid L., Teardon, Timothy G. and Shannon, Gary W., "Telemedicine: A new health care delivery system", *Annual Review of Public Health*, 21, Annual Reviews, Palo Alto, Calif., 2000, pp. 613-637
- [8] Huston, Terry L and Huston, Janis L., "Is telemedicine a practical reality?", *Communications of the ACM*, 43(6), Association for Computing Machinery, Baltimore, Md., 2000, pp. 91-95
- [9] Bashshur, R. L., "On the definition and evaluation of telemedicine", *Telemedicine Journal* 1(1), Mary Ann Liebert, Inc., Larchmont, New York, 1995, pp. 19-39
- [10] Moscovice, I., Wellever, A., Christianson, J., Casey, M. and Yawn, B., "Understanding integrated rural health networks", *Milbank Memorial Fund Quarterly*, 75, Milbank Memorial Fund, New York, NY, 1997, pp. 563-588.

VULNERABILITY OF MEDICAL IT SYSTEMS MANAGEMENT LIFE-CYCLE

Lidya Jordanova, Tzveta Dimitrova

Faculty of Telecommunication, Technical University - Sofia, 8, "Kliment Ohridsky" str., 1000 Sofia, Bulgaria,
E-mail: tz.dimitrova@gmail.com

Abstract

This paper aims at telemedicine practitioners and the challenges they face in managing IT security vulnerabilities in their medical organizations. In the course of this work it is pinned down the most important challenges and introduced possible solutions. The benefits and opportunities that come with these solutions, as well as their limitations are outlined.

The goal is to show how vulnerability management can be a valuable organizational tool for telemedicine companies to:

- 1) Reach continuous compliance with legal regulations,
- 2) become more cost effective in their IT operations
- 3) build a more robust business environment that allows them to compete with ever more professional attackers.

1. INTRODUCTION

Vulnerabilities in medical IT systems and software are caused by various factors, but most commonly faulty system configurations, bad system design or poor quality. In the case of faulty configuration, the cause of the vulnerability and responsibility to fix it lies in the same hands: the users. In the latter cases however, one might argue that the responsibility to find and fix vulnerability are on the vendor's side. Unfortunately, there too the user is often required to take matters into their own hands. Clever vendors have realized the business risks that come with software vulnerabilities and consequently try to externalized them: They've created end-user license agreements (EULA) which free the vendors from security vulnerability related liabilities [1] and place the task of finding and fixing vulnerabilities back in the hands of the use.

2. WHAT IS DRIVING VULNERABILITY MANAGEMENT IMPROVEMENT EFFORTS?

There are three major influences that drive improvement efforts in today's vulnerability management:

- 1) Attacks on the IT systems of medical computer networks and individuals are increasingly professionalized.
- 2) The costs from security incidents and their counter measures are rising: In 2007 the CSI Computer Crime and Security Survey found that the average annual costs for reported security breaches in U.S. companies had nearly doubled since 2006 [Richardson07] [Welberg08].

- 3) New corporate governance legislation now mandates adequate security vulnerability management processes in companies and medical computer networks which handle financial records, payment card information or privacy-critical data.

Individually, these factors already drive medical computer networks to invest more in their security efforts, but where two or more of them apply at the same time, the need for improvement becomes even more evident.

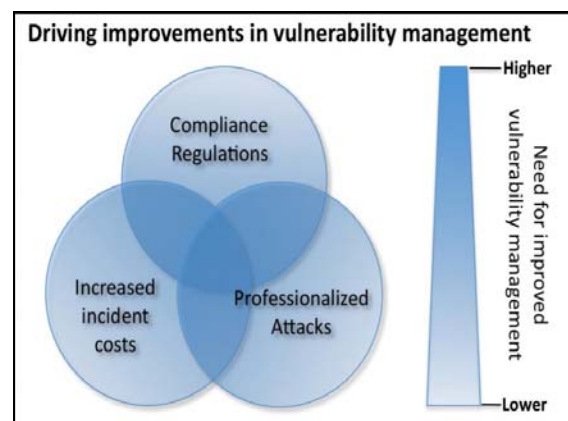


Fig. 1. Depicts the growing importance of improvements in which several vulnerability management several factors overlap

3. CHALLENGES FOR MEDICAL ORGANIZATIONS

Each of the three driving factors of vulnerability management presents a distinct set of challenges that medical computer networks need to address in their improvement efforts.

3.1. Attacker and defender fight on unequal terms

The attacks on medical computer networks and individuals are increasingly professional and profit-driven. In the context of today's Black-Hat1 community, professionalization means more resources are available to develop highly sophisticated tools, which allow attackers to automatically scan for exploitable security vulnerabilities in potential targets. The application of automation further enables attackers to use economics of scale to their advantage, by conducting parallel vulnerability scans on thousands of targets at the same time instead of just one, with little or no additional risk for the attacker.

Attackers can leverage the economics of scale while defenders often rely on individual efforts, resulting in a long half-life of unpatched vulnerabilities in medical organizations.

Protecting the integrity of systems and data is essential for achieving continuous compliance with regulations like the PCI-DSS, ISO 27001, SOX and others.

4. CHANGING THE GAME OF VULNERABILITY MANAGEMENT

How did medical computer networks engage in security vulnerability management before and what changed their way of thinking?

When the vulnerability management issue first appeared in medical organizations, their security staff often created individual solutions that could be executed manually and were tailor-fit to the organizations particular environment.

The manual approach was well suited for highly customized and fairly static systems, but it brought along a series of problems, that did not surface until medical computer networks started to grow and their IT systems began to change. In the context of vulnerability management, four particular issues stand out as „game-changers“: 1) growing dynamics, 2) commercial off-the-shelf software, 3) industry standards, and 4) compliance regulations.

4.1. Change driver: Growing dynamics

Organizational growth, faster technology cycles, and growing business dynamics create a series of problems for manual vulnerability management:

As a company introduces new systems more often, it needs to conduct vulnerability assessments in shorter intervals [3].

Changes in IT systems require customized vulnerability solutions to be adapted or replaced.

Frequent changes in vulnerability management tools and processes make it hard to compare results across platforms or over time. Time comparison is valuable to identify trends and evaluate the success of management decisions (e.g. “have our recent IT investments made us more secure, compared to last year?”).

Timely patching of vulnerabilities becomes increasingly important: The time period between the public announcement of vulnerabilities and the availability of first exploits has been shrinking, thus leaving medical computer networks with less time to find and react to threats.

4.2. Change driver: COTS software

Many custom applications required unique vulnerability management solutions, which effectively prevented medical computer networks from establishing economics of scale in their security efforts. The advent of commercial off-the-shelf software (COTS) products greatly improved this situation by standardizing interoperability between software systems and vulnerability management solutions.

4.3. Change driver: Common standards for vulnerabilities

In an effort to further advance interoperability, industry medical computer networks introduced a set of vulnerability standards.

Two of the most influential ones are the CVE and CVSS: The Common Vulnerability Enumerator “CVE” established a dictionary of publicly known security vulnerabilities and enables different security solutions to share a common language when referring to particular vulnerabilities.

The Common Vulnerability Scoring System “CVSS”, was introduced to enable comparison and prioritizations of vulnerabilities based on their severity. CVSS uses scores between 0 to 10, where 10 indicates the most critical vulnerabilities.

4.4. Change driver: Compliance

Legislators and industry medical computer networks worldwide established corporate governance regulations in an attempt to improve the transparency and accountability of corporate governance processes. A central goal of these efforts was to

establish common standards for risk management across medical computer networks that include the management of information security and vulnerabilities.

Several of these standards, like the PCI-DSS2 , ISO/IEC 270013 , Sarbanes Oxley Act (SOX section 404)4 , GLBA5 or Basel II are particularly relevant for security management issues, and have changed the way vulnerabilities need to be managed [Blount06]. In order to achieve continuous compliance, companies need to fulfill new requirements that strain the possibilities of traditional, manual vulnerability management processes.

Even though the compliance requirements differ between the individual standards, we can identify a set of common requirements in the security and vulnerability management.

Req.1 - Proactive Vulnerability Analysis: An organization needs to actively search for potential points of weakness in their systems.

Req.2 - A consistent auditing model across all platforms: All platforms (e.g. operating systems, application servers, etc.) need to be subject to the same security baseline and auditing.

Req.3 - Documented processes: The security management activities are to follow a consistent and formalized process.

Req.4 - Advanced reporting capabilities: Reports should be generated in human-readable ways, where the understanding of complex issues can be facilitated through meaningful forms of representation (e.g. graphical).

Req.5 - Report customization: Reports should be tailored to the individual business context to improve applicability and reduce overhead.

Req.6 - Flexible Alerting and notification services: Discovered security issues should be brought to the attention of the responsible roles within the organization in a timely manner.

5. VULNERABILITY MANAGEMENT LIFECYCLE

Phase 1 - Identify the threat exposure: Which systems are vulnerable and are those vulnerabilities exposed to potential attackers?

Phase 2 - Quantify the risk: How severe is the vulnerability compared to others, and how dangerous is it in the organizations particular business context?

Phase 3 - Manage countermeasures: Identify and apply available countermeasures to resolve the vulnerability.

Each phase in the vulnerability management lifecycle consists of a number of individual process activities. The following Table 1 lists examples of these activities for each of the three lifecycle phases (P1-P3) and exemplifies how automation can be integrated in them.



Fig. 2: Vulnerability Management lifecycle

6. CONCLUSION

In writing this paper, it is set out to show how medical computer network scan use IT security vulnerability management as a tool to 1) reach continuous compliance, 2) become more cost effective in their IT operations and 3) build a more robust environment that allows them to compete with professional attackers.

For the first goal, it is proposed a vulnerability management lifecycle that is structured, easy to document, and benefits from the use of automated activities.

Automation in the discovery, prioritization, and reporting of vulnerabilities help companies to realize economics of scale and become more cost-effective in their security operations.

While cost-effectiveness was the primary concern of the second goal, the use of automated and consistent auditing models also improves cost-predictability, by combining a defined process with the known execution costs of software tools.

The vulnerability management activities that were presented further strengthen the robustness of systems from both, the compliance as well as the information security perspective.

The inherent documentation of all automated activities facilitates meeting compliance regulations even as they change over time and the ability to re-run automated vulnerability scans on a regular basis, help security managers leap ahead of potential adversaries. This combination of robust security and regulatory compliance creates advantages for medical organizations.

References

- [1] O. Jones, "Article Title", *Journal*, Volume, Publisher, Location, Date, pp. XX-YY.
- [2] O. Jones, M. Thompson, and J.K. Nielsen, *Book Title*, Publisher, Location, Date.
- [3] Anderson, R., "Why information security is hard - an economic perspective". 17th Annual Computer Security Applications Conference. ACSAC. Proceedings (2001)
- [4] Blount, Summer. "The role of security management in achieving continuous compliance", Whitepaper: Compliance, CA Security Management, October 2006
- [5] Brenner, M. Classifying ITIL Processes; A Taxonomy under Tool Support Aspects. Business-Driven IT Management, 2006. BDIM '06. The First IEEE/IFIP International Workshop on, (2006), 19-28.
- [6] Chen, Y. Stakeholder Value Driven Threat Modeling for Off The Shelf Based Systems. International Conference on Software Engineering, IEEE Computer Society Washington, DC, USA (2007), 91-92.
- [7] Frei, S., May, M., Fiedler, U., and Plattner, B. Large-scale vulnerability analysis. Proceedings of the 2006 SIGCOMM workshop on Large-scale attack defense, ACM (2006), 131-138.
- [8] [Frühwirth Christian. "On Business-Driven IT Security Management and Mismatches between Security Requirements in Firms, Industry Standards and Research Work". PROFES 2009: pp. 375-385 (2009)

Note: *The scientific results described in this paper have been obtained on the base of support of contract No.102nd41-7*

COMPUTER SIMULATION OF INTERPOLATION OF THE SPECTRUM OF ECG SIGNAL

Assoc. Prof. Dr. Mariya Nikolova¹, Eng. Tzveta Dimitrova²

¹Department of Mathematics and Informatics,
N. Y. Vaptsarov NAVAL ACADEMY
73 V. Drumev St., Varna 9026, BULGARIA

²Technical University Sofia
8 Bul. K. Ohridski
E-mail: mpn@abv.bg; tz.dimitrova@gmail.com²

Abstract

Computing experiments for restoration of the ECG signal's spectrum by means of interpolation were carried out. A loss of spectrum for different frequency values was simulated. The computations were made in Matlab. The built-in functions for interpolation in Matlab were used, as well as the mathematical method of L. Aizenberg for analytical continuation of finite spectrum. The software, which provides application of Aizenberg's method, has been programmed also in MATLAB. The errors of signal's restoration in the cases of different number of values of loss have been calculated.

The results received from the built-in Matlab functions and algorithm written on the Aizenberg's method was compared.

1. INTRODUCTION

It is quite often necessary to remove the noise, focused in determined band while accepting a signal with finite Fourier spectrum. Or, which is mathematically the same - to eliminate noise in the spectrum focused on the Fourier finite signal in a band. This is a task for the interpolation of the spectrum of Fourier of a finite signal or a task for signal interpolation of finite spectrum. The report presents the results of interpolation of the spectrum of cardio signal.

In order to support clinical decision-making, reasoning tool to the ECG signal must be clearly represented and filtered, to remove out all noises and artifacts from the signal. ECG signal is one of the biosignals that is considered as a non-stationary signal and needs a hard work to denoising. Interpolation of signal, which is lost at a certain time interval must be used.

In regard to this, in the computer experiments Aizenberg's formulas have been used for interpolation of the analytical functions and built-in Matlab functions `interp 1` and `interpft`.

2. INTERPOLATION OF THE SPECTRUM OF ECG SIGNAL WITH AIZENBERG METHOD

Viner's class W_{α}^{+} , consists of functions, which have Fourier spectrum, concentrated in the interval $[0, \alpha]$. The task for interpolation of the function $f(x)$

in W_{α}^{+} is solved from L. A. Aizenberg [1]. If $f \in W_{\alpha}^{+}$, the formula for interpolation of $f(x)$ has the following form (1):

$$f(x) = \lim_{m \rightarrow \infty} \sum_{k=1}^m f(x_k) \frac{2i\sigma}{x - x_k + 2i\sigma} \prod_{\substack{j=1 \\ j \neq k}}^m \frac{(x - x_j)(x_k - x_j + 2i\sigma)}{(x - x_j + 2i\sigma)(x_k - x_j)} \quad (1)$$

The known values of the spectrum are marked with $f(x_k)$, they are numbered m .

The above formula can be applied for interpolation of the spectrum of one-dimensional signals and in item 4 the results of the recovery of spectrums of ECG signals will be presented as a simulated loss of spectral values.

Formula (1) contains two parameters m and σ . The accuracy of signal restoration depends on their values. Results from previous experiments show that the number m of the known values of the spectrum must be not more than 30.

The parameter σ is defined by searching of the minimal root mean-square error ε_{sqr} by formula (2) between the real and interpolated spectral values:

$$\varepsilon_{sqr} = \sqrt{\frac{1}{n} \sum_{i=0}^n (x_i - \tilde{x}_i)^2} \quad (2)$$

where x_i and \tilde{x}_i are the values of the real and restored signal.

3. COMPUTER EXPERIMENTS FOR SPECTRUM INTERPOLATION OF ECG SIGNAL

Data from echograph are entered in the form of Microsoft Excel WorkBook (xls). The Excel table contains 3 columns of 7680 values for the cardiac signal parameters. Each of these columns is imported into the Matlab's Array Editor and stored as a separate variable in Matlab's Workspace. Then it is stored in Workspace as a .mat-file. Formula (1) is programmed on Matlab as a function, called in program in the form of m-script file. The algorithm of the program is as follows:

1. .mat-file with cardiogram data opens
2. With the function fft from Matlab the spectrum of the signal (separately for the both channels) is found
3. The user enters the values of the start and end points of the frequencies of both intervals in which the signal (named s0) of the first channel is known.
4. Function is called, in which formula (1) is programmed. The missing spectral values can be found by it using interpolation.
5. Graphs of the theoretical ECG signal' spectrum and the signal obtained by formula (1) are plotted.
6. The results for the absolute and root mean-square errors of the signal from the first channel are found.
7. Steps 3 - 6 are repeated for the signal (named s1)'s spectrum from the second channel.

Computational experiments for restoration of the signal are performed by the use of the functions interp1 and interpft as well. The values of the spectrum are introduced as complex numbers in the function using the algorithm Aizenberg. The functions interp1 and interpft required values of the function that will interpolate to be real numbers. Therefore, as input data for these functions amplitude signals from each of the two channels of the ultrasound are used.

In the spectrum of the interpolation with interp1 a method 'pchip' is used. (Piecewise cubic Hermite interpolation). It gave better results (less error recovery) compared with the methods 'linear' (Linear interpolation) and 'nearest' (Nearest neighbour interpolation). Interpolation according to the method 'spline' was not done, because during its performance interp1 function failed and issued an error. Since when interpft function was used a very large absolute error $\varepsilon_{abs} = 69.8726$ was ob-

tained, in section 4 only the results of interpolation with interp1 are presented.

A computing experiment on interpolation of a spectrum with noise of ECG signal using the method of Aizenberg, was carried out. A block diagram of the algorithm of Matlab-function that realizes the formula (1) is presented in Fig. 1. Variables in it have the following meanings: Input parameters: IN1B - the first frequency from x_k in the first interval (before the area with noise) where the values of the spectrum are known; IN1E - the last frequency of x_k in the first range; IN2B - the first incidence from x_k in the second interval (after the area with noise) where the values of the spectrum are known; IN2E - the last frequency from x_k in the second interval; M - the number m of formula (1) of all the known values of the spectrum; sf - the input spectrum (with noise) signal; sigma - parameter σ of (1); MAXABSER - first value of absolute error, MAXABSER = 0.001; MAXSQRER - first value of mean-square error, MAXSQRER = 0.001.

Output parameters: MAXSQRER1 - calculated mean square error; MAXABSER1 - calculated absolute error; S - interpolated amplitude spectrum of f(x) of (1); F2 - interpolated spectrum in complex form; Stru - the real amplitude (spectrum with noise)

Auxiliary variables: L, J and K are used for management of the cycles, P - production Π in (1), SUM - Σ of (1) X - vector of frequencies x from (1); LL - secondary variable for calculating mean square error.

4. RESULTS FROM THE COMPUTING EXPERIMENTS

On Figure 2 it is shown the interpolation, using (1) of a spectrum of a recorded ultrasound signal in time domain. The spectrums of the signals s0 and s1 from the two channels are calculated and it is modelled loss of one spectral component under number 16. On Fig. 2 in both signals the number of known spectral values $m = 28$. Errors of the recovered signals in the frequency domain are: for s0: absolute error: $\varepsilon_{abs} = 0.9505$, root mean square error $\varepsilon_{sqr} = 0.1796$; for s1: $\varepsilon_{abs} = 0.7642$, root mean square error $\varepsilon_{sqr} = 0.1419$. On all figures the graph of the interpolated values is in blue, and the real (unprocessed) signal values are in red.

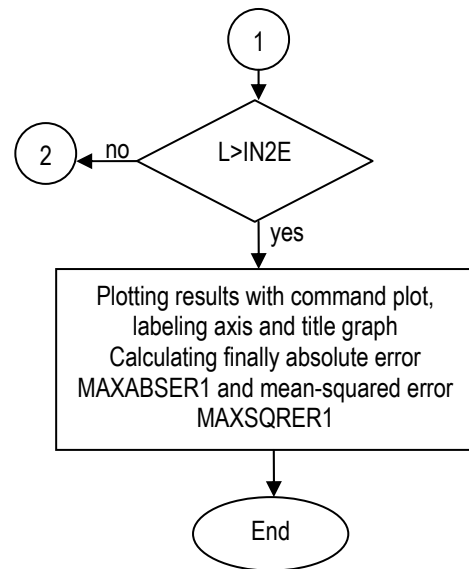
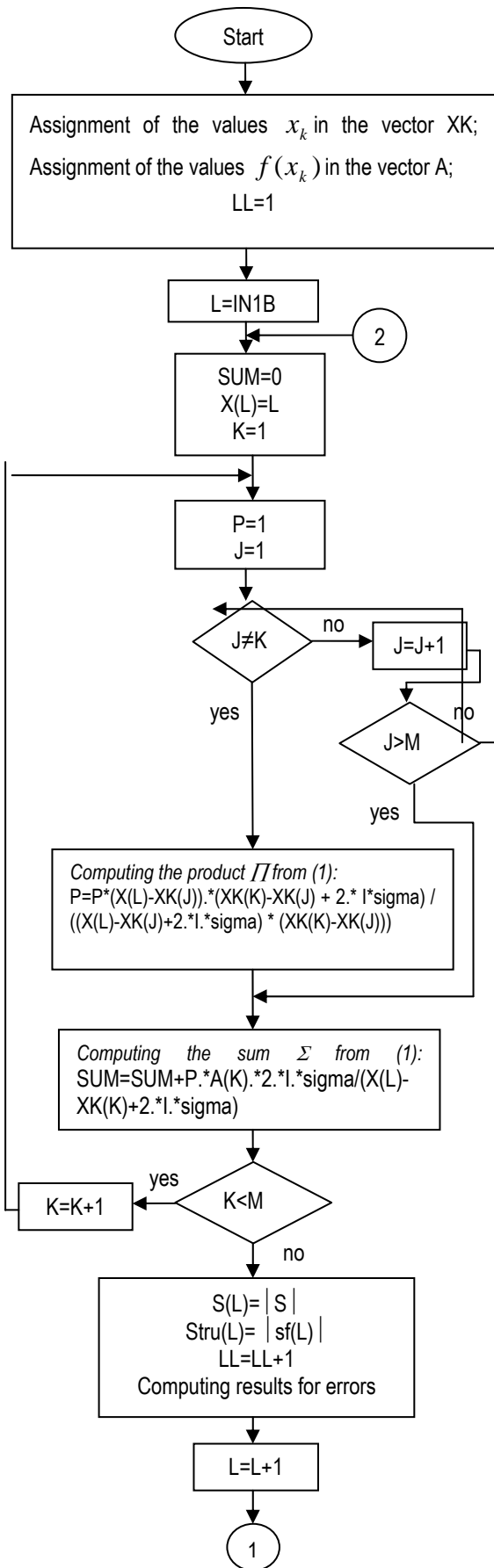


Fig. 1. Scheme of algorithm, computing formula (1)

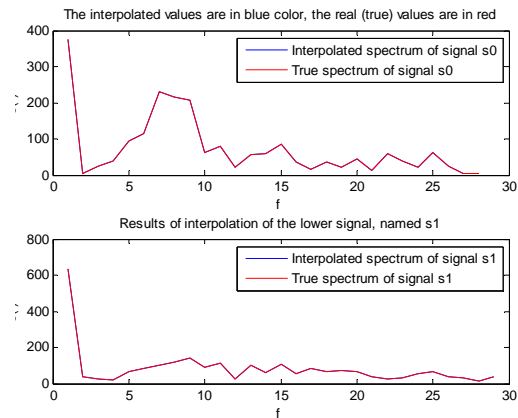


Fig. 2. Interpolation of the spectrum by the method of Aizenberg when 1 spectral value is lost

Fig. 3 shows the interpolation of 16 component of the spectrum signal s0, using built-in function interp1, method pchip. Values obtained for mean-square and absolute error were as follows: $\mathcal{E}_{sqr} = 2.6605$ и $\mathcal{E}_{abs} = 14.3271$.

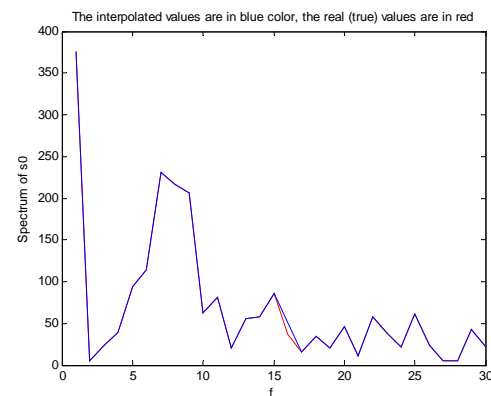


Fig. 3. Interpolation of the spectrum by interp1 when one spectral value is lost

From Fig. 2, Fig. 3 and the values of the errors show that better results in the interpolation of a value obtained through the application of the method of Aizenberg. In Fig. 4 a) is presented the spectrum of ECG with noise, and in Fig. 4 b) - interpolated spectrum for frequencies in the range [41, 42] where there is noise.

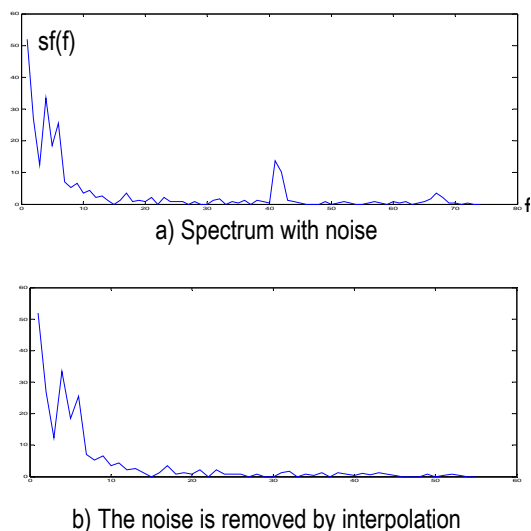


Fig. 4. Interpolation of the noised spectrum by the method of Aizenberg when two spectral values are lost

5. CONCLUSION

The Aizenberg method gives more accurate results (less error) for the recovery of the spectrum of ECG signal in comparison with built-in Matlab function `interp1` and `interpft`. For recovering the values in a larger interval the formula (1) can be repeatedly used, as x_k are taken also from the frequency of recovered intervals in previous figures.

Note: The scientific results described in this paper have been obtained on the base of financial support of contract No.102nđ41-7

References

- [1] Aizenberg L., Dimiev S. P., Marinov M. S., Complex analysis and some applications, TU - Sofia, 1992, Bul.
- [2] Henzel N., and J. Leski, 1999. Efektywna obliczeniowo metoda analizy acyklicznych zdarzeń przy pomocy technik wieloczesotliwościowych. XI konferencja Biocybernetyka i Inżynieria Biomedyczna, pp 188-122.
- [3] Matlab Help.
- [4] Thakor N.V., J. G. Webster, and J. Tompkins, 1985. Estimation QRS complex power spectra for design of QRS filter, IEEE Transactions on biomedical engineering, Vol. 31, pp: 702-706.
- [5] V.Almenar, A.Albiol, 1999. A new adaptive scheme for ECG enhancement, Signal Processing 75, pp: 253-265

NETWORK PERIMETER SECURITY FOR MEDICAL INFORMATION SYSTEMS

Tzveta Dimitrova

Faculty of Telecommunication, Technical University - Sofia, 8, "Kliment Ohridsky" str., 1000 Sofia, Bulgaria,
E-mail: tz.dimitrova@gmail.com

Abstract

This study analyzed vulnerabilities in networked computer systems that are accessible from the internet. Vulnerabilities are defects, bugs or misconfigurations in software that can be exploited by an attacker to compromise the confidentiality, integrity or availability of information. Vulnerabilities in networked systems are a major source of today's information security risks, as they expose an organization and its assets to external threats like black-hat hackers, crackers or plain criminals. New vulnerabilities are discovered every day. Thus, with the development of telemedicine, hospitals that rely on dependable information systems need to frequently assess their exposure to these vulnerabilities in order to be able to manage their risk. Today, vulnerability management is no longer just a technical need, it has become a legal requirement for many medical organizations that seek to fulfill modern compliance regulations and conduct business internationally. The article presents the results of a recent vulnerability exposure assessment conducted in 32 different medical organizations. The results show the most vulnerable system types, service families and network ports. They further evaluated differences in the risk exposure of medical organizations with different kinds of vulnerability management practices such as regular automated vulnerability scans.

1. INTRODUCTION

The following analysis is based on the assessment of 523 Vulnerabilities on 42 hosts in 32 medical organizations. To protect the identity of the participating medical organizations and because the same standard software products like Apache web servers or PHP are used in all medical organizations regardless of their size, headcount or business area we have excluded that information from the assessment. The purpose of the analysis is not to provide statistical proof for particular claims, but to learn from examples to help better protect all medical organizations' assets.

2. KEY FINDINGS:

High-risk vulnerabilities make up one third (33%) of the total number of identified vulnerabilities.

A large part of the analyzed medical organizations (47%) suffered from such high-risk vulnerabilities. However, 41% managed to have neither high nor medium-risk vulnerabilities. (Figure 1)

Medical organizations that manage their vulnerability exposure through regular vulnerability scans or security audits show a tendency of reduced risk exposure compared to other medical organizations.

The most common vulnerability had an average CVSS severity score¹ of 5.86 (at a standard deviation

of 1.79) and is found on a web server running PHP behind the ports 80 or 443.

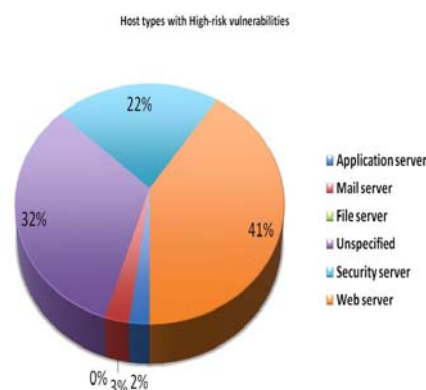


Fig. 1: The share of hosts that suffered from high-risk vulnerabilities - by host type.

3. RISK FACTORS OF VULNERABILITIES BY HOST TYPE²

The identified vulnerabilities were unevenly distributed among the analyzed host types. The largest share of high-risk vulnerabilities was found on web servers, followed by application and security servers. An explanation for the surprisingly high number of vulnerabilities on security servers, such for example firewalls, could be the fact that many of these security systems are themselves based on vulnerable

¹ The Common Vulnerability Scoring System (CVSS) measures the relative severity of a vulnerability on a scale from 0 (low) to 10 (high). CVSS is used by the National Vulnerability Database (NVD). Specification available online at <http://www.first.org/cvss/>

² The type of a server was determined by the its main use in the organization and not by its technical characteristics such as installed software. The main use was provided by the organization in a pre-study questionnaire.

platforms like Linux, Unix or provide user interfaces using insecure PHP/HTTP components. (Table 1)

Table 1: The share of host types that suffered from high-, medium- or low risk vulnerabilities

Host Type	High	Medium	Low	Total
Application server	2%	1%	0%	1%
Mail server	3%	1%	0%	1%
File server	0%	0%	0%	0%
Unspecified	32%	80%	74%	71%
Security server	22%	8%	12%	10%
Web server	41%	10%	14%	16%
Total	100%	100%	100%	100%

4. VULNERABILITY FAMILIES

PHP vulnerabilities were overall the most common, followed by those related to the Apache web server and SSH, SSL. When only severe vulnerabilities (with a CVSS score >7) are taken into consideration however, the Apache vulnerabilities are almost insignificant whereas PHP weaknesses dominate the picture. (Figure 2). The common web ports 80 (HTTP) and 443 (HTTPS) lead in all risk categories. Most vulnerability that were found on the standard SSL port 22 were only of low risks. (Table 2).

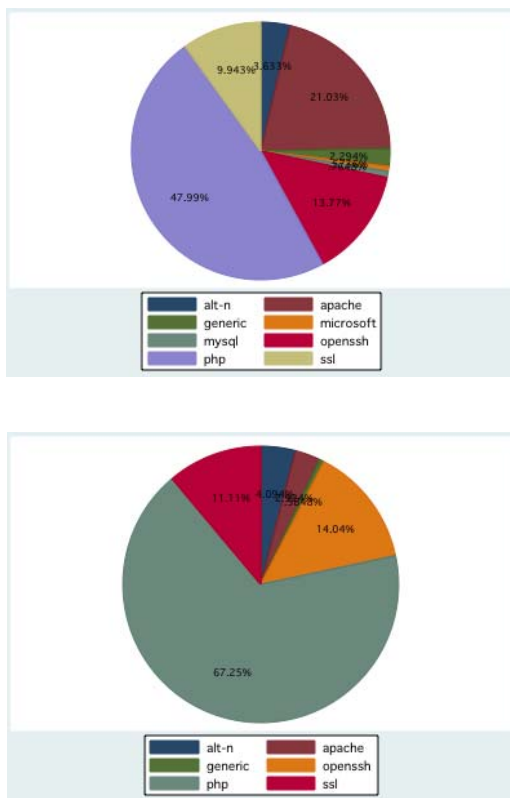


Fig. 2. Up - all vulnerabilities – Down: Vulnerabilities with CVSS score > 7

Table 2: Suffered from vulnerabilities with a risk factor of:

Port	High	Medium	Low	Total
21	0%	2%	0%	1%
22	9%	8%	26%	10%
25	0%	1%	0%	0%
80	58%	38%	34%	44%
110	4%	4%	5%	4%
443	19%	21%	8%	20%
445	1%	1%	3%	1%
465	1%	0%	0%	0%
587	0%	0%	0%	0%
666	1%	6%	3%	4%
822	5%	3%	11%	4%
995	1%	1%	0%	1%
3306	0%	1%	5%	1%
3389	0%	0%	0%	0%
4242	1%	6%	3%	4%
7600	1%	6%	3%	4%
8088	1%	1%	0%	1%
19638	1%	1%	0%	1%
Total	100%	100%	100%	100%

5. MEDICAL ORGANIZATIONS

A quarter (25%) of the analyzed medical organizations were evaluating their vulnerability exposure on a regular basis either through security audits (9%), automated (16%)- or manual vulnerability scans (19%). Medical organizations that did not conduct such evaluations showed a tendency towards larger numbers of high- and medium risk vulnerabilities on their hosts. (Figure 3).

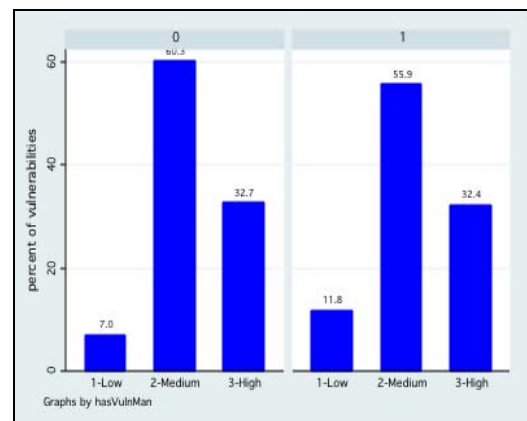


Fig. 3: Left: Medical organizations without vulnerability management activities. Right: Medical organizations conducting Security audits or automated or manual vulnerability scans.

Average vulnerability severity in medical organizations

A large part of the analyzed medical organizations (47%) suffered from high-risk vulnerabilities. However, 41% managed to have neither high nor

medium-risk vulnerabilities. The average severity score across all identified vulnerabilities was 5.86 (with a standard deviation of 1.79). (Figure 4) (Table 3).

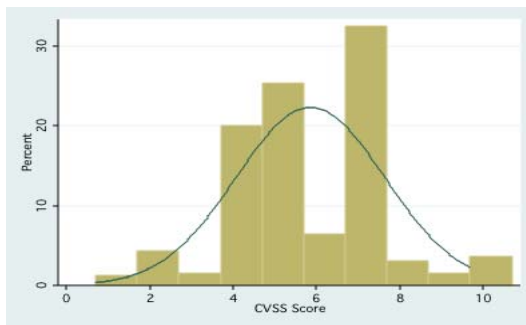


Fig. 4: Histogram of the CVSS scores of all identified vulnerabilities

Table 3: Suffered from 1 or more vulnerabilities with a risk factor of

Organization	High	Medium	Low
ID001	yes	yes	no
ID002	no	yes	no
ID003	yes	yes	yes
ID004	no	no	no
ID005	no	no	no
ID006	yes	yes	yes
ID007	no	no	no
ID008	no	no	no
ID009	yes	yes	yes
ID010	no	no	no
ID011	yes	yes	yes
ID012	no	no	yes
ID013	yes	yes	yes
ID014	no	yes	no
ID015	yes	yes	yes
ID016	no	yes	no
ID017	yes	yes	no
ID018	yes	yes	no
ID019	yes	yes	no
ID020	no	no	no
ID021	yes	yes	no
ID022	no	no	no
ID023	no	no	no
ID024	no	no	no
ID025	no	no	no
ID026	no	yes	no
ID027	yes	yes	no
ID028	yes	yes	no
ID029	yes	yes	no
ID030	no	no	no
ID031	yes	yes	yes
ID032	no	no	no

6. CONCLUSIONS

Among the participating medical organizations in this study, many showed a low level of vulnerability exposure and demonstrated that high-risk vulnerabilities are not inevitable. Based on their success, we suggest the following actions to be taken by organization managers and network administrators.

Network administrators

There are clear hot spots for vulnerabilities: Services related to web servers are among the most common sources for vulnerabilities. These systems are worthy extra attention and should be evaluated more regularly by administrators and their security staff.

All of the vulnerabilities identified in this study were found using automated vulnerability scanning tools that are publicly available. Administrators should make increasing use of the automated tools in order to be able to reduce their workload and conduct evaluations more frequently.

Organization Managers

Many of the found vulnerabilities had been publicly known for a long time. Establish an organizational process to find and react on new vulnerabilities in a timely manner.

As medical organizations change so do their Medical IT systems and their exposure to vulnerabilities. The more dynamic a network or a system becomes the more frequent vulnerability exposure assessments should be carried out.

References

- [1] O. Jones, M. Thompson, and J.K. Nielsen, *Book Title*, Publisher, Location, Date.
- [2] Anderson, R., "Why information security is hard - an economic perspective". 17th Annual Computer Security Applications Conference. ACSAC. Proceedings (2001)
- [3] Blount, Summer. "The role of security management in achieving continuous compliance", Whitepaper: Compliance, CA Security Management, October 2006
- [4] Brenner, M. Classifying ITIL Processes; A Taxonomy under Tool Support Aspects. Business-Driven IT Management, 2006. BDIM '06. The First IEEE/IFIP International Workshop on, (2006), 19-28.
- [5] Chen, Y. Stakeholder Value Driven Threat Modeling for Off The Shelf Based Systems. International Conference on Software Engineering, IEEE Computer Society Washington, DC, USA (2007), 91-92.

- [6] Frühwirth Christian. "On Business-Driven IT Security Management and Mismatches between Security Requirements in Firms, Industry Standards and Research Work". PROFES 2009: pp. 375-385 (2009)
- [7] L. Cranor, P. Guduru, and M. Arjula. User interfaces for privacy agents. *ACM Transactions on Computer Human Interaction*, 12(2):135–178, 2006.
- [8] R. de Paula and et. al. Two experiences designing for effective security. In *SOUPS '05: Proceedings of the second symposium on Usable privacy and security*, New York, NY.
- [9] R. Dhamija, J. Tygar, and M. Hearst. Why phishing works. In *Proceedings of the SIGCHI Conference on Human Factors in Computing Systems*, 2006.
- [10] J. S. Downs, M. B. Holbrook, and L. F. Cranor. Decision strategies and susceptibility to phishing. In *SOUPS '06: Proceedings of the second symposium on Usable privacy and Security*, New York, NY, USA, 2006. ACM.
- [11] D. Florencio and B. C. Cormac Herley. Do strong web passwords accomplish anything? In *Proceedings of the USENIX Workshop on Hot Topics in Security (HotSec)*, 2007.

The author wish to thank the European Commission for the grant in the Lifelong Learning Programme, the Executive Agency for its help and all the partners of the project for their contribution.

*Project Number: 142814-LLP-1-2008-FR-ERASMUS-ENW
Instrument type: ERASMUS NETWORK*

AN EOG BASED HUMAN COMPUTER INTERFACE SYSTEM FOR ONLINE CONTROL

Carlos A. Vinhais, Fábio A. Santos, Joaquim F. Oliveira

*Departamento de Física, ISEP – Instituto Superior de Engenharia do Porto
Rua Dr. António Bernardino de Almeida, 431, 4200-072 Porto, Portugal
Tel: +351 228340500, Fax: +351 228321159
cav@isep.ipp.pt | fabioss.k@gmail.com | mail@filipeoliveira.info*

Abstract

Human to machine interfaces have received more and more attention of researchers in recent years. Electrooculography (EOG) is a new technology to sense eye signals and can be used as an efficient bio-based human computer interface (HCI). The paper is concerned with the design and implementation of an eye movement detection system for biomedical research. The described system includes several electronic units for acquisition, conditioning, amplification and noise filtering of measured voltage signals. Analog to digital conversion of such biopotentials is achieved with an Arduino BT board. With its built-in Bluetooth module, it allows for wireless communication to personal computers for further signal processing and analysis. Experimental results based on real-life EOG signals show that the developed system is efficient in terms of accuracy and applicability. The proposed solution is a low-cost general purpose EOG-based HCI system that can be used by patients with disabilities for communication.

1. INTRODUCTION

Traditional methods of control or communication between humans and machines, e.g. mouse and keyboard, require a certain control motor on the part of the users. However, many people with severe disabilities only retain their control capacity over the oculomotor system. Therefore, the focus on the development of new human computer interface (HCI) and communication systems based on the detection of eye position has increased in the last years.

Electrooculography (EOG) is a new technology of recording both horizontal and vertical eye movements, by measuring, in real time, very small electrical potentials that exist across the cornea and the retina. Such signals are easily detected by placing electrodes on user's forehead around the eyes. Also, the relationship between EOG waveforms and eye movements is almost linear.

EOG based HCI is becoming the hotspot of bio-based HCI research in recent years, since it provides users with a degree of independence in the environment. This method was used as the guidance strategy in assistive devices for controlling wheelchairs for disabled people [1]. It also represents an efficient computer interface to improve communication abilities of those patients [2, 3, 6]. EOG has also been used as a measurement device used in psychophysiological tests as research equipment for recording facial expressions during human emotion studies [4]. Furthermore, applica-

tions can be extended to normal persons as well, in robotics and entertainment.

As a contribution in this area of biomedical research, we present a general purpose EOG based HCI system for online control. The proposed approach includes several electronic modules for acquiring and filtering EOG waveforms, generated from different eye movements such as looking up/down, right/left and eye blinking. The system also provides wireless data transmission to a personal computer (PC) for further signal processing and analysis.

The paper is organized as follows: Section 2 introduces the fundamental principles of detecting and acquiring EOG signals. Section 3 describes the design of the proposed HCI system in detail. Experimental results of several eye movements and blinking are illustrated in Section 4 and the conclusion is given in Section 5.

2. EOG DETECTION PRINCIPLES

EOG is a method for sensing eye movement and is based on recording the standing corneal-retinal potential arising from hyperpolarizations and depolarizations existing between the cornea and the retina [1]. Such biopotential, commonly known as an electrooculogram, is captured by five surface electrodes placed around the eyes, as shown in Figure 1.

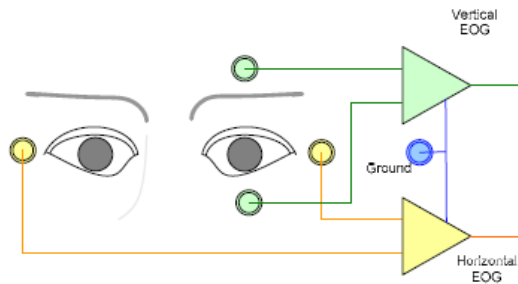


Fig. 1. Electrodes placement [2, 5]

Independent measurements can be obtained: two electrodes are placed on the temples to detect horizontal movements, while another pair above and below the eye is used to detect vertical motion and eye blinking. A reference electrode (ground) is placed on the forehead or at the mastoid [6].

The corneal-retinal potential is roughly aligned with the optic axis and hence rotates with the direction of gaze. When the gaze is shifted, positive or negative pulses will be generated when the eyes are rolling, e.g. upward or downward. The amplitude of EOG pulses will be increased with the increment of rolling angle, and their width is proportional to the duration of the eyeball rolling process.

EOG values vary from **tens to hundreds of** μV , with a frequency range of about DC-100 Hz. The EOG signal changes approximately $20 \mu\text{V}$ for each degree of eye movement and is practically linear for gaze angles up to 30° [1]. Therefore, with proper calibration, EOG can be used to accurately specify the angular position of the eyeball in both vertical and horizontal channels.

3. HCI SYSTEM DESIGN

The block diagram of the proposed HCI system is shown in Figure 2. The system is microcontroller (μC) based, battery powered, and is composed of four main parts or units: signal pre-amplification, signal filtering, analog to digital conversion (ADC) and data transmission to PC.

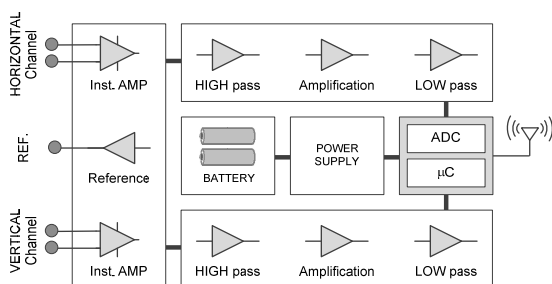


Fig. 2. EOG based HCI system block diagram

Five Ag/AgCl electrodes (two for each channel and one for ground) are used to acquire EOG signals. The pre-amplification circuit is intended to amplify the signals to appropriate amplitude. The EOG signal filtering unit includes a band-pass analog filter (a combination of high-pass and low-pass filter) to remove the baseline and higher frequency interference. The total gain of the system is achieved by implementing signal amplification into two stages, each having a fixed gain. Analog to digital conversion is then performed, and horizontal and vertical EOG signals are finally transmitted to the PC serial port over Bluetooth wireless technology. Free open source is used to program the microcontroller and display EOG waveforms in real-time.

3.1. Power Supply

The whole circuit is operated from a single +5 V power supply, by using a 7805 voltage regulator. The chip ICL7660 was used to perform supply voltage conversion, resulting in complementary output voltage -5 V . The circuit has been powered with a simple +9 V battery.

3.2. Pre-amplification

According to the characteristics of EOG signals, the differential amplifier chip INA126P was selected for the acquisition and pre-amplification step, as it can handle EOG signals in μV range. The INA126P is a precision instrumentation amplifier for accurate, low noise differential signal acquisition. The gain of the INA126P is set by simply adjusting the value of a single external resistor R_G :

$$G_1 = 5 + (80 \text{ k}\Omega / R_G) \quad (1)$$

A protection system in the form of an RC low-pass filter was also implemented at the INA126P's inputs, in order to remove electro-static discharge and radio frequency interference [2].

3.3. Reference Electrode

To improve the INA126P's common mode rejection ratio (-94 dB), a driven-right leg circuit was implemented. Here, a low-noise high-precision OPA2227 dual amplifier was used. This circuit reads what it believes to be noise and transfers a minute signal back to the body through reference electrode to negate its effect. This technique is

normally used in medical operations when reading a very small electrical potential from the body.

3.4. Signal Filtering

A critical issue in accurately acquiring and amplifying the EOG potential, is overcoming a substantial DC offset generated by the potential difference between the reference electrode and each of the active electrodes. For reducing DC offset and some other shifting resting potentials, an active high-pass filter is employed with cutoff frequency at 0.20 Hz. Once DC component is removed, an OPA227 amplifier circuit is designed to complement the entire magnification required. The formula for gain depends on two resistors R_A and R_B :

$$G_2 = 1 + (R_B / R_A) \quad (2)$$

The power line noise and high frequency components of EOG signals are then greatly reduced with low-pass filtering. A cutoff at 32 Hz was selected due to bandwidth of EOG signals. A single OPA4227 was used to implement both 4th order Bessel filters.

3.5. Data Acquisition

After all amplifications and filtrations, EOG signals are digitized and transferred to PC. Analog to digital conversion with 10 bits of resolution is done using a microcontroller board *Arduino* BT [7]. Since it supports wireless serial communication over Bluetooth, software was written in *Processing* [8] to read incoming data from the PC serial port and display the measured signals on the screen saved real-time.

4. EXPERIMENTAL RESULTS

In building the whole circuit, number of components was tried and final component selection was based on optimal performance. Therefore, the two-stage signal amplification was implemented by using $R_G = 806 \Omega$, $R_A = 994 \Omega$ and $R_B = 55.8 \text{ k}\Omega$. From equations 1 and 2, $G_1 = 104$ and $G_2 = 57$. Thus, for each EOG channel, the total gain of the system was set to $G = G_1 * G_2 = 5928$. Some examples of EOG waveforms acquired from horizontal and vertical eye movements and eye blinking are shown in Figure 3.

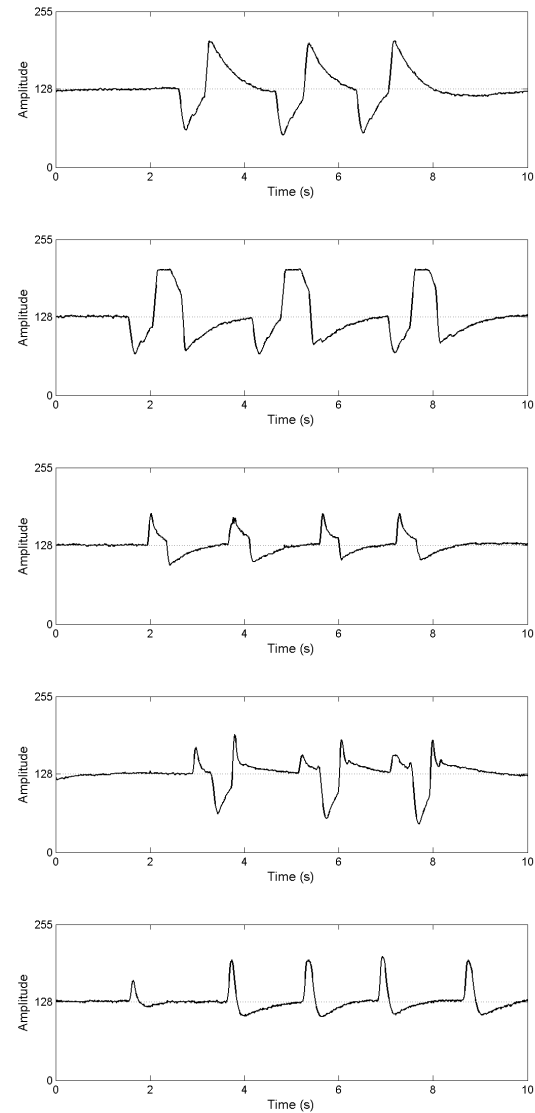


Fig. 3. EOG waveforms. From top to bottom: Center-RIGHT, Center-RIGHT-LEFT, Center-UP, Center-UP-DOWN and eye blinking

All signals were sampled at 100 Hz (10 ms per sample), which rightly follows the Nyquist rate. Experiments with higher sampling frequency (500 Hz and 1 kHz) were also performed. In all cases, similar results were obtained.

5. CONCLUSION

A general purpose EOG based HCI system for eye movement detection was presented. With a simple design, the system is μC -based, battery powered and supports wireless data transmission to PC. The results show that the proposed system has stable performance and can be used as an effective low-cost solution for online control applications.

References

- [1] R. Barea, L. Boquete, M. Mazo, and E. López, System for Assisted Mobility Using Eye Movements Based on Electrooculography, *IEEE Trans. on Neural Systems and Rehabilitation Engineering*, 10(4), 209-218 (2002).
- [2] A.O. Malik, and J. Ahmad, Retina Based Mouse Control (RBMC), *World Academy of Science, Engineering and Technology*, 31, 318-322 (2007).
- [3] B. Usakli, S. Gurkan, F. Aloise, G. Vecchiato and F. Babiloni, On the Use of Electrooculogram for Efficient Human Computer Interfaces, *Computational Intelligence and Neuroscience*, Vol. 2010, Article ID 135629, 5 pages (2010).
- [4] A.T. Vehkaoja *et al.*, Wireless Head Cap for EOG and Facial EMG Measurements, *Conf Proc. IEEE Eng Med Biol Soc*, 5865-5868 (2005).
- [5] Y. Chen, "Design and evaluation of a human-computer interface based on electrooculography", *Master Thesis* (2003) *unpublished*.
- [6] Zhao Lv, Xiao-Pei Wu, Mi Li and De-Xiang Zhang, Development of a human computer Interface system using EOG, *Health*, 1, 39-46 (2009).
- [7] Arduino – <http://arduino.cc/>
- [8] Processing – <http://processing.org/>

AUTHOR INDEX

AMPILOVA, N.	78	KOLEV, S.	29
ANTONOVA, V.	31	KOUNTCHEV, R.	54,58
BARBAROSOU, M.	85	KOUNTCHEVA, R.	54
BERŠKIENĖ, K.	93	MANOLOVA, A.	69
BIKULCIENE, L.	89	MARATOS, N.	85
BOULTADAKIS, G.	13	MARTINS, M. J.	19
CARVALHO, C.	31	MILEV, D.	116
CHAZIACHMETOVAS, A.	39,47	MIRONOV, R.	58
CHRISTOPOULOU, M.	82	NAVICKAS, Z.	89,93
CITAVICIUS, A.	47	NIKITA, K.	82
DEMIREV, V.	22,25	NIKOLOVA, M.	124
DIMITROV, D.	31	OLIVEIRA, J.	132
DIMITROVA, TZ.	120,124,128	PAPAGEORGIU, K. A.	1
DRAGANOV, I.	65	POPOVA, A.	65
DUMBRAVA, V.	39,43	RODRIGUES, J. F.	19
ESCUDEIRO, N.	35	SANTOS, F.	132
ESCUDEIRO, P.	35	SAUTBEKOV, S. S.	5
FRANGOS, P. V.	5,13	SAVOV, S.	104
GEORGIEVA, V.	108,112	SHTARBOVA, S.	112
GUREVICH, E.	78	ŠMIDTAITĖ, R.	89
GRIGORATOU, E.	13	SOLOVIEV, I.	78
HRISTAKIS, H.	13	SPIROV, R.	73
HRISTOV, V.	50	STERGIANNIS, E.	13
ILIEVA, R.	97,101	SVILAINIS, L.	39,43,47
JARUŠEVIČIUS, G.	93	TSEREMOGLU, I.	13
JORDANOVA, L.	120	UZUNOGLU, N.	82
KALLITSIS, E.	13	VAGIANOU, A.	13
KARAKASILLOTIS, A.	13	VAINORAS, A.	89,93
KARANASIOU, I.	82	VALCHEV, D.	62
KASIMKHANOVA, R. N.	5	VASILEVA, V. Y.	9
KITOV, S.	43	VINHAI, C.	132
KLIROS, G. S.	1		